VIEW SYNTHESIS FOR KINETIC DEPTH X-RAY IMAGING

Omar Abdulmola Abusaeeda

A thesis submitted in partial fulfilment of the requirements of Nottingham Trent University for the degree of Doctor of Philosophy

December 2012

Declaration

Abstract

This thesis reports the development and analysis of feature based synthesis of transmission X-ray images. The synthetic imagery is formed through matching and morphing or warping line-scan format images produced by a novel multi-view X-ray machine. In this way video type sequences, which periodically alternate between synthetic and detector based views, may be formed. The purpose of these sequences is to provide depth from motion or kinetic depth effect (KDE) in a visual display; while the role of the synthesis is to reduce the total number of detector arrays, associated collimators and X-ray flux per inspection. A specific challenge is to explore the bounds for producing synthetic imagery that can be seamlessly introduced into the resultant sequences. This work is distinct from the image collection and display technique, termed KDEX, previously undertaken by the Imaging Science Group at NTU. The ultimate aim of the research programme in collaboration with The UK Home Office and The US Dept. of Homeland Security is to enhance the detection and identification of threats in X-ray scans of luggage.

A multi-view 'KDEX scanner' was employed to collect greyscale and colour coded image sequences of 30 different bags; each sequence comprised of 7 perspective views separated from one another by 1^0. This imagery was organised and stored in a database to enable a coherent series of experiments to be conducted. Corresponding features in sequential pairs of images, at various different angular separations, were identified by applying a scale invariant feature transform (SIFT). The SIFT was additionally bounded by epipolar-line and disparity window criteria. Experiments revealed that around 37% of unfaithful matches were removed. This approach was applied to greyscale imagery and colour coded materials discriminated views, produced by a dual-energy X-ray technique. Two competing approaches namely, direct matching versus material segmentation were developed and tested. The 'direct method' provided relatively enhanced matching performance.

The SIFT matching results are employed by a novel material based morphing to synthesise colour coded X-ray imagery. The technique was designed to conserve the colour coding scheme employed to represent the three different material classes. Error analysis revealed the presence of blurring and ghosting artefacts in the resultant synthetic views. In response a competing translation based image synthesis algorithm was proposed. This rival method reduced the blurring and ghosting artefacts to zero but at the expense of some shape distortion. However, it did provide marginally improved performance when the angular separation between generating views exceeded 5^0.

The fidelity of the synthetic imagery degraded as the angular separation between perspective views was increased. This finding is consistent with the commensurate increase in disparity and therefore dissimilarity between perspective views. The best fidelity intermediary views recorded in this research occurred at 2^0, which is the minimum angular separation of interest. This result is highly significant as for a given 3D or KDE imaging performance it can reduce the total number of X-ray sensor arrays, collimators and X-ray beams required by a factor of two.

Acknowledgements

It has been great honour and pleasure to undergo this PhD research project. One of the most significant challenges that I have ever had is the writing of this doctoral thesis and it would not have been achievable without the help and the support of the kind people around me. I would like to take the opportunity to express my humble gratefulness to thank and acknowledge several individuals who in whatever way contributed and extended their valuable assistance, patience and guidance in the preparation and completion of this thesis.

The first sincere gratitude should go to my director of studies, Professor Paul Evans for his guidance, valuable suggestions and encouragement all over the duration of this research programme. I would also like to express my deepest appreciation to my second and third supervisors Dr. Jer Wang Chan and Dr. David Downes for their efforts in getting the experiment data as well as their continuous assistance, guidance, and useful advice which have made the existence of my thesis.

Also, I would like to acknowledge the financial support of my beloved country, Libya which hopefully I will be able by one way or another to contribute in building it after the revolution to witness the new era of my much-loved country.

I would also like to be exclusively grateful to my mother, for her unwavering, continual and unlimited support. I wish my father was here to witness and admire my achievements but unfortunately he passed away since my childhood. I believe this thesis would not have been possible without the parent's encouragement. I am also highly thankful to my sisters and brothers for their care and countless support. Special thank must go to my elder brother; Mohamed whose wife and son passed away during my PhD programme.

Last but by no means least, I would like to express my gratefulness to my wife, daughter; Abrar and son; Abdulmola who have made my life undemanding, relaxed, cheerful and full of joys throughout my stay in the UK.

It is to all above, I owe my deepest gratitude!

List of Publications

Chan, J., Omar, A., Evans, J., Downes, D., Wang, X., & Liu, Y., "Feasibility of SIFT to synthesise KDEX imagery for aviation luggage security screening". IET, *Imaging for Crime Detection and Prevention (ICDP 2009), 3rd International Conference on,* pp. 1-6. London, UK, 3rd December 2009.

Abusaeeda, O., Evans, J., Downes, D., & Chan, J., "View synthesis of KDEX imagery for 3D security X-ray imaging". IET, *Imaging for Crime Detection and Prevention (ICDP 2011), 4th International Conference on,* pp. 1-6. London, UK, 3rd - 4th November 2011.

Abusaeeda, O., Evans, J., Downes, D., & Chan, J., "Animated depth employing image synthesis for 3D security X-ray imaging". *Signal Processing and Information Technology (ISSPIT 2011),* 11th *IEEE International Symposium on,* pp. 161-166. Bilbao, Spain, 14th -17th December 2011.

Abusaeeda, O., Evans, J., Downes, D. "Color view synthesis for animated depth security X-ray imaging". *32th International Conference on Computer Vision, Image and Signal Processing (ICCVISP 2012),* ISBN 2010-3778, pp. 1024-1029, Paris, France, 25th - 26th April 2012.

Table of Contents

List of Figures

List of Tables

Abbreviations

2D	Two-dimensional imaging
3D	Three-dimensional imaging
CT	Computer tomography
CAT	Computed axial tomography
CAST	Centre for Applied Science and Technology
H.O.S.D.B.	The UK Home Office Scientific Development Branch
US DHS	The US Department of Homeland Security
KDE	Kinetic depth effects
KDEX	Kinetic depth X-ray imaging
CCD	Charge coupled device
Lo	Low-energy signal
Hi	High-energy signal
Z	Material atomic number
FLXDA	Folded linear X-ray detector array
SIFT	Scale invariant feature transform
PCA-SIFT	Principal Components Analysis SIFT
SURF	Speeded-up robust features
b	Bag or luggage item
ERR	The number of pixel errors
ROI	Region of interest
GT	Ground truth image
ERR-I	Intensity error
ERR-II	Material class error
O	Organic material class
M	Metallic material class
X	Mixture material class
G	Greyscale material class
L	Left perspective view
R	Right perspective view
O_L	Left view organic class
M_L	Left view metallic class
X_L	Left view mixture class
G_L	Left view greyscale class
O_R	Right view organic class
M_R	Right view metallic class
X_R	Right view mixture class
G_R	Right view greyscale class
P	Positive matches
N	Negative matches
IEDs	Improvised explosive devices

List of Keywords

Ground truth image	The image produced by X-ray sensor
Synthetic image	The image produced by proposed synthesis algorithm
Repeating features or local similarity	Group of object features place close to each other in X-ray projection tend to limit the performance of the stereo matching algorithms
Overlapping structure	overlapping structures commonly found in cluttered X-ray images. overlapping refers to structures from different discrete objects, which overlap each other in the resultant image
Local contrast	The contrast is determined by the differential amount of X-ray attenuation produced by the two or more objects, which is a function of material compositions and thickness
Cross-fade or cross-dissolve	A common expression used to describe the linear combination of colours typically used by visible light image morphing techniques
Fold-overs	A geometric distortion arises from the inability of a warp to adequately respond or process the changing size of a corresponding object's, usually accrued when corresponding features between the source and destination objects are ill defined or incorrect
Multi-layered structure	Structure where many different objects in the projected X-ray overlap each other are produce significant shape change as they slide and rotate from view to view
Successive views	Two candidate images used to generate corresponding matches and synthetic views between them

Chapter One Introduction

1.1 Background

Airport luggage inspection is a challenging task, which involves numerous technological and human factors to consider. For example, identifying everyday items within complex arrangements and unusual juxtapositions is often difficult or impossible using a two-dimensional (2D) projection produced by a basic X-ray machine. This situation is compounded by any decrease in the screeners' alertness when constantly gazing at the display screen and observing similar objects over and over again. An informed terrorist will take advantage of all these 'natural' difficulties to conceal weapons, explosives and other paraphernalia of terrorism. Potential threats range from dense items such as metallic guns and knives through to less dense objects such as liquid explosives, plastic or ceramic guns, glass and wooden sharp items. The low density threats can produce very faint responses in the resultant X-ray projections, making them very difficult to detect and identify by screeners [1-3] and significantly compound luggage inspection problems [4]. In addition, the screening task includes several target categories whose full member set is not known (e.g. improvised guns, knives and explosives) and is exacerbated by the lack of visual cues to depth in an image that has been produced by transmitted radiation [5]. A number of different X-ray imaging techniques are used in airports for the inspection of luggage [6-8]; however, the workhorse of the security industry is the single view or 2D transmission X-ray machine with colour coded materials discrimination presented on a visual display.

The 2D transmission imaging system [9, 10] is fast and cost effective to operate but it produces visual images that do not contain any depth information. Owing to this lack of visual cues to depth in an image that has been produced by transmitted radiation many objects cannot be identified. This is particularly prevalent when there is a significant number of overlapping image features. Computer tomography (CT), originally known as computed axial tomography (CAT) employs image reconstruction to generate 3D images. CT technology can produce very high quality 3D image [11-14]. However, CT is costly, large in size and time-consuming in comparison to the conventional 2D transmission imaging system. Hence their deployment at airports is limited. Owing to fast stream and high volume of passengers at airports, X-ray imaging systems which

produce depth information may provide a smaller, faster and cheaper alternative to CT. Over the past twenty-years, the University team in collaboration with the Home Office Centre for Applied Science and Technology (CAST), formally the UK Home Office Scientific Development Branch (H.O.S.D.B.) developed a novel binocular stereoscopic X-ray technique [15, 16], to aid the detection and identification of objects in X-ray scans of luggage. Imaging technology based on this early work is now commercially available. More recently, through on-going collaboration with the CAST and the US Department of Homeland Security (DHS), the University team has developed multiple view techniques that combine binocular stereoscopic imagery with motion or kinetic depth effects (KDE) to produce three-dimensional imagery [16-19]. Motion provides a powerful visual cue to depth, which greatly enhances the interpretation of spatially complex structures [20] in shadowgram images and identified as kinetic depth X-ray or KDEX imaging in this thesis. The practical implementation of KDEX requires multiple views of the luggage to be acquired from an arrangement of linear (or folded linear) X-ray detector arrays. Each array is illuminated by a thin curtain of X-rays originating from a single X-ray source. The views are captured during a linear translation of the object under inspection through the interrogating X-ray beams. The ability effectively to "look around" an object under inspection using multiple views is particularly advantageous in comparison with standard stereoscopic techniques [21-24]. Linear "motion parallax" refers to the differential angular velocities of retinal images of points moving laterally with the same speed, but at different distances. Therefore, this effect can be used to produce motion perspective in which the viewer is able to extract depth information from continuous movement occurring in a visual display.

To produce a smooth image rotation over sufficiently wide angles suitable for security screening applications does require a relatively large number of views (up to 32). The implementation of such a large number of folded array [21] detectors presents a number of serious practical problems for the construction of the X-ray collimators and the configuration of the dual-energy sensor modules. This problem is exacerbated by the small angular increments, of the order of 1^0, required between each successive view and the physical bulk of the sensor arrays. These physical constraints currently preclude the development of a "single pass" KDEX imaging system. In visible light images, research work attempts to establish whether image synthesis [25-31] can be used to compute intermediary views of sufficiently high visual quality (e.g. stereo vision and film

industry). In particular, matching algorithms encountered in visible light scenarios might not directly applicable to the x-ray scenario due to the inherent transparency property in the transmission X-ray images and its theoretical considerations which have been reported in Chapter 2, Section 2.8.

This research investigates the possibility of replacing some of the X-ray sensor views with synthetic images. If adequately high quality synthetic colour images can be generated then intermediary X-ray sensors can be discarded to minimise the hardware requirements. Together with sensor images, the synthetic images are used to provide a sequence of KDEX images. The imaging geometry of the KDEX technique presents a number of distinctive and challenging problems for the design of algorithms, which relate motion parameters to image intensities and contrast. Earlier work by the university team [32] has developed image synthesis algorithms that operate on greyscale imagery to synthesise views. The algorithms were designed based on a correlation matching approach. The limitations of correlation matching approach have been reported in Chapter 2, Section 2.6.1. Also, the prior synthesis algorithms developed by the university team were mainly designed to cope only with greyscale imagery and dealt with a very limited input data. Due to the small number of sample images, the general trends in terms of number of matches and error pixels have not been achieved.

The research programme reported here is instigated to explore feature matching approaches to match the perspective views. Existing image synthesis algorithms are developed for visible light images. Due to fundamental differences between visible light and X-ray images, those algorithms are not directly applicable to the X-ray scenario. Therefore, initial consideration was given to improve the performance of the SIFT; a feature matching algorithm in order to deal with the line-scan imaging system being used in this research programme. SIFT alteration as well as the boundary conditions added on the top of SIFT have formed the basis of what so called optimized SIFT algorithm. Full description of optimized SIFT algorithm is reported in Chapter 3.

Dependence on the imagery system being used (either greyscale of colour coded), different morphing and warping techniques have been pioneered by the author. In terms of greyscale a novel morphing technique termed, epipolar based morphing was designed to generate the intermediary views. the algorithm is fully described in Chapter 4 of this

thesis. In terms of colour coded imagery and since the dual-energy images are colour coded according to colour gamut defined for each material class (Metallic, Mixture and Organic), the author has also devised another morphing technique which avoids linear cross-fade of colours typically accoutred with visible light image morphing techniques. The technique is termed, material based morphing and fully described in Chapter 5.

The performance of the adopted matching algorithm as well as the morphing algorithms has been tested by operating a considerable amount of input imagery. Images were carefully arranged from simple to very complex structured luggage items. This arrangement covers large numbers of the scenarios routinely encountered in X-ray screening applications. The performance has also been assessed as a function of angular separation between perspective views in which the general trends of the number of matches and the number of error pixels was accomplished.

1.2 Research objectives

The aim of the research programme is design an improved system for facilitating a smooth motion and KDE in a visual display through computational synthesis of intermediary views within a sequence of previously captured X-ray views. The synthesis algorithm is achieved by utilizing a novel materials discriminating 3D X-ray imaging technique for security screening applications. The following objectives support and inform the research aim:

- to assess feature matching techniques to match perspective images and identify their limitations when applied to transmission X-ray images;
- to investigate a new matching criterion suitable for transmission greyscale and colour encoded X-ray images;
- to assess the matching algorithm as a function of the angular separation between the X-ray beams employed to produce the input images;
- to develop algorithms to synthesize greyscale intermediary views and amend the algorithm in order to cope with colour encoded X-ray images;
- to investigate image segmentation based on materials discrimination;
- to design an image fidelity metric for greyscale and colour coded dual-energy X-ray images;

- to formulate a comparative study on the synthetic images and ground truth provided by calibrated object structures;
- to evaluate the synthesis algorithm performance as a function of the angular separation between the X-ray beams employed to produce the input images;

1.3 Research contributions

The research programme is structured to draw upon the strength of the University team in 3D X-ray imaging, visualisation and materials ID. The programme is divided into the phases summarised below.

Phase I

Conduct a literature review of security X-ray imaging technologies including; X-ray line-scan imaging (2D and 3D) binocular stereoscopic imaging and CAT scanning to develop an understanding of the technological context of the project. Conduct a more detailed review of the following areas:

- dual-energy (materials discriminating) X-ray imaging;
- image matching / correspondence problem;
- image warping and morphing;
- image synthesis;
- video processing;
- image error analysis and quantification;

Investigate the application of the above areas to transmission dual-energy X-ray images and identify limitations and problems as the basis for formulating a new approach.

Phase II

- Identify and apply image matching techniques to greyscale KDEX imagery. Identify the limitations of existing algorithms and where possible modify their boundary conditions to accommodate the imaging geometry of the KDEX technique.
- Construct and fabricate calibrated structures and organise luggage items to test algorithm performance.

- Evaluate the performance of the matching algorithm as a function of the angular separation between the X-ray beams employed to produce the input imagery.
- Develop an image synthesis algorithm employing epipolar based morphing and apply to the greyscale X-ray image sequences.
- Design, develop and test appropriate image metrics to establish the fidelity of the new algorithm.
- Assess the synthetic algorithm performance as a function of the angular separation between the X-ray beams employed to produce the input imagery.

Phase III

- Identify and apply the boundary conditions within the image matching technique for colour encoded KDEX imagery. This approach is obtained by first matching the whole colour encoded images and then matches them according to their segmented material classes.
- Evaluate the algorithm performance as a function of the angular separation between the X-ray beams employed to produce the input imagery.
- Develop a novel synthesis algorithm employing a material based morphing technique to utilise the materials segmentation information provided by the dual-energy X-ray discrimination technique.
- Design an integration method to combine potentially differently coloured spatially corresponding regions, in the left and the right perspective views to produce an appropriately coloured synthetic view.
- Design, develop and test appropriate image metrics to establish the fidelity of the new synthetic algorithm.
- Assess the synthetic algorithm performance as a function of the angular separation between the X-ray beams employed to produce the input imagery.

1.4 Structure of the report

The report consists of seven chapters.

- Chapter One **Introduction** introduces the work by summarising the research objectives, describing the research contributions and by presenting the structure of the report.

- Chapter Two **Background** provides context for the scope of the multidisciplinary work and includes; a discussion on X-ray techniques together with an overview of the existing image synthesis approaches, followed by considerations that have been taken to address the correspondence problem and X-ray transparency; this chapter concludes by presenting image warping and morphing techniques used to generate intermediary or in-between views.
- Chapter Three **Image Matching Algorithm** describes the matching algorithm used to locate the corresponding features in a sequence of perspective views, limitation of the standard approaches and the proposed new boundary conditions, which take advantage of the imaging geometry of the KDEX technique.
- Chapter Four **Greyscale Image Synthesis Algorithm** discusses the experiment methodology, experiment plan, results and analysis of generating the in-between greyscale imagery.
- Chapter Five **Colour Image Synthesis Algorithms** the experiment methodology, experiment results and analysis of generating the in-between colour encoded images for different experiment conditions.
- Chapter Six **Translation Based Colour Encoded Image Synthesis Algorithm** describes experiment methodology, results and analysis of generating the colour encoded synthetic views from single view for different experiment conditions.
- Chapter Seven **Summary, Conclusion and Future Work** finally, the contribution of this work is summarised and concluded, and the direction of future work is suggested.

Chapter Two Background

2.1 Introduction

The materials in this chapter presents an overview of the technologies concerning the X-ray imaging used to generate the X-ray data employed in this research. Also, theoretical considerations necessary for the development and investigation of the synthetic algorithm presented in the coming chapters are also discussed.

Some pertinent aspects of X-ray imaging are briefly discussed before the multiple view X-ray imaging techniques previously developed by the University team are also reviewed. Two different experimental X-ray scanners are presented as the practical source of the perspective image sequences used for the algorithm development and investigation. The basic principles of image matching techniques and their limitation when applied to X-ray imaging scenarios are presented. Image matching is the process implemented to 'solve' the correspondence problem in which features between perspective views are identified. The correspondence problem encountered in X-ray image sequences is ill posed and similar to its visible light counterpart, although the inherent transparency property of X-ray images exacerbates matching problems. Finding the correspondences however is only part of the synthesis technique explored in this work.

Image warping and morphing are also important aspects in the image synthesis algorithms presented in this work [33-36]. Image morphing is applied to the matching algorithm output and used to generate in-between views. The fundamental principles of warping and morphing techniques are reviewed and their weakness when applied to X-ray images explored and identified. Accordingly, the algorithms are modified and boundary conditions are imposed, which help them cope with the imaging geometry used to generate the data analysed and presented in this work. Additional factors to be considered include the amount of attenuation experienced by the X-ray beam and the properties of the X-ray detectors. The polychromatic nature of the X-ray source (required for dual-energy materials discrimination) installed in typical airport luggage security scanners, is also an important aspect of the imaging chain under consideration in this work.

2.2 Stereoscopic X-ray imaging

Since the discovery of X-rays [37] to the present, X-ray imaging has undergone constant development, particularly in the field of medicine [38-42], non-destructive inspection and security screening [15, 43-48]. In aviation security screening, X-rays are routinely used to examine baggage contents to help detect dangerous or illegal items. The prime directive for aviation security personnel is to achieve high detection rates during airport luggage inspection.

Previous work by the University team has developed a unique binocular stereoscopic X-ray imaging technique, which also enables the screener to discriminate between different materials [23, 24, 49]; the resultant colour coded imagery can significantly enhance the human observer's understanding of the true nature of the 3D scene under observation.

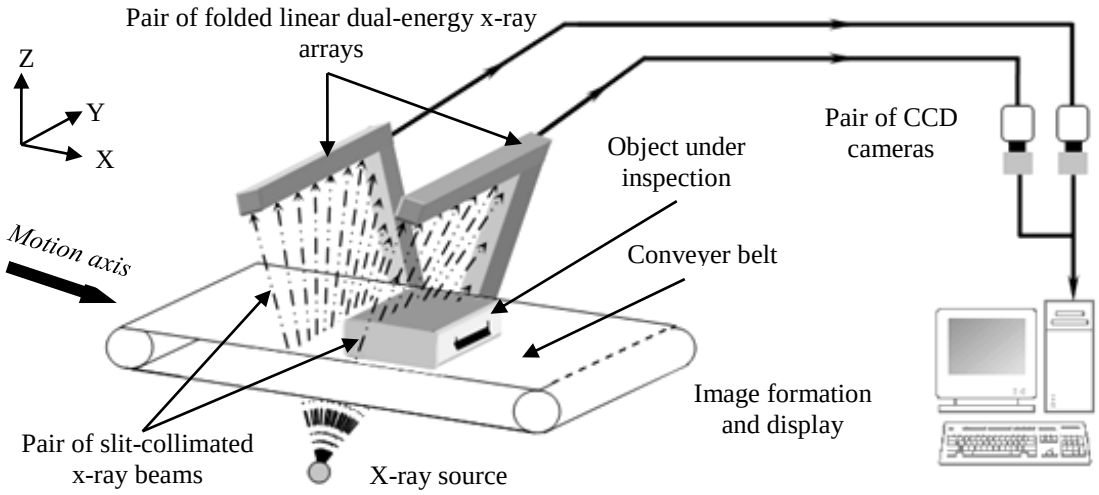

Figure 2.1: The schematic of the binocular stereoscopic folded dual-energy X-ray screening system invented and developed by the University team [24]**.**

The stereoscopic imaging technique developed by the University team, utilises a single X-ray source, a pair of folded linear dual-energy X-ray arrays and a pair of charge coupled device (CCD) cameras as illustrated in figure 2.1. The two slit-collimated X-ray beams are arranged to irradiate a left and a right folded configuration of linear detector

arrays. This geometric technique has formed the basis of several commercially available products, manufactured by 3D X-ray Ltd (http://www.3dx-ray.com/).

2.3 Material identification and coding (Dual-energy X-ray imaging)

Material discrimination requires measurements of two X-ray signals taken at two different X-ray energy levels. Typically, measurements are taken at 75keV and 140keV to generate low-energy (Lo) and high-energy (Hi) image sets, respectively. Low-energy and high-energy signals are required for colour encoding; each pixel in the resultant dual-energy image requires a corresponding energy discriminating X-ray sensor. Theoretically, a screening technique that utilises the dual-energy X-ray technique can potentially offer a major advance in the ability to distinguish between materials under inspection.[50, 51]. Detection of two different X-ray energy levels is a fundamental requirement for a dual-energy X-ray system. In this research programme, the system implemented uses a single broad spectrum X-ray source and detectors with differential energy discrimination (high-energy and low-energy) to differentiate 'low-energy' X-ray radiation at 75 kVp and 'high-energy' radiation at 140 kVp as illustrated in figure 2.2.

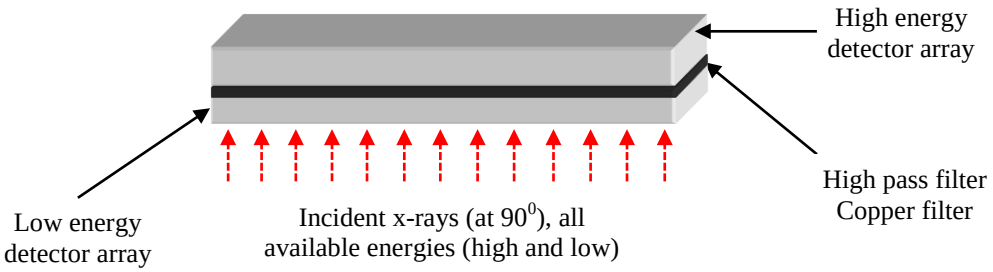

Figure 2.2: Linear sandwiched dual-energy x-ray detector array.

When the transmitted X-ray beam passes through the object under inspection, two detector arrays work in tandem to record two separate images of the same object at different energies. The low-energy arrays are mounted on top of the high-energy array with a copper filter sandwiched between them. X-rays first pass through the low-energy X-ray energy detector, and then the copper filter helps to remove low-energy components from the spectrum incident on the high-energy sensors. Therefore, a dual-energy radiograph can be produced from a single exposure for materials discrimination purpose. The relative difference in magnitude between (Hi) and (Lo)

energies is exploited to broadly discriminate an inspected object into three material classes as function of atomic number, Z. The organic class $Z \leq 10$, a mixture class $10 < Z < 20$ and the metallic class with $Z \geq 20$ [18, 24]. The resultant discrimination information is presented to the human operators by colour coding the X-ray images.

The colour encoding algorithm initially divides the material under inspection (pixel-by-pixel) into one of the three main categories: organic, inorganic and metal. The organic elements are displayed in an orange colour; the inorganic elements are presented in a green colour, while the metallic elements are shown in blue. Sometimes the X-ray beam cannot penetrate or achieve a sufficiently intense penetration of the object under inspection in which case the pixel is assigned a low intensity grey level value and is classified as an indiscriminable signal i.e. no materials discrimination can be achieved. Figure 2.3 illustrates the process of coding material discrimination information into final colour image. The low and high-energy images appear very similar to the human eye, however in the material discrimination process the fine difference is exploited to distinguish between the imaged materials: metallic, organic, mixture, and impenetrable material. The images are finally displayed together as a compound image. In an airport security system, such techniques are used to help detect illegal materials such as explosive or narcotics. To formulate the colour encoding scheme, three material discrimination curves acquired from organic, mixture and metal materials are required [52]. These curves are illustrated in figure 2.4, and are generally known as ‘banana curves’ in context of aviation security screenings. To produce the three materials discrimination curves, a plastic, aluminium (Al) and a metal (Fe) step-wedges are employed as illustrated in figure 2.4. Curves A and B are the two midpoint curves produced to establish two discrimination boundaries respectively. The area below curve B represents the signature region for organic materials, the area between curves A and B is the mixture materials’ signature region while the area above curve A is the metallic region.

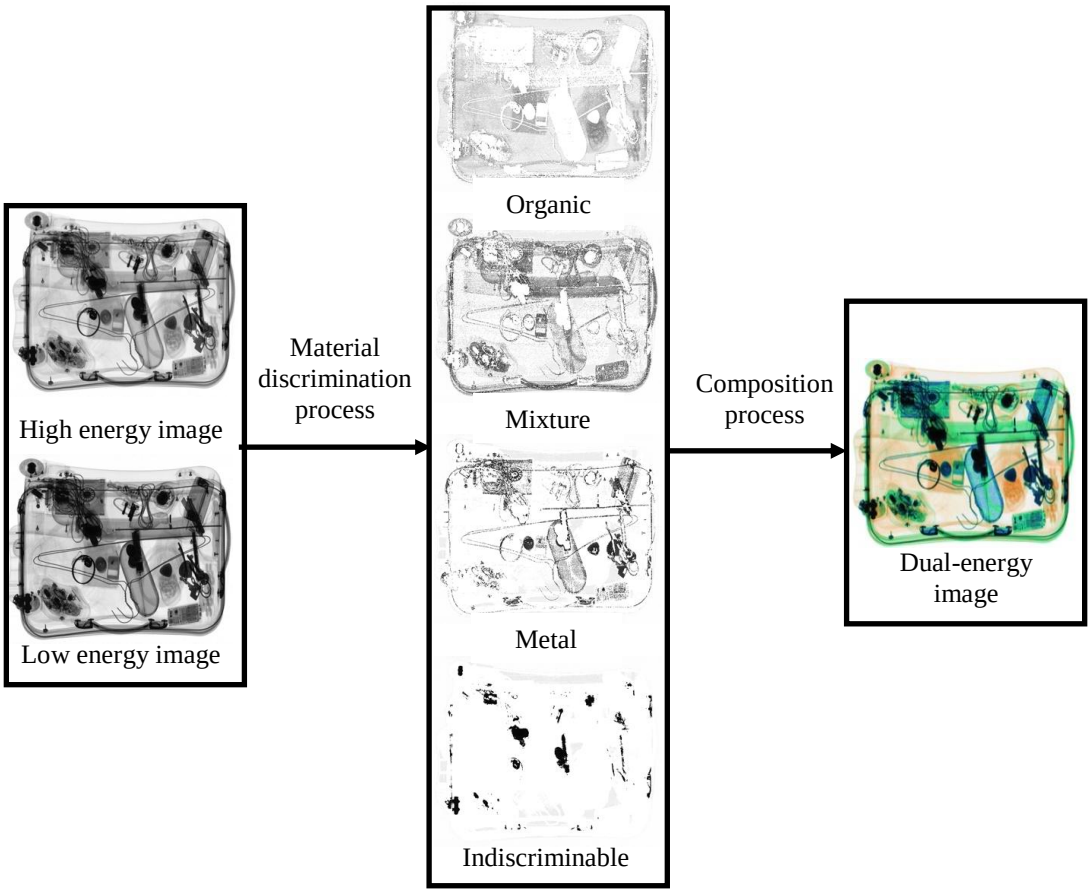

Figure 2.3: Colour encode of the dual-energy X-ray images.

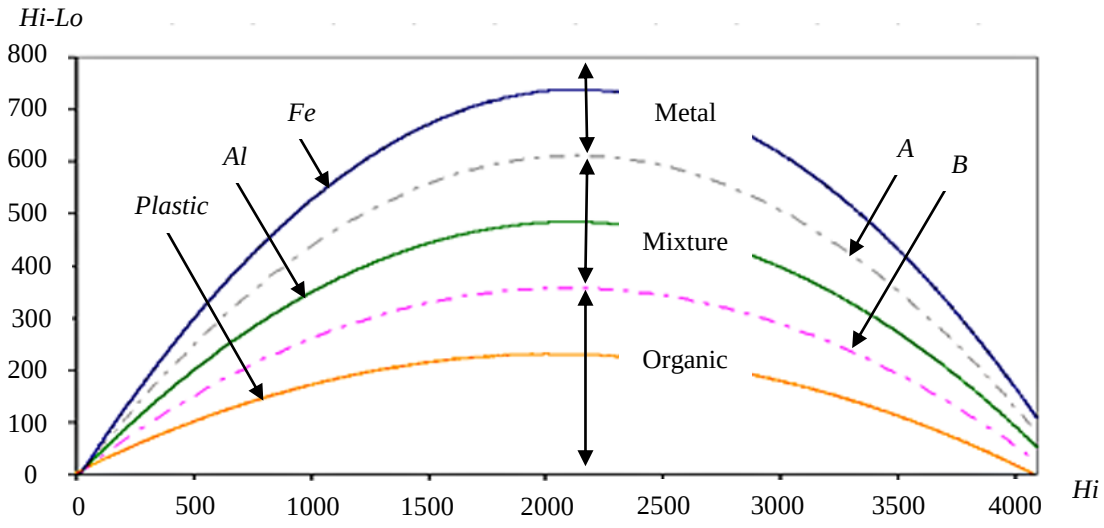

Figure 2.4: 'Banana curve' for materials discrimination plotted as the differential of Hi-Lo X-ray data, against Hi X-ray data.

The colour encoding algorithm begins with categorising the raw image data of the object under inspection (pixel-by-pixel) into one of the three material classes.

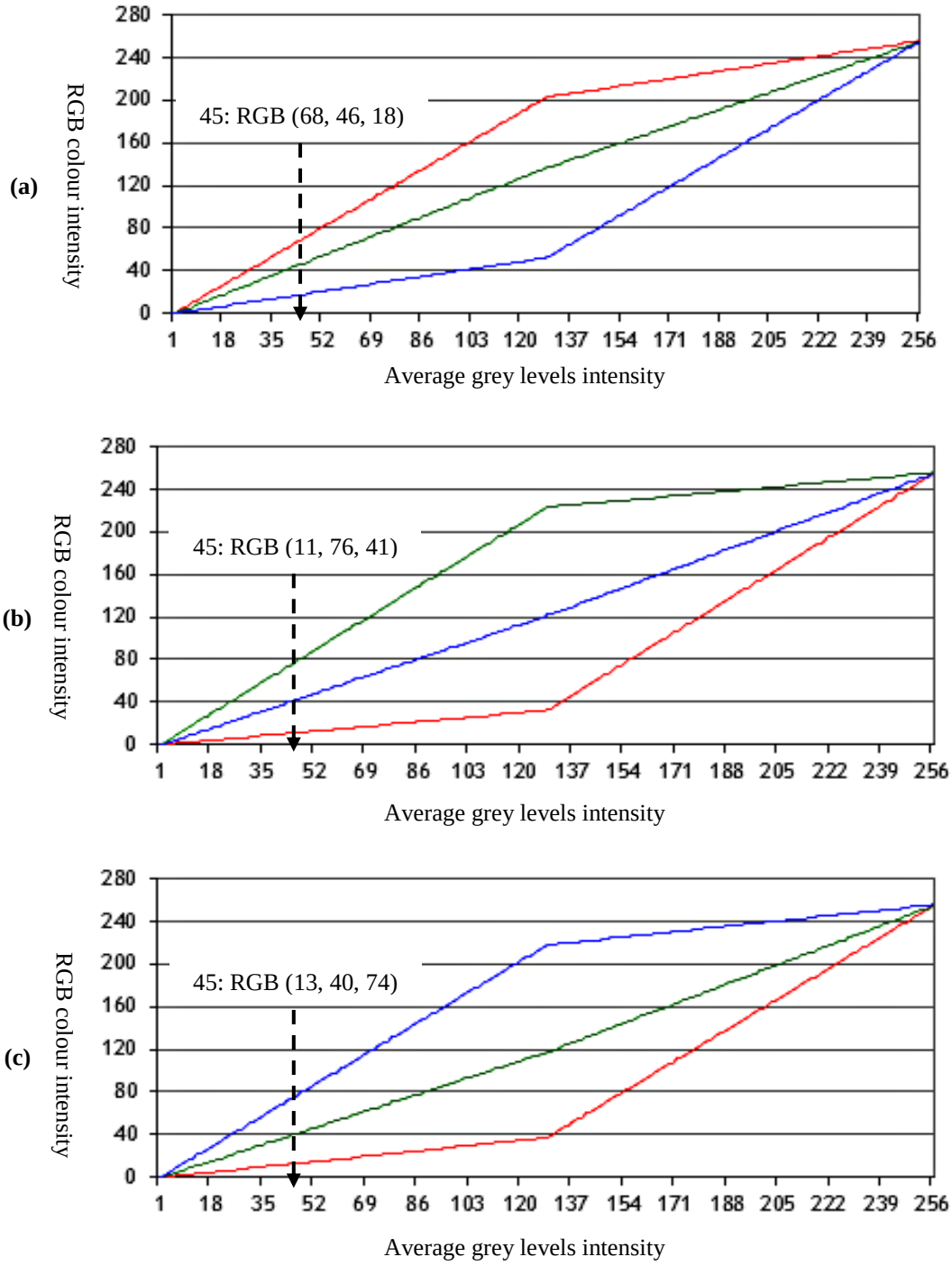

Figure 2.5: Example of an industry RGB colour palette for (a) organic, (b) mixture and (c) metallic.

The raw image data (typically generated as 12-bit grey levels format) is converted into an 8-bit format which allows average of the low-energy and high-energy X-ray data to be calculated. Each averaged image data is assigned to the appropriate 24-bit RGB (Red, Green, Blue) colour intensity by utilising the industry 'standard' colour palettes as illustrated in figure 2.5. For instance, given an average intensity value of 45 grey levels, in organic material, its corresponding RGB colour intensity would be 68, 46, 18 respectively, in mixture material, the corresponding RGB colour intensity would be 11, 76, 41 respectively while in metal material the corresponding RGB colour intensity would be 13, 40, 74 respectively. These three examples are highlighted in figure 2.5 (a), (b) and (c) in that order. The algorithm for the colour encoding is presented as a flowchart in figure 2.6.

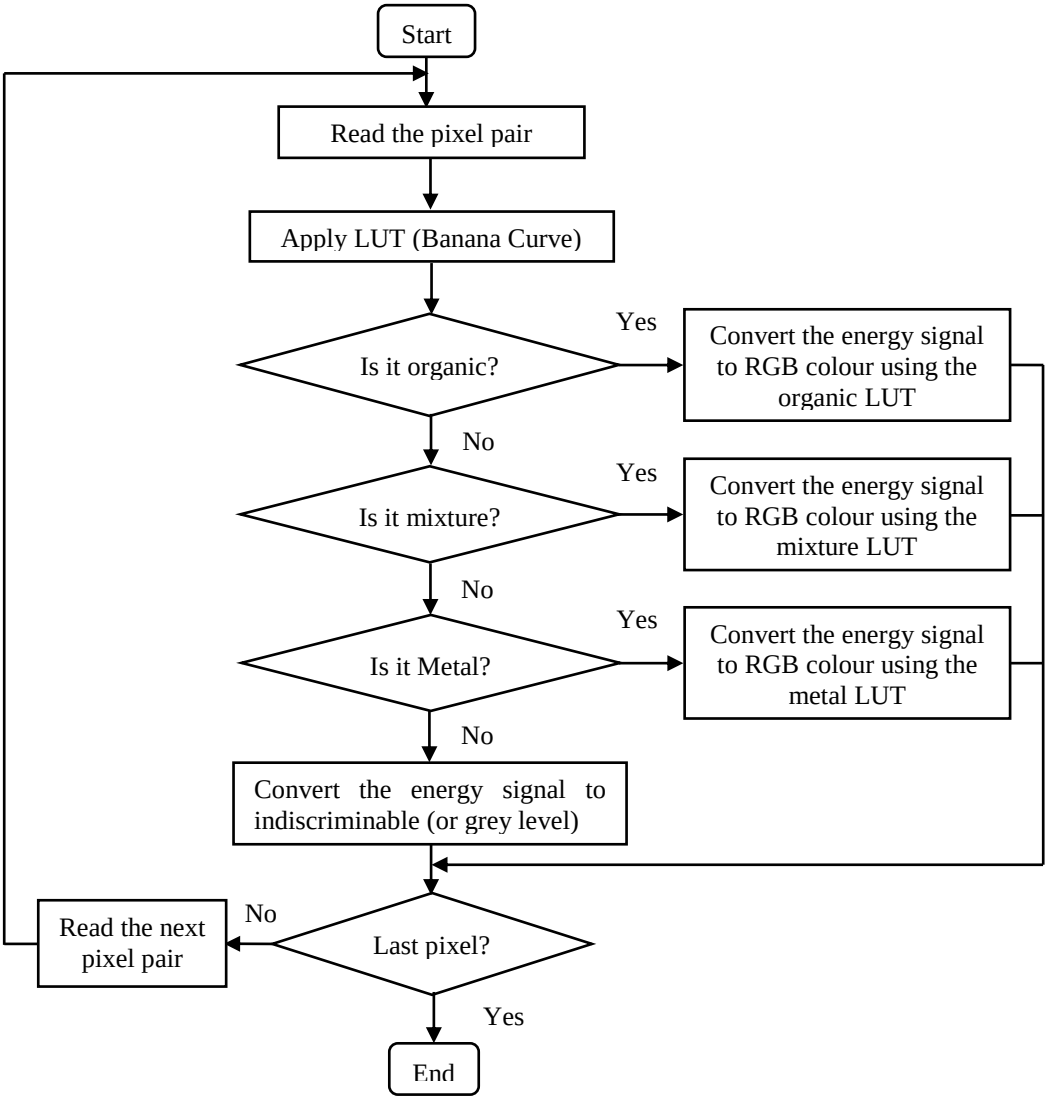

Figure 2.6: Flowchart of the colour encoding algorithm.

2.4 Multiple view and kinetic depth X-ray imaging

The University team led the development of the KDEX technique [53, 54] in collaboration with the UK Home Office and the US Department of Homeland Security (DHS). The technique is designed to capture a sequence of X-ray perspective images to provide binocular parallax and or kinetic depth effect imagery in a visual display. This approach greatly improves an observer's interpretation of a three dimensional aggregate of objects. A key aspect of the design is that it accommodates the strict operational constrains imposed by the aviation authorities [32, 55, 56]. This research builds upon the University team's prior work [17], which has been commercially exploited in the UK and US.

Binocular parallax and motion parallax are important visual depth cues. Each cue depends upon the parallax in retinal images of spatially separated features. The parallax occurs sequentially in motion parallax rather than simultaneously in binocular parallax [57, 58]. When an object is rotated about an axis other than the line of sight, the relative motions of object features can specify the 3D structure of the object hence producing a vivid depth sensation. The kinetic depth effect (KDE) is a special case of motion parallax. KDE was first analytically investigated (and named) by Wallach and O'Connell [59]. This effect involves the rotational motion of objects, rather than observers; a figure looks flat when it is stationary and appears to have depth once it moves. They concluded that KDE requires: "…the shadows cast to display contours or lines which change their length and their direction simultaneously". The resultant depth effect is compelling and the observer can work out the shapes of certain objects with remarkable accuracy from the shadows during a full or partial rotation. KDEX employs novel line-scan techniques, utilising a relative linear translation of the object under inspection with respect to the X-ray source sensor configuration, to capture and display imagery exhibiting KDE. The resultant image sequence can also be displayed as a dynamic binocular stereoscopic sequence. The ability to look around objects under inspection afforded by the KDEX technique enables the spatial segregation of complex overlapping structures that are commonly found in cluttered X-ray images. As a result, threat objects that are camouflaged by local masks in some views may become visually prominent in other views. The practical implementation of the technique requires multiple views of the luggage to be acquired from an arrangement of linear X-ray detector arrays.

Two different experimental X-ray machines have been used to produce the image sequences utilised by the University group. Each system has a high degree of utility for experiments and is described in the following Sections but each is very different in terms of their physical construction and imaging capabilities. In this research all the image sequences are produced by the X-ray machine described in Section 2.4.2, which employs an inspection tunnel capable of imaging typical size suitcases.

2.4.1 Flatbed multiple view X-ray scanner

Initial research [19] concentrated on simulating complex multiple line-scan X-ray source configurations with an X-ray image intensifier system (see figure 2.7). In order to store electronically the shadowgram information projected onto the input window of the image intensifier, the output window is optically coupled to an area array camera. Thus as the object under inspection is translated through the X-ray beam, image information is produced by collecting and storing data from the selected photosite columns on the charge coupled device (CCD) array.

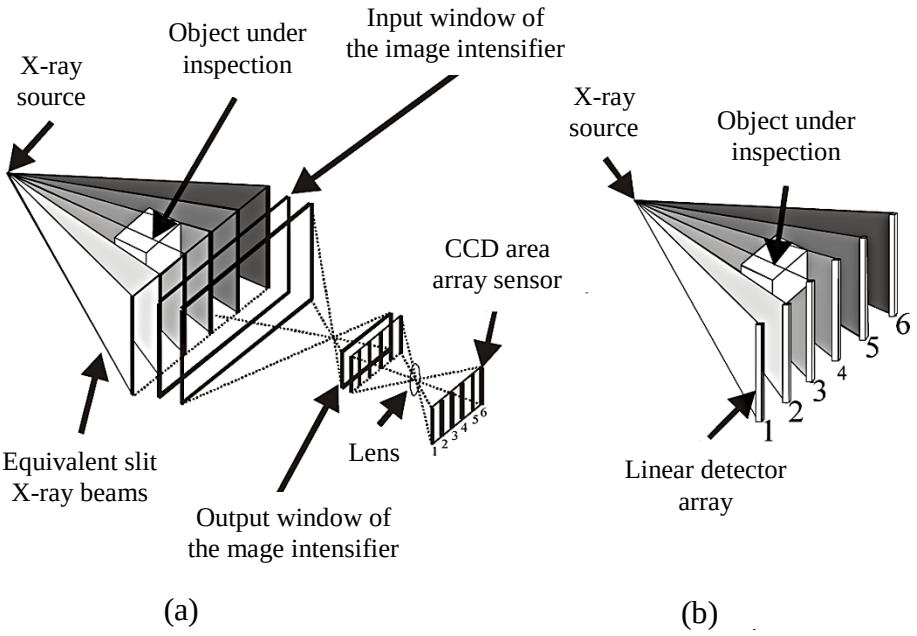

Figure 2.7: Line-scan principle utilising a) image intensifier X-ray system b) linear X-ray detector array system [32].

The selected column on the area array maps to a line on the 9cm diameter input window of the image intensifier. In this way a novel line-scan system can be produced. To

produce motion parallax in a sequential display of images requires that each successive pair of perspective images exhibit parallax as a function of range from the perspective centre (i.e. X-ray point source) of the imaging system. The practical system within the University's Laboratory is limited to imaging relatively small objects but the concept is scalable.

2.4.2 Folded array multiple view X-ray scanner

The multiple view dual-energy X-ray scanner employed to produce the imagery for this research is illustrated in figure 2.8. This scanner utilises a 'folded' linear X-ray detector array (FLXDA) to image typical luggage. The resultant images are stored in a greyscale image format with an 8 bit intensity range.

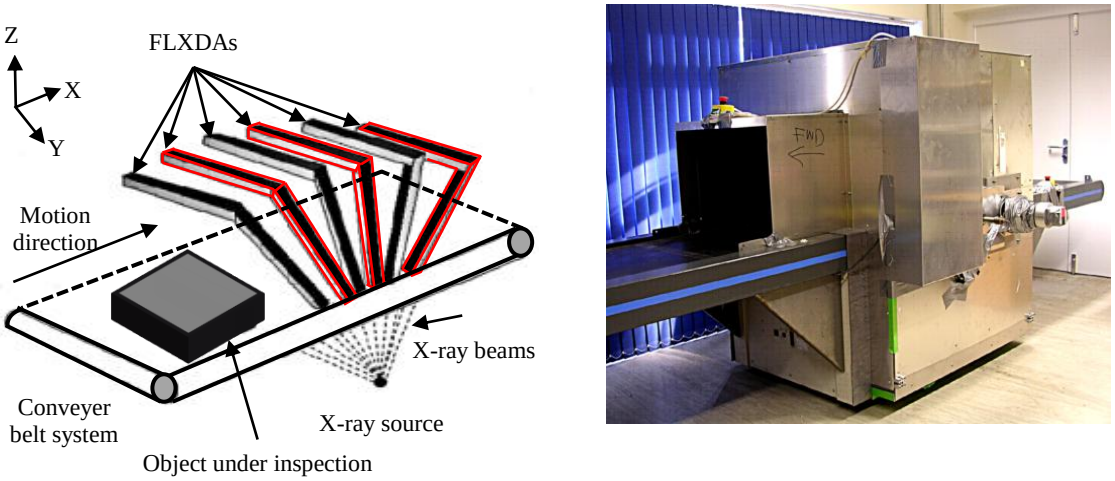

Figure 2.8: (a) Depiction of the experimental system with a single folded array in multiple positions and (b) Photo of the experimental system in the Imaging Science Group's Laboratory at Nottingham Trent University.

This X-ray machine employs a 140 kVP polychromatic X-ray source and a FLXDA depicted in figure 2.9 [17, 22, 53, 56, 60, 61]. The X-ray source/sensor assembly may be rotated about the conveyor belt to enable the collection of the multiple views at different angular positions. In this way the image output of a single pass multiple view scanner can be simulated.

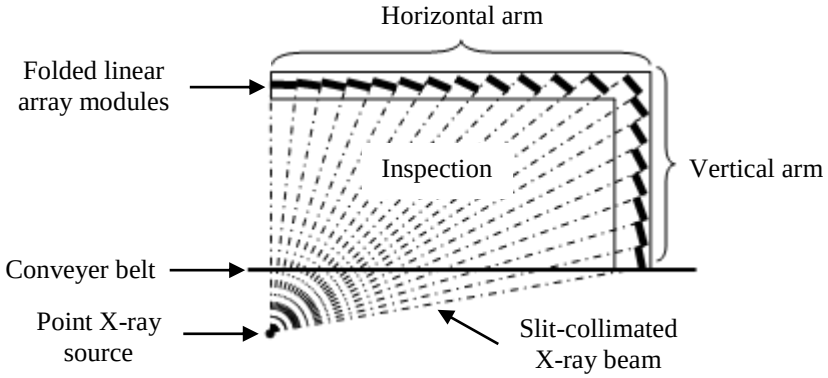

Figure 2.9: Modular configuration of the folded linear (dual-energy) X-ray detector array [32]**.**

The experimental machine was designed by the University team for the investigation of depth from motion (or kinetic) binocular stereoscopic imaging. It was originally designed by the University team and constructed at the Home Office Ionising Laboratories at Sandridge UK, before being transported to Nottingham.

2.5 Image synthesis and sensor eliminations

In this research programme synthetic perspective images are introduced into a sequence of sensor derived images to produce smooth motion. The resultant image sequences can be displayed in various visual modes, which include KDE only or in a combined binocular stereoscopic and KDE display. The production of each synthetic image negates the requirement (cost, bulk and complexity) for a corresponding X-ray detector array and its associated X-ray collimators. Also, this approach reduces the total amount of X-ray flux required per inspection.

Image synthesis may be classified broadly as model based or image based. Model based techniques are designed to compute and manipulate a 3D mathematical representation of the scene. Such techniques computationally reconstructed other viewpoints, as required, and are highly computationally intensive [31]. Image based techniques employ matching processes to identify correspondences between two or more input images that refer to the same scene point [62]. Given two different perspective images, a pixel in one image is the corresponding pixel in the other image if both pixels are projections

along the lines of sight of the same physical scene element. Consequently, if both pixels do not lie on the same line, then one of the images or both original images need to be rectified. Image rectification is the process used to facilitate the analysis of a stereo pair of images by enforcing this two view geometric constraint. For a pair of related views, the epipolar geometry provides a complete description of the relative camera geometry. Once the epipolar geometry is determined, it is possible to constrain the match for one point in one image to lie on a line (the epipolar line) in the other image and vice versa. In the dual-energy X-ray scanner described in Section 2.4.2, the object under inspection is constrained nominally by the epipolar line being parallel with the motion axis or X-axis in the display; therefore, no image rectification is required. Once the correspondence points between given pairs of images are known, the world coordinates of each image point can be reconstructed by image interpolation. In this research, the image based approach is adopted to synthesize new images from a sequence of originals obtained from an X-ray scanner.

One prerequisite of an image synthesis algorithm is to solve the correspondence problem. However, the correspondence problem is inherently ill-posed, and is practically unsolvable. This problem may be exacerbated by the transparency property of X-ray images. Such conditions imposed by the X-ray images have instigated the original research and novel algorithm development undertaken at the University as reported in this thesis. Prior work by the University team focused on analysing pixel based matching techniques to locate correspondence in X-ray images [32, 55, 56]. The results obtained thus far have been promising and formed an integral part of the development of the KDEX technology. The US DHS has released funding to industry in the US to build and trial prototype KDEX systems. This encouraging outcome spurred on the University team to consider an alternative approach, which may act alone or be integrated within the existing algorithm to improve further refine the ‘synthetic approach’. In this research programme, when adequately high quality synthetic images are generated then in-between sensors and their associated hardware may be discarded. In practice, this approach can also enable relatively bulky sensors/collimators to be employed when otherwise they could not be mounted close enough to satisfy the geometric requirements of image capture and display.

2.6 Multiple view stereo matching

Stereo matching is the problem of identifying correspondences between two input images obtained from different station points. It is a fundamental computer vision problem with a wide range of applications [63-66], and it has been extensively studied in the computer vision field for decades. Despite the advances in computing and electronics technology, the correspondence problem remains relevant and challenging [67-69]. There are two basic techniques widely used, correlation-based, and feature-based methods. Correlation-based methods attempt to establish a correspondence by matching image intensities while feature-based methods attempt to establish correspondence by matching a sparse set of image features. Each approach is discussed in the following text.

2.6.1 Correlation based methods

Correlation based methods usually rely on statistical correlations between local intensity regions to enable similarity measurements [70-74]. Typically, they implement various types of statistical correlation between colour or intensity patterns in the local support windows [75]. By using local support windows, image ambiguity is reduced efficiently while the discriminative power of the similarity measure is increased [72, 76]. The method has the advantage of directly producing dense disparity maps. However, it has the following disadvantages.

- Correlation based matching methods tend not to work well when the viewpoints are very different.
- They assume that all pixels in a correlation window have the same depth. However, correspondences are identified by comparing this local window of pixels. Yet, this assumption is not valid at depth discontinuities and wide baseline images.
- Most of the correlation based matching methods tend to blur and remove small details or objects.
- Window size must be carefully chosen. Too small a window may not capture enough image information and increases noise, while too large a window tends increase the variations in image intensity.

2.6.2 Feature based methods

Feature matching can be defined as the process of matching corresponding points between two or more images of the same scene. It is worth noting that in the literature a feature may refer to a point, keypoint or region of interest. It is fundamental in many computer vision applications, including object recognition and tracking, recovering camera motion, image registration, 3D reconstruction and stereo correspondence [77]. Feature based methods match special features of two images, such as corners or edges to produce a sparse disparity map [67, 78-80]. This method matches more features, rather than matching textured regions in the two images [81]. Feature based methods provide more precise positioning for the matching results and are more reliable than correlation-based matching when good image features can be extracted from the scene [82]. They are also faster than correlation based methods, and relatively insensitive to illumination changes. Feature based methods are widely used in wide-base stereo image matching [28, 83, 84].

A vital aspect of feature matching is the detection and description of interest features. The detection of interest features determines stable points that are to be matched, and the description of interest features involves creating a unique descriptor for each point by describing the point and the region around it [85, 86]. It is important that a feature's descriptor be as distinguishable as possible so that it can be discriminated from descriptors of other features in the same image. It is necessary that a feature's descriptor be as stable and robust as possible so that it can be matched to descriptors of features in transformed images while allowing for various image transformations due to change in camera pose, object movement, difference in lighting and even image deformation. Correspondences between two images may then be established by matching the descriptors of both images [87].

Numerous variations exist on the computation of interest points matching. It can be traced back to the work of stereo matching using a corner detector [88], which was later improved by Harris and Stephens [89, 90]. Consequently the Harris corner detector has since been extensively used for various other image matching tasks. The approach was presently expanded to match Harris corners over a large image range by using a correlation window around each corner to select likely matches [91]. Moreover, Harris corners were used to select interest points, but rather than matching with a correlation

window, they used a rotationally invariant descriptor of the local image region. This allowed the matching of features under arbitrary orientation change between the two images [92]. Additionally, it was demonstrated that multiple feature matches could accomplish general recognition under occlusion and clutter by identifying consistent clusters of matched features [93].The local feature approach was extended to achieve scale invariance and more distinctive features whilst being less sensitive to local image distortions such as 3D viewpoint change [94].

In recent times, there has been an inspiring body of work on extending local features to be invariant to full affine changes [81, 95, 96]. However, none of these approaches are yet fully affine invariant, as they start with initial feature scales and locations selected in a non-affine-invariant manner due to the prohibitive cost of exploring the full affine space. Most recently, there has been an impressive effort on expanding the approach of local feature descriptor [97-101]. While this method is not completely affine invariant, a different approach is used in which the local descriptor allows relative feature positions to shift extensively with only small changes in the descriptor. This approach produces descriptors which are consistently matched across a substantial range of affine distortion. It also makes the features more robust against changes in 3D viewpoint. This approach not only has the advantages of extracting more efficient feature, but it also able to identify larger numbers of features. Furthermore, Principal Components Analysis SIFT (PCA-SIFT) was introduced [102-104]. This technique accepts the same input as the standard SIFT descriptor. The advantage of this approach is the size of the descriptor. It produces a more compact descriptor in comparison to standard SIFT. On the other hand, it tends to blur the edges [105]. Another local feature descriptor named, Speeded-up robust features (SURF) was proposed [106-108]. SURF is mainly designed for real time application where the speed is the main concern. SURF performance is similar to SIFT but it is not invariant to rotation and illumination changes [105]. The choice of methods is informed by the computer vision application under consideration [80, 101, 109-117]. It has been demonstrated recently that features identified by SIFT are highly distinctive and invariant to image scales and rotations, and partially invariant to a change in illumination [118].

It is implied that using multiple images might help to solve some problems associated with stereo matching. However, more information may also carry the risk of increased

uncertainties. Some common problems encountered by stereo matching algorithms that apply feature based method for visible light images include repeating features, overlapping and discontinuity. In addition, X-ray images exhibit modified versions of these problems. The following sub-sections are organised to illustrate the advantages and disadvantages of employing multiple images for addressing the remaining three common problems.

2.6.2.1 Repeating features

The images in figure 2.10 provide a good example of repeated features, which are commonly found in luggage scans, where 2.10 (a) and (b) are the images obtained at -2^0 and 2^0 respectively. To study the effect of local similarity, consider the repeating features Object 1 and Object 2, illustrated in figure 2.10 (a) and (b). By applying the stereo matching criterion on this pair images, on one hand, and as these features are clear enough, the opportunity to match them is significant.

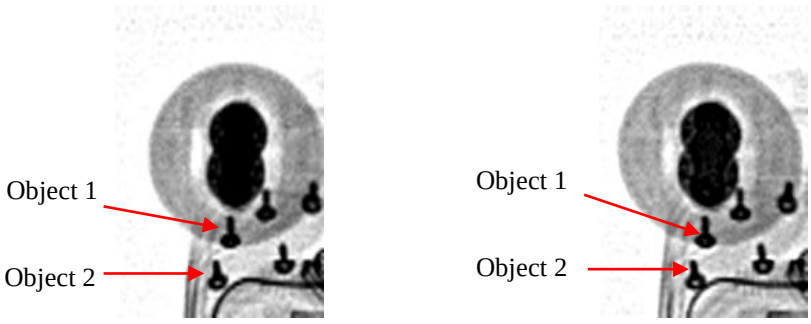

(a) (b)

Figure 2.10: Repeating features are present in ROI extracted from two different X-ray images produced at (a) -2^0 and (b) 2^0 respectively.

On the other hand, unless special care is taken, Object 1 would have an equal opportunity to match with Object 1, Object 2 or other similar features. As a result, an error in matching could occur. This finding is exacerbated when considering overlapping structures commonly found in cluttered X-ray images.

2.6.2.2 Overlapping structure

In this research programme the term ‘overlapping structure’ refers to structures from different discrete objects, which overlap in the resultant image. Over the past decades, extensive research has been devoted to solving the problems produced by overlapping structures, which destroys the parallax information associated with foreground or background occluded objects. The nature of occlusion in X-ray images is different from visible light images as figure 2.11 shows. The transparency property of the X-ray images presents a unique matching challenge. Common matching constraints derived for visible light images such as uniqueness, smoothness, ordering constraints may not translate well to transmission X-ray images. Acquiring images from multiple perspectives can improve the probability of obtaining unoccluded ray paths from at least some the perspective image sequence. In this case, threat objects, which are imperceptible in some views, may become visible in other views.

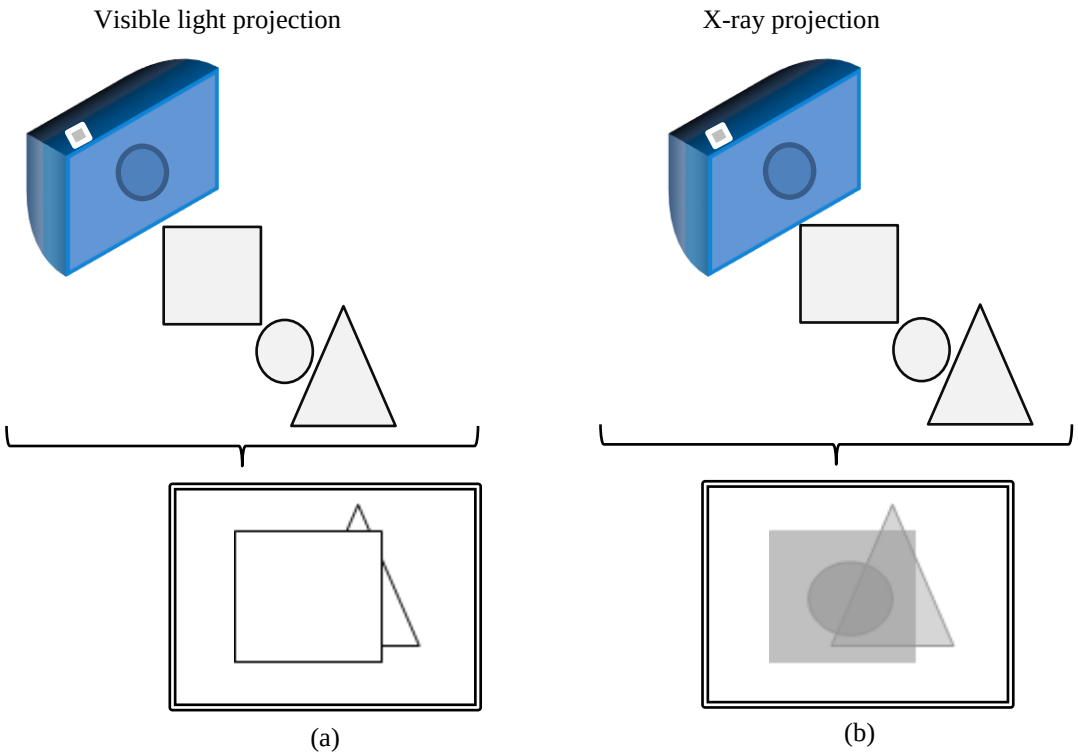

Figure 2.11: A hypothetical example of a square object, a circular object and a triangular object, where (a) represents the visible light image and (b) the X-ray image.

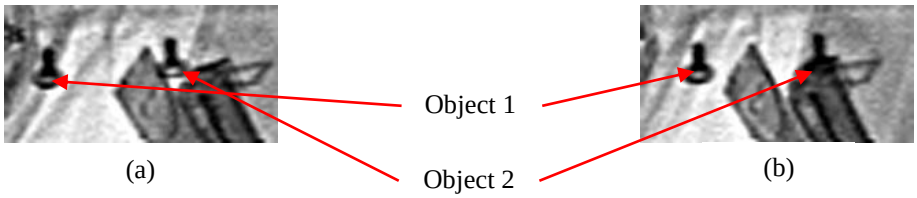

Figure 2.12: Effect of using multiple images for overlapped features where (a) and (b) are images generated at -2^0 and 2^0 respectively.

Figure 2.12 illustrate images obtained at -2^0 and 2^0. Object 1 could be easily identified by applying stereo matching. However, Object 2 would be problematic as it is visible in one view while it is camouflaged in other view. Object 2 is partially occluded in the -2^0 image but it is fully overlapped by other object in the 2^0 image.

2.6.2.3 Structural unsharpness and local contrast

Unshapness refers to the inherent blurred appearance of edges in transmission images. This effect is a natural consequence of transmission imaging and is the result of the variation in ray paths, especially near object boundaries, through an imaged object. Typically, structural unsharpness may be observed near the boundaries of imaged objects. The effect tends to limit the performance of the stereo matching algorithms. Local masking conditions such as the contrast between the feature and the background "i.e., local contrast" is an important consideration in solving the correspondence problem. The contrast is determined by the differential amount of X-ray attenuation produced by the two or more objects, which is a function of material compositions and thickness. In practical cluttered conditions an infinite number of different combinations of foreground and background features/objects can occur. It is therefore, very difficult to surmise any 'typical' scenario on which to test the performance of stereo matching.

2.7 Common matching constraints

There are many constraints employed in stereo matching. The common ones are briefly described in the following list.

2.7.1 Epipolar

Epipolar geometry is the geometry of stereo vision. The epipolar line is defined as the intersection of the epipolar plane with the image plane [119, 120]. The epipolar line, in practical terms, is the image in one camera of a ray through the optical centre and object point of interest in the other camera. In such a scheme a corresponding point must lie somewhere along this epipolar line; thus reducing the potential 2D search space into 1D search. The epipolar constraint can be reliably applied only after the geometry of the system is known and a series of corresponding epipolar lines in both stereo images is estimated [121, 122]. Calibration is used to make two images satisfy this criterion [91]. The epipolar lines are of fundamental importance in the design of a KDEX system as they describe the motion trajectory of features as a function of depth.

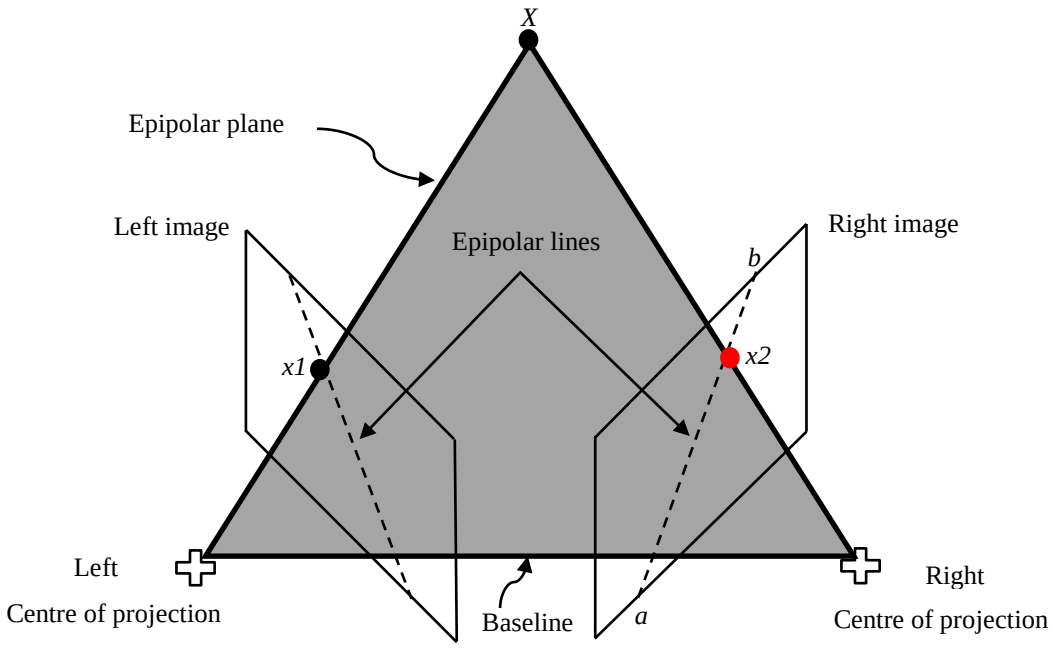

Figure 2.13: Interpretation of the epipolar geometry constraint.

Careful consideration of the epipolar geometry enables an efficient search for corresponding points in stereo matching. With reference to figure 2.13, suppose the point X is imaged in two views, at x1 and x2 respectively. Assuming that x1 is known then the position of the corresponding point x2 must lie along the epipolar or line ab. It can be appreciated from figure 2.13 that the epipolar lines are formed at intersections of the epipolar plane with the image planes. In terms of identifying stereo correspondences

the benefit is that the search for points corresponding to x1 need not cover the entire image plane but can be restricted to a geometrically defined linear space.

2.7.2 Disparity window

The disparity window defines the limits in the x and y-axes for a search space within which all matching criteria can also be applied. The disparity window is calculated by considering the geometric relationship between each overlapping discretised image within the inspection volume. The 3D sampling of the inspection volume can be represented by a voxel model, where each voxel has a unique (x,y,z) coordinate position [56, 123]. Figure 2.14 illustrates a voxel as a function of the angle σ between the intersecting lines of sight of two X-ray sensing elements. The size of the voxel in the depth (or z-axis) is δZ, and δX is the motion axis resolution (horizontal in the display).

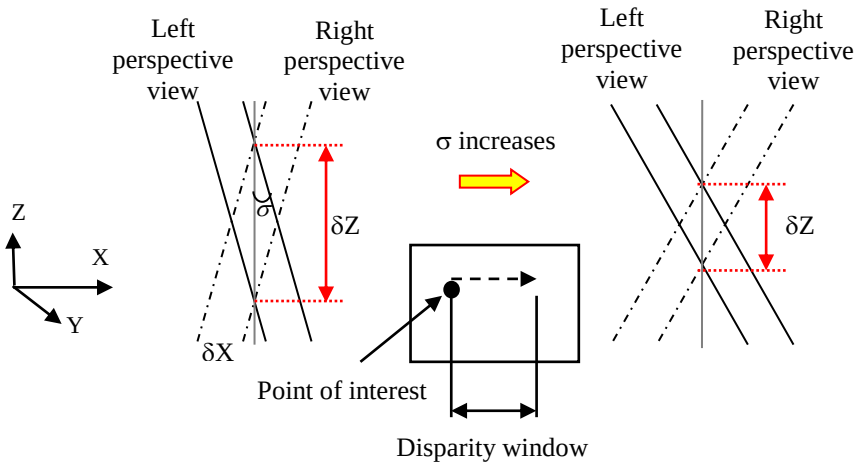

Figure 2.14: Dependency of voxel dimensions on σ and disparity window search along the motion axis.

It is readily appreciated from the simple geometry that when the angle σ increases, the minimum detectable increment in object space δZ decreases. However, in binocular stereoscopic systems the maximum allowable σ is limited by the maximum permissible parallax in the resultant display, which in turn is determined by the maximum disparity that can be fused by an observer comfortably [124-126]. Voxels that have the same z-axis coordinate value may be simplistically represented as an iso-disparity surface or depth plane. In the experimental KDEX scanner employed in this research programme,

the disparity window is nominally limited to a 1D search space for corresponding points along the motion or x-axis. The design of KDEX systems have been published in the literature [53, 54]. The design necessarily employs the inspection chamber's far and near boundary to coincide with maximum positive and negative disparity, respectively. A smaller δZ will provide enhanced depth resolution and can be accomplished by employing a larger convergence angle [24]; the resultant disparity window will also increase in size. The implication for stereo matching is that an increased search space coupled with increasingly dissimilar imagery will tend to decrease the likelihood of identifying corresponding points.

2.7.3 Other constraints

There are other matching constraints which might be applied in stereo matching. The so called uniqueness constraint is one of them [127, 128] where pixels, from each of the two images, are forced into a one-to-one mapping. Also, the compatibility constraint assumes that intensities of a point in the first and second images only change a little. The intensities may not be exactly the same due to many different effects such as the light source and surface normal, but the difference is expected to be relatively small. Geometric similarity is also considered as a potential constraints in which the shape of corresponding features do not change too much.

2.8 Theoretical considerations

Since this research programme dealt with multiple view X-ray imaging, it is important to highlight some theoretical considerations, which contribute to understanding why visible light images and X-ray images might require different treatments.

2.8.1 Transparency

The transparency property of X-ray images distinguishes them from most visible, reflected light images. This property presents additional considerations and complexities for the development of image synthesis techniques.

(a) Visible light image

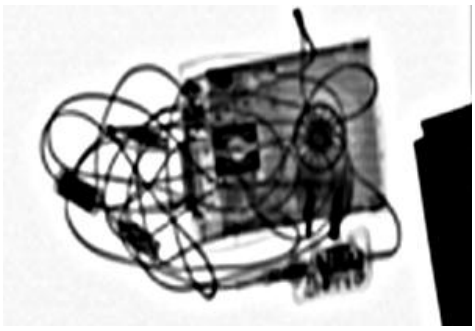

(b) X-ray image

Figure 2.15: A visible reflected light image and a transmission X-ray image of the same scene.

Images in figure 2.15 give a hypothetical example of difference between visible light and X-ray images where object (a) was imaged employing visible light while the same object was imaged using transmitted X-rays in (b). Due to the transparency property of X-rays, it is a common attribute of such imagery that the X-ray beams transmitted through an object producing a shadowgraph. As a result, an overlapping structure in an X-ray image may appear as an integral part of two or more spatially separate objects.

2.8.2 Multiple correspondence

The intensity of each pixel in the resultant images is an aggregated intensity of all points along the ray path under consideration. Each pixel may have multiple correspondences associated with a number of different overlapping structures encountered along the ray path. Figure 2.16 presents the scenario where objects under inspection are imaged by X-rays which are incident normal to the detector plane and alternatively at an angle to the detector plane. Two different interrogating rays image the section of the rectangular object in the diagram. The resultant pixels P1 and P1', produced by the inclined and the normal rays respectively, are a corresponding pair, although their intensities are different. However, P1' is also the corresponding point for P2. As a result, P1' has two potential correspondences arising from the transparency property in the transmission image.

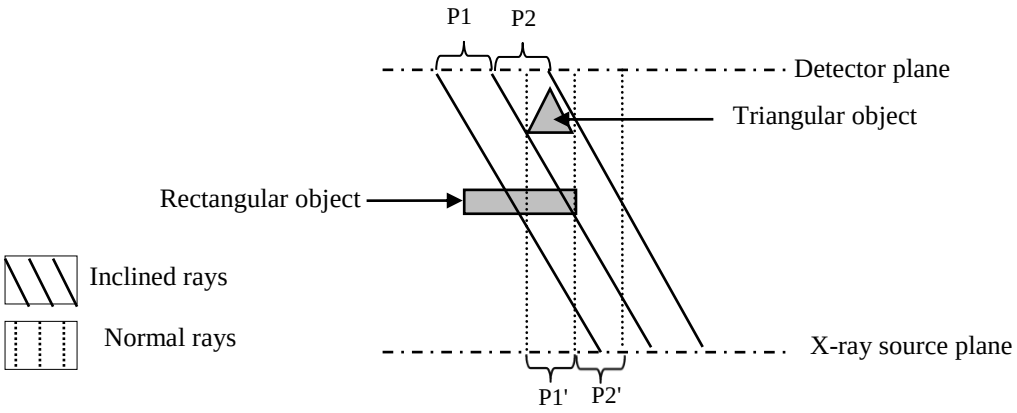

Figure 2.16: Illustration of multiple correspondences; P1 and P2 record the X-ray attenuation from the inclined ray, while P1' and P2' record the X-ray attenuation from the normal rays.

In contrast, pixels in visible light images are not, in general, subject to such uncertainty for potential matches. Any matching error produced by the multiple correspondences has the potential to negatively affect the resultant synthetic images, which requires further computational measures to be undertaken to produce acceptable synthetic imagery.

2.8.3 Effective thickness

In the context of this research, the effective thickness of an object is defined as the length of the ray path through the object or objects under inspection. The intensity of the pixels is proportional to the amount of attenuation experienced by the X-ray beam. The distance travelled through a given material or object largely determines (for a given density) the amount of attenuation. When an object is acquired at different perspective angles, the commensurate change in the ray path through the object (or effective thickness) produces a relative change in the image intensity. In practice, the thicker the object, the greater the intensity fluctuation observed for different perspective views. Thus even a relatively straightforward correspondence-matching task can be problematic. The complex overlapping patterns of objects routinely encountered in images of luggage items further exacerbate the problems associated with integrated thicknesses.

2.8.4 Material composition

Given the two objects depicted in figure 2.16, suppose that the rectangular object is made of a highly attenuating dense material (e.g., metal) and the triangular object is made of a less dense material (e.g., plastic). On one hand, the difference in intensity between P1 and P1' could be minor, leading to a potentially robust match. On the other hand, a switch of the material characteristics of the two objects would confound a matching process due to occlusion. Therefore, the density and chemical composition of an object plays an important role in its X-ray attenuation properties and the resultant image intensity.

2.8.5 Angular separation of the perspective images

In the context of this research, the angular separation between two views is defined as the angle between the slit collimated X-ray beams that were used to collect the imagery. As the angular separation is increased, the perspective views tend to become increasingly dissimilar in terms of shape, overlapping features and intensity simply because of the factors discussed in Sections 2.8.3 and 2.8.4. In the case of simple scenes it may be advantageous to acquire highly disparate imagery in which objects and their relative features are conveniently separated, in the x-axis, by virtue of their relative location in range (or z-axis). Equally it is relevant to consider the case of complex scenes in which increasing parallax results in highly dissimilar imagery leading to difficulty in automatically identifying corresponding features. Figure 2.17 is organised to illustrate the possible effect of increasing the angular separation between views.

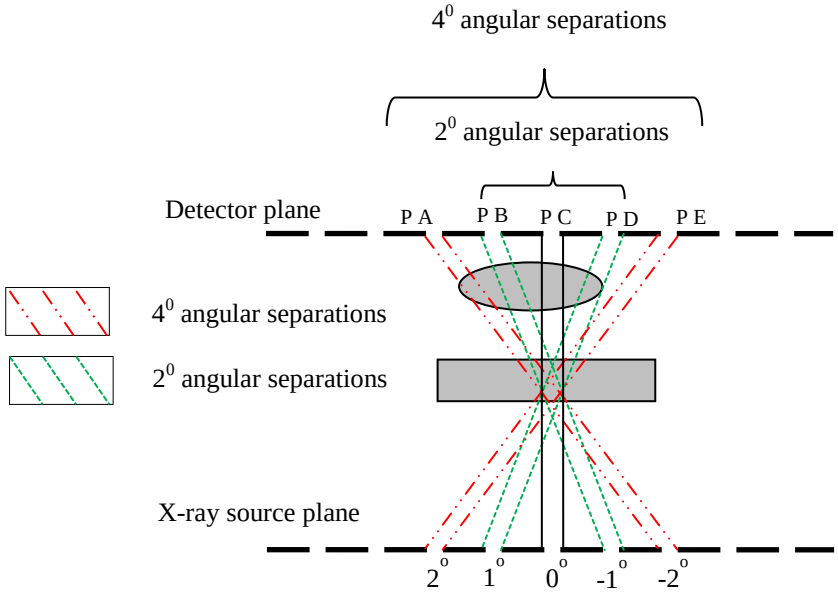

Figure 2.17: Relationship between the angular separation between views and intensity the smaller separation produces a smaller intensity difference (PB and PD) while the larger separation produces a larger intensity difference (PA and PE).

Consider the pair of pixels PB and PD. Assume that they were corresponding features and identified when the angular separation was 2^0. The intensity difference between PB and PD are relatively small and favourable to matching correspondences and influencing the intensity of the synthetic pixels. In contrast, as the angular separation is increased the perspective views tend to become dissimilar in terms of overlap leading to major difference in intensity. This case is highlighted when taking into consideration the pair of pixels PA and PE where the angular separation between them was 4^0.

2.9 Limitations of common matching constraints

In stereo matching, the search for corresponding points is limited within a maximum allowable disparity window, which in turn is determined by the design parameters of the experimental system. As illustrated in figures 2.11 and 2.15 and due to the fundamental difference between X-ray and a visible light images common matching constraints may not be directly applicable to the X-ray scenario. In X-ray imagery searching for correspondences along a search direction (x-axis), will encounter depth discontinuity, inconsistency and, variation in pixel values. Thus one pixel from the left view may be

associated with several correspondences in right view thereby increasing the matching ambiguity. In contrast, a comparable search in the visible light image does not encounter this effect. This situation can be further exacerbated in the X-ray case when the material composition of the different objects is taken into account. Common matching constraints have good performance in visible light image matching. But, due to the multiple potential correspondences in X-ray images, constraints which are commonly used for visible light images may become inappropriate and produce unstable results.

2.10 Image warping and morphing

Image warping is defined as a geometric operation, which maps all positions from one image plane to a second image plane. It has been applied in different areas such as modelling, image analysis and image synthesis [129-131]. View morphing, in particular, is a process which combines a geometric warp with an intensity blend (in grayscale images) or mixing colour information (in colour images). In this process, two images are superimposed and then colour or intensity is blended to achieve a smooth transition from the source image to the target image. This visual effect is known as cross-dissolve.

Numerous approaches towards the problem of warping and morphing were documented by [132-140]. Good morphing algorithms are those in which the shape of the objects is preserved. In terms of quality, to obtain well-behaved morphing which preserve the shape of objects; forward warping (source to target image), inverse warping (target to source image) and blending the two warped images are required. A simple image morphing process is illustrated in figure 2.18. In visible light images, the linear combination of colours exhibited in figure 2.18 (a) is appropriate as the three colour channels (RGB values) of each pixel may vary. As discussed in Section 2.3, the imaging system used in this research employs industry ‘standard’ colour encoding with three different colour palettes to represent three different material classes; organic, mixture and metallic. Therefore, a linear combination of different coloured pixels may not produce a viable resultant colour. This scenario is an especially important consideration in a security screening context where certain colours are associated with specific threats. Also, the fact that a linear combination of colours would often introduce new colours or

'unknown materials' in addition to the three existing classes could cause improper detection and identification of threat objects.

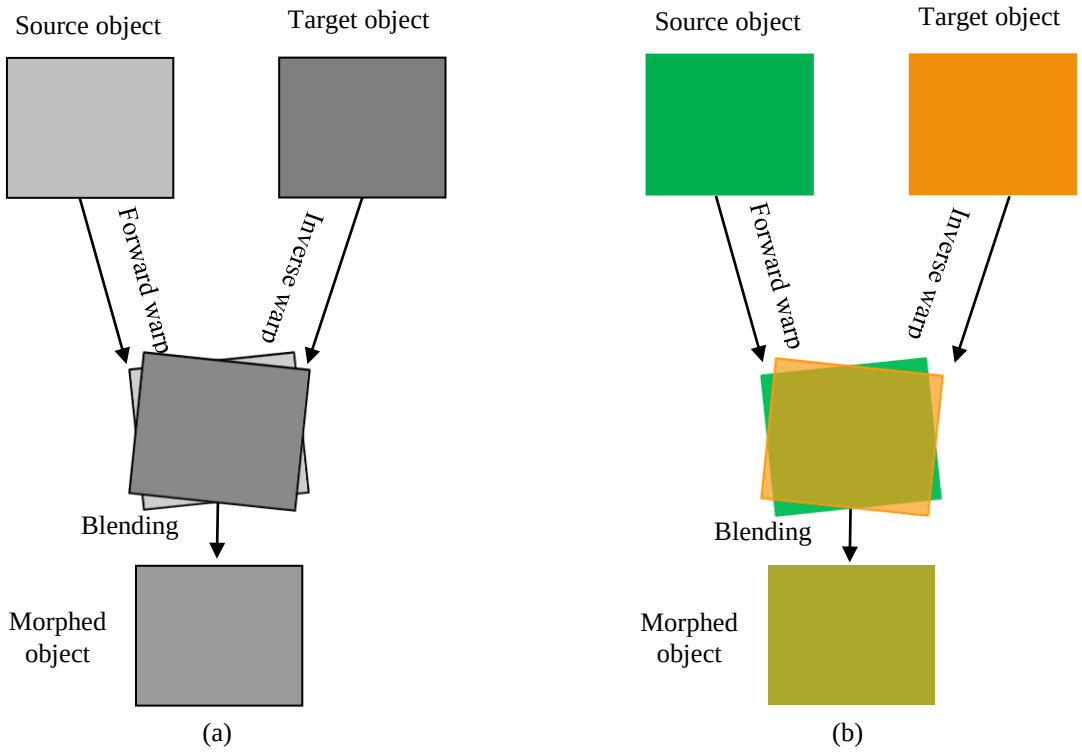

Figure 2.18: Simple structure of two morphed objects where (a) intensity blend (in grayscale images) and (b) mixing colour information (in colour images).

To warp an image into another requires some corresponding points to be identified. The majority of warping methods are based upon the principle of identifying a set of keypoints, which act as geometric references for the subsequent warp. In practice, the methods used to identify the keypoints, together with the method of interpolation are very significantly. The following section is organised to describe some of the warping and morphing techniques commonly used in the field of computer graphics.

2.11 Warping and morphing techniques

In the area of computer graphics, vision and pattern recognition, warping and morphing is used as an aid to perform tasks such as segmentation, shape reconstruction, and motion tracking. The transformation of an image into a new different image may be

informed by coordinate points, vectors, curves and meshes [141-147]. Some of techniques used to compute image warping and morphing are reviewed in the following text.

Affine warping is common technique and is employed when the object of the warping requires rotating, translating or scaling. It is an important class of linear 2D geometric transformations, which maps variables (e.g. pixel intensity values located at position (x1,y1) in the source image) into new variables (e.g. (x2,y2) in the target image) by applying a linear combination of translation, rotation, scaling operations [148]. Point based or feature based variants are the most appropriate technique when the object of the warping is to map image features. Piecewise projective warping and piecewise bilinear reconstructions warping are a good examples of the point based techniques [149, 150]. Point based techniques require a finite set of features to represent the source object and a corresponding set for the target object. The warping is achieved by mapping each feature in the source object to its corresponding position in the target object. The final warp is achieved by extending this process to the whole shape of object by interpolation. Vector-based and curve-based methods are alternative warping techniques. Line-based methods employ oriented lines instead of points. Source and destination vectors are enough to specify local features. Warping is executed by mapping each vector in the source object to its corresponding position in the target object [135, 151]. Point, vector and curve techniques are conceptually similar since are all based on feature-based warping techniques. In order to obtain a good resultant morphology, good alignment for the warping together with good blending is required.

2.12 Image combination

As stated in Section 2.10, morphing is a combination between a geometric warp and an intensity or colour blend. Image combinations are used to reduce the artifacts caused by either forward or inverse transform [152-155]. Linear crossfading involves creating a series of image frames composed of a linear combination of two original images; source and target. In terms of grayscale images, the pixel intensity of the source image is linearly crossfaded with its corresponding pixel in the target image to form the final morph [138]. Colour image combinations are achieved in a slightly different manner in that each colour channel is constructed and combined separately, as if they were three different images with simpler attributes. This approach is acceptable where there are no

colour restrictions. On the other hand, in dual-energy X-ray imaging a linear combination of colours is potentially problematic as it leads to the production of new material classes, as mentioned in Section 2.3. Therefore, an alternative combination strategy, which accommodates the industry RGB colour palettes for organic, mixture and metallic materials, is required.

2.13 Optimal morphing

Computer graphical morphing has multiple applications and there are an infinite number of different ways to define an animation path from the source to the destination. Therefore, it is relevant to raise the question of finding the optimal morphing transformation between two graphical objects. However; as morphing is application dependent, it is demanding to give an accurate meaning to the word optimal [132]. In the special-effects industry such as TV, movies and face morphing industries, morphing is a matter of smooth transition from frame to frame.

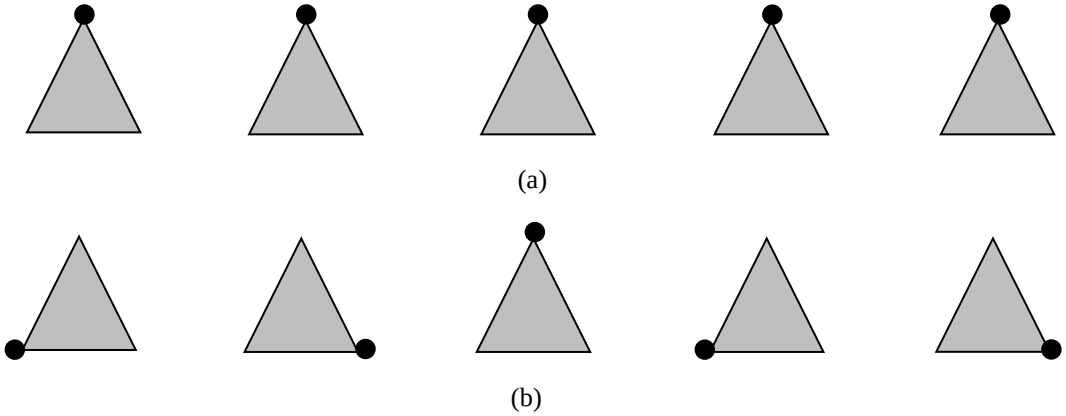

Figure 2.19: Feature preservation morphing sequence of two objects, where (a) preserved features and (b) non preserved features.

Other technical applications such as medical imaging and view synthesis demand that a mathematical approach to morphing is adopted [138]. Although; morphing is mainly application dependent, it does exhibit common properties in order to acquire more natural and pleasing morphing transformation. Feature preservation, in particular, is an important property to consider. Distinguished features of one object should be transformed onto distinguished features of other object. Figure 2.19 (a) shows

a morphing sequence where features are preserved, while features in the morphing sequence in figure 2.19 (b) are not preserved.

In particular, if salient features are not preserved, object shapes are not preserved too. In other words, a new view of the same object should not exist when two different views of an object are morphed. Therefore, it is obvious that unless special care is taken when assigning the corresponding features, dissimilar shapes of the same object might be formed when morphing one object into another object. Images in figure 2.20 are organised to give an example of morphed objects in terms of shape preservation where figure 2.20 (a) and (b) are the source and destination images. If the recognised features are well located and preserved then the shape of the resultant morphed object should also be preserved "e.g. image (c) in figure 2.20". However; if the same features are inadequately preserved then it is expected that the resultant morphed object will be deformed "e.g. image (d) in figure 2.20". This type of shape artifact is produced when the correspondences between the source and destination objects are ill defined or incorrect.

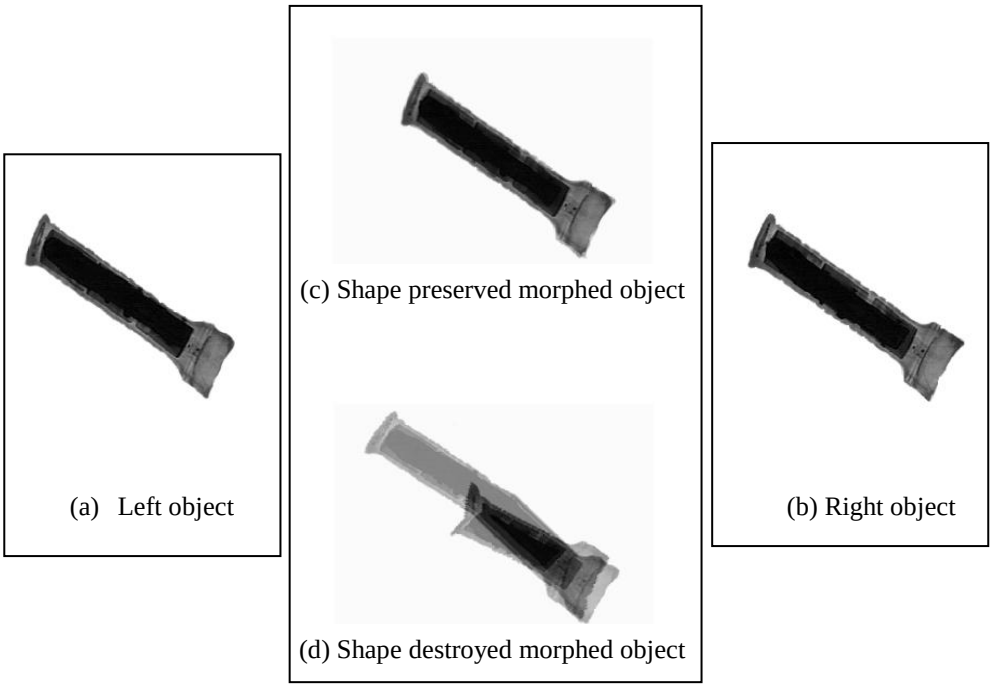

Figure 2.20: Depiction of shape preservation where (a) and (b) are the source and destination objects, while (c) and (d) are the resultant morphed objects with preserved and deformed shapes respectively.

Another important property of a high quality morphing transformation is smoothness preservation between frames. This is achieved when forward and inverse warping is synchronously applied. Also, high quality morphing transformation should avoid so called morphing leakage, which occurs when a limited portion of the perspective views are morphed while other objects are kept static. This is typically occurs when there is a shortage of corresponding features.

2.14 Introduction to Matlab

Matlab can be defined as the language of technical computing. It is high-level language and interactive environment for numerical computation, visualization, and programming. It can be used for data analysis and representation, algorithms development, and even to create your own functions. Matlab software consists of tools and built-in math functions which enable the user to reach a solution faster than traditional programming languages. The software has a range of toolboxes which include signal processing and communications, image and video processing, control systems, test and measurement, computational finance, and computational biology. Additionally, Matlab graphics system enable the user to visualize the data as for two-dimensional and three-dimensional, image objects, animation, and movie files. Matlab can be used as a simulation using what so called 'Simulink', which is a block diagram environment for multi domain simulation (e.g. simulate electrical circuit or control system). Also it can be used as programming language where the so called Mat files (.m) is written.

It is worth noting to mention that the work presented in the thesis was developed, analysed and graphically presented using *Matlab software Version 7.1.0.246(R14) Service Pack 3*. Part of the code was modified and boundary conditions were applied by the author in order to cope with the imaging system being used in this thesis (e.g. the matching algorithm). Also, numerous of different Matlab files (.m files) were designed and written by the author in order to implement the designated synthesis algorithms(e.g. the epipolar based morphing and material based morphing). Since the project deals with X-ray imaging, it is important to note that the majority of Matlab codes were written using *Matlab Image Processing Toolbox.*

The considerations and discussions presented in this chapter informed and supported the investigation and analysis employed in this research programme. It has been reported that identifying corresponding features within a sequence of X-ray images is a fundamental aspect to assist in the warping and morphing of the input X-ray images as the basis for producing synthetic views. Chapter Three presents the methods adopted to identify corresponding features within a sequence of X-ray images.

Chapter Three Solving the correspondence problem in KDEX imaging

3.1 Introduction

Theoretically, image synthesis requires solving the correspondence problem as a precursor to establishing the relative location and orientation of each object in the scene to accurately predict the content of the synthetic image. Factors to be considered include the amount of attenuation experienced by the X-ray beam and the properties of the X-ray detectors. Solving the correspondence problem is a fundamental aspect of many problems in computer vision [82, 85, 96, 97, 100, 156, 157]. It is described as the process of identifying correspondences between two input images obtained with different angular views. Despite the advances in computing and electronics technology, the correspondence problem remains relevant and challenging [67].

The image matching algorithm adopted in this research programme is presented fully in this chapter. The algorithm employs Scale Invariant Feature Transform known as "SIFT". It is a popular feature extraction algorithm proposed by Lowe [97] which extracts features of interest from images that can be used for reliable matching between different views of an object. SIFT has recently gained substantial attention in the computer vision community to address the correspondence problem. Due to fundamental differences between visible light images and X-ray images, the material presented in this chapter discusses the feasibility of applying SIFT to transmission X-ray images. The algorithm is designed to accept X-ray detector images produced by the kinetic depth X-ray (KDEX) imaging techniques previously developed by the university team. To cope with KDEX, SIFT is optimised and bounded by additional criteria. These criteria are of fundamental importance in the design of a KDEX imaging system.

As far as the author can ascertain there is only one previous literature report concerning the application of SIFT to X-ray images [158]. The paper indicated the great potential of SIFT but without presenting empirical evidence. This chapter investigates the ability of SIFT to extract correspondences from cluttered images containing overlapping structures. These conditions are encountered routinely in X-ray screening applications. Empirical results revealed that optimised SIFT has promising potential to search for X-ray image correspondences. The transparency property of X-ray images provides

additional information, which can also limit the matching process under certain conditions. The fidelity of the extracted correspondences is evaluated by analysing the resultant synthetic KDEX imagery. The synthesis also incorporates morphing. Further details on generating the synthetic views are discussed in this chapter and Chapter 4.

3.2 Scale Invariant Feature Transform (SIFT)

SIFT was proposed by Lowe [97] to extract features of interest from images that can be used for reliable matching between different views of an object. The features are invariant to image scaling and rotation and partially invariant to change in 3D viewpoint and additional noise. Over recent years, SIFT has played a significant role in various computing applications such as object recognition, 3D modelling and video tracking. However, the computation employed to generate the set of image features can be split into four main stages. The first stage of computation searches over all scales and image locations "also known as scale space construction". This is implemented efficiently by using a difference-of-Gaussian function to identify potential interest points that are invariant to scale and orientation. Then, at each candidate location, a detailed model is fitted to determine location and scale and the key points are selected based on measures of their stability. Next, orientation is assigned to each key point and finally, a local image descriptor for each keypoint is produced.

3.2.1 Scale space construction

The SIFT algorithm begins with detecting the features of interest, which are known as keypoints, using a cascade filtering approach. The most appropriate scale space kernel is the Gaussian function [159]. The scale space function $\mathrm{L}\left(\mathrm{x},\mathrm{y},\sigma\right)$ can be produced from the input image $\mathrm{I}(\mathrm{x},\mathrm{y})$ as following:

$$\mathrm{L}\left(\mathrm{x},\mathrm{y},\sigma\right) = \mathrm{G}\left(\mathrm{x},\mathrm{y},\sigma\right) * \mathrm{I}(\mathrm{x},\mathrm{y}) \qquad \text{Equation 3.1}$$

Where * is the convolution operation in x and y with Gaussian

$$\mathrm{G}\left(\mathrm{x},\mathrm{y},\sigma\right) = \frac{1}{2\pi\sigma^2} e^{-}(x^2 + y^2)/2\sigma^2 \qquad \text{Equation 3.2}$$

σ is the standard deviation of the Gaussian function. It has been demonstrated by Lowe [156] that difference of Gaussian function $D\left(x, y, \sigma\right)$ is capable of efficiently detecting stable keypoints in the scale space. This function can be computed from the difference of two adjacent scales, which are separated by constant multiplicative factor k:

$$D\left(x, y, \sigma\right) = \left(G\left(x, y, k\sigma\right) - G\left(x, y, \sigma\right)\right) * I(x, y) \qquad \text{Equation 3.3}$$

$$D\left(x, y, \sigma\right) = L\left(x, y, k\sigma\right) - L\left(x, y, \sigma\right) \qquad \text{Equation 3.4}$$

There are numerous reasons for preferring this function. For instance, scale space smoothed images L can be easily computed, therefore; D images can be computed simply by image subtraction. An additional advantage is that D gives a very similar approximation to the scale-normalised Laplacian of Gaussian, $\sigma^2\nabla^2 G$ as stated by Lindeberg [159] where σ^2 is required for scale invariance. Additionally, it is demonstrated by Mikolajczyk [85, 160] that the maxima and minima of $\sigma^2\nabla^2 G$ can produce the most stable image features in comparison to the range of other possible feature detection methods, such as gradient and Hessian or Harris corner detector. The relation between D and $\sigma^2\nabla^2 G$ can be appreciated from the following equation which is parameterized in terms of σ.

$$\frac{\partial G}{\partial \sigma} = \sigma\nabla^2 G \qquad \text{Equation 3.5}$$

Using the difference of adjacent scales $k\sigma$ andσ, $\sigma\nabla^2 G$ can be calculated as:

$$\sigma\nabla^2 G = \frac{\partial G}{\partial \sigma} \approx \frac{G\left(x, y, k\sigma\right) - G\left(x, y, \sigma\right)}{k\sigma - \sigma} \qquad \text{Equation 3.6}$$

In other words the above equation can be rewritten as:

$$G\left(x, y, k\sigma\right) - G\left(x, y, \sigma\right) \approx (k - 1)\sigma^2\nabla^2 G \qquad \text{Equation 3.7}$$

Examples of one octave of scale space where Gaussian images and difference of Gaussian images are illustrated in figure 3.1.

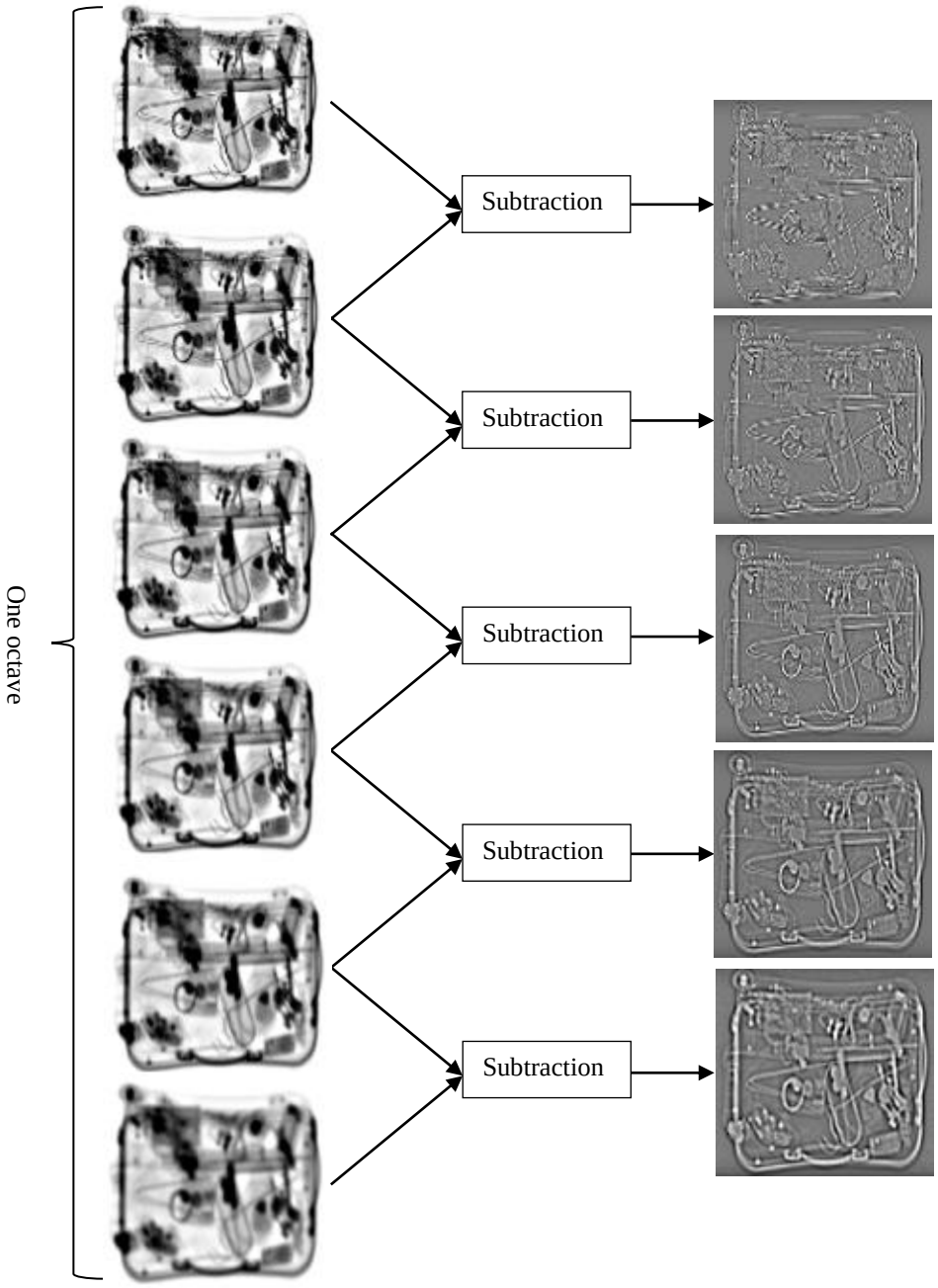

Figure 3.1: One octave of scale space illustrates Gaussian images on the left with difference of Gaussian on the right.

It is demonstrated and accepted in the literature that the best number of scales at each octave is 3. However, the number of images in each octave can be expanded by

doubling the σ value. This means the total number of images at each Gaussian octave is 6 and for the difference of Gaussian is 5. The reason behind doubling the images is that the number of stable features is amplified. But, no additional enhancements were found with a larger expansion factor [97].

3.2.2 Keypoint localization

As stated in the previous section, local extrema provides the best image features in terms of stability. Therefore, it is important to detect the local maxima and minima of $D(x, y, \sigma)$. This is acquired by comparing the intensity of each pixel of interest to its eight neighbours in the current image and nine neighbours in the scale above and below. In other words, the pixel of interest is compared with 28 pixels.

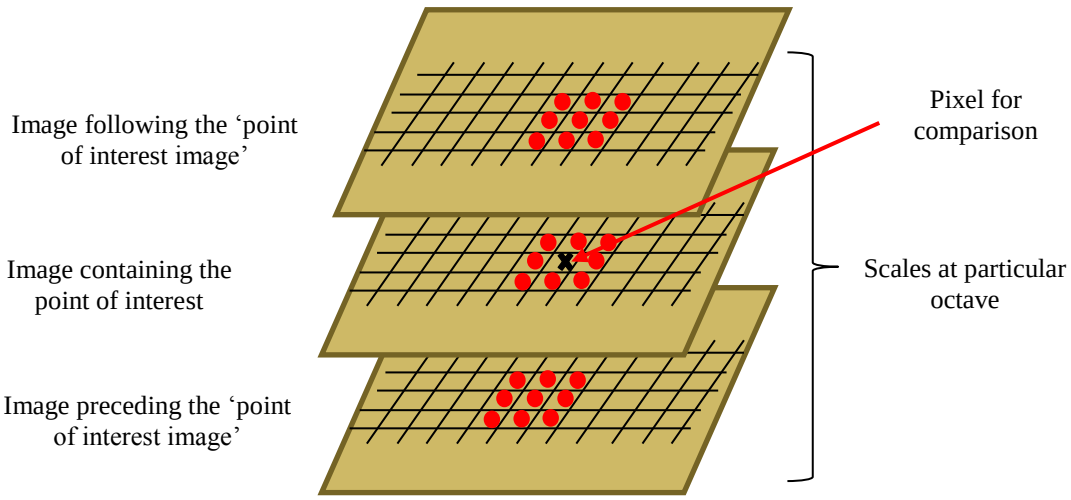

Figure 3.2: Maxima and minima of different of Gaussian (detection of keypoint).

Accordingly, the pixel is selected if it is larger or smaller than all of these neighbours. Once the keypoint is chosen, an orientation is assigned to that keypoint according to local image properties. Figure 3.2 exhibits the procedure of local extrema detection.

3.2.3 Orientation assignment

Gaussian smoothed image L is selected based on the scale of the keypoint. At a particular scale, each image sample $l(x, y)$, the gradient magnitude $m(x, y)$ and orientation $\theta(x, y)$ are computed as:

$$m(x,y) = \sqrt{Lx^2 + Ly^2} \quad \text{and} \quad \theta(x,y) = \tan^{-1}\left({}^{Ly}/_{Lx}\right) \qquad \text{Equation 3.8}$$

$$Lx = L(x+1,y) - L(x-1,y) \qquad \text{Equation 3.9}$$

$$Ly = L(x,y+1) - L(x,y-1) \qquad \text{Equation 3.10}$$

Where Lx and Ly are pixel difference values.

Within a region around the keypoint, an orientation histogram is formed from the gradient orientations of sample points. The orientation histogram has 36 bins covering the 360 degree range of orientations. The peaks in the orientation histogram correspond to the dominant directions of local gradients. The highest peak in the histogram is detected, and then any other local peak that is within 80% of the highest peak is used to also create a keypoint with that orientation. Therefore, for multiple peaks of similar magnitude, there will be multiple keypoints created at the same location and scale but different orientations. Figure 3.3 illustrates the detected keypoints' location, orientation and scale of an X-ray image of a suitcase and contents produced by the author.

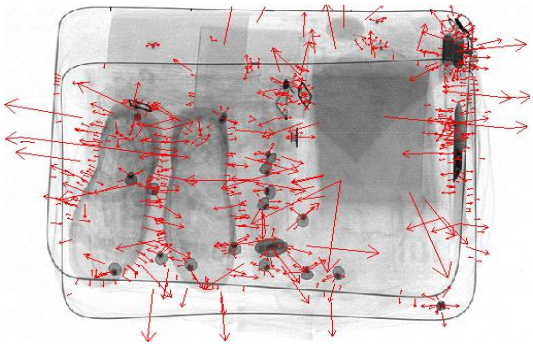

Figure 3.3: Gradient magnitude and orientation of produced keypoints.

3.2.4 Feature descriptor generation

Once the keypoints are generated, a local image descriptor for each keypoint is produced. A keypoint descriptor is created by first computing the gradient magnitude and orientation at each image sample point, in a region around the keypoint location using the scale of the keypoint to select the level of Gaussian blur for the image, as shown in figure 3.4.

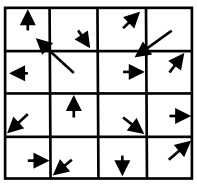

Figure 3.4: Magnitude and orientation of an image point.

These samples are then accumulated into orientation histograms summarising the contents over 4 × 4 sub-regions. Figure 3.5 illustrates the creation of each feature descriptor. Lowe used a 4 × 4 array of histograms [97] with eight orientations in each bin. The length of each arrow is corresponding to the sum of the gradient magnitudes near that direction within the region. However, adding more orientations or a larger descriptor can damage the matching since it can make the descriptor more sensitive to distortion. Consequently, each descriptor vector for a particular keypoint will be of length 4 × 4 × 8 = 128. Finally, to limit the effect of illumination change the feature vector is normalised to unit length.

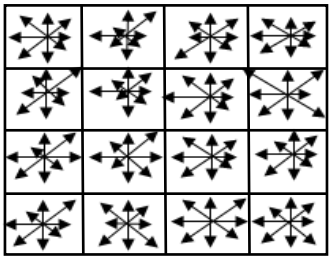

Figure 3.5: 4 x 4 feature descriptor.

An example of feature descriptors for image is demonstrated in figure 3.6 (a). The image of figure 3.6 (b) is the magnified corresponding regions obtained at -2 and +2 degrees (a knife inside the bag is highlighted by the black dashed rectangle in figure 3.6(a)). For brevity, just one pair of corresponding features is considered.

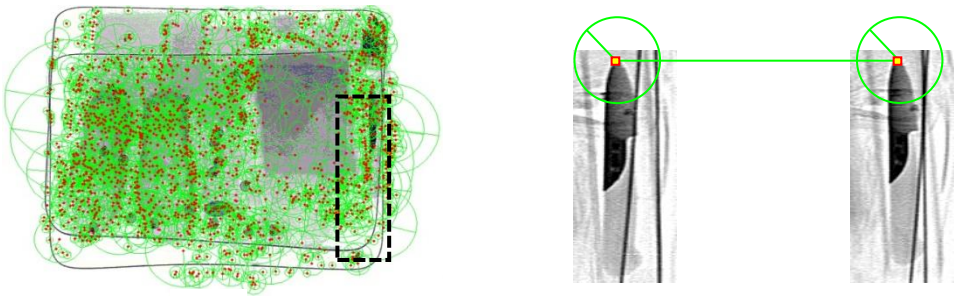

(a) (b)

Figure 3.6: (a) A practical X-ray image populated with the location of keypoints indicated by red spots, and the location of feature descriptors indicated by green circles (b) the horizontal green line links the location of matched feature descriptors in view-2 and view+2.

The yellow/red spot characterizes the location of the feature (keypoint) at the tip of the knife's blade while the green circle describes the feature descriptor. It is said that the two keypoints are matched if their descriptors are matched.

3.3 Limitations of the SIFT matching criteria

A fast nearest-neighbour algorithm is used to identify the best match for a particular keypoint in a large database of keypoints. Since the keypoint is described by its descriptor, the nearest neighbour is defined as the keypoint with minimum Euclidean distance from the invariant descriptor vector. Nevertheless, numerous features from the target image will not match correctly in the derived keypoints database. This is for the reason that they were not detected in the reference image. Also, features might be incorrectly matched with other features simply because they were similar descriptors. It was suggested by Lowe [97] to discard all matches in which the distance ratio between closest neighbour to that of the second closest neighbour is greater than 0.8. It has been found that this ratio is a good metric as it tends to remove around 90% of the false matches; while discarding less than 5% of the true matches.

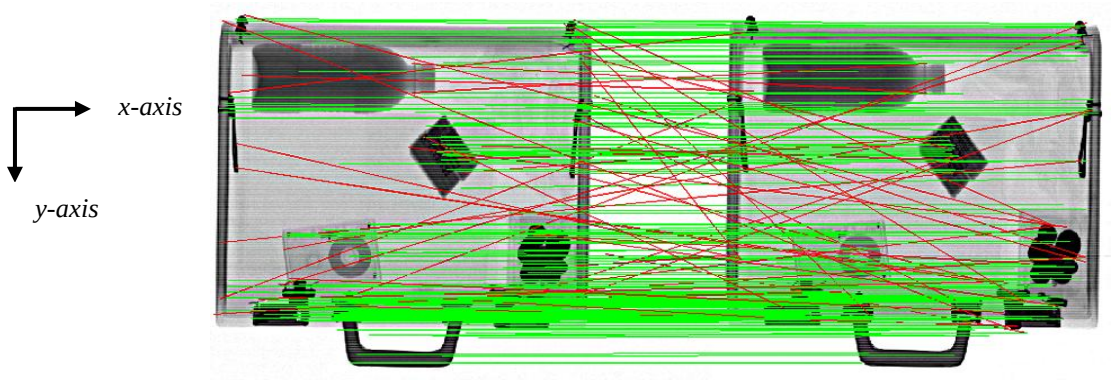

Figure 3.7: Matching result between view-2 and view+2 perspective images.

Figure 3.7 presents the matching result between two perspective views. The matches were produced by utilizing the standard SIFT matching criteria. To aid the visual inspection, each corresponding pair is connected with a line. In the image of figure 3.7, green lines are used to link the "positive matches" (i.e., correct matches) while negative matches are highlighted by a red line. The success of the image synthesis algorithm relies upon the quality of the correspondences (keypoints) generated in the image matching stage and; the reliability of the image morphing process to make use of the keypoints to create intermediary images. It has been proven that the keypoints generated by standard SIFT are invariant to image rotation, scaling as well as being robust across a substantial range of affine transformation. Unfortunately, this broader affine invariance can be detrimental to our application. Figure 3.8 provides an example of a matched stereo pair in which the right view was rotated by 30^0 about the normal to the page; green lines link each matched pair.

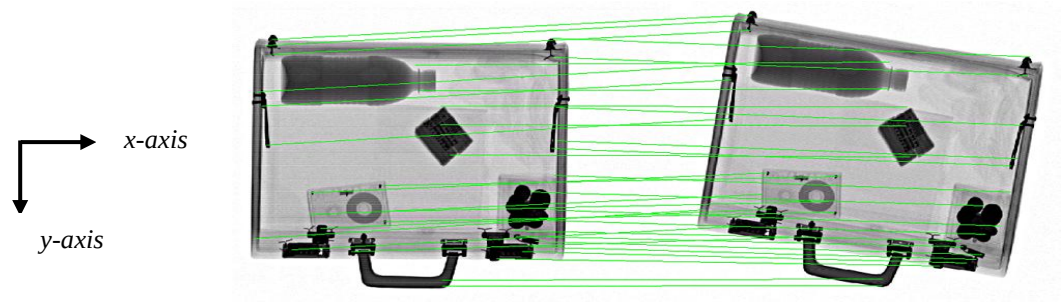

Figure 3.8: The ability of SIFT to locate matches when image rotation has been applied to one view.

As it can be deduced from this figure 3.8, the standard SIFT is able to match correspondences even if they have large difference in y-positions (vertical disparity). SIFT has also demonstrated the ability to locate corresponding features under different image scaling conditions as revealed in figure 3.9, where the right perspective view was scaled down by 20% of the original size. This capability however, is not useful for our application as image magnification is preserved from view to view in KDEX imagery.

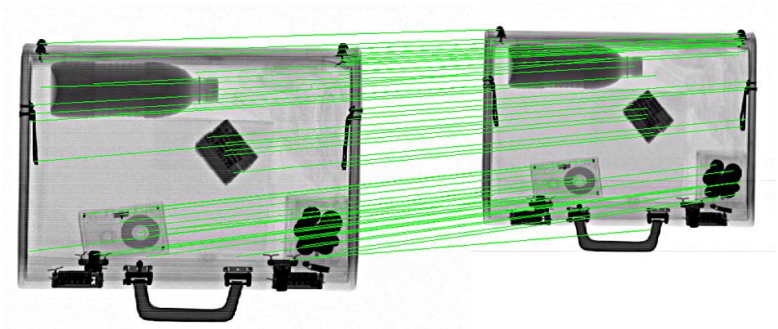

Figure 3.9: The ability of SIFT to locate matches when the image scale for one view is varied.

The generation of KDEX imagery is based on the line-scan imaging principle. The resultant images are expected to exhibit no (or very small in practice) vertical disparity between the corresponding pairs. However, the SIFT's ability to match across large vertical disparities could generate matches that statistically satisfy the SIFT criteria but are not possible due to geometric constraints of KDEX imaging. These matches will be incorrect and can lead to significant or catastrophic errors in the synthetic images. The KDEX imagery employed in this research does not exhibit vertical disparity. Therefore, corresponding pairs of matches have to occur at the same y-axis coordinate position. It can be appreciated from the matching result in figures 3.7, 3.8 and 3.9 that corresponding pairs of similar features will be matched across different y-positions as indicated by non-horizontal lines in the diagrams. This observation suggests that the application of an additional geometric criterion would improve the accuracy of matching. Another limitation of the matching criterion adopted by SIFT is the absence of a disparity window limit. Again, the search for corresponding pairs can be informed by the specific design of the KDEX system employed in this research. In general, a KDEX scanner has a finite inspection volume, which is bounded a physical inspection chamber. The resultant disparity in the display is a carefully controlled parameter that is

naturally limited by the far and near extent of the inspection chamber. Therefore, the imposition of a finite search window will reduce the search space and also exclude impossible negative matches.

3.4 Proposal of new matching criteria

To tackle the limitations associated with the standard SIFT matching criterion, two new criteria are proposed, namely the epipolar line criterion and the disparity window criterion. The following paragraphs are organised to describe the new proposals and the experimental details of the investigation.

3.4.1 Epipolar line criterion

The epipolar line criterion is implemented by extracting the location of features and their correspondences in the perspective views. These features are identified by applying the standard SIFT algorithm. Each feature or keypoint has a (x_1, y_1) position and potentially a corresponding keypoint located at (x_2, y_2). Taking into account various practical fluctuations (i.e., system noise) together with a tolerance of ±1 pixel difference in the y-position informs a practical epipolar line criterion. In other words, pairs that have a y-axis difference "$y_2 - y_1$" greater than ±1 are discarded. It should be noted that this criterion is only applied to corresponding pairs that have met the standard SIFT matching criterion. The corresponding pairs that satisfy the standard SIFT criteria as well as the epipolar line criterion and the disparity window criterion are potentially valid matches. The epipolar line criterion is graphically explained in figure 3.10.

3.4.2 Disparity window criterion

The disparity window criterion is designed to further increase the accuracy of matching. Both epipolar and disparity window criteria are of fundamental importance in the design of a KDEX imaging system. Unlike the epipolar criterion, the disparity window size is a function of the angular separation between the views under consideration. The disparity window criterion is illustrated figure 3.10.

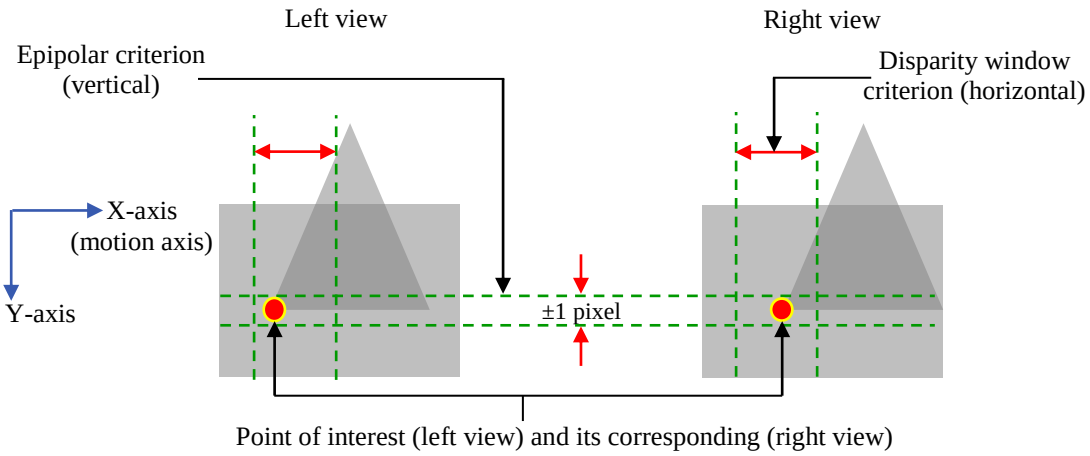

Figure 3.10: The epipolar line is defined, nominally, in the horizontal direction for the KDEX imaging technique; the disparity window defines the maximum potential length along this line that supports potentially valid matches.

The application of the disparity window can be applied by applying the maximum allowable offset values in the x-axis and y-axis. In other words, pairs those have x-axis difference "$x_2 - x_1$" greater than the agreed disparity window may be discarded. This criterion is only applied to those corresponding features that have already met the standard SIFT and epipolar matching criteria.

In this way matched features may be categorised into two groups; negative and positive matches. The positive matches are the matches that satisfy the standard SIFT, epipolar and disparity window criteria while the negative matches satisfy the standard SIFT criterion but violate either the epipolar line or disparity window criteria. Figure 3.11 presents an example of the matching results recorded for two perspective views obtained at -3^0 and -2^0.

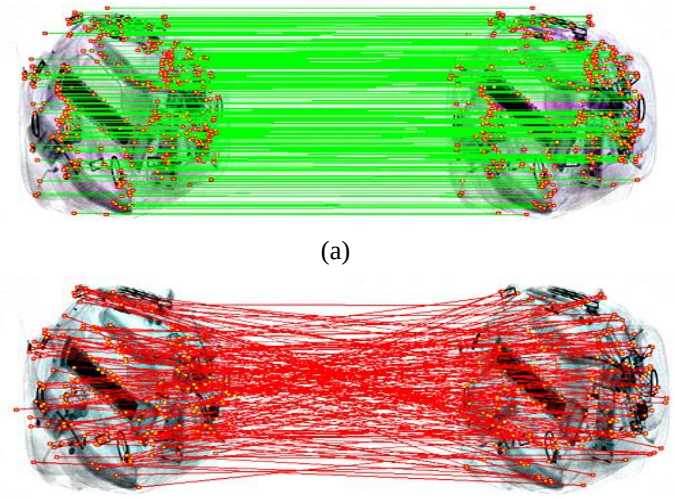

(a)

(b)

Figure 3.11: Optimised SIFT matching result (a) positive 'green' matches and, (b) negative or false 'red' matches.

Figures 3.11 (a) represents the positive matches indicated by horizontal green colour lines connecting the corresponding pairs, while the negative or erroneous matches are presented in figure 3.11 (b) and are shown as red colour lines.

3.4.3 Implementation of optimized SIFT using Matlab

The standard SIFT Matlab open source code is available online at [164]. This software accepts two perspective views and matches them according to its standard matching criteria described in Section 3.3. The standard SIFT provides a single number which represents the total number of matches (including the positive and negative matches represented by the green and red lines in figure 3.7). The author designed and implemented additional criteria to reject geometrically impossible matches as determined by the novel line-scan imaging configuration. The code was modified to record the (x,y) location of all the corresponding features in each view. An epipolar line criterion was implemented in code to remove automatically all correspondences that exhibited a vertical disparity greater than ±1 pixel. A disparity window criterion further limited the search space along the motion or x-axis. The boundaries for this criterion were calculated using the angular separation between the views under consideration and implemented automatically. In the context of this work, the modified code is termed the optimized SIFT algorithm. This modified algorithm also provides the percentage of the total number of matches being removed by either or both criteria with respect to the

total number of matches produced by the standard SIFT. The algorithm also displays the matching results visually by showing the positive and negative matches in two separated figures. Once the perspective views are matched, the code was also altered to save two (*.mat*) files. Each file consists of one perspective view and its corresponding features map. These two (*.mat*) files are then made available and exploited by the morphing/warping techniques where one or more synthetic views are generated.

The Flowchart in figure 3.12 explains the matching approach adopted in this research. The matching procedure starts by applying the standard SIFT matching criteria followed by the proposed two new criteria. To assess the effectiveness of using the proposed criteria, percentages of negative and positive matches for stereo pairs are computed. This study employs a total of 30 different luggage items or bags. From each different bag, 6 successive stereo pairs were selected from a total of 7 images (from a KDEX sequence) and have been employed as per the scheme presented in figure 3.13.

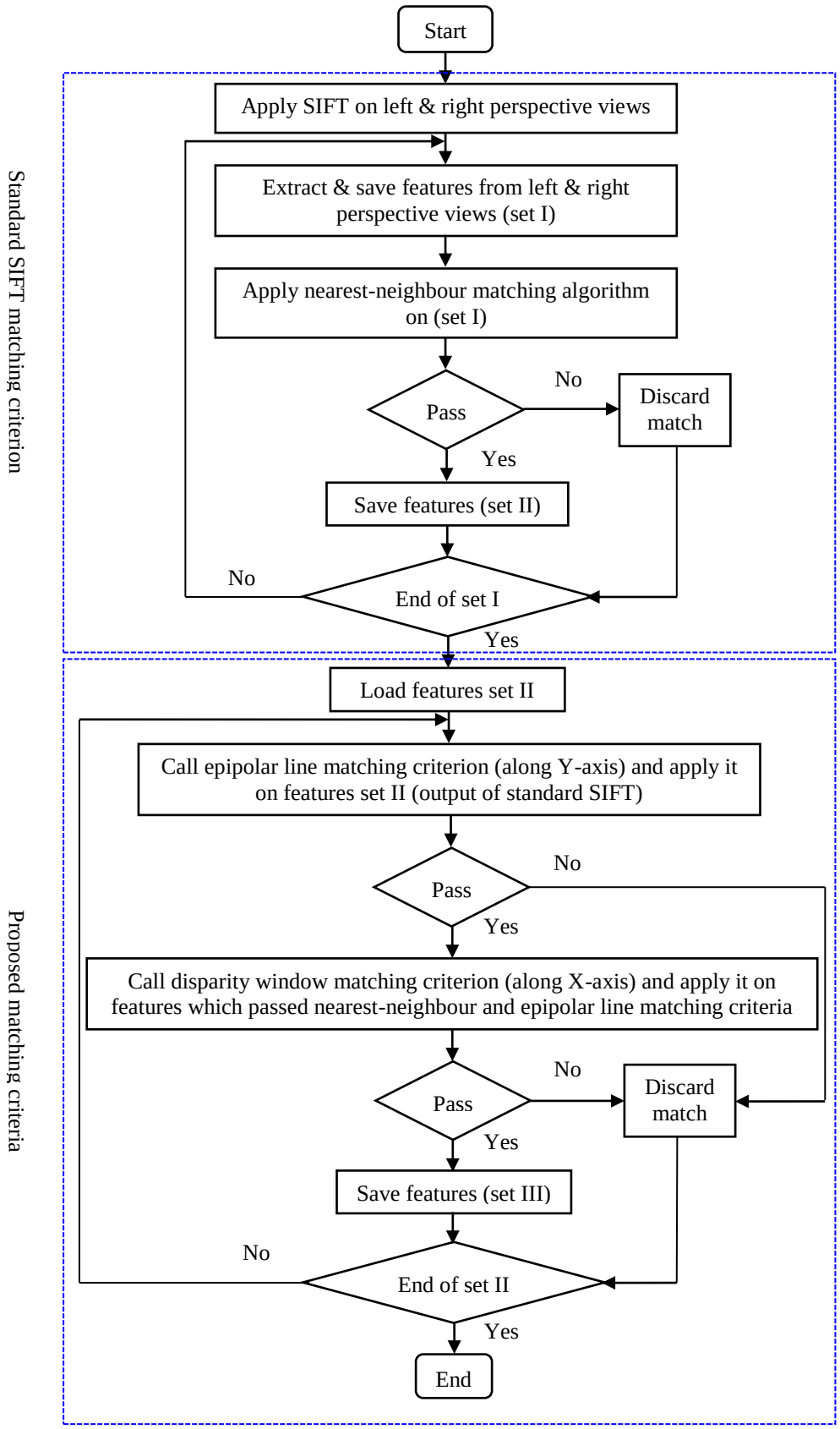

Figure 3.12: Flowchart for the proposed matching route.

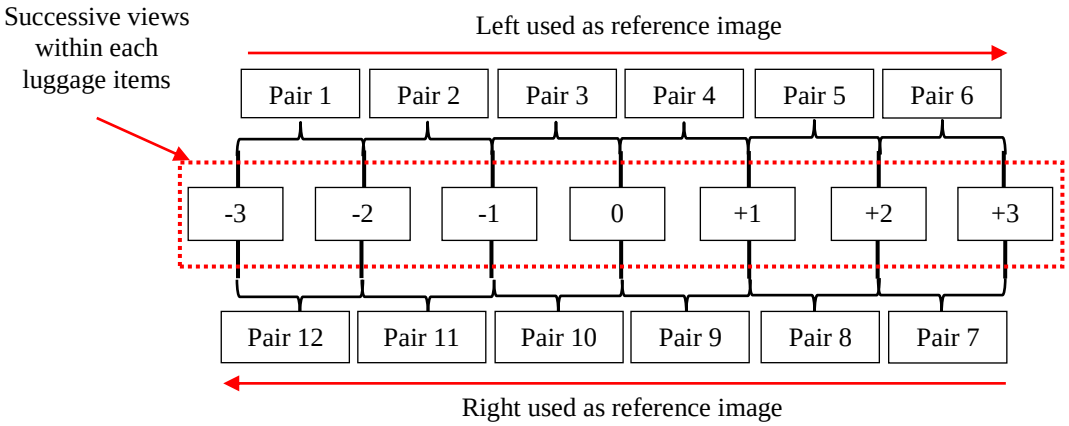

Figure 3.13: Organisation of the image pairs employed to study the dependency of the matching results upon the epipolar line and disparity window criteria.

The angular separation between each successive view is 1^0, taken over an angular range of $\pm 3^0$ about the 0^0 or normal view position. Each pair is analysed twice to accommodate either perspective view as the reference image. This implies that 12 image pairings are processed for each luggage item. This study employs 30 different bags therefore, a total of 360 image pairings were available for analysis. To demonstrate the effect upon matching performance for both new criteria, consider the images shown in figure 3.11. The combination of matched features in Figures 3.11 (a) and (b) is 1640 as identified by standard SIFT; a total of 444 matches were discarded (from a base of 1640) when the new criteria were applied, see the first row of data presented in Table 3.1. To make the discussion easier, a graphical representation of the data presented in Table 3.1 is reproduced in figure 3.14; all the matches were identified via standard SIFT and are indicated by the black bars. Positive and negative matches are recoded at each stage to identify the presence of 'geometrically impossible' matches. Also, it should be appreciated that the total number of positive and negative matches are conserved e.g. the blue bar and the red bar 'total' are equal to the green bar and pink bar 'total' (which is also equal to the black bar 'total').

successive stereo pairs	Standard SIFT keypoints	Epipolar line criterion		Epipolar line + Disparity window criteria	
		Positive matches	Negative matches	Positive matches	Negative matches
Pair 1 (-3 to -2)	1640	1335	305	1196	444
Pair 2 (-2 to -1)	1533	1260	273	1009	524
Pair 3 (-1 to 0)	1521	1242	279	853	668
Pair 4 (0 to +1)	1607	1350	257	1206	401
Pair 5 (+1 to +2)	1673	1383	290	1100	573
Pair 6 (+2 to +3)	1738	1420	318	1185	553
Pair 7 (+3 to +2)	1727	1408	319	1180	547
Pair 8 (+2 to +1)	1670	1387	283	1096	574
Pair 9 (+1 to 0)	1646	1359	287	1202	444
Pair 10 (0 to -1)	1533	1231	302	859	674
Pair 11 (-1 to -2)	1482	1240	242	999	483
Pair 12 (-2 to -3)	1636	1340	296	1181	455

Table 3.1: Matching results for the stereo pair shown in figure 3.11 where positive and negative matches were recorded when applying the epipolar-line criterion only and when applying both new criteria.

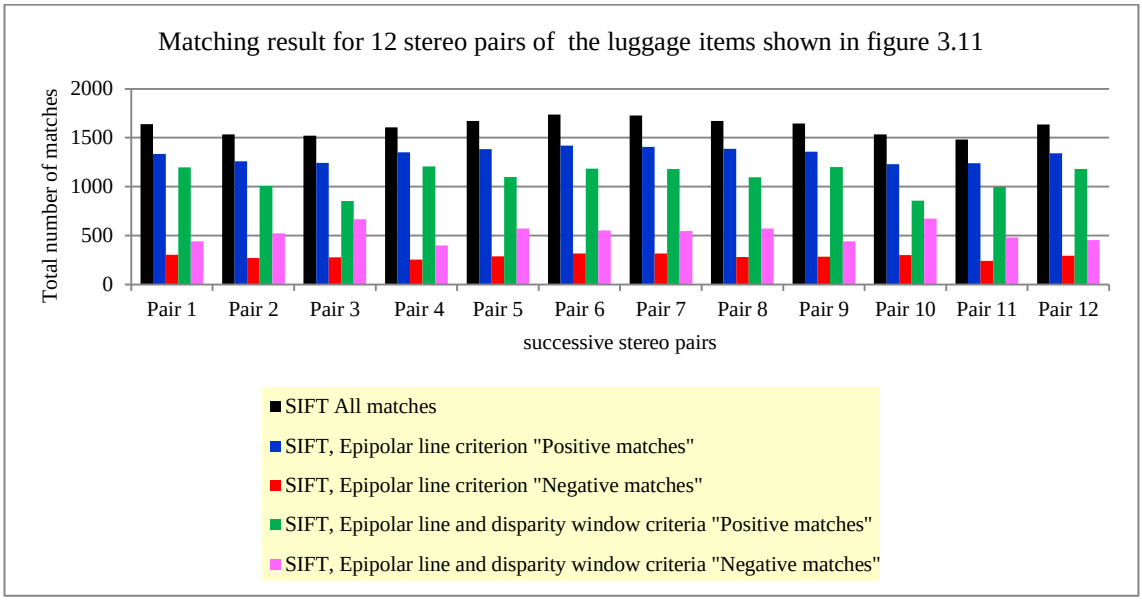

Figure 3.14: Matching result of the luggage item shown in figure 3.11 where matches are classified as positive or negative according to the proposed matching criteria.

The concatenation of the criteria tighten the support of standard SIFT. The increase in negative matches (and the corresponding decrement in positive matches) is the expected consequence of logically 'ANDing' the criteria. It is important to note that only the positive matches "shown as green bars in figure 3.14" which meet standard SIFT, epipolar line and disparity window criteria are considered for input to the morphing

algorithm and will be used to synthesise in-between views. Briefly, together with their stereo pairs, the corresponding keypoints are loaded and operated by a morphing algorithm to create the synthesis view. This finding will be discussed in more detail in the following chapters.

The procedure described in Table 3.1 has been repeated for 30 bags and the average numbers of positive and negative matches for each matching criterion are presented in figure 3.15. The bar chart in figure 3.15 has been plotted to demonstrate the effectiveness of new criteria in rejecting incorrect matches. The first bar in black represents the average number of matches generated by the 360 stereo pairs, which corresponds to matches that have met the standard SIFT criteria. Similarly, matches that have satisfied the epipolar line criterion, matches that have failed the epipolar line criterion, matches that have fulfilled the epipolar and disparity window criteria, and matches that have violated either or both new added criteria have been computed and plotted sequentially in the bar chart below.

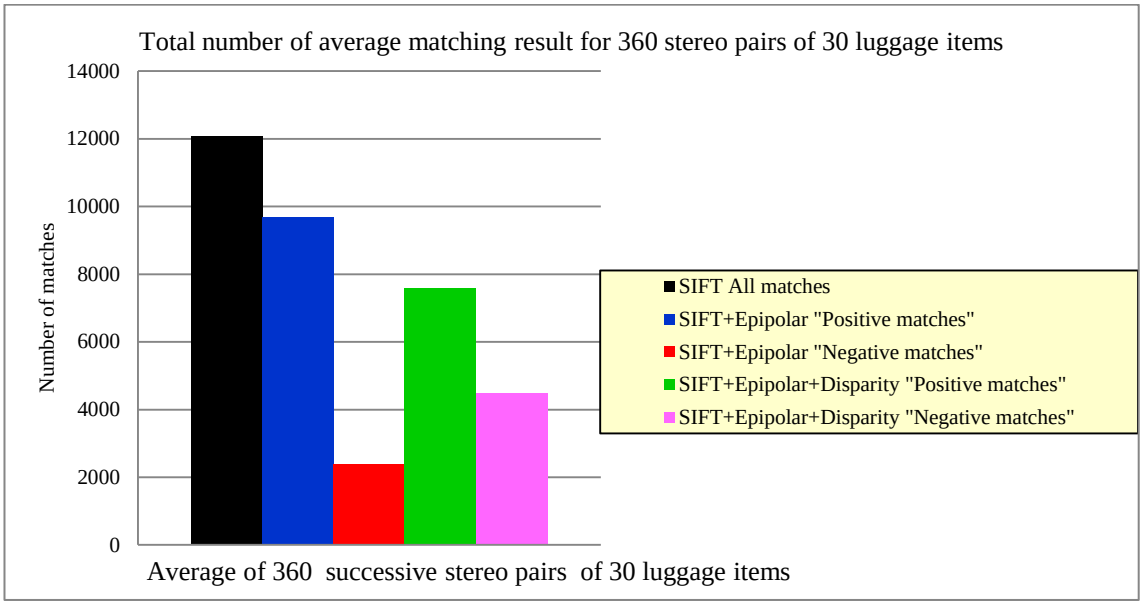

Figure 3.15: Total number of averaged matches for 360 image pairs produced from 30 different experimental bags.

The proposed criteria have demonstrated that they can remove 37.2% of unfaithful matches i.e. 19.8% are attributed to the epipolar line criterion and a further 17.4% attributed to the disparity window criterion. An indication of the benefit afforded by the

optimised SIFT algorithm is presented in the form of the synthetic results for a "torch" as extracted from one of the experimental bags, see figure 3.16. Out of the 79 detected matches, 26 positive matches are linked by green lines "figure 3.16 (a)" while the red lines link 53 negative matches "figure 3.16 (b)". When all the 79 matches produced by the standard SIFT are used to synthesise a resultant image "figure 3.16 (c)" it has undergone substantial distortion; making it unrecognisable. Fortunately, the optimised SIFT has demonstrated a significant potential to improve upon this situation, as evidenced in the synthesised image of the "torch" in figure 3.16 (d).

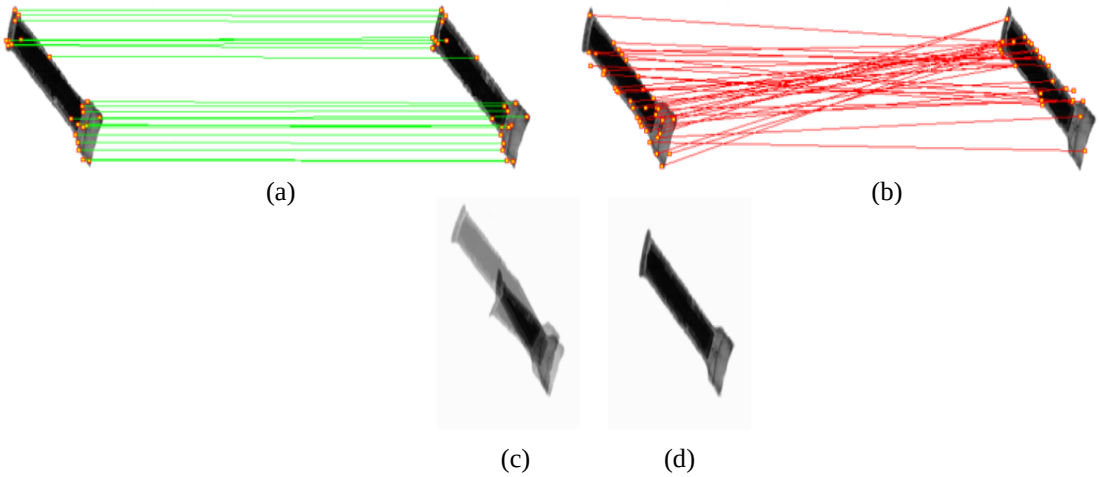

Figure 3.16: The matching and synthetic results for the X-ray images of a torch where (a) and (b) show the positive matches and negative matches respectively, (c) and (d) are the synthetic views produced by employing matches detected by standard SIFT and optimised SIFT, respectively.

The KDEX imagery employed in this pilot study is of practical luggage and was produced in the Imaging Science Group's laboratory at the University. These empirical results demonstrate that SIFT has a promising potential to search for X-ray image correspondences. The following paragraphs are organised to question the viability of operating SIFT on X-ray images under the more varied and complex conditions routinely encountered in security X-ray imaging.

3.5 Analysis of optimised SIFT

The transparency property of X-ray images provides additional information, which can constrain the matching process under certain conditions. Besides, addressing the correspondence problem is subject to conditions commonly encountered in imagery of practical luggage items include overlapping semi-transparent structures, local masking and repeated or similar objects. To study these conditions, consider the image of luggage exhibited in figure 3.17.

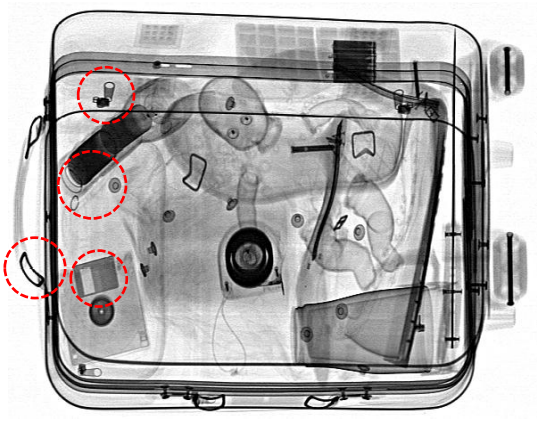

Figure 3.17: X-ray image of a suitcase with highlighted regions of interest.

ROI's highlighted by the red dashed circles are considered for further discussion.

3.5.1 Effect of overlapping

Figure 3.18 organises examples of image regions that are extracted from the stereo pair of the image illustrated in figure 3.17 to illustrate the effectiveness of optimized SIFT for no overlapping and overlapping conditions; the term overlapping refers to structures from different discrete objects, which overlap in the resultant image. Figure 3.18 depicts "part of the bag handle and it is labelled as exhibiting no overlap" and demonstrates the expected capability of optimized SIFT under a no overlapping condition. In addition, it can be deduced from the same sub-figure that optimized SIFT can also extract correspondences from the overlapping region presented by the "shutter of the floppy disk at the left and zip slider at the right both labelled as simple overlap". Although, both objects were cluttered by organic material such as clothes and plastic, optimized SIFT was able to extract features from these objects. Due to the significant difference in

X-ray attenuation, the shutter of the floppy disk and zip slider are highly salient objects under this overlapping condition hence aiding the search of correspondences. However, if the same scenario is replicated in visible light images, both objects will either be seen if it is located in front of the organic material, or totally buried by the organic object. This simple overlapping scene exemplifies the fundamental difference between X-ray images and visible light images as well as the nature of the challenge in solving correspondences.

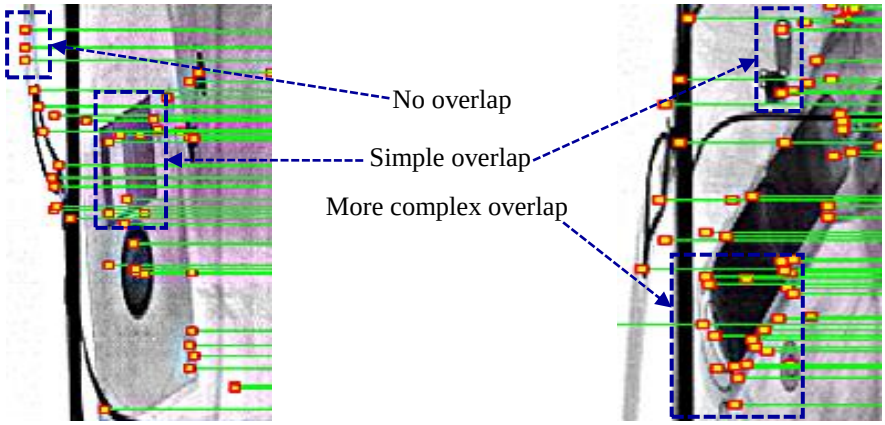

Figure 3.18: Image regions in the stereo pair of view 1-2 to emphasize the performance of SIFT in terms of overlapping structure.

The region of figure 3.18 labelled as 'more complex overlap' is another example to support the capability of optimised SIFT of extracting features under further dense scene. This region represents part of the cell battery of the torch overlapped with the torch plastic body as well as by the amorphous organic material which made the scene much more intense. It is very encouraging to obtain positive outcomes even when SIFT is faced by multi-layered overlapping structures. The SIFT has to cope with not only the change in material compositions, but also variations in shape and relative positions and orientation in 3D space of the objects under inspection. For example, the change in spatial orientation of the cell battery when translating from one view to the other.

3.5.2 Local contrast

It can be deduced from figure 3.19 that the local masking conditions such as the contrast between the keypoint and the background (i.e., local contrast) play important roles to search for correspondence features. The local contrast factor affected the detection of

the local extrema. The images of figure 3.19 are a good example to illustrate the effect of the local contrast. The images are zoomed in area extracted from matching view-2 and view-1 of the image revealed in figure 3.17. Two regions of interest are highlighted by blue dashed circles in figure 3.19 which are part of the bag handle as well as the bottom edge of the floppy disk. The contrast is determined by the amount of X-ray attenuation produced by the two objects, which is a function of material compositions and thickness. The contrast between the objects can be minimised by either reducing the difference in X-ray attenuation imposed by the objects, or increasing the thickness of the organic material such as the material overlap with the floppy disk.

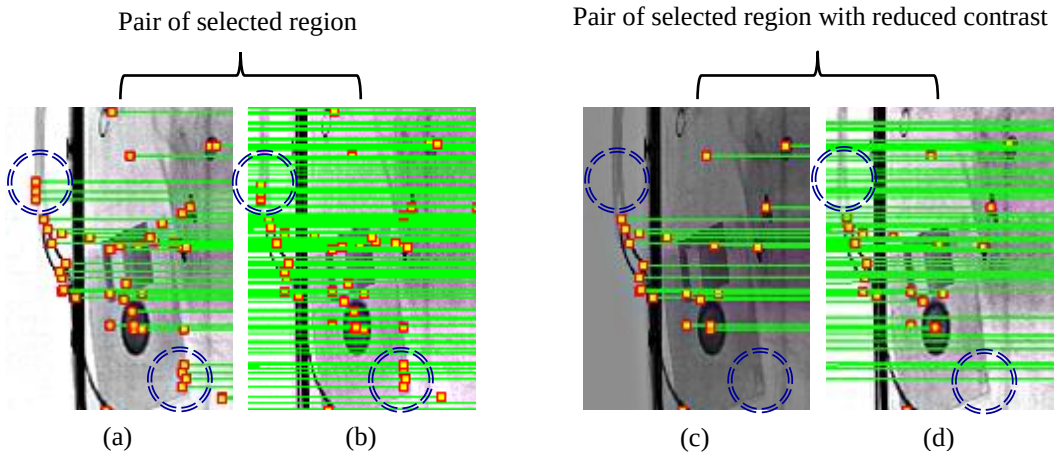

Figure 3.19: Effect of local contrast to search for correspondences where (a) and (b) are the image regions in view-2 and view-1 respectively, (c) and (d) are identical to (a) and (b) except (c) is presented with reduced contrast as compared to (a) region. A blue circle is used for aiding visual comparison and it is apparent that SIFT failed to detect the same features once the contrast is reduced.

The contrast can also be minimised by reducing the thickness of shutter of the metallic material embedded in the floppy disk. In a practical scenario, any of these conditions can occur, which may negatively affect the SIFT performance, as presented in figure 3.19. Figure 3.19 (a) and (b) are the corresponding image regions in view-2 and view-1 respectively where correspondences are detected and highlighted by blue circles. However, figure3.19 (c) and (d) are identical to (a) and (b) except that the contrast of (c) is reduced. It can be noticed that the optimized SIFT failed to find not only the

highlighted correspondences but even other correspondences as indicated in figure 3.19 (c) and (d), hence; reduction of contrast can adversely influence the performing of the matching algorithm.

3.5.3 Local similarity

Another factor that may determine the matching result is the local similarity of the neighbourhood around the feature of interest. To study the effect of local similarity consider the luggage item demonstrated in figure 3.20, where region of interest is highlighted by red circle.

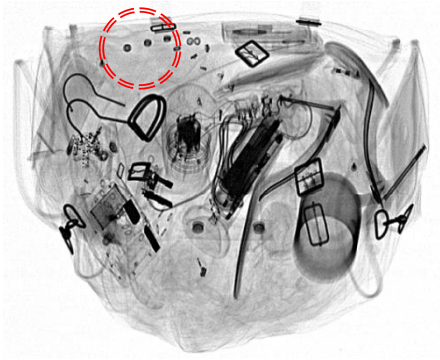

Figure 3.20: Luggage item with highlighted region of interest to show the effectiveness of local similarity to search for correspondences.

The region of interest is magnified as indicated in figure 3.21 where two repeated features are emphasized for the purpose of comparison (see figure 3.21 (a)). Features in figure 3.21 (a) are extracted from view-3 and -2. Similar, closely located features are accurately matched. Similar result obtained when view-1 and view 0 are considered. Different views give different results as indicated in figure 3.21 (b) where the stereo pairs of view-2 and view-1 are involved. It is noticeable that only one of the two selected features is found. This is simply because when the view is changed, either the epipolar line or disparity window criteria are not satisfied, therefore; the correspondence pair of matches is discarded. Figure 3.21 (b) and (c) highlight the matching result for (1) view-2 and view-1 and, (2) view-1 and view 0, respectively. Both stereo pairs have the same angular separation between views (i.e. 1^0) but exhibited a different result. This finding simply demonstrated that the transparency property of X-ray images can cause

a drastic change in the immediate neighbourhood of the features and hence affect the matching results.

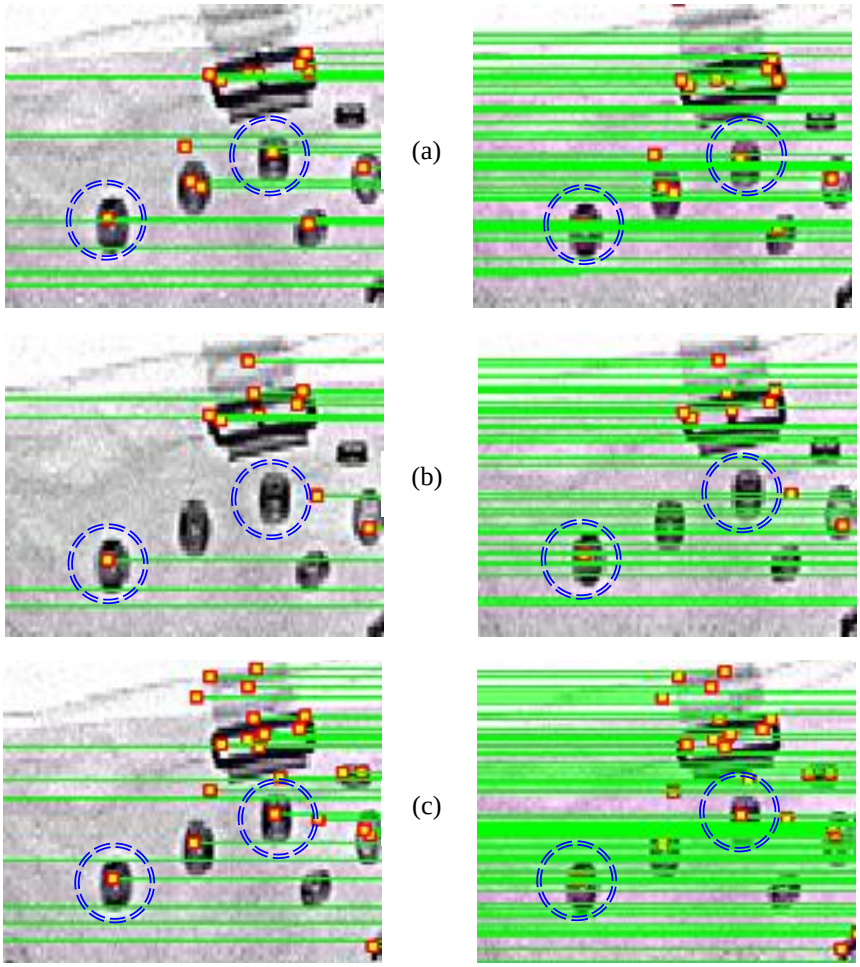

Figure 3.21: Image regions in the stereo pair between (a) view-3 and view-2, (b) view-2 and view-1 and, (c) view-1 and view 0 to exemplify the effect of local similarity on the correspondence search.

The material presented in this chapter assessed the performance of optimized SIFT when dealing with X-ray imaging. 30 sets of luggage items are processed and analysed. 6 successive stereo pairs from a total of 7 views KDEX sequence images are employed for each set of luggage items. Pairs are analysed twice to accommodate either perspective view as the reference view which produces 12 image pairings being processed for each luggage item. The angular separation between each successive view is 1^0 taken over an angular range of $\pm 3^0$ about the 0^0 or normal view position.

Initially, the matching algorithm was employed to minimum degree of angle separation between adjacent pairs (1^0). This approach assumes that if SIFT has produced unsatisfactory results at a relatively small angular separation, then its performance will further degrade as the separation is increased. Empirical evidence in figure 3.18 revealed that optimized SIFT is capable of finding the correspondences in X-ray images under no overlapping and full overlapping conditions. The success of optimized SIFT can be associated with two factors: the local contrast and local similarity, which directly affect the detection of corresponding features. These factors also play an important role in searching for correspondences in visible light applications. However, the transparency property of X-ray images posed a different set of challenges. This point can be appreciated further by referring to figures 3.19 and 3.21. The complex masking and unmasking inherent in KDEX imagery tends to increase the probability that the features of interest will be partly or fully occluded in at least one view, hence increasing the matching uncertainty. The problem is further exacerbated if the overlapping structure is comprised of many individual objects that have diverse properties in terms of material composition, thickness and shape. Overall, optimized SIFT has produced encouraging results in searching for X-ray image correspondences. The complexity presented by the transmission property of X-ray images presents a unique challenge in terms of solving the corresponding problem.

In the context of the following chapters, the performance of the optimized SIFT algorithm will be assessed as a function of angular separation between views (or X-ray beam angle). The investigation addresses greyscale X-ray images along with dual-energy X-ray images in which materials discrimination information is colour coded. The results of the optimised SIFT will provide the required information for image morphing to provide the required synthetic imagery. Limitations of the developed synthesis algorithms will be investigated by employing ground truth imagery for comparative error analysis.

Chapter Four Greyscale image synthesis algorithm

4.1 Introduction

The greyscale image synthesis algorithm developed in this research programme is presented fully in this chapter. The algorithm is a combination of optimized SIFT and morphing techniques termed, ‘epipolar based morphing’. The algorithm is designed to accept greyscale X-ray detector images produced by the kinetic depth X-ray (KDEX) imaging techniques previously developed by the University team. The algorithm produces synthetic images, which may be used to replace the X-ray detector images. Therefore, enabling a reduction in the total number of detectors and their associated hardware required to realise KDEX sequences.

The synthesis algorithm is divided into two major stages, namely matching and morphing. Optimized SIFT is employed as a matching algorithm to accurately extract the corresponding keypoints from a successive pairs of perspective views. The resultant corresponding features are loaded into an epipolar based morphing algorithm, which generates the synthetic view. The combination of detector images and synthetic images are viewed in sequence, the resultant transition from one view to another should, ideally, be natural to the observer. Therefore, the fidelity of the synthetic images is established by comparing them with detector images produced at the appropriate X-ray beam angle by the scanner. This approach enables a direct measure on how well the synthetic images resemble the detector images. In the context of this research programme, these detector images that are used for comparison are defined as the ground truth (GT) images. It should be noted that GT images were solely used for comparative study but not as the input images to the synthesis algorithm. An image subtraction method is used as the quantitative measure to compute the number of pixel errors between the GT images and the synthetic images. Further details on the comparison are presented in the Section 4.5. The matching and synthesis algorithms performance is assessed as a function of X-ray beam angle. This is accomplished by increasing the angular separation between the X-ray beams used to produce the synthetic perspective images.

4.2 Experiment setup

The experimental X-ray machine employed to produce the perspective images used in this research is illustrated in figure 2.8. This X-ray machine utilises a ‘folded’ linear X-ray detector array (FLXDA) to image typical luggage. The resultant images are stored in a greyscale image format with an 8 bit intensity range. The scanner employs a 140 kVP polychromatic X-ray source. The X-ray source/sensor assembly may be rotated about the conveyor belt to enable the collection of the multiple views at different angular positions. In this way the image output of a single pass multiple view scanner can be simulated. The experimental machine was designed by the University team for the investigation of depth from motion (or kinetic) binocular stereoscopic imaging and was constructed originally at the Home Office Laboratories at Sandridge UK.

The FLXDA illustrated in figure 2.9 is comprised of a contiguous set of linear dual-energy [51] X-ray detector array modules are positioned such that their midpoint normal will intersect the point X-ray source in the plane of the collimated X-ray beam. The resultant line-scan format image exhibits a nominally constant magnification in the (conveyor belt) motion axis (i.e. X-axis and horizontal axis in the visual display). The FLXDA produces an image distortion along its length, which is observable in the vertical display axis (i.e. Y-axis and vertical axis in the visual display). The bottom third of the image is ‘folded out’ due to the perspective view through the luggage produced by the side arm of the folded array.

The dual-energy X-ray materials discrimination information is not analysed in this chapter but is described briefly for completeness and will be discussed further in the next chapter. The dual-energy X-ray detector array consists of low-energy scintillator elements and high-energy scintillator elements in a ‘sandwiched’ configuration [60]. A thin copper filter is placed between the front and rear arrays to enhance energy separation between the low-energy and high-energy X-ray data (see figure 2.2). The front array is exposed to the full X-ray spectrum and absorbs the low-energy portion of the polychromatic spectrum. After passing through the filter, a significant amount of low-energy X-rays together with a small amount of high-energy X-rays are removed from the spectrum. The remaining high-energy X-rays are subsequently detected by the rear array. Therefore, the low-energy (~75keV) and high-energy (~140keV) X-ray data of the irradiated object are simultaneously produced from a single exposure. Materials

discrimination information is derived from the dual-energy X-ray data and is made available to the human observer by colour encoding the resultant images. It is planned to use the materials discrimination data in next chapter where the image synthesis technique is described according to material discrimination.

The material in this chapter describes the optimum combination SIFT, additionally bounded by epipolar and disparity window criteria to provide input to an epipolar based morphing method to generate synthetic views at different angular separations. To ensure realistic and satisfactory outcomes, the proposed synthesis algorithm is assessed using 30 different luggage arrangements. The images used for the indicative analysis presented in this thesis were chosen carefully to include objects composed of different material classes arranged in spatially complex scenes. The inclusion of dense amorphous structure together with overlapping high frequency details exhibits the multi-layered translucency typical of images routinely encountered at security checkpoints.

In this chapter, the luggage items (or bags) termed; b1, b2……b30 were employed. For each bag under inspection, 7 sequential perspective images are acquired and stored (producing a total number of 210 perspective images). The angular separation between each successive view is 1^0, taken over an angular range of $\pm 3^0$ about the 0^0 or normal view position, as illustrated in figure 4.1.

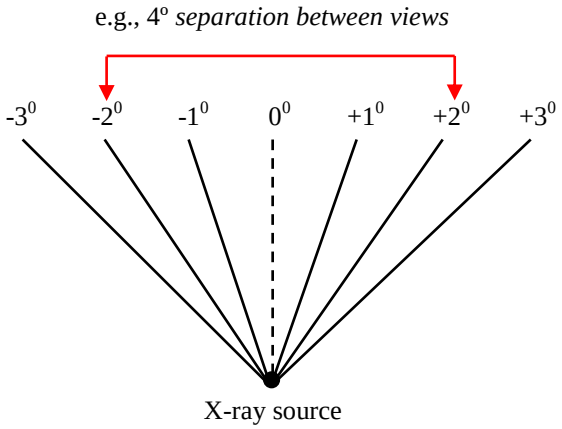

Figure 4.1: Angular separation of the X-rays beams used to image each of the 30 different bags.

The synthesis algorithm initially matches the perspective views with a minimum separation of 2^0 followed by the generation of one synthetic view using the proposed morphing algorithm e.g., -1^0 and $+1^0$ were employed to generate the view at 0^0. Furthermore, the synthesis algorithm is appraised by increasing the angular separation between the 'generating' views, in which more than one synthetic view is produced e.g. up to five synthetic views produced between the two generating views at -3^0 and $+3^0$, respectively.

4.3 Experimental imagery

To provide task relevant outcomes practical luggage items were used throughout the investigation. The image in figure 4.2 is an X-ray image of hand baggage. The bag contents includes a hair dryer which is partly occluded by a printed circuit board, copper wire, organic materials, pair of shoes and pistol overlapped with torch. The objects are arranged over the full volume of the bag.

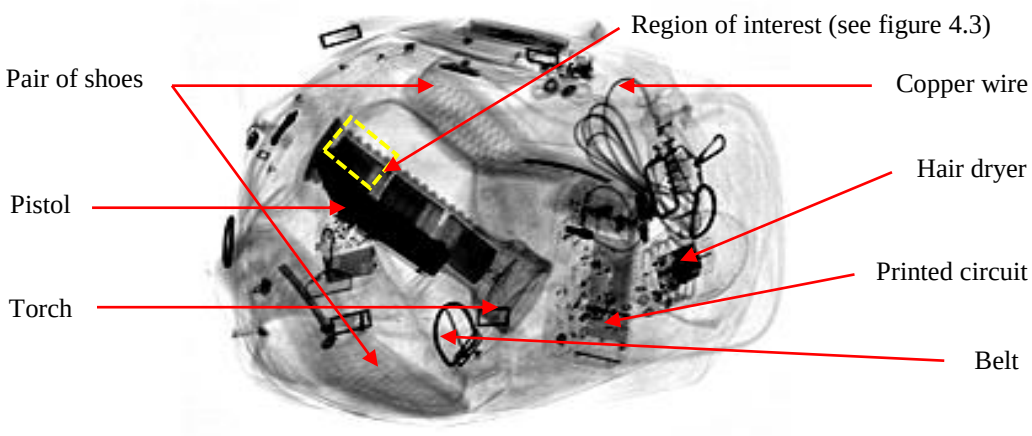

Figure 4.2: Structure of one of the experimental images used in this research.

4.4 Image synthesis via epipolar based morphing

To the authors' knowledge, there is no evidence in the literature that the SIFT based epipolar based morphing presented here has been applied to a sequence of transmission (dual-energy or polychromatic) X-ray images to produce synthetic intermediary views. In particular, image morphing is a popular visual effect in which one image is transformed into another. Morphing a stereo pair I_0 and I_1 requires two correspondence

maps C_0 and C_1 where $C_0: I_0 \rightarrow I_1$ and $C_1: I_1 \rightarrow I_0$. In practice, C_0 and C_1 are derived by having the user to manually select critical points on the two corresponding images as a set of common features. Using these manually selected points, the remaining correspondences are then established automatically by interpolation [132, 138-140]. Any incorrect manual selection of the critical points can generate distracting artifacts such as ghosting and shape distortion. As a consequence, this will be detrimental to the fidelity of the corresponding maps (C_0, C_1) and the resultant 3D depth sensation of the KDEX imagery.

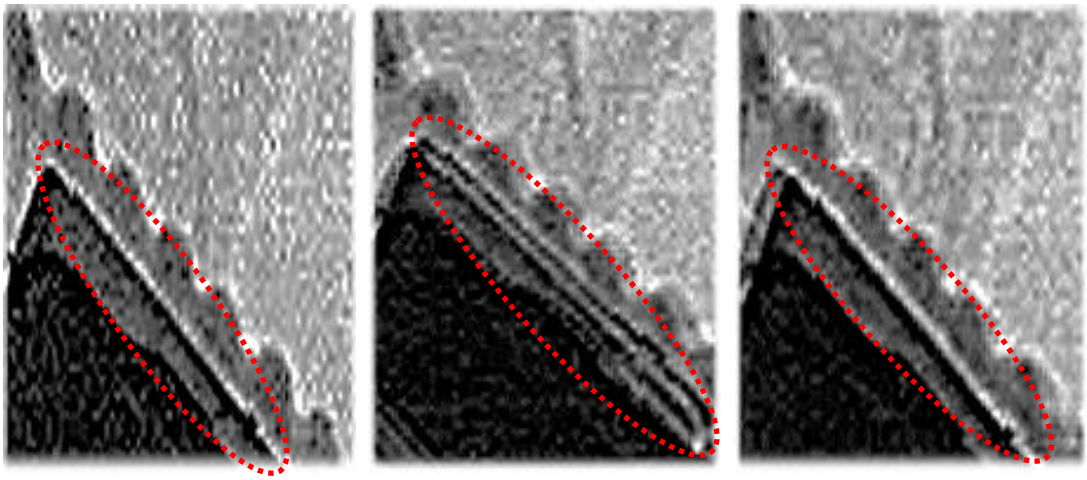

(a) Ground truth region

(b) Synthesised region with standard morphing

(c) Synthesised region with epipolar based morphing

Figure 4.3: ROI for in-between view of figure 4.2 where (a) is the ground truth region, (b) and (c) are the synthetic results using standard morphing and epipolar based morphing correspondingly; where the ROI in (b) illustrates significant distortion.

Epipolar based morphing is proposed here to address such unwanted artifacts. The idea is to employ the output of optimized SIFT as the critical points rather than creating them manually. Initially, I_0, I_1, C_0 and C_1 are input to the epipolar based morphing algorithm. Automatic linear interpolation (employed within the existing morphing technique) is then executed to estimate the positions of the correspondences, C_0 and C_1. As soon as the pixels in I_0 and I_1 are interpolated, the morph is computed by applying the mapping incrementally on both x and y directions, i.e. to shift the features in the original image towards the final image and vice versa. In this research, however, the mapping is

restricted along the x-axis because the KDEX imagery produced by line-scan imaging technique should reveal no vertical (y-axis) disparity as explained in Section 3.4.

Figure 4.3 is organised to illustrate the proposed epipolar based morphing method, which is employed to generate the synthetic views. Figure 4.3 (a) is a region extracted from ground truth view between the pair of images illustrated in figure 4.2. It is the part of the image where the torch is fully occluded by the pistol. In figure 4.3 (a), the region of interest is surrounded by a red dashed oval. Due to unconstrained mapping along the y-axis and x-axis, the standard morphing algorithm has produced ghosting (double edges) along the pistol edge as shown in figure 4.3 (b). Interestingly, as evidenced in figure 4.3 (c) the image produced by the proposed method does not exhibit such artifacts. The number of in-between views depends upon the angular separation between the sensor views and the angular increment under consideration. For instance, if the separation between the two perspectives views I_0 and I_1 is 4^0, then the three middle frames $I_{0.25}$, $I_{0.5}$ and $I_{0.75}$ represent the three in-between views each separated by 1^0. To evaluate the quality of the synthetic imagery requires an appropriate comparison with respect to GT.

4.5 Synthesis algorithm performance measurements

Image subtraction is used to evaluate the synthetic image with regard to the GT. To account for various practical fluctuations (e.g., system noise), the number of errors (ERR) computation includes a tolerance given by the value of the square root of the intensity. This approach is based on the prior research work [60, 161] on measuring the practical noise recorded by a typical X-ray luggage scanner. Ultimately, the acceptable limitation to the fidelity of the synthetic images is task dependent and would entail conducting a series of meticulous human factors investigations [162], which is beyond the scope of this thesis. Nonetheless, besides comparing the ERR produced, a visual inspection was undertaken to assist in evaluating the results within the context of visual displays. The quality of the synthetic images was determined by comparison with the GT according to the following formula:

$$\text{ERR} = \left\| \{ \text{P} \in \text{M} \left| \text{abs}\big(\text{G(P)} - \text{S(P)}\big) > \sqrt{\text{G(P)}} \right. \} \right\| \qquad \text{Equation 4.1}$$

Where M is dependant on the image size, G(P) is the intensity of the ground truth image at position P, and S(P) is the intensity of the synthetic image at position P. An error is recorded if the difference in intensity between the ground truth and synthetic is greater than the square root of the ground truth intensity.

Owing to the highly varied nature of the three dimensional aggregate of objects within each different bag, it was considered useful to normalize the number of pixel errors and the number of matches. This approach enables the performance of the algorithm to be more easily compared over a representative range of practical scenarios. The errors recorded for each bag are normalised with respect to the minimum error recorded for that bag whereas the matches are normalized with regard to the maximum number of matches recorded for that bag. The minimum errors and maximum matches occur when the angular separation between the successive views is also at a minimum, which is 2^0 in this study. This approach enables the relative error and matches behaviour associated with each individual bag to be presented and studied more easily.

4.6 Manipulating the epipolar based morphing in Matlab

The Matlab code for the epipolar based morphing was designed by the author to cope with the novel imaging system employed in this research programme. The approach incorporates a 'built-in' Matlab linear interpolation function, which was designed to accept the two (*.mat*) files produced by the optimized SIFT (as mentioned in Section 3.4.3). The two files are loaded into the epipolar based morphing to inform view synthesis. The code was designed by the author to linearly interpolate pixels along the motion or x-axis to incrementally shift the pixels from each view towards each other. Once the interpolation was completed, the intensity of the pixels were linearly combined, which preserves the natural flow from one frame to another. The code automatically changes the number of in-between frames according to the degree of angular separation. For instance, if the separation is 5^0, then the number of synthetic views required is four, as depicted in figure 4.1. Finally, the code saves the synthetic view, which is later compared to its corresponding GT by utilizing additional Matlab code written by the author. This code loads automatically the synthetic view and its GT to facilitate a pixel by pixel comparison according to Equation 4.1. The code records the total number of pixel errors as well as the average number of pixel errors. For example, given the angular separation of 5^0, four synthetic views are compared to their respective

GT's. The resultant pixel errors for each of the four synthetic views are recorded individually. The calculation of an average error, produced in this example by four views, enabled a convenient representation of the combined error. The code also produced error maps, which enabled the dynamic visualization of pixel errors throughout the resultant image sequences.

4.7 Results and discussion

4.7.1 Matching results as a function of the angular separation between X-ray beams

Figure 4.4 reports the matching results of two perspective views separated by 2^0 for one of the 30 experimental luggage items. A total of 874 matched features (see figure 4.4 (a)) are produced by standard SIFT algorithm. The matches that do not satisfy the standard criteria are highlighted in red colour while the matches that do match the standard criteria are indicated in green colour. When the epipolar-line and disparity window criteria are applied, 189 previously 'successfully' matched features were discarded.

To aid the visual inspection of the number of matches, the positive and negative matches are considered separately as illustrated in figure 4.4 (b) and (c) respectively. The rejected matches presented in figure 4.4 (b), have passed the standard SIFT matching criterion but have not satisfied either the epipolar or disparity window criteria. The green colour lines in figure 4.4 (c) link up the successful candidates (positive matches) that will be used by the epipolar based morphing algorithm. Evidently from the bar chart presented in figure 3.15, further increase in the number of negative matches and reduction in the number of positive matches were recorded when the two additional criteria were employed by the SIFT. This tightening of the SIFT criteria produces an expected increment in total number of negative matches and a decrement in the total number of positive matches.

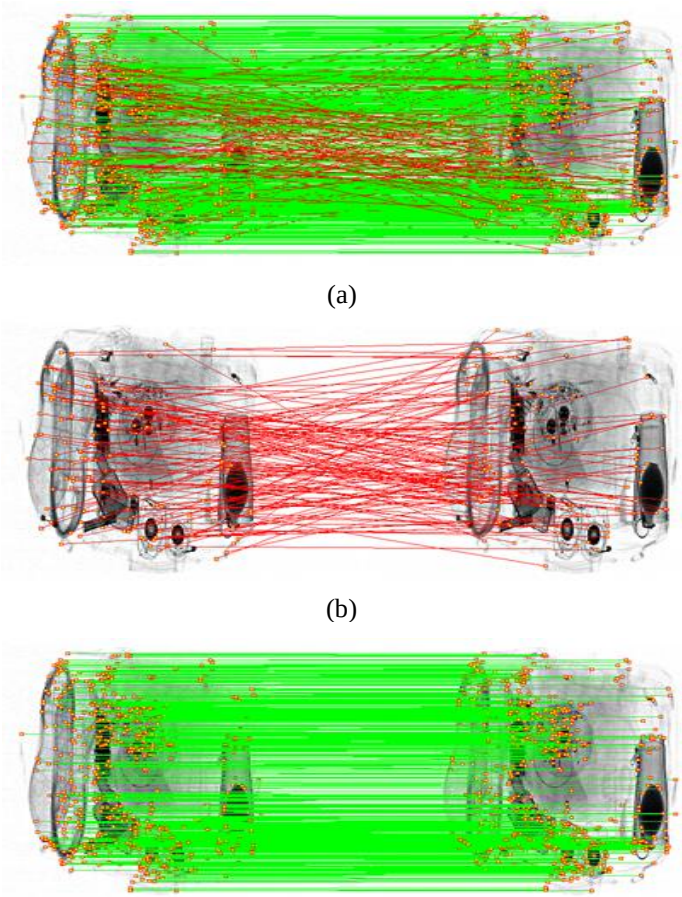

(a)

(b)

(c)

Figure 4.4: (a) SIFT matching result, (b) negative matches, (c) positive matches.

Images organized in figure 4.5 are extracted from the image of figure 4.4 (c) and arranged to enable the convenient comparison of a family of matches for the same objects, but with different angular separation. It can be appreciated by the visual inspection of the matching results organized in figure 4.5 that there is a significant reduction in the total number of matches when the separation between views is increased. This observation is further supported when comparing the result of matching two perspective views separated by 2^0 of angle separation (see figure 4.5 (a)) and same objects with wider separation between them (see figure 4.5 (g)- when the views are separated by 14^0). To provide an indication of the effectiveness of standard and modified SIFT, part of the bag in figure 4.4 is considered in figure 4.6.

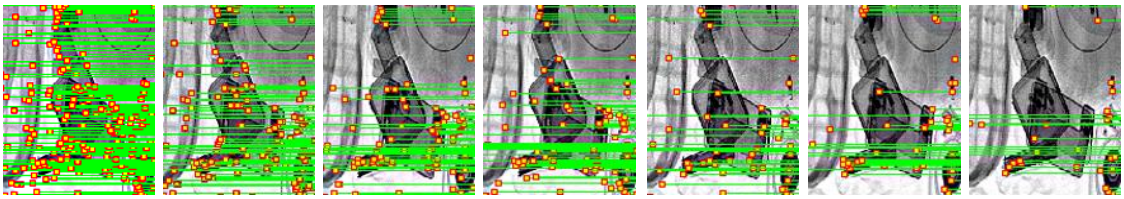

(a) (b) (c) (d) (e) (f) (g)

Figure 4.5: (a)-(g) matching results obtained at 2^0, 4^0, 6^0, 8^0, 10^0,12^0 and 14^0 of angular separation between views in that order.

The images in figure 4.6 (a) and (d) are the ground truth left and right perspective views separated by 2^0. The image in figure 4.6 (b) was generated by employing the matches illustrated in figure 4.4 (a), while; the image in figure 4.6 (c) was produced using the matched features shown in figure 4.4 (c).

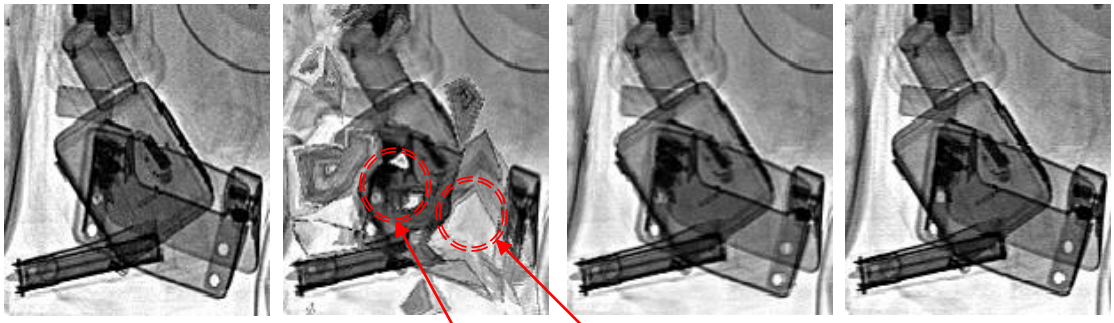

(a) (b) (c) (d)

Figure 4.6: (a) and (d) are ground truth left and right views, (b)and (c) are the synthetic views generated using standard and optimized SIFT respectively.

It is clear from the synthetic view in figure 4.6 (b) that shapes of objects were not preserved when all the features produced by SIFT were used. However, shapes of the same objects have improved in appearance when standard SIFT was tightened by the inclusion of additional criteria (see figure 4.6 (c)). The total number of matches obtained for each of the thirty different experiment bags, as a function of the angular separation of the X-ray beam (or perspective views), is illustrated in the graph of figure 4.7.

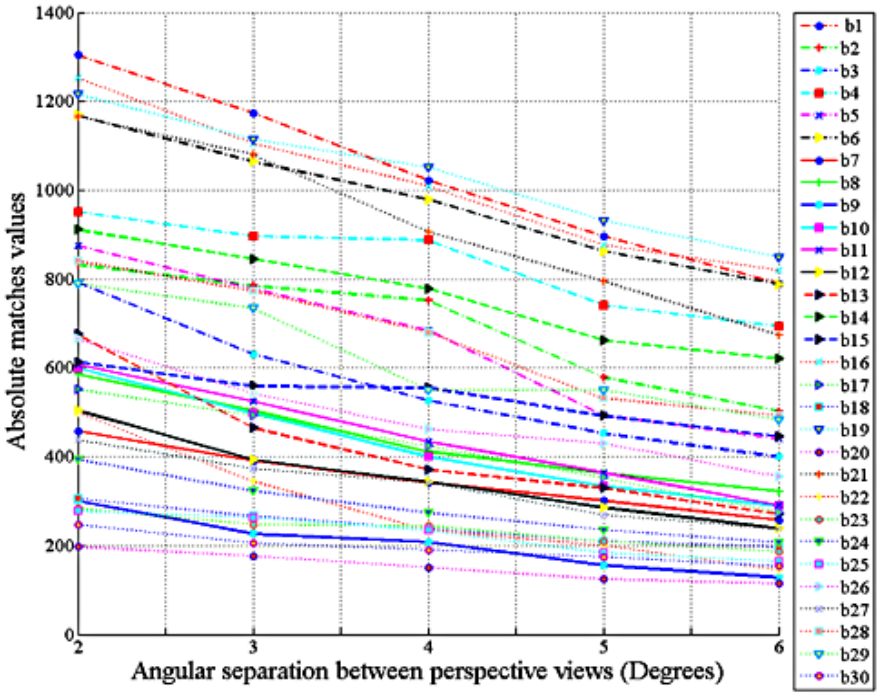

Figure 4.7: The total number of matches for 30 luggage items at 2^0, 3^0, 4^0, 5^0 and 6^0 of separation.

Initially, the matching employed the minimum amount of separation (2^0) for which only one synthetic view is required. Then, the angular separation between the perspective views was increased in 1^0 increments up to a maximum of 6^0. There is a significant reduction in the total number of matches recorded as the angular separation between views is increased. For example, 1304 matches were recorded for bag b1 employing a 2^0 separation between views, which was subsequently reduced to 790 matches for a 6^0 separation. Similarly, bag b20 produced 197 and 115 matches for separations of 2^0 and 6^0, respectively. The average trend in matching performance is represented by the central red colour curve in figure 4.8. The upper and lower bounds of the maximum and minimum number of matches recorded for any of the 30 bags has also been illustrated graphically.

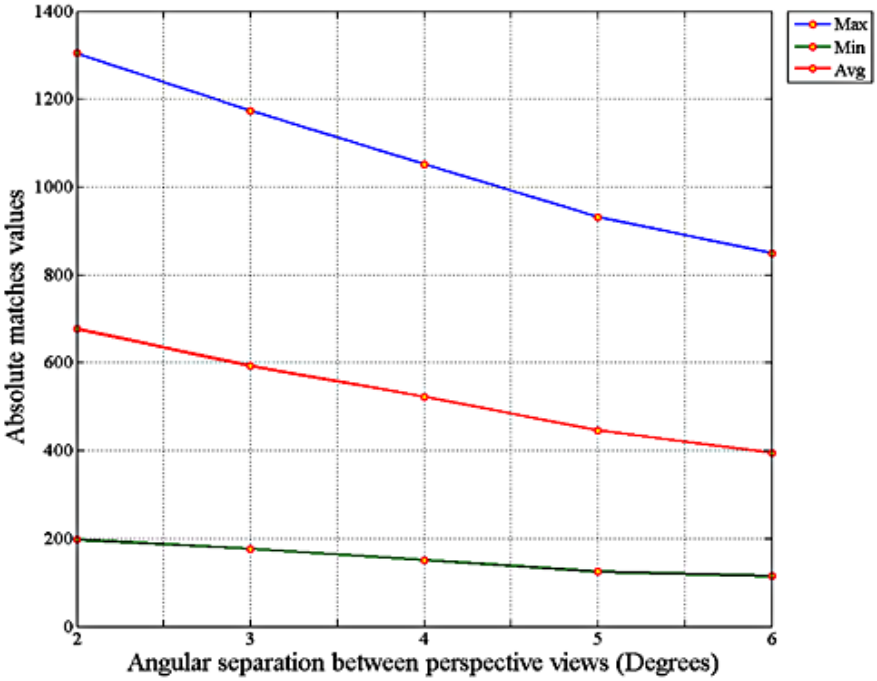

Figure 4.8: Maximum, minimum and average number of total matches for 30 different bags as a function of the angular separation of views.

It is important to note that the difference in the bag contents has resulted in variation in the total number of matches recorded, as indicated in figure 4.7 and 4.8. Therefore, as mentioned in Section 4.5, normalizing the number of matches provides the opportunity to view a family of curves pertaining to a highly dissimilar set of luggage items. Figure 4.9 shows the normalized matches' values. A global trend of matches is presented by normalizing the matches with respect to the matches produced by the minimum degree of angle separation, (2^0 in this case). It is evident from figure 4.9 that the number of matches was reduced when the angular separation between views increased. This observation however is expected as views become increasingly disparate and difficult to correlate due to a commensurate increase in the search space. The average and the possible fluctuation of the number of matches are represented by the three characteristic plots illustrated in figure 4.10 for completeness.

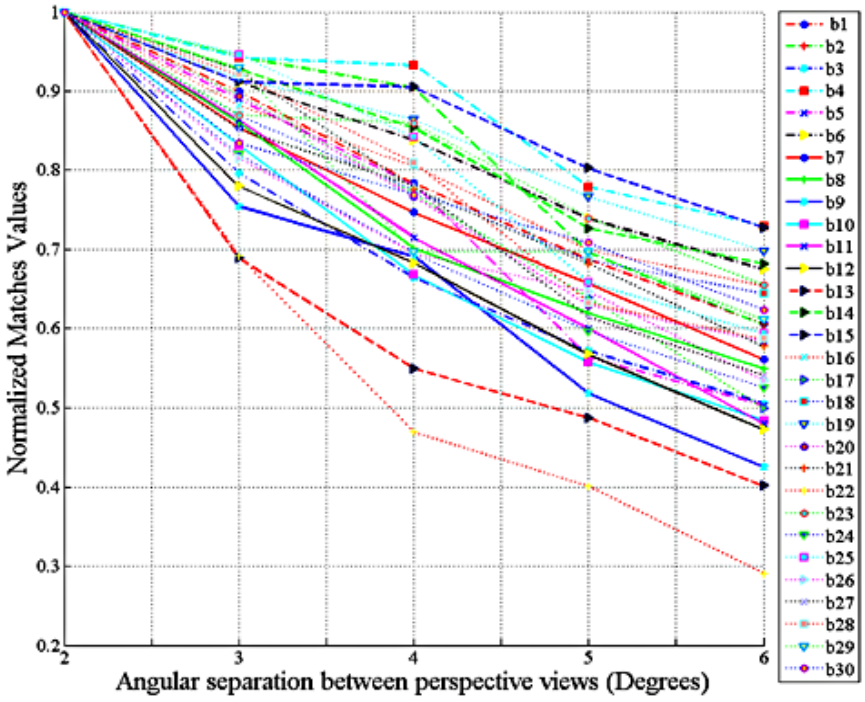

Figure 4.9: Normalized number of matches for 30 luggage items at 2^0, 3^0, 4^0, 5^0 and 6^0 of separation.

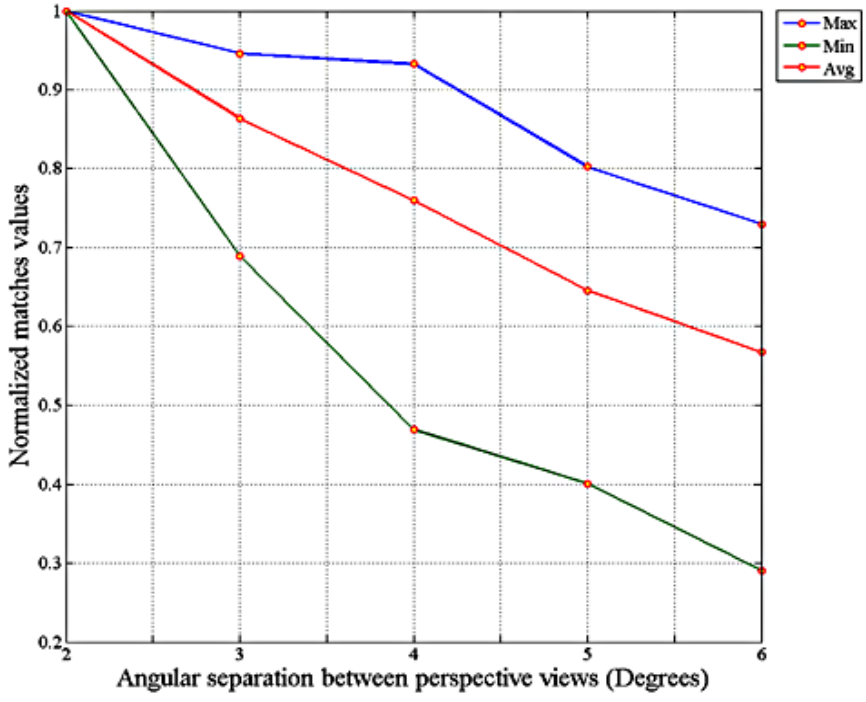

Figure 4.10: Maximum, minimum and average number of matches for 30 bags as a function of angular separation.

It should be noted that there is steady reduction in the number of matches as the angular separation between views is increased. This finding is demonstrated by the average number of matches for the 30 bags indicated by the red colour line presented in the graph of figure 4.10. As a pilot study and to further value the results obtained from the above graphs, bags which produce the maximum and minimum number of matches at 4^0 are considered and illustrated in figure 4.11.

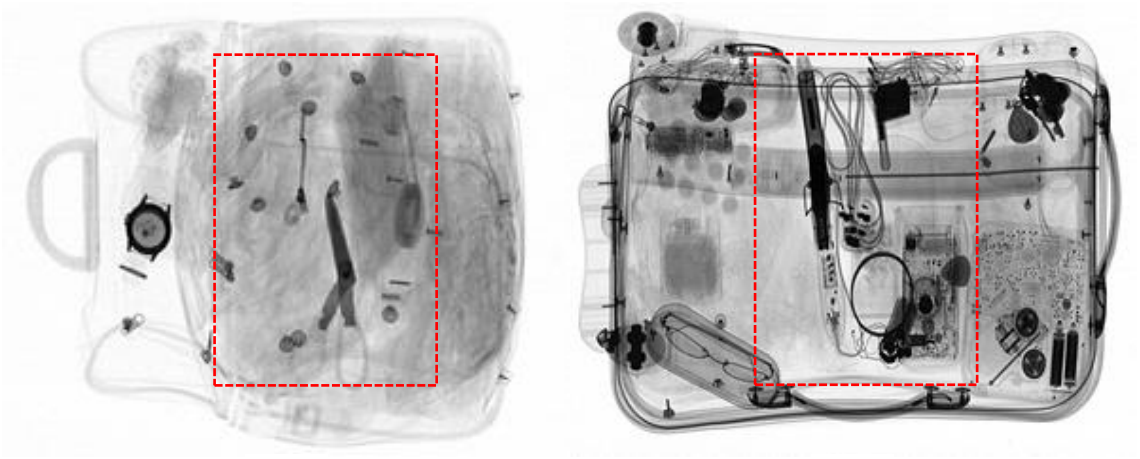

(a) (b)

Figure 4.11: An example of two images obtained at a 4^0 X-ray beam angle, where the bag in (a) produced the lowest number of matches and the bag in (b) produced the highest number of matches.

It is observed from the image in figure 4.11 (a) that the lowest number of matches was produced when the structure of the bag contained a relatively small number of sparsely distributed low contrast features. Consequently, the extrema identified from the difference of Gaussian levels, as explained in Section 3.2, produce fewer features capable of being matched. This finding is discussed comparatively with the help of the two different ROIs, each highlighted by the red rectangle in figure 4.11; the ROIs are presented as a three image sequence collected at; -15^0, 0^0 and 15^0, as presented in figures 4.12 and 4.13. The largely soft image structure, presented in figure 4.12, limits the potential for successful and robust correspondences to the disparate small pixel coverage features.

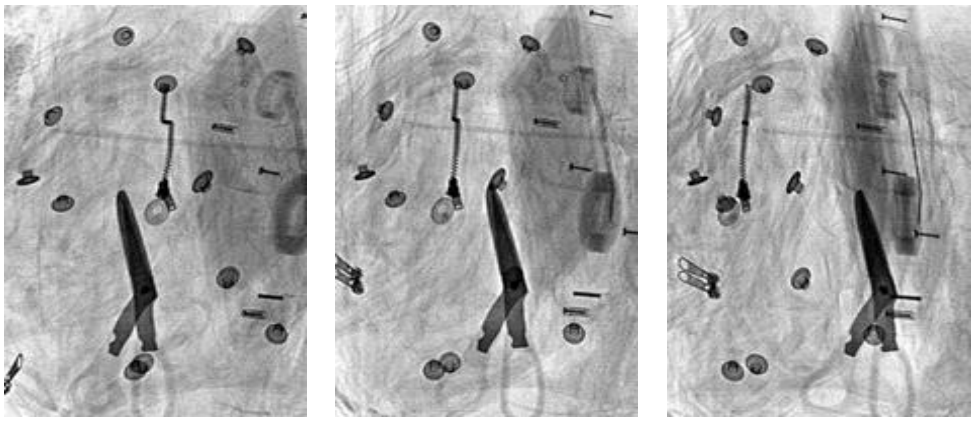

(a) (b) (c)

Figure 4.12: ROIs extracted from an image sequence at different angular positions; (a) -15^0, (b) 0^0 and (c) +15^0; a full image of this bag is presented in figure 4.11(a).

The three images in figure 4.13 are obtained using the same ROI coordinates as in figure 4.12. It is observable that the views contain relatively complex overlapping structures as well as significant variation in spatial segregation. In addition, some features are not visible in all views. The relatively high density of salient features provides significant stability in the detection of local maxima and minima and enables a higher matching denser to be achieved.

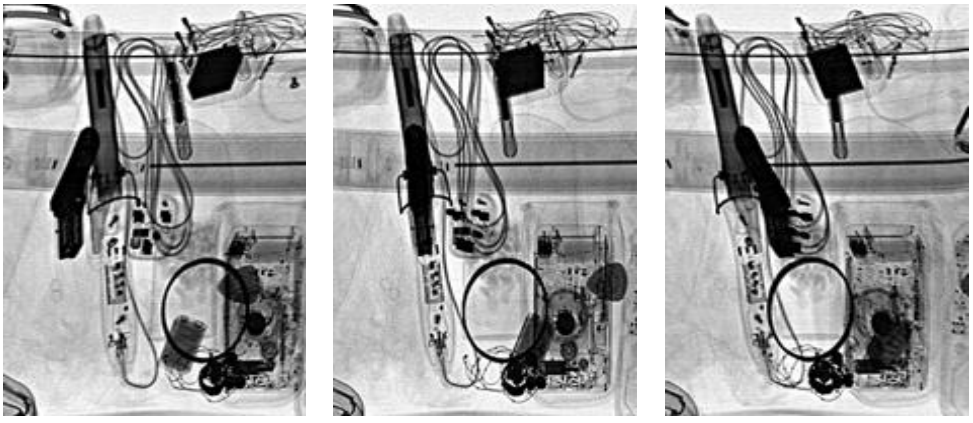

(a) (b) (c)

Figure 4.13: ROIs extracted from an image sequence at different angular positions; (a) -15^0, (b) 0^0 and (c) +15^0; a full image of this bag is presented in figure 4.11(b).

4.7.2 Synthesis and error analysis results as a function of X-ray beam angle

Before presenting the synthetic view results produced using the epipolar based morphing, it is useful to compare the quality of the synthetic images produced by the proposed technique with the synthetic images generated by a 'standard' morphing approach. The comparison is based on Equation 4.1, where an average ERR is generated for epipolar based morphing and for standard morphing. It is worth noting that the input keypoints for both standard and epipolar based morphing were generated using the optimized SIFT algorithm. The graph in figure 4.14 was produced by taking the average number of pixel errors for 30 pairs of different images separated by 2^0. The graphical representation indicates the improved performance of epipolar based morphing in comparison to standard morphing. Both standard and epipolar based morphing were utilized to generate one synthetic view at the minimum degree of separation between perspective views (2^0 in this case). This low angular separation represents a best case scenario.

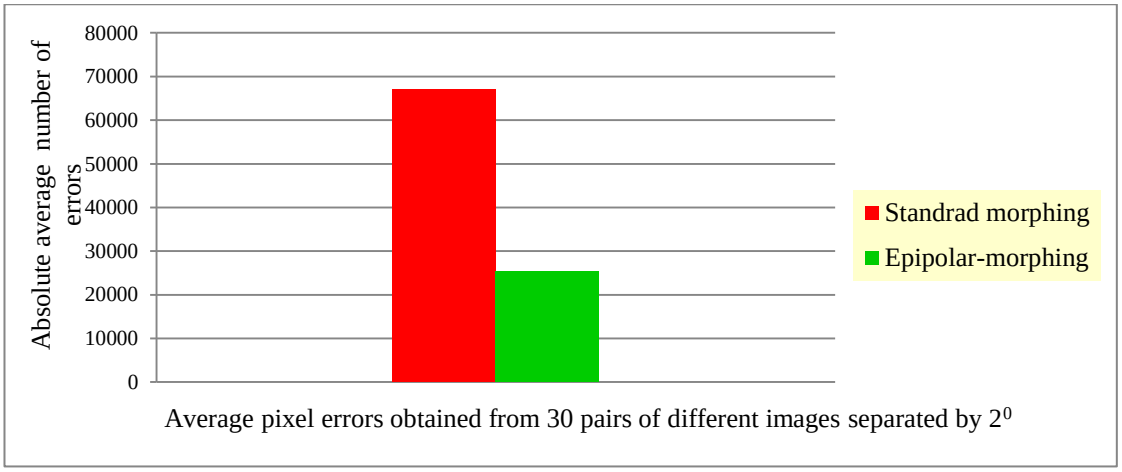

Figure 4.14: Total number of average pixel errors generated at 2^0 of separation for 30 successive pairs of different luggage items.

It is apparent from the bar graph illustrated in figure 4.14 that the number of pixel errors is reduced when the epipolar based morphing is employed. This improvement occurs because the left and right perspective views are interpolated along the motion axis "$x\text{-}axis$" to generate the synthetic view. This constraint, described in Section 4.4, reduces the potential for errors along the vertical axis "$y\text{-}axis$", which are typically generated by two direction standard morphing.

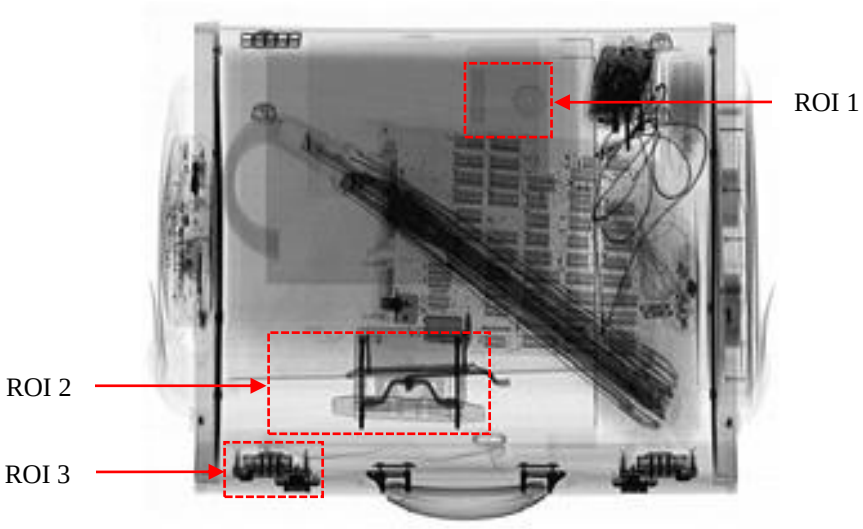

Figure 4.15: A ground truth image of a briefcase produced by the FLXDA machine and used for the purpose of comparison.

Increasing the angular separation between the X-ray detector arrays provides the basis for a more cost effective scanning technology. This approach enables the total number of X-ray detectors arrays and collimators to be reduced for a specified imaging performance. For instance, if the synthesis algorithm is able to produce an acceptable synthetic view when the two perspective views are separated by 4^0, then no intermediary detector or collimator is required. In order to study the fidelity of the resultant synthetic imagery a comparative analysis employing ground truth is employed. A ground truth image produced by the FLXDA machine is presented in figure 4.15 and was used to assess the fidelity of the synthetic views at different angular separations.

The group of images in figure 4.16 are arranged to enable the visual comparison of a family of synthetic images generated at different angular separations with regard to ground truth view presented in figure 4.15. The equivalent synthetic views at 2^0, 4^0 and 6^0 separations are presented in figure 4.16 (a), (b) and (c) respectively. It is worth noting that as the separation is increased, the resultant synthetic view reduces in fidelity.

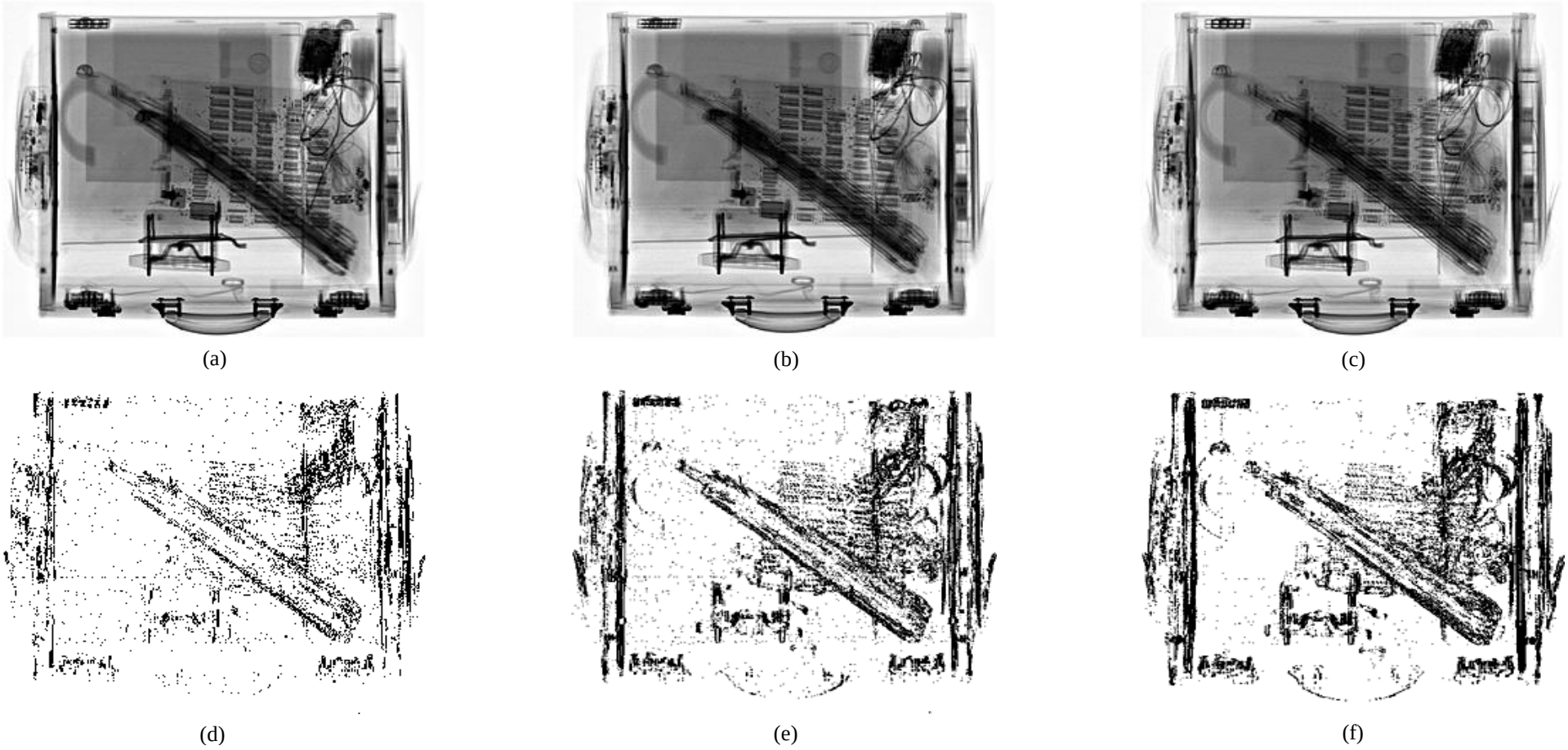

(a) (b) (c)

(d) (e) (f)

Figure 4.16: (a), (b) and (c) are synthetic images produced using perspective views separated by 2^0, 4^0 and 6^0 while; (d), (e) and (f) are error maps generated using Equation 4.1.

Images in figure 4.16 (d), (e) and (f) are error maps generated by comparison with synthetic views at 2^0, 4^0 and 6^0 of separation respectively according to Equation 4.1. It is undoubted that the pixel errors are accumulated as the angle of separation between views is increased. The best intermediary view however, is generated when the separation between views was at minimum (2^0 in this case). As the angular separation between perspective views is increased the shapes of objects are preserved with respect to vertical and horizontal linear features, although edges of objects tend to become more blurred. Three ROI's highlighted in figure 4.15 are selected for further analysis in the coming text. Care was taken when choosing the ROI's to ensure that they encompass partially and fully overlapping objects as well as different materials, thicknesses and shape, to exhibit the multi-layered translucency typical encountered in security scans of luggage.

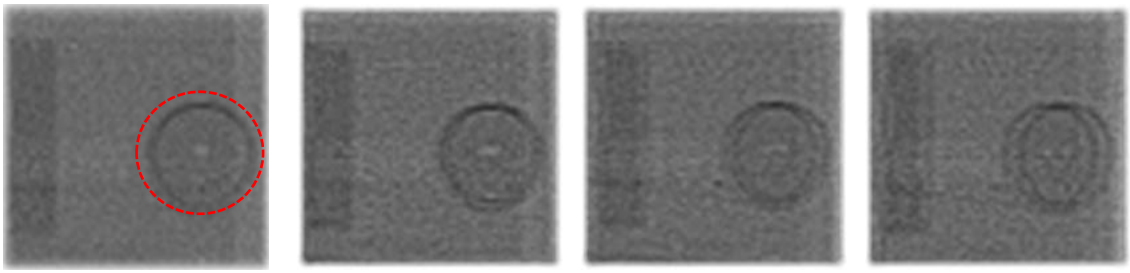

(a) (b) (c) (d)

Figure 4.17: (a) is the GT of ROI1, (b), (c) and (d) are the synthetic views obtained at 2^0, 4^0 and 6^0 respectively.

The image in figure 4.17 (a) represents a magnified section of the ROI1 highlighted in figure 4.15. It is a hub ring of a floppy disk, which is totally masked by an organic material. The synthetic results of this portion at 2^0 and 4^0 and 6^0 have shown acceptable results although edges of the ring (highlighted by dashed red circle in figure 4.17 (a)) tended to blur at 4^0. This observation is highlighted in figure 4.17 (b), (c) and (d). It is expected that the synthetic results would reduce in quality as the separation between the views was expanded up to 6^0. It is obvious that common morphing artifacts, such as ghosting and blurriness (highlighted in figure 4.3) which are due to the cross-dissolve have been minimized. This effect can be seen in the ROI 2 enlarged in figure 4.18 (a), which encompasses the metal components inside an A4 lever arch folder. The proposed synthesis algorithm preserves horizontal and vertical edges (see the objects highlighted

in red in figure 4.18 (a)). Synthetic views of the ROI 2 at 2^0, 4^0 and 6^0 are shown in figure 4.18 (b), (c) and (d) respectively.

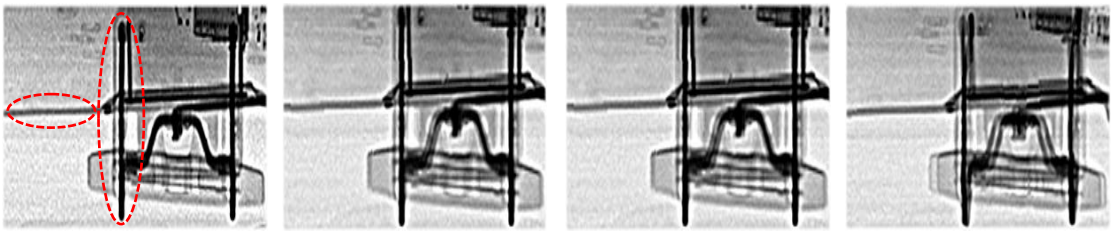

(a) (b) (c) (d)

Figure 4.18: (a) GT of ROI2, (b), (c) and (d) are the synthetic views obtained at 2^0, 4^0 and 6^0 angular separation respectively.

Other common morphing artifacts such as 'fold-overs' and 'holes' due to warping failure, see figure 4.6 (b), have also been reduced. However, it is significant to note that the presence of ghosting appears to increase as the separation between views was increased. The growth of ghosting can be observed in the features highlighted by the red colour circles in figure 4.19.

(a) (b) (c) (d)

Figure 4.19: (a) is GT of ROI3, (b), (c) and (d) are the synthetic views obtained at 2^0, 4^0 and 6^0 of angular separation respectively.

The region ROI3, shown in figure 4.19, highlights a barrel combination lock positioned on the left hand side of the briefcase (illustrated in figure 4.15). The images consist of (a) ground truth and the intermediary synthetic views (b), (c) and (d) produced using 2^0, 4^0 and 6^0 separations respectively. It is noticeable that the objects surrounded by red colour dashed circles are subject to increasing amounts of ghosting. The maximum ghosting is apparent in image (d) and demonstrates that ghosting tends to increase as the generating pair of images becomes increasingly disparate. This result was expected

when considering the increasing angular separation between the generating views. This effect occurs as the size of the disparity window along the motion axis is increased; therefore, the search space for correspondences is increased. Also, image structures that subtend a significant distance along the depth or z-axis (due to relative alignment within the inspection tunnel and or their natural three dimensional proportions) will increasingly change their 'footprint' shape (i.e. in the x-axis and y-axis image space) as the angular separation between the views is increased. This statement requires a counterpoint insomuch as the difference between the images of a 'corresponding object', when viewed from different directions is, in fact, the basis for the extraction of three dimensional data. The separation between the views improves the depth resolution (i.e. the minimum detectable depth increment in the z-axis reduces in size). However, for increasingly disparate views the correspondence problem becomes increasingly difficult to solve. The synthesis of an intermediary view is required to cope with reducing correspondences and increased differential shape within the generating views. These compounding effects are identified in this analysis as a major source of the ghosting artifacts. The analysis of pixel error is presented graphically in figure 4.20 as a function of the angular separation of the X-ray beams.

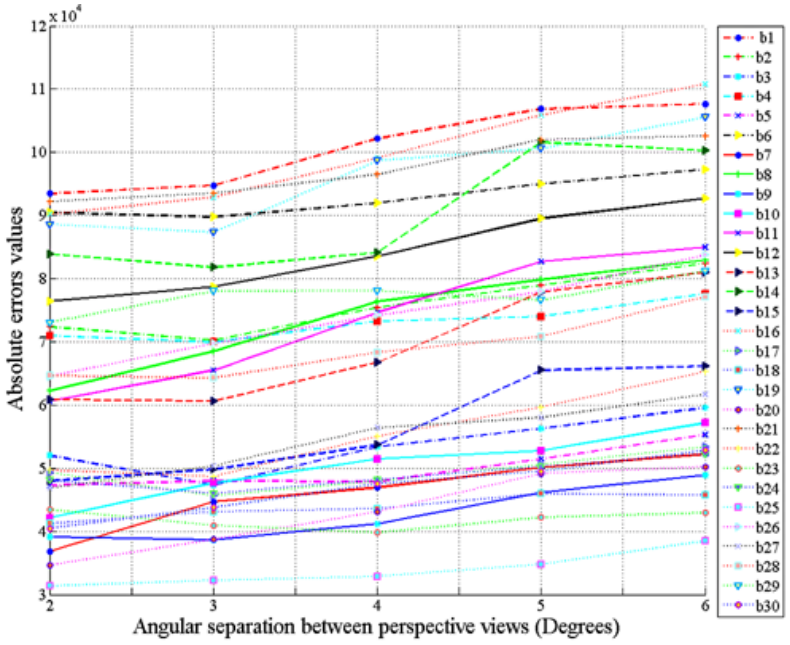

Figure 4.20: Total number of pixel errors for 30 bags recorded at 2^0, 3^0, 4^0, 5^0 and 6^0 of angular separation.

The total number of pixel errors tended to increase as the angular separation between the views is increased. This effect was expected as the 'generating' perspective images exhibit increasing variations in shape, overlap and pixel intensity, which also tend to reduce the total number of corresponding matches. If the number of matches is insufficient, then the performance of the epipolar based morphing also reduces, which tends to increase the total number of pixel errors. For example, the total number of pixel errors recorded for bag b1 at 2^0 and 6^0 was 93479 and 107658 respectively. The bag b25, produced an approximate threefold increase in the total pixel errors compare to the bag b1, 31331 and 38478, at 2^0 and 6^0 respectively. These examples support the finding that the total number of pixel errors recorded is very sensitive to the individual bag's image structure, which, of course, arises from the amount and relative positioning of the physical contents within each different bag. Figure 4.21 graphically illustrates the effect of the luggage structure on the range of pixel errors; the graph shows the upper and lower bounds of the maximum and minimum as well as the average number of errors recorded for any of the 30 bags.

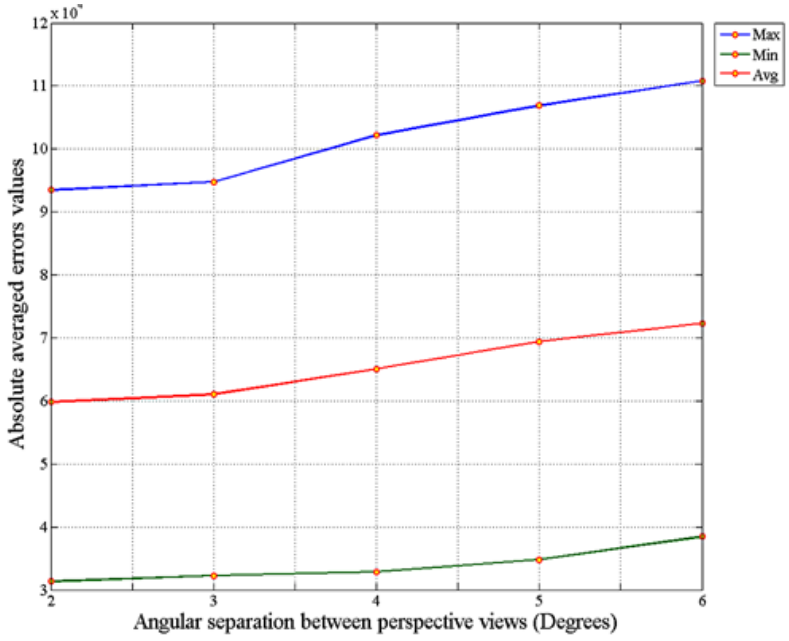

Figure 4.21: Maximum, minimum and average total number of pixel errors for 30 bags as a function of angular separation.

As determined in Section 4.5, it is useful to normalize the number of pixel errors with respect to the minimum error recorded for each different experiment bag, which occurs

at the minimum angular separation of interest of 2^0. This approach enables trends in vastly different bag structures to be more easily identified and interpreted.

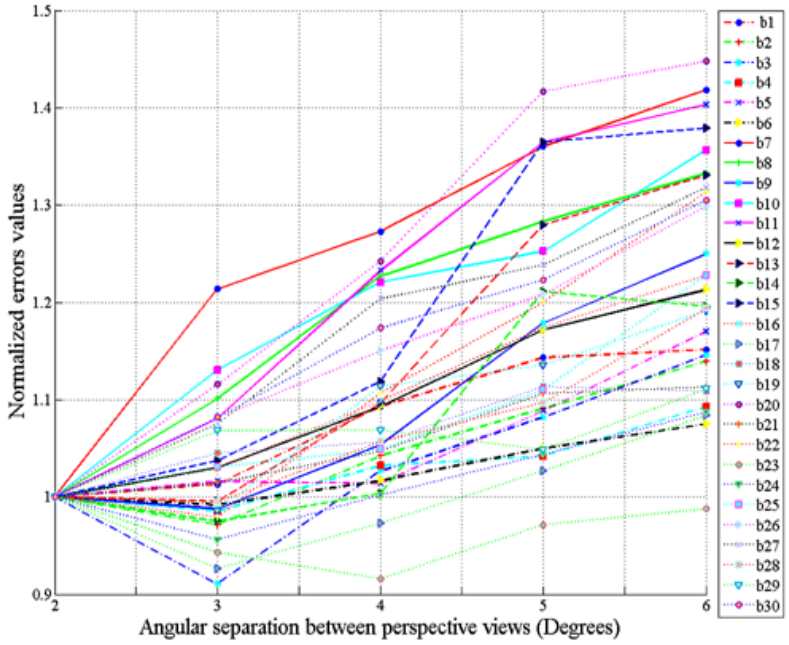

Figure 4.22: Normalized number of pixel errors for 30 luggage items at 2^0, 3^0, 4^0, 5^0 and 6^0 of separation.

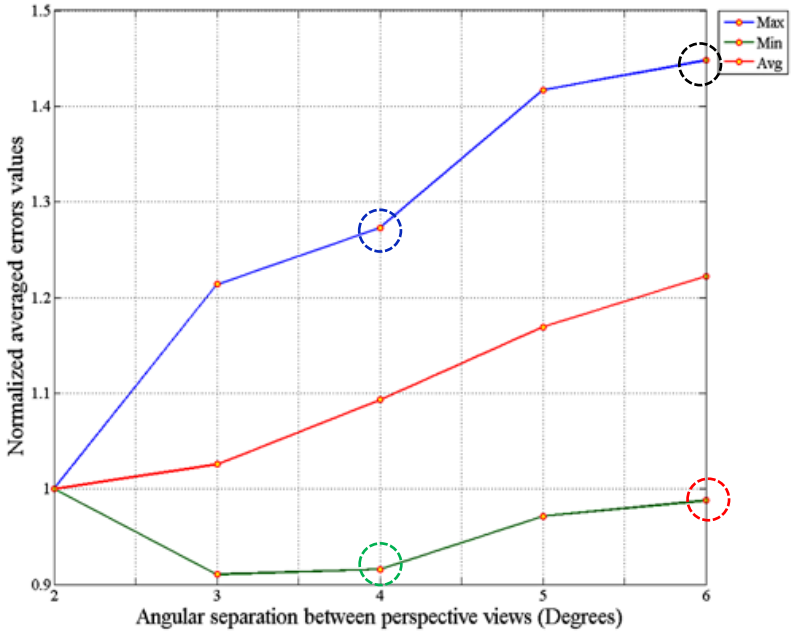

Figure 4.23: Maximum, minimum and average normalized number of pixel errors for 30 bags as a function of angular separation.

Figure 4.22 shows the normalized number of pixel errors as a function of angular separation between generating views. A significant trend for the total number of pixel errors to increase as the generating images become more disparate is evident in the graph of figure 4.22 for each of the 30 different bags. The overall trend in this data is comprehensively represented in figure 4.23. The normalized average number of pixel errors is presented by the red colour curve in figure 4.23, while the upper and lower bounds of the maximum and minimum number of pixel errors recorded for any of the 30 luggage items are also illustrated graphically by the blue and green colour curves respectively. To further appreciate the results obtained from the above graphs, bags which produce the maximum and minimum number of matches at 4^0 are considered for further discussion. These bags are illustrated in figure 4.24; two ROIs highlighted by red colour rectangles are presented for further analysis.

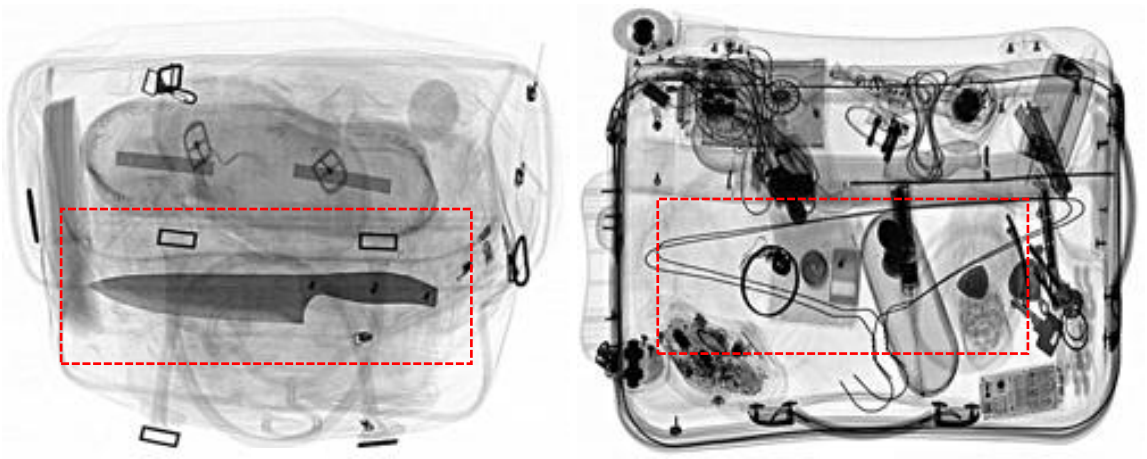

(a) (b)

Figure 4.24: An example of two images where (a) bag image that produced the lowest total number of pixel errors and (b) bag image that produced the highest total number of pixel errors; both images were obtained at a 4^0 view separation.

The ROI in figure 4.24 (a) bounds a relatively simple image composition exhibiting a small number of high contrast features. This ROI position is used to provide a sequence of three different perspective views (obtained at -15^0, 0^0 and 15^0) shown in figure 4.25. The salient features are well behaved over a large total view separation of 30^0. Their 'long axis components' are confined to a small number of depth planes, which tends to minimise the amount of shape change from view to view

i.e. simplistically, parallax manifests itself as an image translation as opposed to an image rotation of the features under consideration. Consequently, the views are very similar when in comparison with ground truth and produce minimal pixel error counts in the resultant synthetic imagery.

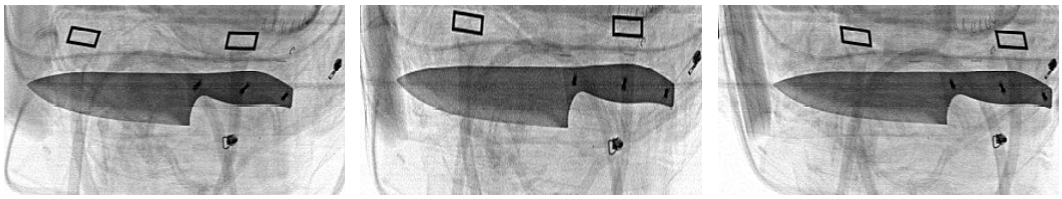

(a) (b) (c)

Figure 4.25: (a) and (c) are ROIs extracted from the image of figure 4.24 (a) at -15^0 and +15^0 respectively and (b) is the ROI extracted at 0^0.

The simple in scenario figure 4.25 can be contrasted with the more complex image composition bounded by the ROIs in figure 4.26. Again, the ROI positions are used to provide a sequence of three different perspective views (obtained at -15^0, 0^0 and 15^0). The resultant image structure is multi-layered with many different overlapping features that produce significant shape change as they 'slide' and 'rotate' from view to view. Also, significant changes in 'corresponding' pixel intensities are produced.

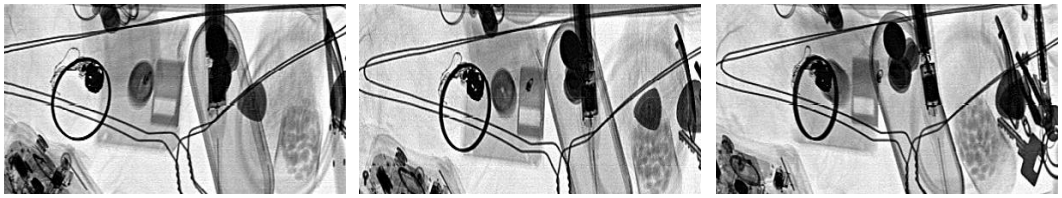

(a) (b) (c)

Figure 4.26: (a) and (c) are ROIs extracted from the image of figure 4.24 (b) at -15^0 and +15^0 respectively and (b) is the ROI extracted at 0^0.

Under such conditions even small changes in viewing angle can produce relatively large pixel error values. This comparative analysis supports the causal linkage between the generating images or 'bag' complexity and the trends in algorithmic performance.

4.7.3 Further Analysis

Further analysis is required to investigate if the errors at specific angular positions and separations are coherent and consistent with these earlier findings. The working hypothesis is that the pixel errors recorded for each different synthetic image within a given KDEX sequence should not exhibit large variances. To establish the validity of this hypothesis the remaining synthetic images that form each full KDEX sequence are analysed in detail and presented in the following text.

The maximum and minimum number of pixel errors recorded during the 30 bag experiments, at view separations of 4^0 and 6^0, are highlighted by the coloured dashed circles in figure 4.23. When each successive pair of views is separated by 4^0, see graph of figure 4.27, three intermediary views are generated. For instance, generating views at -14^0 and -10^0 are employed to synthesise the three middle images at; -13^0, -12^0 and -11^0. The three different synthetic views are compared with their respective ground truth views and the number of pixel errors is calculated and recorded for each view.

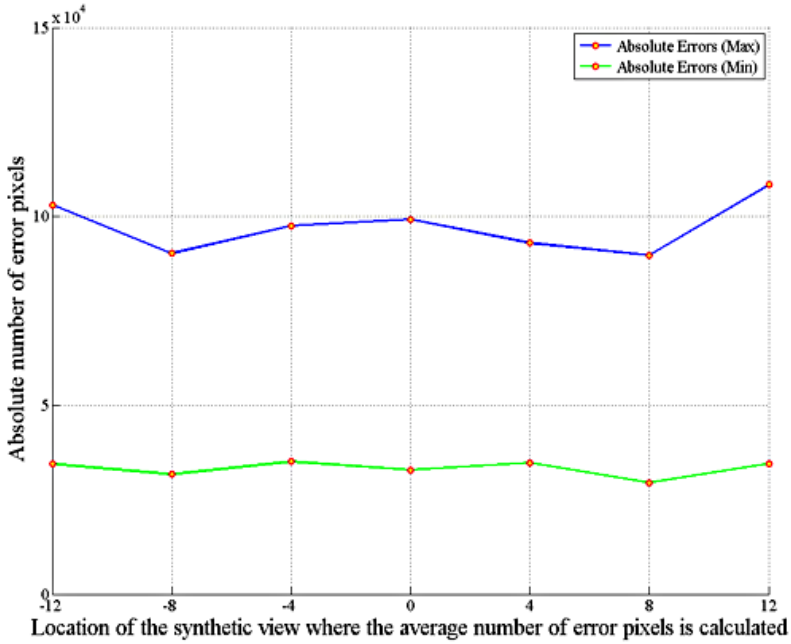

Figure 4.27: Total number of pixel errors associated with sequence of images separated by 4^0 of angle separation where the blue and green curves indicate to the bags produced the maximum and minimum number of pixel errors respectively.

In addition, a representative average error value for the triplet is also calculated. This procedure was repeated for each different triplet of synthetic views within the full sequence. As previously mentioned the results of this analysis are presented graphically. The curves in figures 4.27 represent the average number of pixel errors for a sequence of views separated by 4^0. The blue curve is the result of processing a sequence of images of the bag (b1), which produced the maximum number of pixel errors at 4^0 of separation as highlighted by the blue colour dashed circle in figure 4.23. The green curve indicates the minimum number of pixel errors recorded by the sequence of images of bag (b25) highlighted by the green dashed circle in figure 4.23.

A similar approach was adopted to analyse the synthetic images that produced the maximum and minimum number of pixel errors at 6^0, see graph of figure 4.28. The 6^0 separation requires five synthetic intermediate frames. For example, if views -3^0 and $+3^0$ are employed, then synthetic views at; -2^0,-1^0, 0^0, 1^0 and 2^0 are compared with their respective ground truth images.

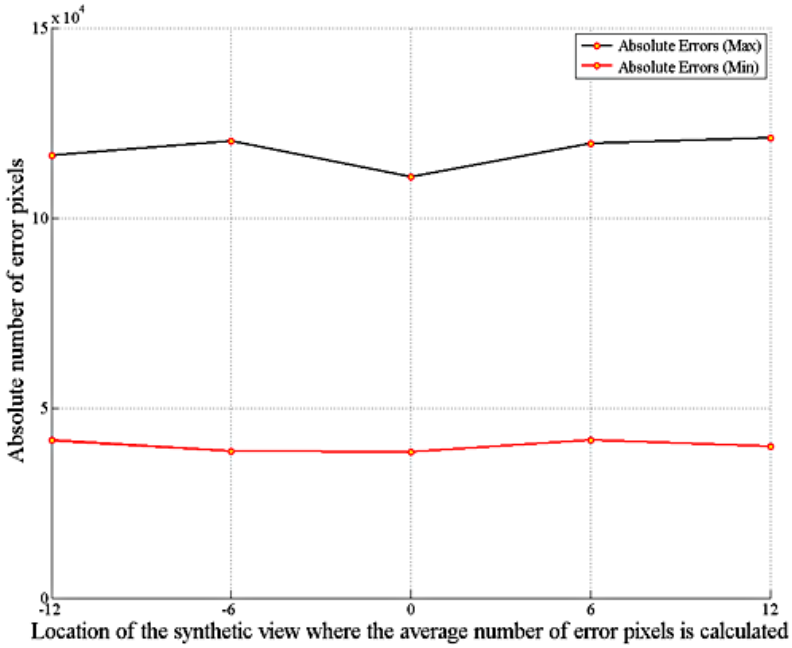

Figure 4.28: Total number of pixel errors associated with sequence of images separated by 6^0 of angle separation where the black and red curves indicate to the bags produced the maximum and minimum number of pixel errors respectively.

The representative error is calculated as the average number of pixel errors for each synthetic view. Again, this procedure was repeated for the full synthetic requirements of the given KDEX sequence. The reader is reminded that the ground truth images were generated at the appropriate X-ray beam angles by the scanner and were not input to the synthesis algorithm. The black and red curves in figure 4.28 indicate to the average number of pixel errors for the sequence of images of the bags highlighted by the black and red dashed circle in figure 4.23, respectively.

Figures 4.27 and 4.28 illustrate that the overall fluctuation in the number of pixel errors seemed to be steady. Generally, the relative small fluctuations are anticipated as any change in viewpoints leads to change in the number of correspondence matches, which certainly affect the number of pixel errors. It is important to note that the pixel errors have shown a similar trend throughout the whole of image sequence. This finding validates that features generated by the optimized SIFT algorithm were stable and strong, otherwise significant variation in the number of pixel errors would be observed from frame to frame throughout each sequence.

4.7.4 Interim discussion and conclusion

The experimental work presented in this chapter explores the possibility of applying optimized SIFT along with epipolar based morphing to synthesising greyscale KDEX images. This effort is in fact essential as regards to founding the possibility of synthesising more than one view between the X-ray detector arrays to reduce the total number of detectors required for a practical scanner. The literature reports the effectiveness of SIFT on dealing with visible light images. This research study investigates the potential of SIFT to locate correspondences in KDEX images. The appropriateness of optimized SIFT results were reported in Section 4.6.1 and supported by the matching curves organised in figures 4.7-4.10. Initially, the algorithm operated on images obtained at the minimum angular separation between views of 2^0. This decision was predicated upon the finding that the number of robustly identified corresponding features is reduced as the input views become more disparate. Therefore, the minimum angular separation condition represents the least difficult scenario for the combination of SIFT matching and synthesis employing the epipolar based morphing.

It can be appreciated from the synthetic results presented in Section 4.6.2 that the image fidelity is degraded as the X-ray beam angle increases. The best result on the contrary is obtained for 2^0, which can be appreciated from the synthetic image illustrated in figure 4.16 (a). This finding was expected for two reasons. The first reason is that increasing the separation of the X-ray beams produces increasingly dissimilar perspective views, which negatively affects the identification of corresponding features. The second reason concerns the disparity window criterion. As the separation between the generating views (or generating X-ray beams) increase there is a commensurate expansion in the disparity window or search space for feature matching. The expanded search space coupled with increased dissimilarity between the generating views reduces the likehood of correctly identifying corresponding features. These general observations are supported by inspecting the curves organized in figures 4.20-4.23. Additional assessment of the pixel errors for each synthetic image required for full KDEX sequences were also undertaken. This analysis concentrated on using the bags that produced maximal and minimal number of pixel error at 4^0 and 6^0. Results have shown that the errors were stable across each different sequence of luggage items as supported by the approximately 'flat line' responses recorded in the graphs arranged in figures 4.27 and 4.28.

This investigation has provided the impetus to expand the research to encompass dual-energy X-ray materials discrimination in which different material classes are colour coded to aid threat detection. The scheme for designing and developing the new algorithmic approach to produce colour synthetic imagery is analysed in the context of the 'industry standard' colour palette for dual-energy X-ray imaging. The results and findings are reported in the material presented in the Chapter 5.

Chapter Five Colour image synthesis algorithm

5.1 Introduction

Dual-energy X-ray imaging is widely adopted by the security screening industry to provide colour coded materials discrimination information in a visual display. The colour image synthesise algorithm developed in this research programme is reported exclusively in this chapter. The dual-energy method employs low and high energy X-ray signals and is described in more detail in Chapter Two. Typically; organic, mixture, and metallic material is displayed in orange, green and blue colour respectively, as illustrated in figure 5.1. This encoding is not based upon an accurate scientific classification but nonetheless provides a useful discrimination between different types of materials e.g. a metal knife blade will be rendered in blue colour while plastic explosives will be rendered in orange colour. Imaging technology incorporating dual-energy materials discrimination is used in single view, multiple views and computed tomography security screening systems. Such technologies are deployed routinely in all the major airports throughout the world.

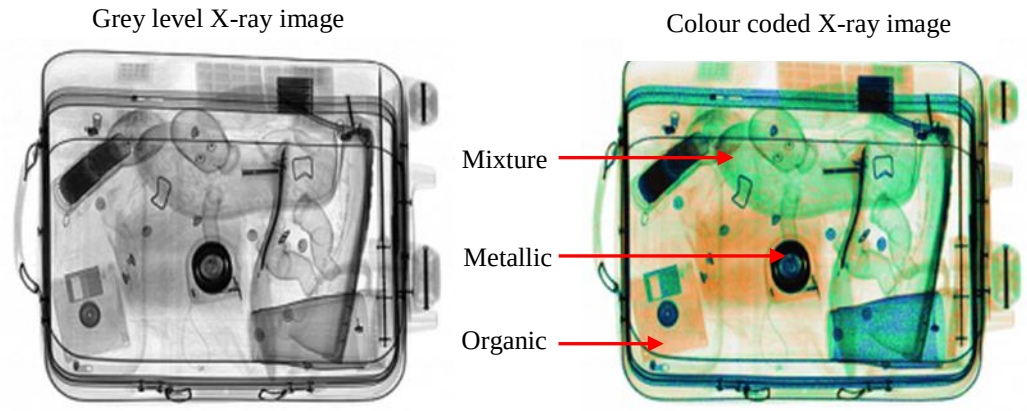

Figure 5.1: Examples of a grey level image and a colour coded X-ray image of a suitcase.

The increased complexity of the dual-energy detector arrays in comparison to the relatively simple ‘greyscale’ detectors makes for an even more compelling argument for their functional replacement by computational synthesis developed here. However, the general approach to synthesising the colour imagery is similar to the greyscale approach described in Chapter 4. Although, there are significant and important differences from

the greyscale algorithm both in the matching approach and the "material based morphing" required to generate the colour synthetic views. The fidelity of the synthetic imagery is established through comparative measures employing colour ground truth.

Optimized SIFT is employed to identify and extract the corresponding keypoints from a pair of perspective views. In the colour work the matching algorithm is operated in two distinctly different modes. The first mode employs the direct matching of the entire colour coded image. The second mode is based upon the initial segmentation of the input image according to material classes; organic, mixture and metallic as provided by the dual-energy encoding process. The motivation for developing these two competing schemes is to identify the approach that produces the greatest number of matches. The identification of a sufficiently high total number of correct matches is essential to the production of high quality synthetic views. The output from the matching algorithm is supplied to the material based morphing algorithm together with a pair of generating views to enable a new view to be synthesised.

The fidelity of the synthetic images is established by comparing them with detector images produced at the appropriate X-ray beam angle by the scanner. The error analysis records two different types of error, namely intensity and class errors. The intensity error or ERR-I is obtained by calculating the difference between pixel intensities in the GT images and the corresponding synthetic images. The class error or ERR-II is measured by comparing the material class of each synthetic pixel with GT; an error is recorded if the synthetic view pixel and the corresponding GT do not belong to the same class. Both errors enable a direct measure on how well the synthetic images resemble the detector images. The number of matches along with number of pixel errors (intensity and class) is assessed as a function of the angular separation of the generating images. Both types of error accommodate the effects of concatenated noise present in the GT (and generating views) by applying appropriate threshold conditions.

5.2 Dual-energy X-ray image matching

The analysis of the optimized SIFT algorithm when applied to greyscale images is reported in Chapter Three, and also assessed as a function of the angular X-ray beam separation between generating views in Chapter Four. The analysis of the colour coded synthetic imagery, presented in this chapter, has to account for the potential changes in

material classification or 'colour call' for pixels, which compose the generating views. This effect is a fundamental consequence of applying the dual-energy technique, at different X-ray beam angles, to overlapping arrangements of potentially different materials encountered routinely in luggage screening.

The experiment approach to evaluate comparatively the two different algorithm modes namely; direct matching and segmented materials matching, each involved employing increasingly disparate views. The views were obtained by systematically increasing the angular separation between the generating pairs of X-ray beams according to the scheme presented in figure 5.2.

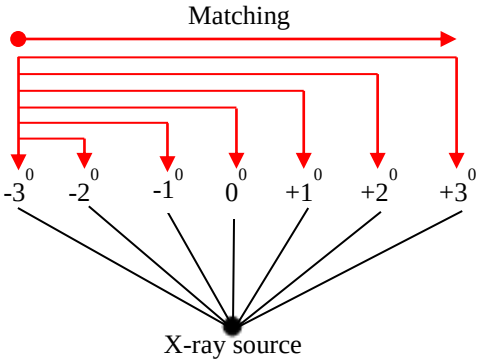

Figure 5.2: Incremental angular separation between X-ray beams for the colour coded images employed in the comparative matching analysis.

The initial 1^0 separation, between views at -3^0 and -2^0, is increased in increments of 1^0 up to a maximum separation of 6^0, between the extreme views at -3^0 and $+3^0$ as indicated in the figure.

5.2.1 Direct matching of colour coded images

The direct matching of the colour coded imagery does not take into account the three different material classifications, which are encoded by the dual-energy x-ray imaging process. The optimized SIFT is applied only once to each successive view and resultant positive matches and negative matches are recorded. The matches are classified according to the bounding criteria described in Chapter Three, which tighten the support of SIFT. The direct matching experiment requires seven sequential perspective images to be acquired and stored for each bag under inspection. The angular separation between

each successive view is 1^0, taken over an angular range of $\pm 3^0$ about the 0^0 or normal view position, as discussed in the previous section and illustrated in figure 5.2. A total of 30 different bags termed; b1, b2…b30 are processed, according to the flowchart presented in figure 5.3, to provide data for a total number of 180 successive image pairs.

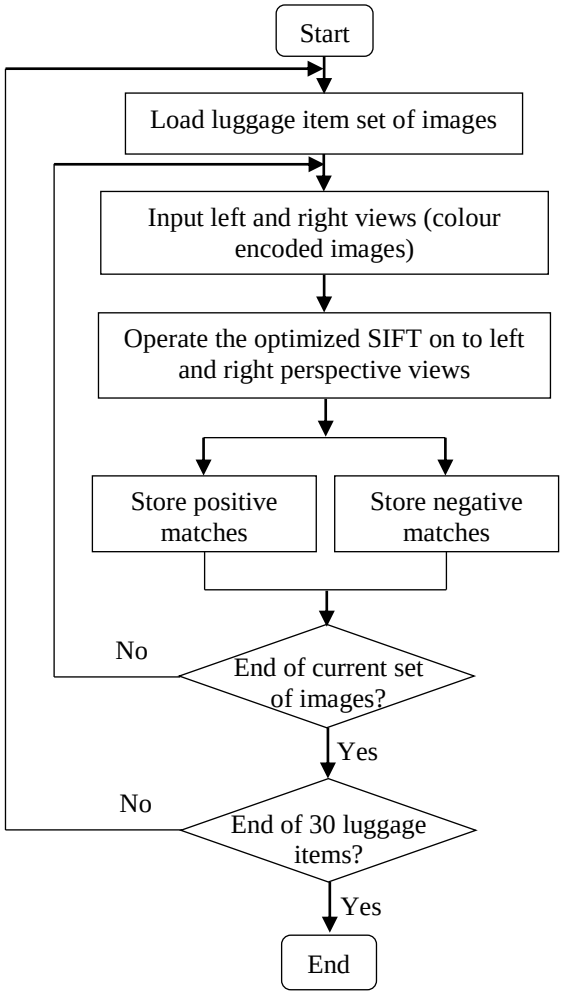

Figure 5.3: Data collection for direct matching of colour coded imagery.

The direct matching experiment was designed to provide results to enable a comparison with the competing 'materials segmentation matching' described in the following section.

5.2.2 Materials segmentation image matching

This matching approach focuses on investigating the utility of the material information that is segmented naturally by the dual-energy X-ray discrimination process. Initially,

the colour coded image is spilt into its three material classes; organic, metallic, mixture. It is worth noting at this juncture that each material class has distinct and important roles in assisting threat detection and identification. To acquire the full spatial information (i.e. the total number of pixels that compose the image) requires an additional fourth class, which does not provide any specific materials information. This latter class is referred to as the non-discriminated class or grey level class; a pictorial example of the class segmented imagery is presented in figure 5.1. The grey level class arises when the X-ray signal incident upon the X-ray detectors is too weak to enable materials discrimination. This occurrence arises when the structures in the path of the X-ray beam are either too dense and or too thick to enable sufficient X-ray photons to reach the detectors.

In the context of this Thesis, the four material classes, organic, metallic, mixture and greyscale are referred to as; O, M, X and G, respectively. Also, left and right are referred to as L and R, respectively. For example, the organic class originating from the left and the right views is termed O_L and O_R, respectively. Positive and negative are indicated as P and N, respectively. The materials segmentation matching and data recording scheme process is explained in the flow chart in figure 5.4.

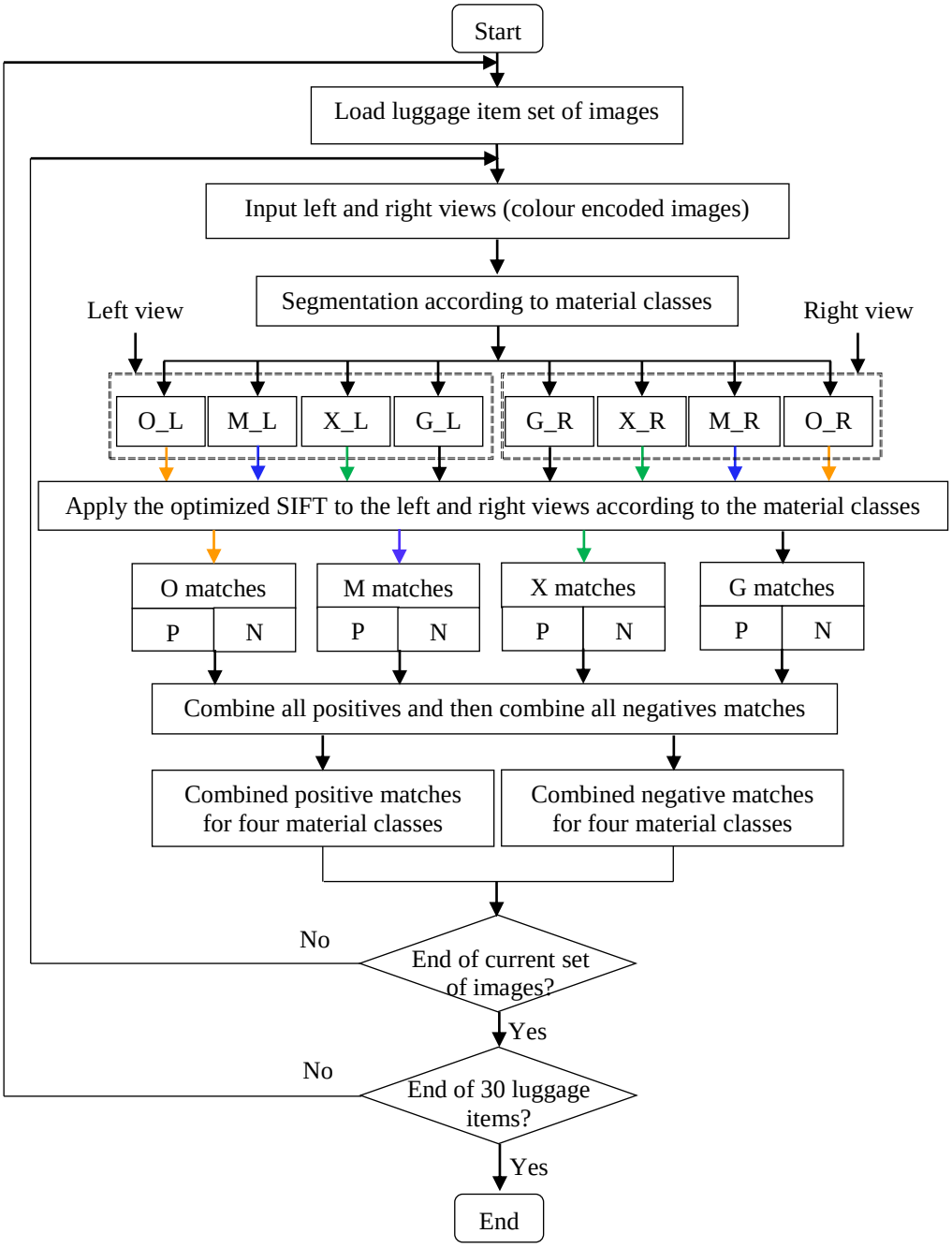

Figure 5.4: Flowchart for the segmentation of the four different material classes, application of the optimised SIFT and recording of the matching results.

The algorithm interrogates all the pixels in the left view and the right view as depicted in the flowchart in figure 5.5. Each interrogated pixel is replicated and stored, at its original (x, y) location in one of the four material class frames. Each left and right input image will generate four separate material class frames; a total number of eight frames.

The matching algorithm operates exclusively within each class. For example, the organic class left view is matched with the organic class right view. The positive and negative matches are recorded for each the four classes. In particular, all the positive matches, for each input pair of colour images, obtained from organic, metallic, mixture and 'grey' materials is aggregated in a single file. Negative matches from the different classes are also aggregated in a different file.

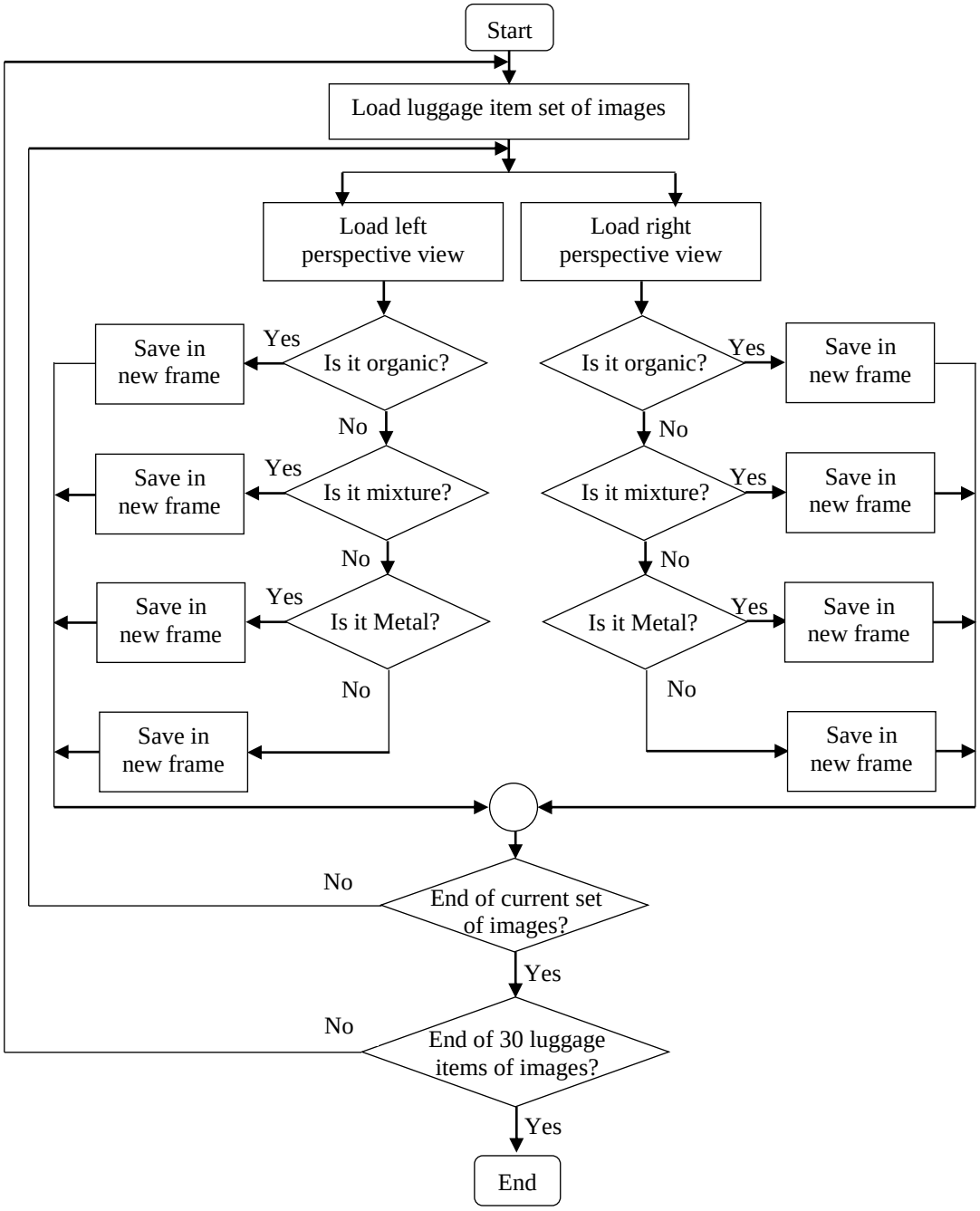

Figure 5.5: Flowchart for the production of the four material class images for each successive image pair.

An example of the different class frames produced by the image segmentation algorithm is shown in figure 5.6.

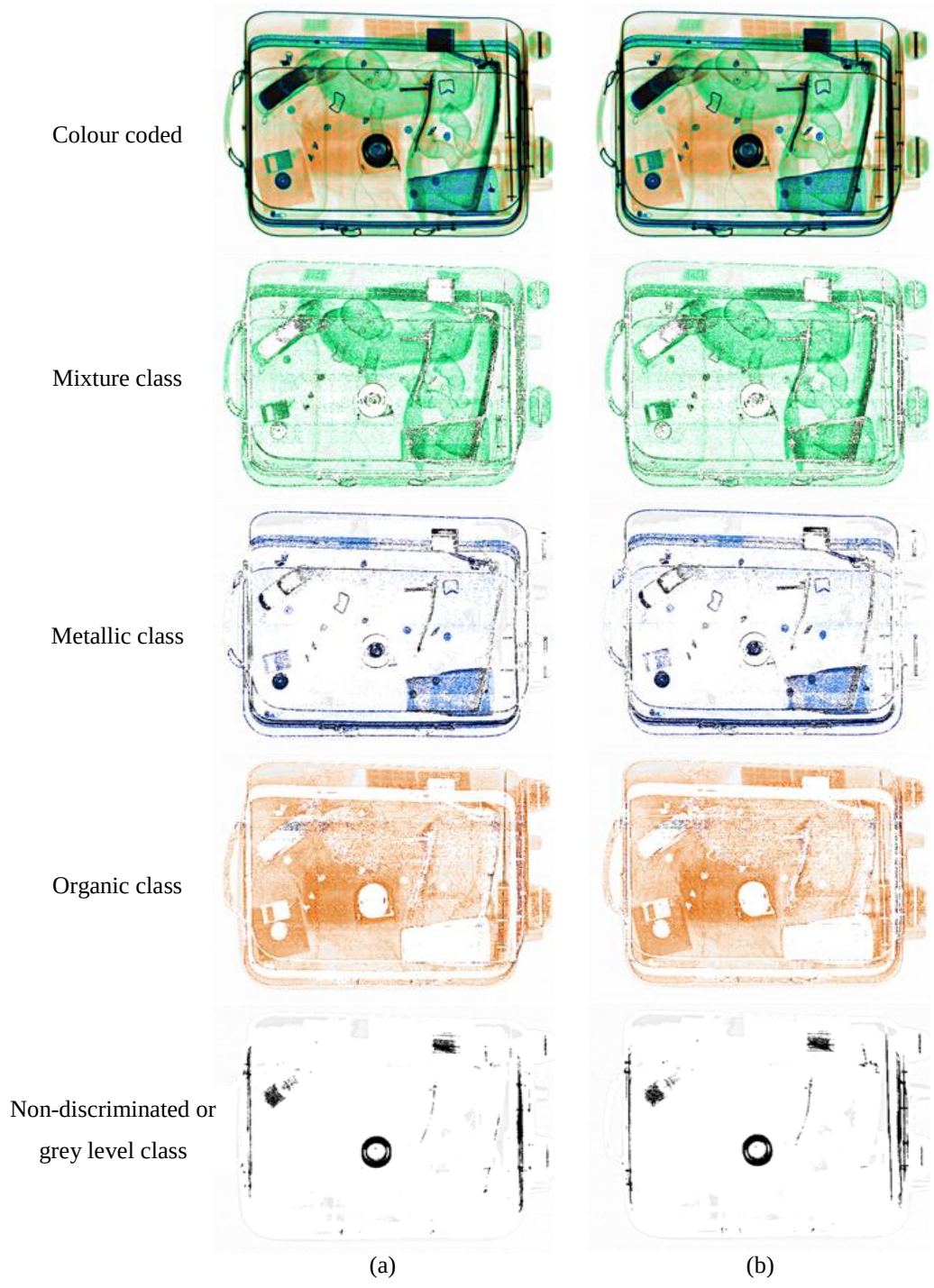

Figure 5.6: Pair of colour input images (top) and their respective segmented material or class images, where (a) was obtained at the -3^0 position, and (b) at the $+3^0$ position.

The input colour images, at the top of the figure, were obtained at -3^0 and $+3^0$ positions, respectively. Both images are segmented according to their material classes. Each class from the first view will be matched to its equivalent class in the second. Both approaches previously described are based on colour encoded X-ray images.

5.3 Experimental imagery

The 30 different bags; b1, b2,.., b30 used to generate the experiment input and GT colour imagery in the study described in this chapter were also rendered in greyscale. This approach enables reliable comparisons between the greyscale study, presented in Chapter Four, and the colour results. Seven sequential perspective images are acquired and stored for each bag (producing a total number of 210 perspective images). The angular separation between each successive view is 1^0, taken over an angular range of $\pm 3^0$ about the 0^0 or normal view position, as illustrated in figure 4.1. The image in figure 5.7 is a colour coded version of the image illustrated in figure 4.2.

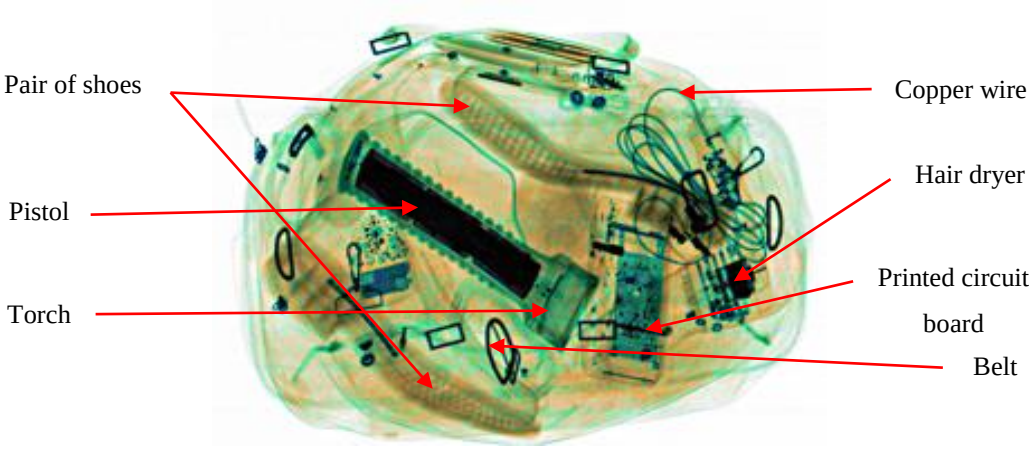

Figure 5.7: Colour coded bag with labelled contents; the amorphous orange background corresponds to items of clothing.

The luggage imaged contained a mixture of 'typical' objects composed of different materials, thicknesses and shape. Objects shown as grey levels in figure 4.2 are colour coded in figure 5.7. For instance, the printed circuit board is contains some metal material that under careful scrutiny appears coded in blue colour. Similarly, the pair of shoes is made from organic material and appears rendered in orange colour. Each luggage item's location is arranged carefully to ensure that overlapping objects and

structures provide the multi-layered translucency typically encountered in security scans of luggage. The position of the objects along the depth or z-axis are also carefully arranged to provide realistic imaging scenarios.

5.4 Dual-energy X-ray image synthesis via material based morphing

In the previous chapter, linear interpolation and linear cross-fade operations were employed to generate synthetic greyscale views. The fidelity of the synthetic views was established by calculating the intensity error for each synthetic pixel relative to its GT pixel. This approach however, is not directly applicable to dual-energy X-ray imaging due to the limited colour gamut employed in the materials encoding process. For example, a synthetic pixel colour established by employing a linear combination of the RGB values from the left and the right views can produce a 'new' colour that falls outside the standard colour gamut defined for each material class. Another possibility is the 'natural' occurrence of corresponding features or pixels appear colour coded differently in each generating view. This latter situation also requires class disambiguation to be carefully considered. Ultimately, inconsistent pixel colour calls have the potential to disrupt the detection and identification of threats in a visual display.

A so called 'material based morphing' approach was designed and developed to ensure that all synthetic pixels fall within the standard colour gamut and therefore, represent valid material classes. The 16 (i.e. 2^4) permutations obtained by considering the four material classes for each of the two corresponding features are presented in Table 5.1. This table also presents two different interpretations of the 'correct' synthetic pixel class; the rightmost column of the table was designed to bias ambiguous material calls in the generating images towards the 'threat' classes in the resultant synthetic imagery according to the following criteria.

The synthetic class is unchanged if the corresponding features belong to the same class; the synthetic class is a Mixture if the corresponding features belong to the Organic and Metallic classes; otherwise the following class precedence is applied:

Organic has precedence over a Mixture;
Metallic has precedence over a Mixture;

Organic or Mixture or Metallic has precedence over Grey.

The rationale for this approach takes into consideration that primary threats such as IEDs are often composed of plastic or liquid explosives, which are characterised as low-density responses in X-ray projections [1, 3, 152].

Index	Left view material class	Right view material class	Output colour I (optimized material identification)	Output colour II (optimized threat identification)
1	O	O	O	O
2	O	M	X	X
3	O	X	X	O
4	O	G	O	O
5	X	X	X	X
6	X	O	X	O
7	X	M	X	M
8	X	G	X	X
9	M	M	M	M
10	M	O	X	X
11	M	X	X	M
12	M	G	M	M
13	G	O	O	O
14	G	M	M	M
15	G	X	X	X
16	G	G	G	G

Table 5.1: The 16 different combinations of four different material classes represented by corresponding (left and right) features; where O, X, M and G refer to organic, mixture, metallic and grey classes respectively.

A second interpretation, presented in the penultimate column in Table 5.1, applies the same criteria as previously explained but this time precedence is given to the Mixture class over the Organic and Metallic classes. Both approaches are analysed and discussed in the following text.

5.5 Dual-energy X-ray synthetic algorithm performance measurements

Before the synthetic views results are presented, it is necessary to discuss the metrics employed to evaluate them. As previously indicated, two types of errors are recorded when the synthetic views are analysed. In the greyscale work, the error was recorded using an image subtraction where the intensity of the synthetic view was compared to the intensity of GT using formula 4.1. A similar approach is adopted for the colour coded images, where ERR-I is determined by comparison with the GT according to the following formula:

$$ERR\text{-}I = \left\| \left\{ P \in M \left| abs\left(G(P) - S(P) > \sqrt{G(P)} \right) \right. \right\} \right\| \quad \text{Equation 5.1}$$

Where M is dependant on the image size. In previous chapter, G(P) and S(P) were used to indicate to the intensity of the GT and synthetic views at position P, respectively. The intensity of the colour pixels is taken as the average value of the RGB triplet. An error is recorded if the difference in intensity between the GT and synthetic views is greater than the square root of the GT intensity [161, 163]. This justification is based on the prior research work on measuring the practical noise recorded by typical X-ray luggage scanner arising from various practical fluctuations (e.g. system noise).

A second type of error, ERR-II is required to record changes in the material class of the synthetic pixels with respect to GT. Both types of errors are assessed as a function of the X-ray beam angles. Also, errors recorded for each bag are normalised with respect to the minimum error recorded for that bag, which occurs at a 2^0 separation in this study. Normalizing the number of pixel errors enables the results of different bags to be more easily compared. For completeness, upper and lower bounds of the maximum and minimum number of each type of errors recorded for any of the 30 bags are illustrated graphically.

5.6 Manipulating the material based morphing in Matlab

The Matlab code for material based morphing was designed by the author to prevent the linear cross-fade of colours; such effects are typically encountered with standard morphing techniques but are problematic in the context of colour coded imagery. The code was designed to accept the optimized SIFT output (Direct matching approach) to enable the interpolation of pixels in a fashion similar to the one described in Section 4.6. However, instead of linearly combining the colours from perspective views, the Matlab code was written in a way which satisfies the colour gamut defined for each material class. In other words, upon the completion of pixel interpolation, the code reads the material class for each individual pixel in the left view and its corresponding class in the right view. The resultant colour code for the synthetic pixel is chosen according to the approach described in Tale 5.1. This technique preserves the original colour gamut and ensures that only valid pixel colours are present in the resultant synthetic imagery. If new colours were to be allowed then this situation would infer that new material classes were being generated, which is not the case in this research. As per the scheme

presented in Section, 4.6, the synthetic view is compared to its corresponding GT in which ERR-I and ERR-II are recorded. The Matlab code, which records ERR-I implements a different from that presented in Section 4.6. It is designed to calculate the intensity of the colour pixels by taking the average value of the RGB triplet according to Equation 5.1. ERR-II is also recorded by utilizing Matlab code written by the author to compare the class of each synthetic pixel with its corresponding GT. An error is recorded if the pixels belong to different classes. The average number of total pixel errors (i.e. combining ERR-I and ERR-II) is determined, as per the scheme presented in Section 4.6, to enable the collective error as a function of angular separation between views to be represented. The collective relationship of errors (ERR-I and ERR-II) is calculated with respect to the angular separation while the average number of pixel errors is calculated as per the scheme presented in Section 4.6.

5.7 Results and discussion

Matching and synthesis both are comprehensively described in the following text.

5.7.1 Matching results as a function of X-ray beam angle

The SIFT was incorporated into two different matching schemes. The first scheme, termed direct matching, employs SIFT to operate upon greyscale versions of the colour coded input images. In the second scheme, each input image is segmented into four material class specific sub-images before being input to the SIFT. More details on both arrangements are described in the following text.

5.7.1.1 Direct matching

The image in figure 5.8 is an example of two views, separated by 2^0, of bag b21. A total of 1442 matches were recorded for the standard SIFT algorithm, which dropped to 1020 matches when the additional criteria were incorporated.

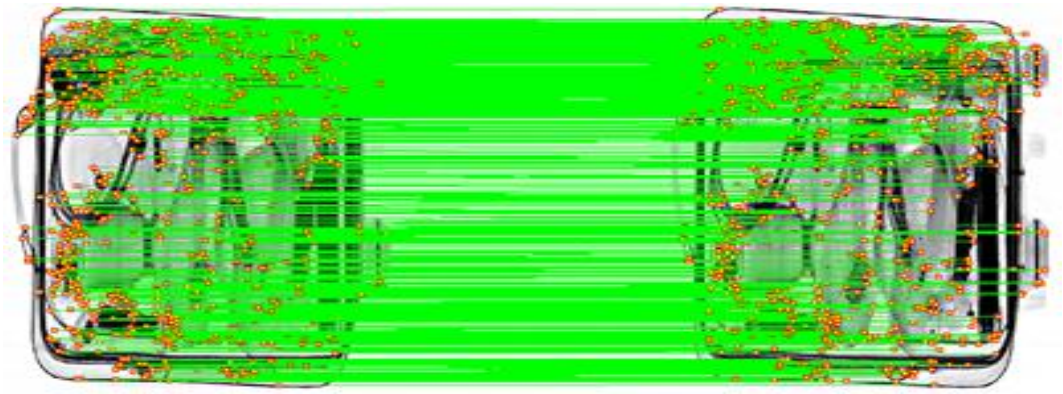

Figure 5.8: Positive matches, highlighted in green colour, for bag b21 when the input images are separated by 2^0.

The ROIs shown in figure 5.9 are extracted from the bottom left quadrant of bag b21, see figure 5.8; each ROI is enlarged and arranged to enable the convenient comparison of a family of matches over increasing angular separations.

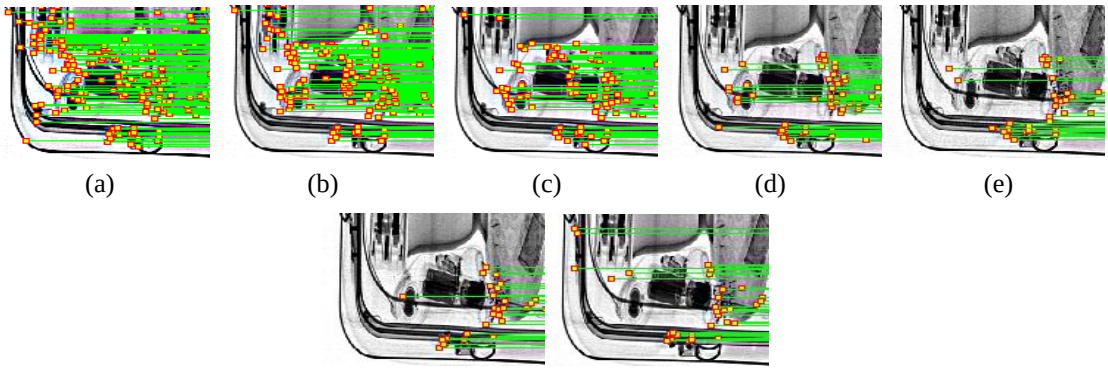

Figure 5.9: (a)-(g) matching results obtained at 2^0, 4^0, 6^0, 8^0, 10^0,12^0 and 14^0 of angular separation, respectively.

It can be appreciated from visual inspection that the matches are significantly reduced when the separation between views is increased, especially when comparing the minimum separation figure 5.9 (a) to the maximum separation condition at (g). Figure 5.10 shows the total number of matches for thirty different bags as a function of the X-ray beam angle or angular separation.

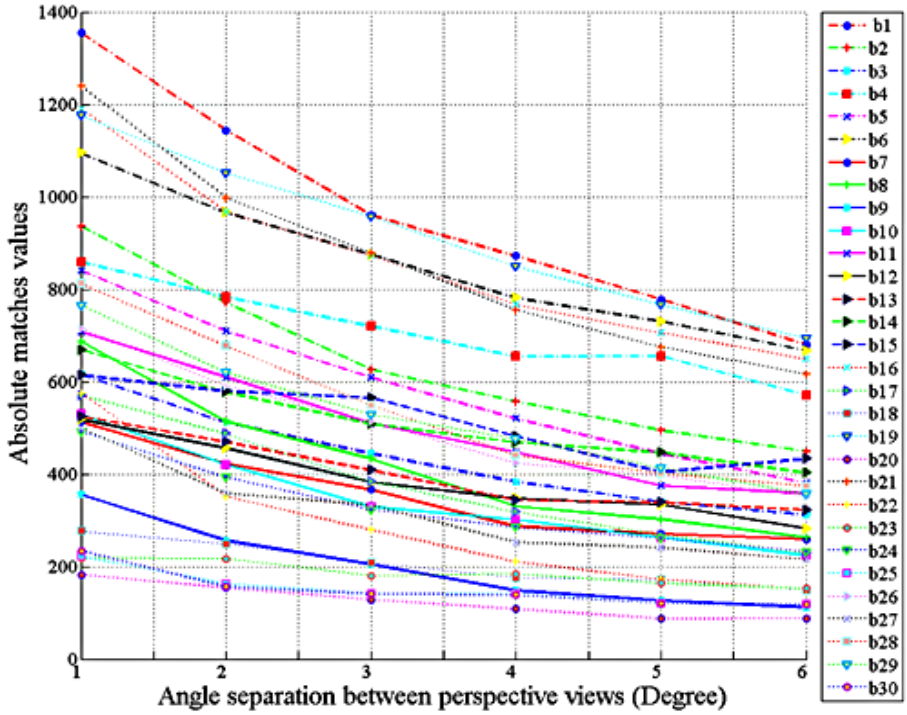

Figure 5.10: The total number of matches for thirty luggage items at 1^0, 2^0, 3^0, 4^0, 5^0 and 6^0 of separation according to direct matching of colour coded images.

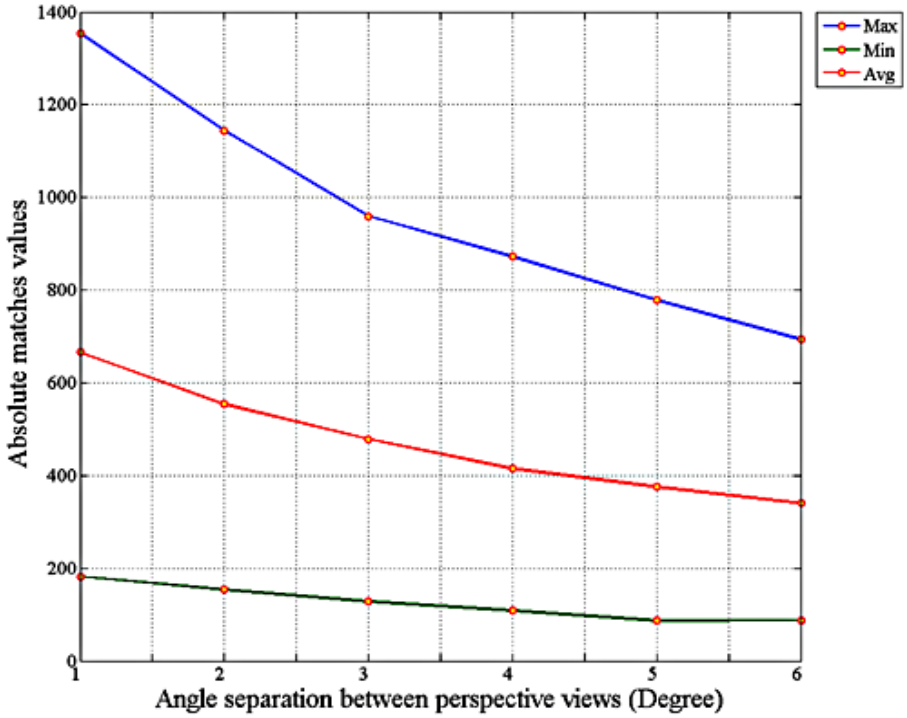

Figure 5.11: Maximum, minimum and average number of total matches for thirty different bags as a function of angular separation.

There is a significant reduction in the total number of matches when the angular separation between views is increased. For instance, bag b1 produced 1354 matches at a 1^0 separation, which reduces to around half this total number at a 6^0 separation. Similarly, the total number of matches recorded for bag b20 was 182 and 88 at separations of 1^0 and 6^0, respectively. The trend for the average number of matches for the 30 different bags, at different angular separations, is illustrated graphically in figure 5.11, along with the maximum and minimum number of matches recorded. It is evident that the total number of matches is dependent largely upon the nature of the bag's contents. For example; bag b1 produced a seven fold increase in matches in comparison to b20. Figure 5.12 shows the matching results normalized to the number of matches obtained at 1^0.

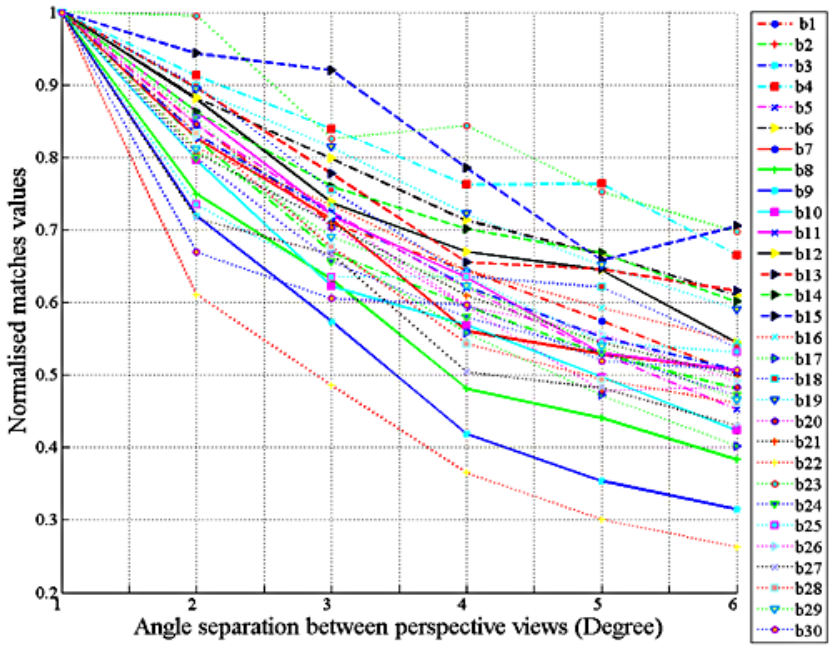

Figure 5.12: Normalized number of matches for 30 luggage items at 1^0, 2^0, 3^0, 4^0, 5^0 and 6^0 separations.

The average and the possible fluctuation of the number of normalized matches are represented by the three characteristic plots illustrated in figure 5.13.

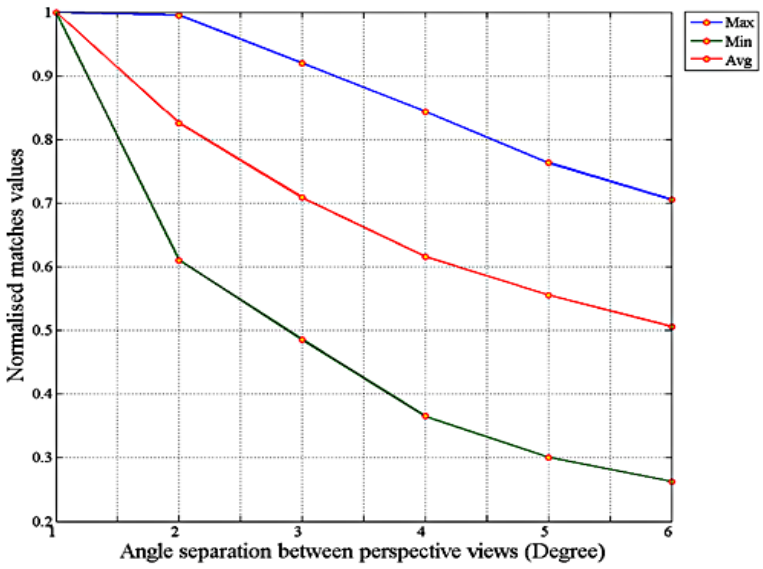

Figure 5.13: Maximum, minimum and average number of matches for 30 different bags as a function of angular separation.

To investigate the nature of the data presented in the graphical obtained from the above matching graphs, bags which produce the maximum and minimum number of matches at 4^0 are considered as a pilot study for further discussion.

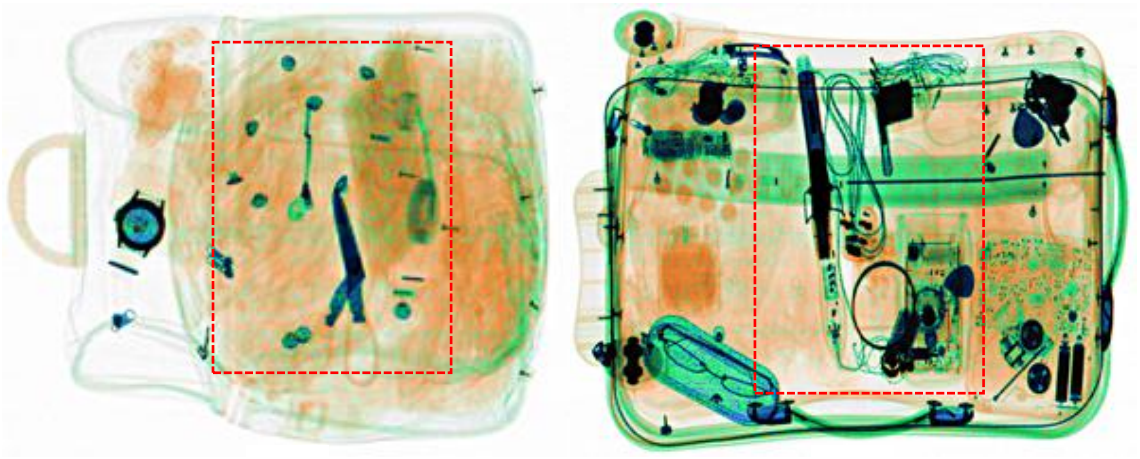

(a) (b)

Figure 5.14: An example of two colour coded images where (a) is the bag that produced the lowest total number of matches and (b) is the bag that produced the highest total number of matches; both examples were recorded for a 4^0 angular separation.

Bags b19 and b20 (4^0 separation) produced the highest and lowest number of matches, respectively. Both bags are illustrated in figure 5.14. These bags also produced the maximum and minimum number of matches, respectively, in the greyscale presented in Chapter 4.

The image in figure 5.14 (a) has a relatively simple arrangement of features in comparison with the image in (b). The two ROIs highlighted in figure 5.14 are reproduced, for detailed discussion, at three different X-ray beam angles; -15^0, 0^0 and 15^0, in the triplet of images presented in figures 5.15 and 5.16. The materials discrimination content of the images in figure 5.15 is relatively uncomplicated. The higher densities (metallic materials) are well delineated against an organic field. The amorphous structure of the organic content is due to the faint responses in the X-ray projections combined with the 'soft' nature of many organic objects such as clothing. Consequently, it is demanding for SIFT to detect corresponding features between perspective views.

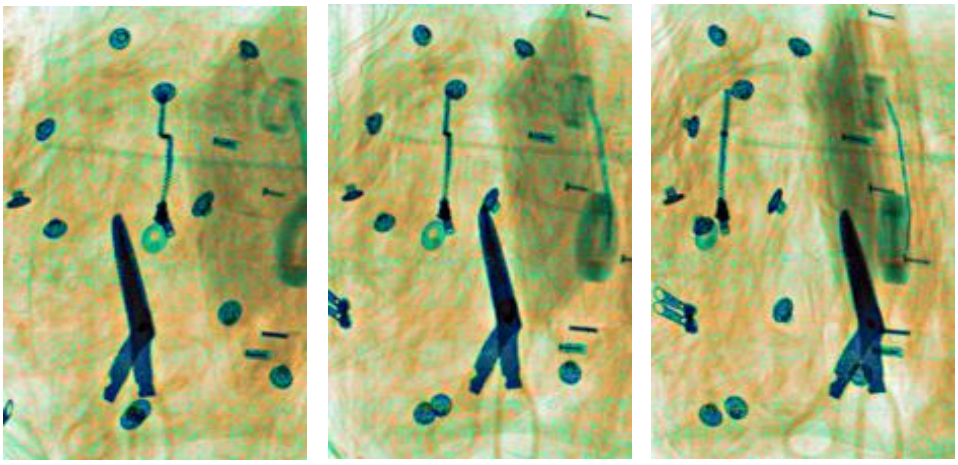

(a) (b) (c)

Figure 5.15: ROIs extracted from an image sequence at different angular positions; (a) -15^0, (b) 0^0 and (c) $+15^0$; a full image of this bag is presented in figure 4.14(a).

The ROIs illustrated in figure 5.16 exhibits a larger number of more complex spatial structures composed of a wider range of different materials in comparison with the content of figure 5.15.

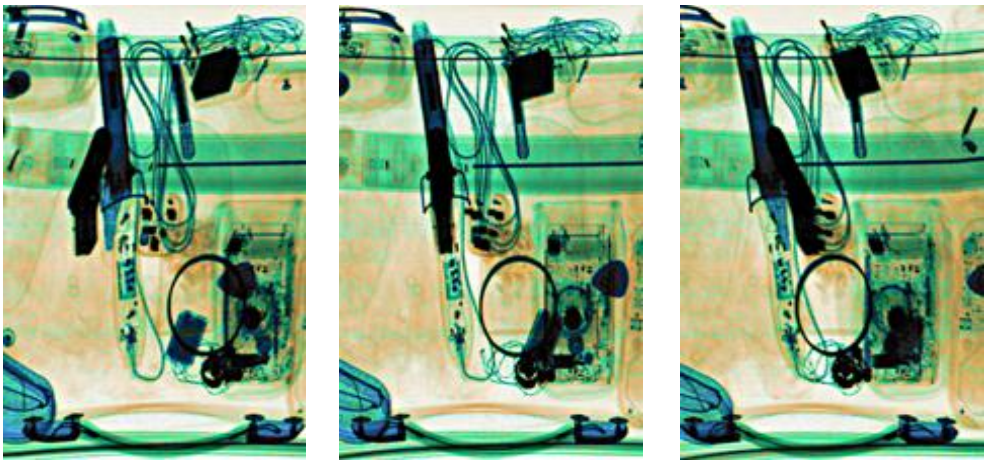

(a) (b) (c)

Figure 5.16: ROIs extracted from an image sequence at different angular positions; (a) -15^0, (b) 0^0 and (c) +15^0; a full image of this bag is presented in figure 4.11(b).

The relatively large number of well delineated high contrast features will increase the likelihood of the SIFT algorithm identifying corresponding features in adjacent perspective views.

5.7.1.2 Materials segmentation matching

As indicated by Section 5.2, the materials matching method employs the 'natural' materials/colour segmentation provided by the dual-energy technique. This approach requires the SIFT to operate independently upon each of the four, material class sub-images. An example of the sub-images is arranged in figure 5.17 to enable conveniently the comparison of a family of matches (bag b21 at a 2^0 separation) within each class. The full 'composite view' of this bag is illustrated in figure 5.8. The metallic class produced the highest total number of matches in comparison to the other classes. Specifically, 276 matches were recorded for the metallic class and 238 for the mixture class. The matching within the grey level and organic classes produced significantly fewer matches, 117 and 104 respectively. The aggregated matches across all four classes totalled 735, whereas employing direct matching produced 1020 matched features for the identical input imagery. This initial finding provided the motivation to conduct a more detailed study to assess the matching performance across the full 30 experiment bag set.

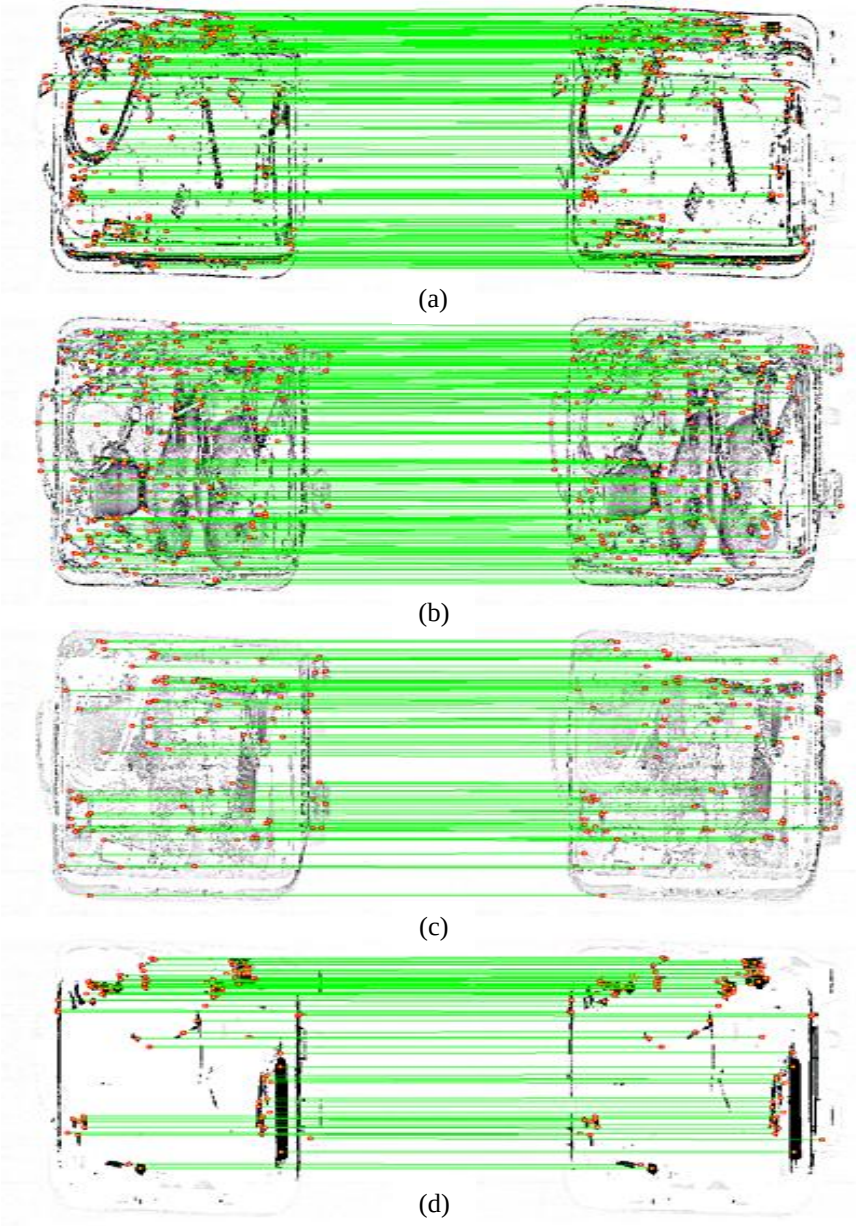

Figure 5.17: Matches recorded at a 2^0 separation for each material class sub-image, where (a) is the metallic class, (b) mixture class, (c) organic class and (d) the grey class.

Figure 5.18 shows the total number of matches of any of 30 bags as a function of the X-ray beam angle. There is significant variation in the number of total matches produced by different language items. For example, the bag b14 generated 679 matches when the angular separation between views was 4^0 whereas 71 were recorded for bag b20. The general trend for all thirty experiment bags is represented by the average number of matches illustrated by the red colour curve in figure 5.19, while the

maximum and minimum numbers of matches recorded for any of the thirty bags are illustrated by the blue and green colour curves respectively.

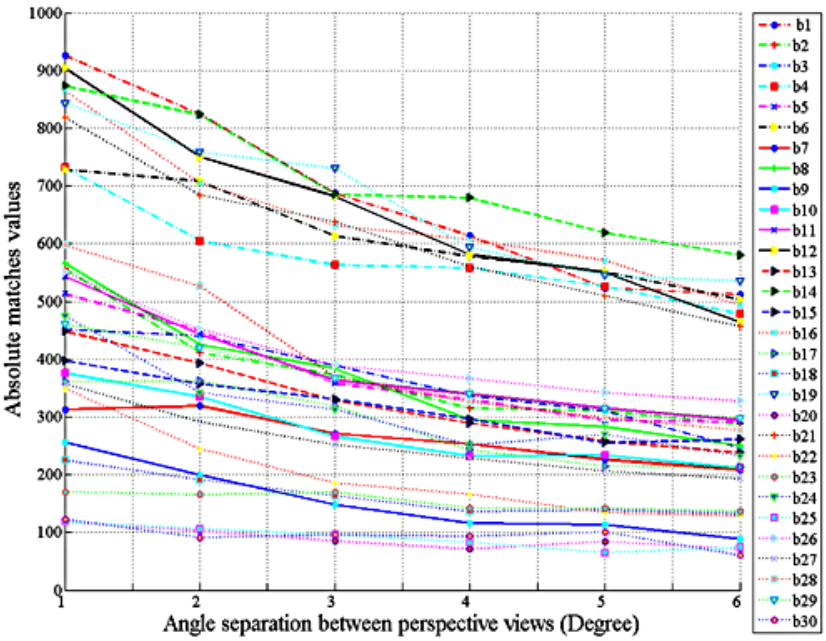

Figure 5.18: The total number of matches recorded employing materials segmentation, for thirty different bags at 1^0, 2^0, 3^0, 4^0, 5^0 and 6^0 view separations.

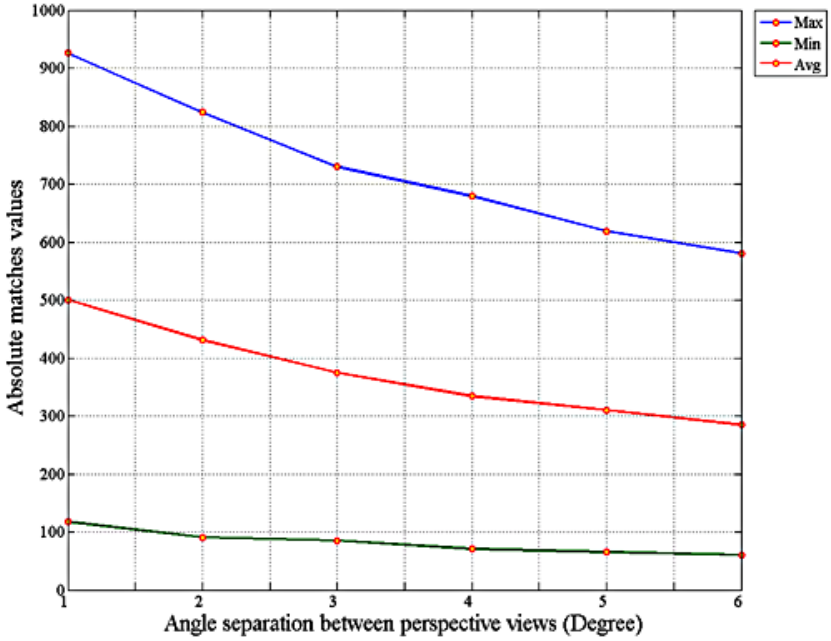

Figure 5.19: Maximum, minimum and average number of total matches for thirty different bags as a function of angular separation.

Figure 5.19 indicates that the average total number of matches reduces as the separation between views increases. The normalized version of this data is shown in graph of figure 5.20, while the trend for the average and maximum deviation from the mean is illustrated graphically in figure 5.21.

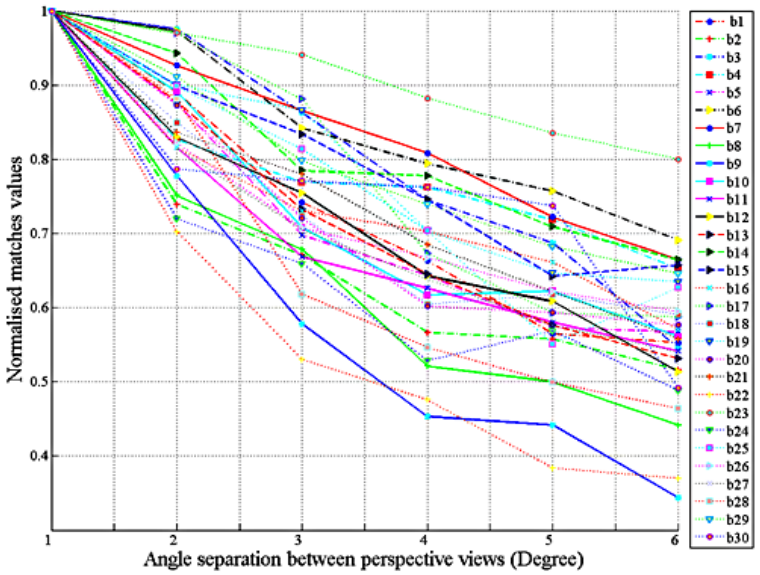

Figure 5.20: Normalized number of matches for 30 luggage items at 1^0, 2^0, 3^0, 4^0, 5^0 and 6^0 separations.

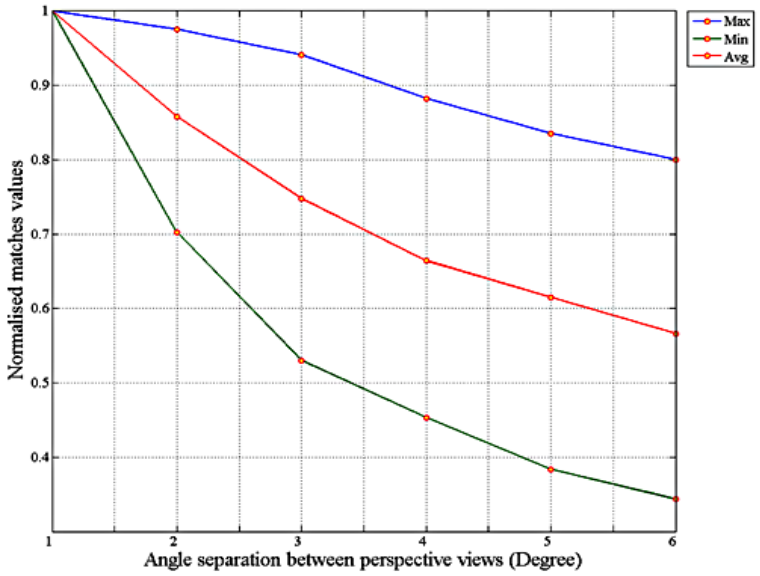

Figure 5.21: Maximum, minimum and average number of matches for 30 different bags as a function of angular separation.

It is worth noting that direct matching and segmented matching both produce minimum matches for bag b20 at a 4^0 view separation. Although, the maximum total number of matches produced at a 4^0 was different in this experiment. The materials segmentation approach shows that b14 (see figure 5.22) formed the maximum number of matches.

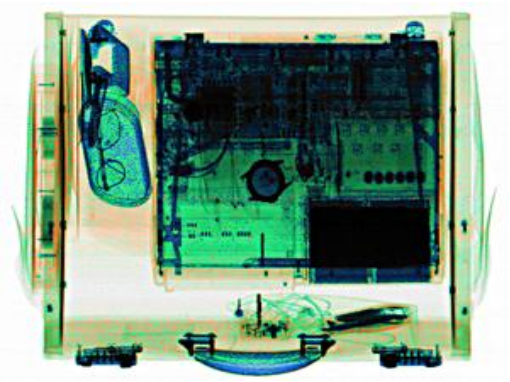

Figure 5.22: Bag b14 produced the highest total number of matches at a 4^0 view separation when employing materials segmentation matching.

The structure of bag b14 is a complex aggregate of objects and demonstrates the potential for high density structures to 'line-up' (due to parallax) and therefore, produce localised occluding conditions in specific views. Also, the bag is relatively deep (large z-axis component) and produces rapidly changing image content with respect to the X-ray beam angle.

(a) (b) (c)

Figure 5.23: ROIs extracted from an image sequence at different angular positions; (a) -15^0, (b) 0^0 and (c) $+15^0$; a full image of this bag is presented in figure 5.22.

Three different ROI extreme views of bag b14 are organized in figure 5.23. While the objects are well delineated in each view they also exhibit very different outline structures. This effect is due to significant z-axis components for each object e.g. the spectacle case is tilted in depth.

5.7.1.3 Interim discussion and conclusion

Two competing matching schemes namely, direct matching and materials segmented matching are analysed comparatively. The overall number of matches produced by the direct matching approach exceeds consistently those produced by the materials segmentation approach. This conclusion is clearly supported by the matching performance data, averaged over 30 different bags and presented in the graph illustrated in figure 5.24 (and the normalised version in figure 5.25). This result is important as an increased total number of robust matches will tend to improve the fidelity of the resultant synthetic image. Also, the sub-image matching inherent in the material segmentation approach incurs increased computational loading in comparison with the direct matching approach.

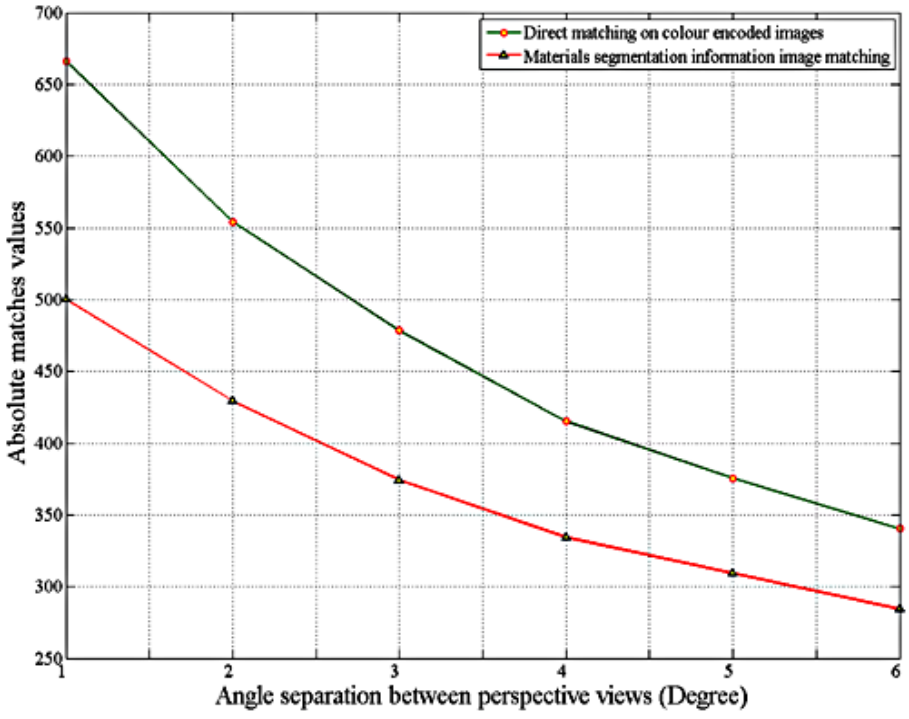

Figure 5.24: The average number of total matches for 30 different bags as a function of angular separation obtained from two different matching approaches.

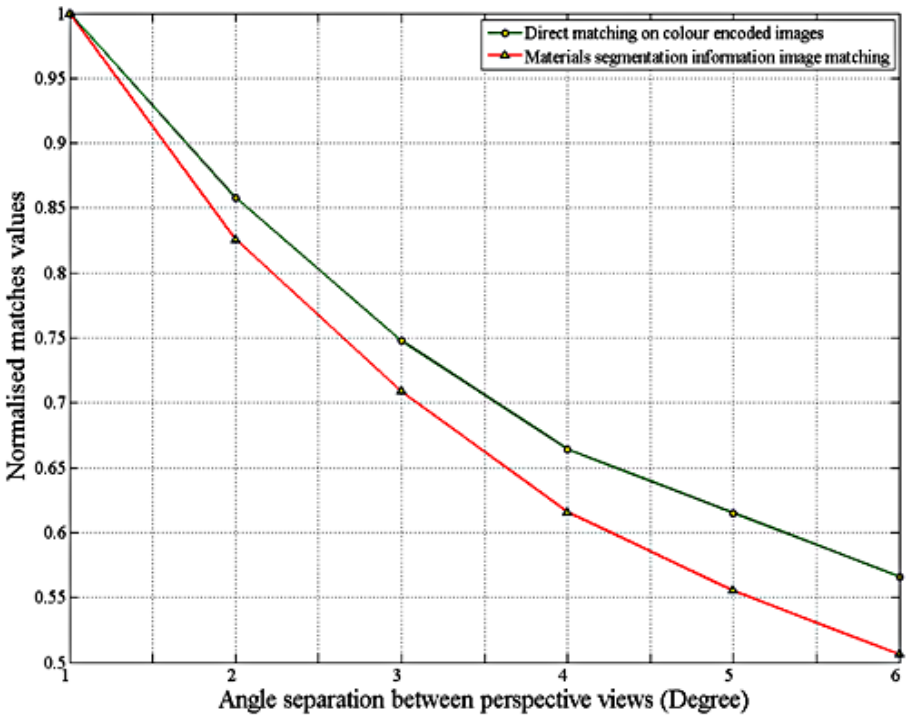

Figure 5.25: The average number of normalized matches for 30 different bags as a function of angular separation obtained from two different matching approaches.

The materials segmentation approach, can disrupt the continuously of a shape or break it into sub-shapes according to its material classes. If the shape is not well-defined, then the matching algorithm might find it difficult to detect corresponding features. However, in the direct matching of colour coded images the shape of an object is preserved and the potential of SIFT to identify corresponding features is enhanced. Therefore, it is demonstrated that the direct matching approach outperforms materials segmentation approach in terms of matching performance. Also, direct matching approach is computationally cost effective. Therefore, it is important to note that the output of the direct matching approach is further considered by the morphing algorithm. In particular, corresponding features produced by direct matching scheme have been exploited by the material based morphing algorithm in which the colour coded synthetic images are generated.

5.7.2 Synthesis and error analysis results as a function of X-ray beam angle

As mentioned in Section 5.4, a linear cross-fade of colours employed typically by morphing algorithms is not directly applicable to dual-energy X-ray imaging as it

creates the possibility for unsupported colours or material classes. In response a material based morphing algorithm is proposed to avoid the issues raised by the linear cross-fade of colours. Examples of the standard morphing and material based morphing results are presented in figure 5.26.

(a) (b) (c)

Figure 5.26: (a) is the GT at normal view position, while (b) and (c) are synthetic images produced by morphing and material based morphing, respectively.

The relatively small differences between the images in figure 5.26 are more easily appreciated by observing the corresponding ROIs presented in figure 5.27 where individual pixels can be inspected. The linear cross-fade has produced undesirable results in terms of material discrimination information. The group of pixels highlighted by yellow squares in figure 5.27 (a) provide examples of unclassified colours Produces by the linear cross-fade process. However, the pixels produced by material based morphing correspond to possible material classes.

The performance of the proposed algorithm is established by comparing the resultant imagery with GT. ERR-I is recorded by an image subtraction method to quantitatively measure the number of pixel errors between the GT images and the synthetic images. The material classes' comparison between GT and its correspondence synthetic view is performed by employing the ERR-II measure. Both types of error allow a direct measurement of the fidelity of the synthetic images.

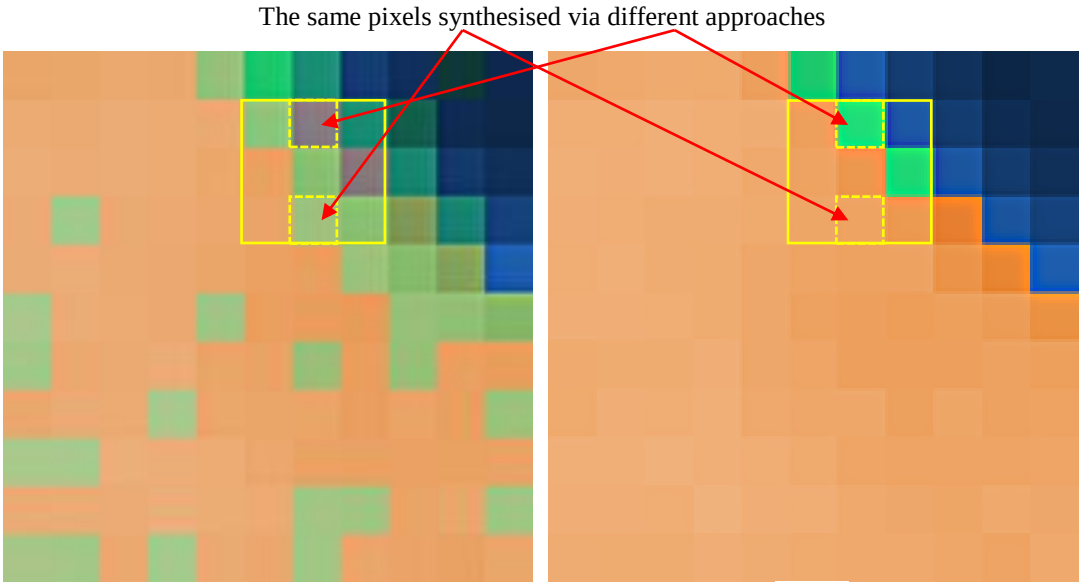

Figure 5.27: Pixel structure in (a) a synthetic image generated using a standard morphing approach, while (b) is the corresponding region produced using material based morphing.

The synthetic views at 2^0, 4^0 and 6^0 separations are presented in figure 5.28 (a), (b) and (c) are organized to enable the visual assessment of a family of synthetic images generated at different separations (GT is presented in figure 5.26 (a)). The best fidelity intermediary view is produced when the separation between views is a minimum.

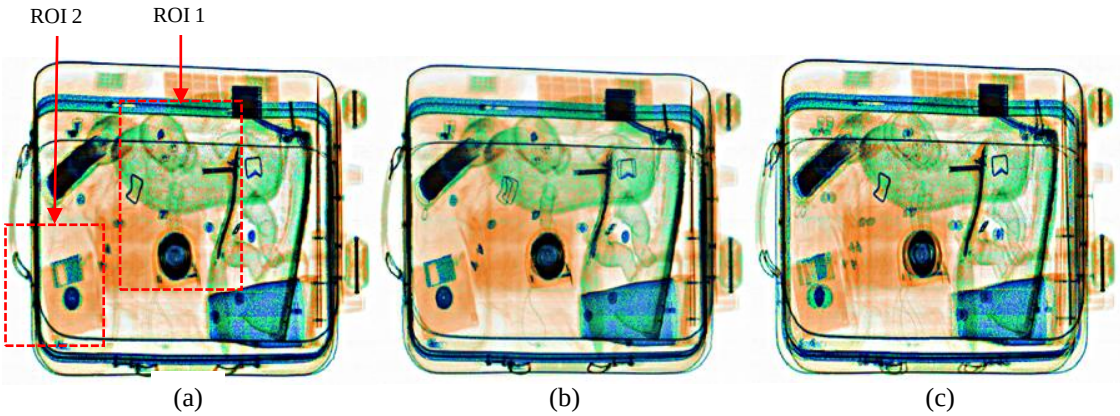

Figure 5.28: (a), (b) and (c) are synthetic images produced using perspective views separated by 2^0, 4^0 and 6^0, respectively; the GT view is presented in figure 5.26 (a).

The minimum separation between perspective views is 2^0. As per the grey level image analysis correct image shape information tends to be better preserved at relatively small separations. To further discuss the performance of the synthetic algorithm, two ROIs, highlighted by the red dashed rectangle in figure 5.28, are selected. Images are chosen carefully to include objects composed of different material classes arranged in spatially complex scenes as routinely encountered at security checkpoints.

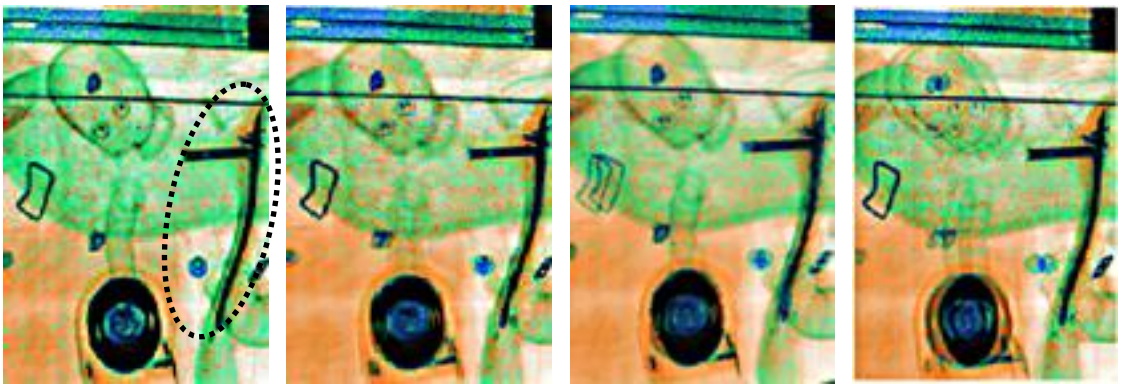

(a) **(b)** **(c)** **(d)**

Figure 5.29: (a) is the ground truth of ROI 1. (b), (c) and (d) are the synthetic views of the same ROI at 2^0, 4^0 & 6^0 separation, respectively.

The images in figure 5.29 are a magnified version of the selected ROI 1 and are arranged to conveniently enable the quality comparison of the synthetic results with regard to the ground truth images. Image of figure 5.29 (a) represents the ROI 1. It is good example of overlap structure where different material classes are exhibited in a multi-layered arrangement. The synthetic views of ROI 1 at 2^0, 4^0 and 6^0 are presented in figure 5.29 (b), (c) and (d). The synthetic results preserve shape 'e.g. metal material embedded in the shoe heel "highlighted by the black dashed oval" and the face of the doll. Also, the capability to preserve near horizontal linear structures is demonstrated. To a certain extent, the algorithm has also conserved the material classes of each object in the synthetic view. Some objects edges tend to blur when the separation between perspective views is increased as highlighted around the speaker, shown in black at the bottom of ROI 1, as well as the face of the toy baby, especially when the separation between views is expanded to 6^0. The GT image of ROI 2 is presented in figure 5.30 (a), while its synthetic views at 2^0, 4^0 and 6^0 are shown in figure 5.30 (b), (c) and (d), respectively. Images in figure 5.30 demonstrate that the algorithm is capable of

preserving curved edges and vertical lines (see the wire supporting the edges of the soft bag).

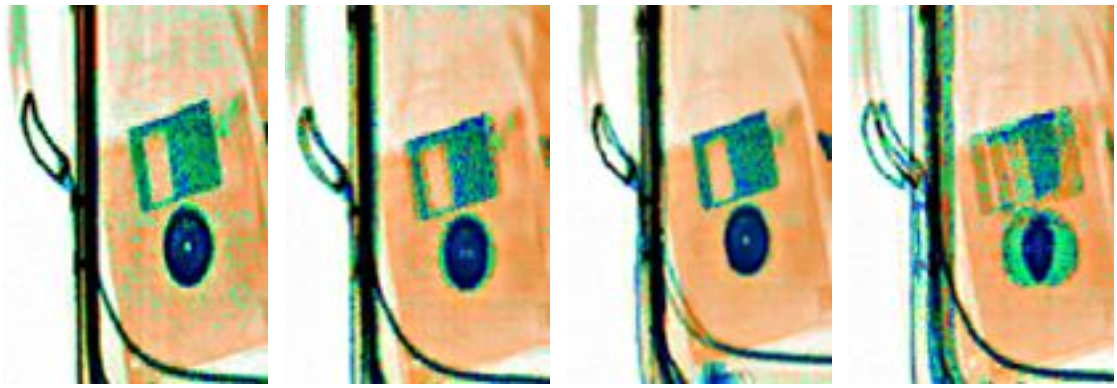

(a) (b) (c) (d)

Figure 5.30: (a) is the ground truth of ROI 2. (b), (c) and (d) are the synthetic views of the same ROI at 2^0, 4^0 & 6^0 of angular separation, respectively.

The hub ring of the floppy disk together with its shutter is blurred when the angle between views is increased (see figure 5.30 (d)). It is interesting to note that these blurred regions are highlighted in green. The synthetic view is colour encoded according to Table 5.1, which is based on the colour of the left and right perspective views (e.g. if the left view is O and the right view is M then the synthetic view has to be X). Hence the artifact along the edges has been emphasized but the material information is preserved. It is noticeable that common morphing artifacts (such as ghosting and blurriness) which are due to cross dissolve have been minimized. Other common morphing artifacts (such as fold overs and "holes" due to warping failure) have also been reduced. An error analysis is formulated in terms of ERR-I and ERR-II to compare the quality of the synthetic images with the ground truth images.

5.7.2.1 Intensity error assessment (ERR-I)

As stated in Section 5.5, ERR-I is a based upon an image subtraction method to count the number of pixel errors on the synthetic images with respect to its GT view. Binary error masks are produced to visualize the pixel errors at different angular separations. Images in figure 5.31 provide examples of GT with their corresponding synthetic views at different separations. Binary error masks (according to Equation 5.1) which present

ERR-I are illustrated in figure 5.32. In the error mask images, a pixel is highlighted by red colour if an error is recorded.

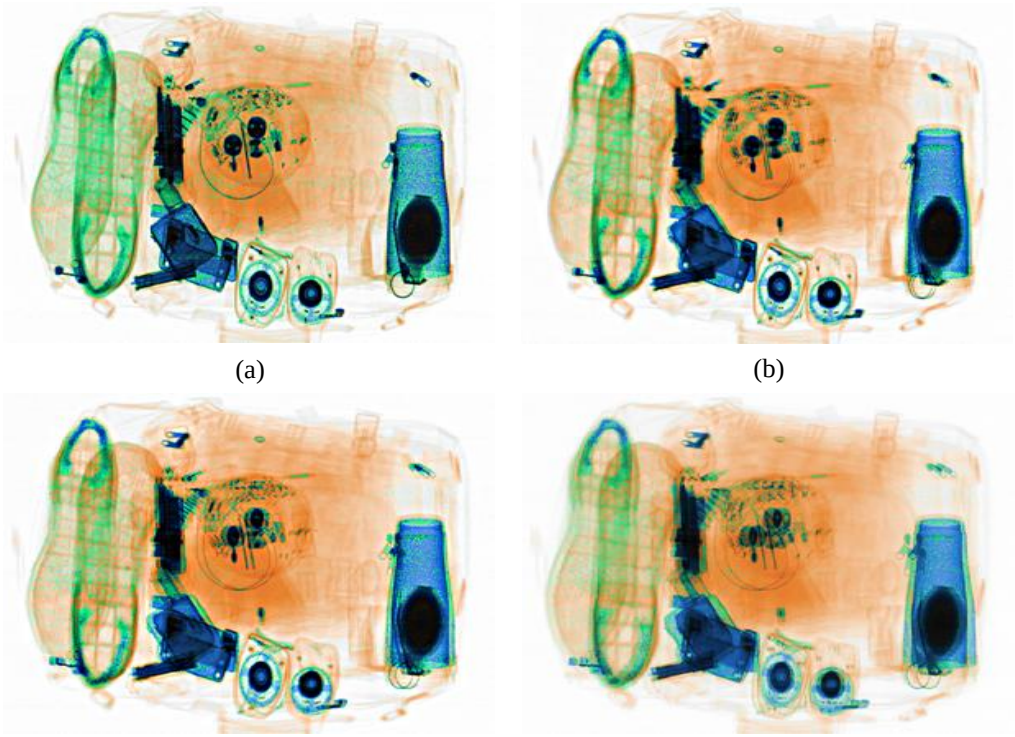

(a) (b)

(c) (d)

Figure 5.31: (a) is the GT view, (b), (c) and (d) are synthetic images produced using perspective views separated by 2^0, 4^0 and 6^0, respectively.

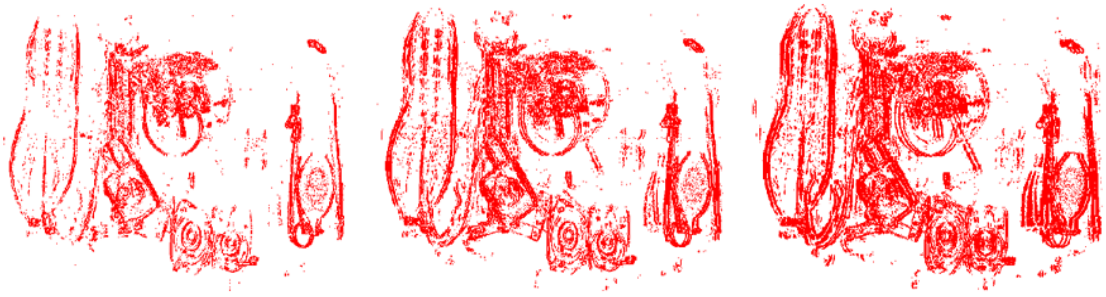

(a) (b) (c)

Figure 5.32: (a), (b) and (c) are binary error masks produced by comparing the synthetic images at 2^0, 4^0 and 6^0 with GT according to Equation 5.1.

It is noticeable that the number of pixel errors increases as the angular separation between perspective views is increased.

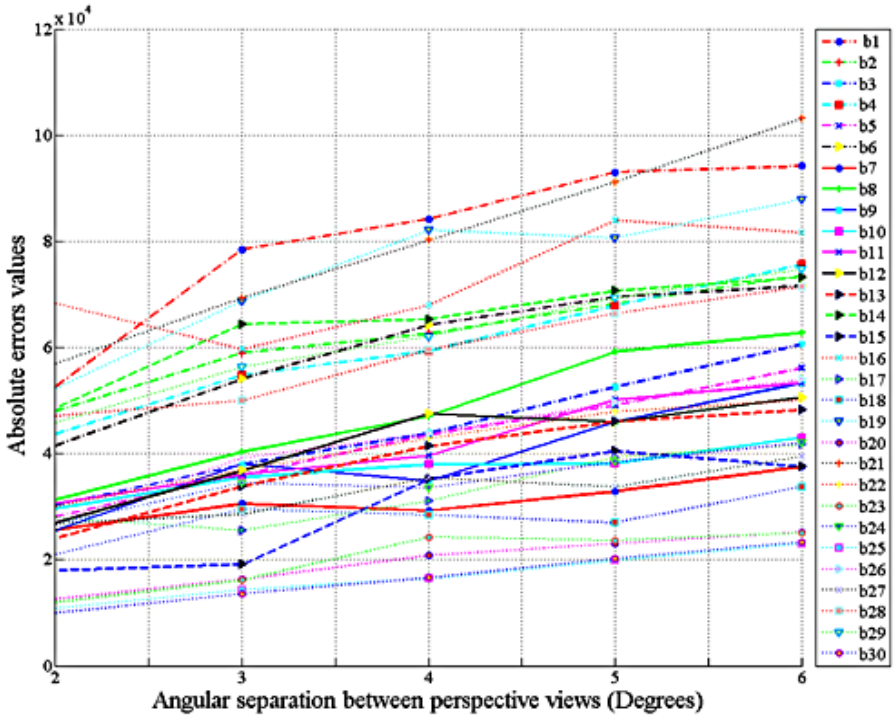

Figure 5.33: Total number of pixel errors for thirty colour coded bags at 2^0, 3^0, 4^0, 5^0 and 6^0, separations.

Curves organised in figure 5.33 show the total number of pixel errors as a function of the angular separation between views. It is evident that the number of pixel errors has been increased when the angular separation between views has been widened. This effect however is anticipated simply because the 'generating' perspective views exhibit increasing variations in terms of shape, overlap and pixel class. Particularly, one visible shape in one view might become partially of fully invisible in other views due to change in the view angle. The number of corresponding matches plays an important role in terms of the number of pixel errors. It is supposed that as the angular separation between perspective views is increased, the number of corresponding matches is reduced. Therefore, under the condition of an inadequate number of corresponding matches, the performance of material based morphing would be negatively influenced producing an increase in the total number of pixel errors. Bag b13 is a good example to show the dependency of the total number of matches on the image content. In this particular example, b13 has produced 24001 pixel errors at a 2^0 separation, which has

almost been doubled to 48208 for a 6^0 of separation. This assumption is further supported by examination of the upper and lower boundaries of pixel errors recorded for any of the thirty bags as illustrated in figure 5.34.

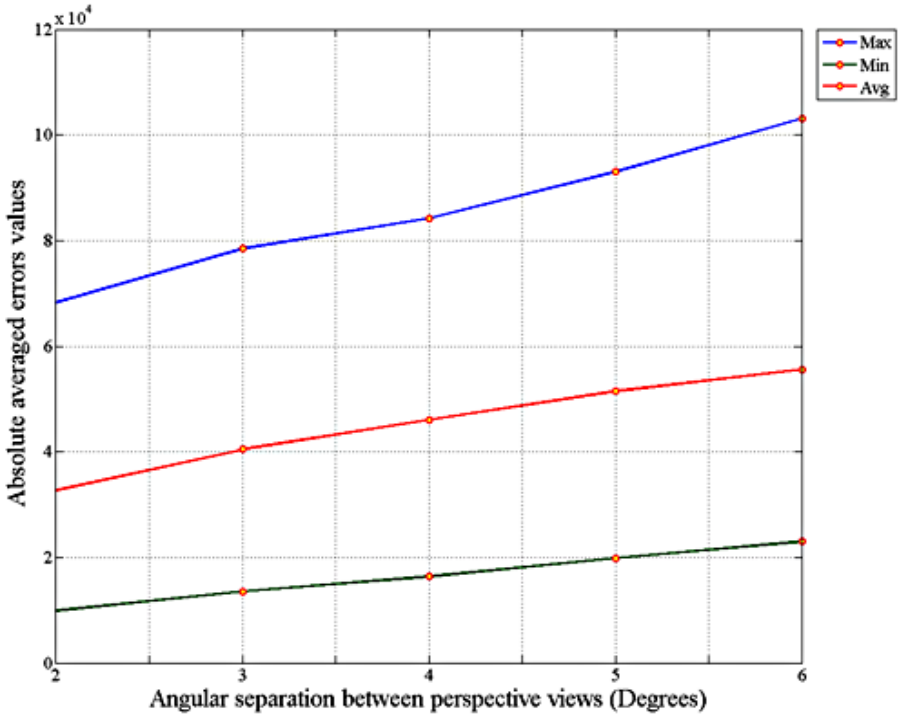

Figure 5.34: Maximum, minimum and average total number of pixel errors for 30 bags as a function of angular separation.

The total average number of pixel errors has been presented by the red colour curve in figure 5.34, while the upper and lower bounds of the maximum and minimum number of pixel errors recorded for any of the thirty bags have also been illustrated graphically by the blue and green colour curves, respectively. The normalized number of pixel errors is presented in figure 5.35 illustrates.

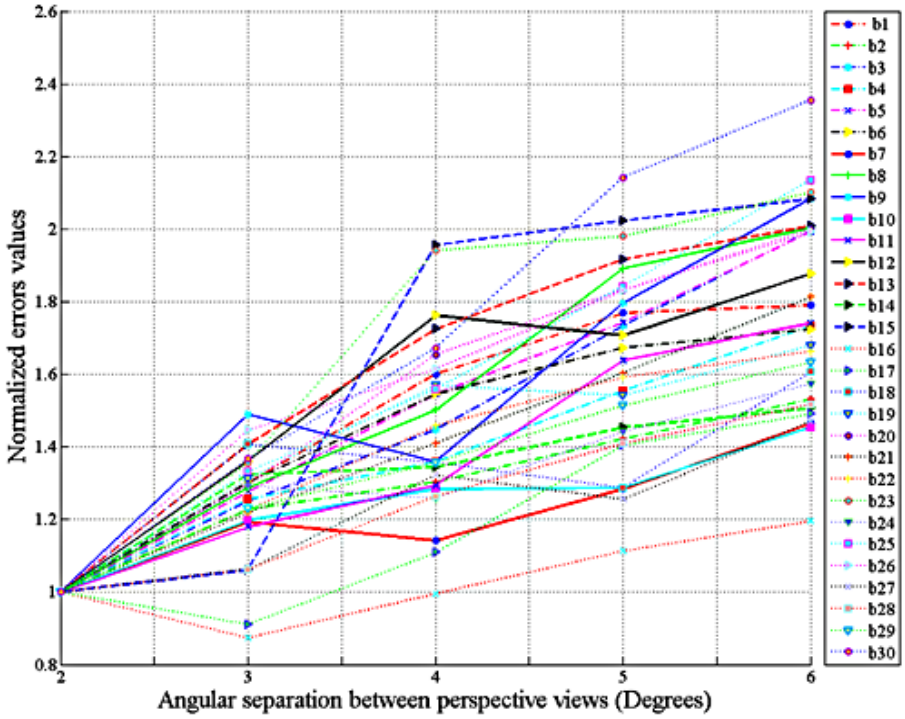

Figure 5.35: Normalized number of pixel errors for 30 luggage items at 2^0, 3^0, 4^0, 5^0 and 6^0 of separation.

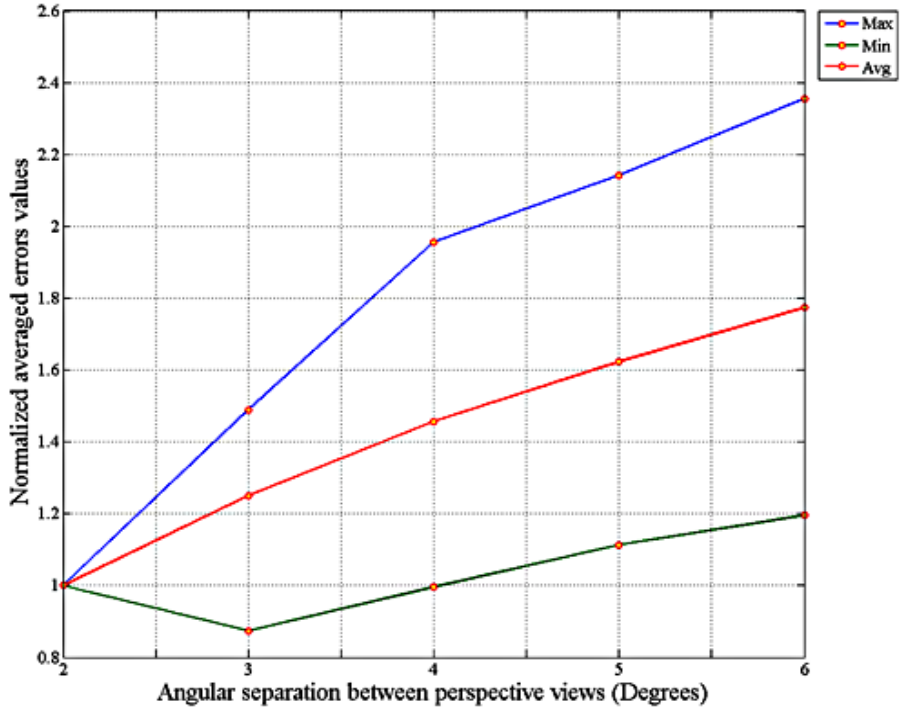

Figure 5.36: Maximum, minimum and average normalized number of pixel errors for thirty bags as a function of angular separation.

In ERR-I, the bag b1 and bag b25 have recorded the highest and lowest number of pixel errors at 4^0 respectively. Interestingly, the same bags have recorded the maximal and minimal pixel errors in the greyscale work presented in Chapter 4.

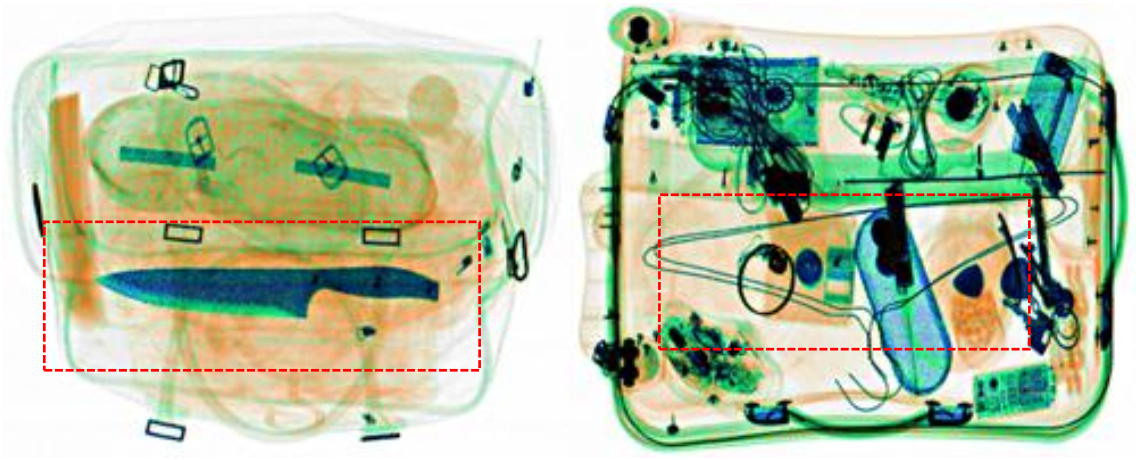

(a) (b)

Figure 5.37: An example of two colour encoded images where (a) and (b) are the luggage items that recorded the minimum and maximum total number of pixel errors at a 4^0 separation, respectively.

Colour coded bags b1 and b25 are illustrated in figure 5.37, and two ROIs are highlighted by the red rectangles for further analysis. The image in figure 5.37 (a) reports that the least number of pixel errors has been recorded when material composition, bag structure and overlap structure are relatively simple. This assumptions is more validated when taking into consideration the magnified ROIs extracted from three different views of the image in figure 5.37 (a) separated by 15^0. Figure 5.38 (b) is the ROI extracted from the normal or 0^0 view while views taken at -15^0 and 15^0 are shown in figure 5.38 (a) and (c), respectively. By means of visual inspection, the three ROIs are relatively alike although they originated from three extreme views. In addition, to the uncomplicated structure of the luggage item, the similarity between the three different views produces a marginal increase to the potential change in the intensity of each material class when the bag is viewed at different perspectives. Consequently, the increase in the pixel errors would be small. Conversely, the highest rates of pixel errors have been recorded with the images which contain many multi-layered structures. Moreover, changes in the overlapping conditions have also played an important role in terms of the total number of pixel errors when the luggage items have been viewed at

different angles. In particular, ROIs extracted from views at -15^0, 0^0 and 15^0 in figure 5.38 (d)-(f) confirms that there is a noticeable variation in terms of structure, overlap and the 3D spatial distribution. The changes in multi-layered and overlapping structure result in variance in the 3D spatial relationship of the objects, which directly affects the intensity of each individual pixel. Therefore, the probability of any synthetic pixel to be recorded as a pixel error is increased.

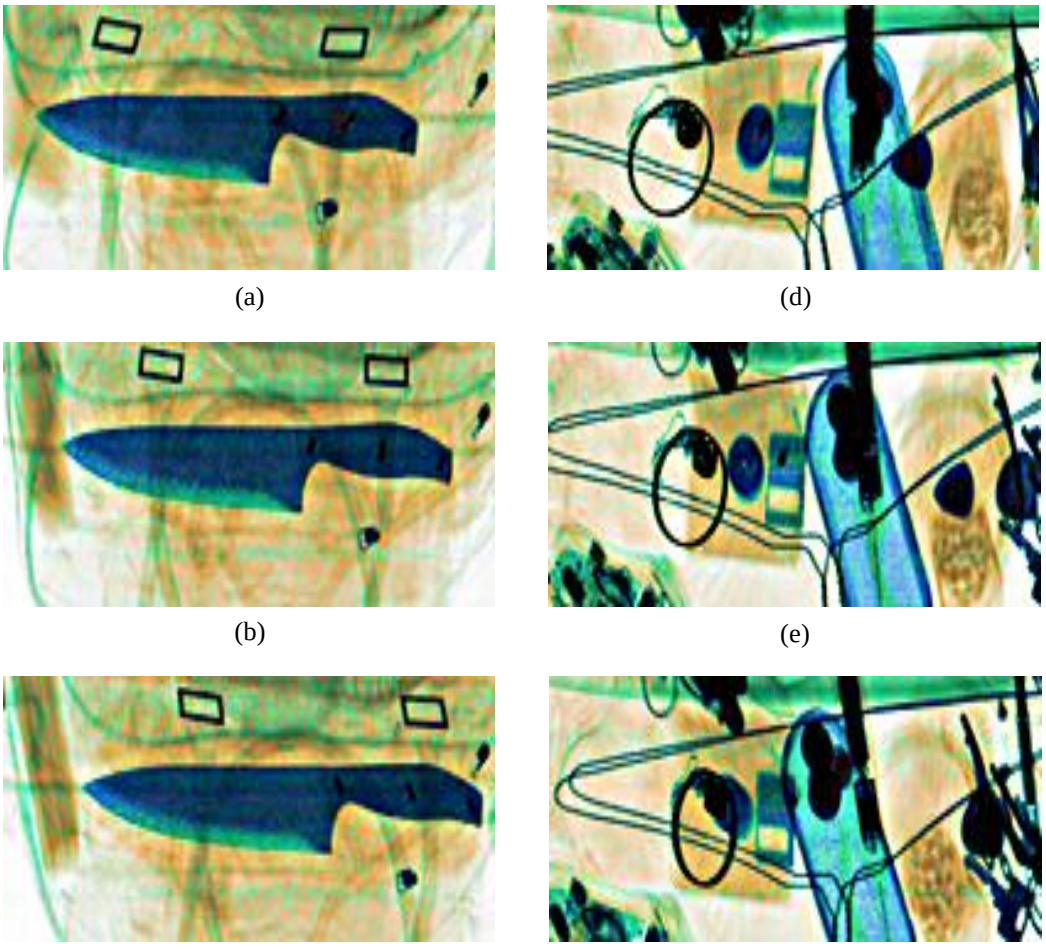

Figure 5.38: (a), (b) and (c) are ROIs extracted from the image of figure 5.37 (a) at -15^0, 0^0 and 15^0, respectively; while (d), (e) and (f) are ROIs extracted from the image of figure 5.37 (b) at -15^0 0^0, and 15^0, respectively.

Nonetheless, any changes in the pixel intensity would have led to change in the material class. Therefore, synthetic view material classes have been compared with the material

classes of the GT, in which the ERR-II has been recorded. More details on analysing the ERR-II are reported in the following text.

5.7.2.2 Material class error assessment (ERR-II)

As indicated in the introductory chapter, aviation security applications require high throughput and threat detection rates. The utility of dual-energy material discrimination information is to provide additional information concerning metal and dense organic threats e.g. guns, knives and plastic explosives. Also, modern threats can be made from a mixture or compound materials. Therefore, the synthetic algorithm is designed to colour encode the synthetic view through equal consideration of the three material classes as reported in Table 5.1. The colour encoding scheme incorporated in this chapter has the potential to increase pixel errors, but circumvents the generation of unsupported and invalid material classes.

Pixels located at identical coordinate positions (x, y) in the synthetic view and the GT were compared. An ERR-II was recorded when the pixel class at each of these locations was not the same. The images in figure 5.39 provide an example of such errors where (a) is a pixelated region from GT and (b) is the 'matching' pixelated region from the synthetic view. The non-corresponding class of 'pixel pairs' is highlighted in the figure by the dashed yellow colour squares.

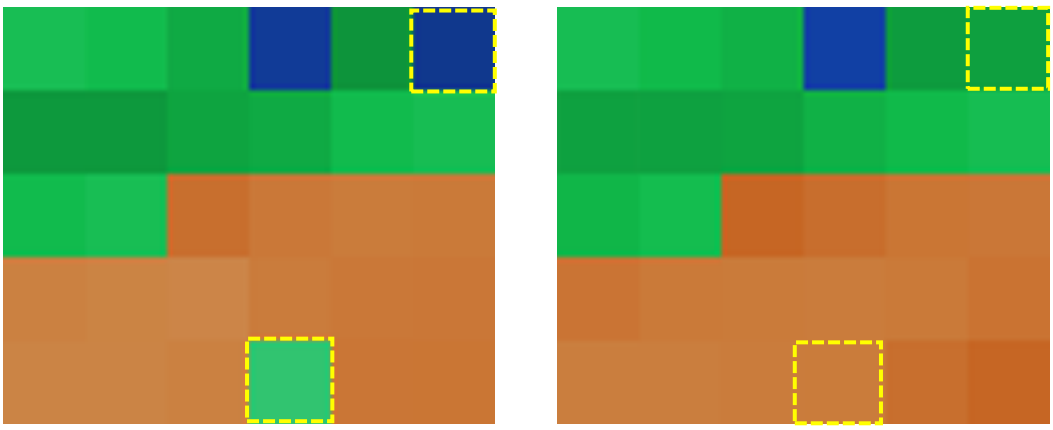

(a) (b)

Figure 5.39: Pixelated regions at identical coordinate locations in the (a) GT and (b) the synthetic view (extracted from figure 5.26 (c)); examples of ERR-II are highlighted by the dashed yellow colour squares.

In this particular example the GT pixel located at the top right corner of the figure 5.39 (a) is classified as metallic, while it's corresponding synthetic pixel in (b) is classified as a mixture, the latter is recorded as erroneous; a similar occurrence of a class error can be observed for the bottom middle pixel locations.

The ERR-II results are graphically represented as a function of X-ray beam angle as per the ERR-I analysis. From the graphs in figure 5.40, it can be appreciated that the pixel error tends to increase with increasing angular separation of the generating views. This general trend is similar to that observed for ERR-I although the total number of errors recorded for ERR-II are significantly larger. In ERR-I and according to Equation 5.1, a single value is used for comparison when calculating the error. However, in ERR-II the potential to record pixel errors is increased as there are 16 different potential states in Table 5.1. Therefore, the potential for generating ERR-II type errors is inherently higher.

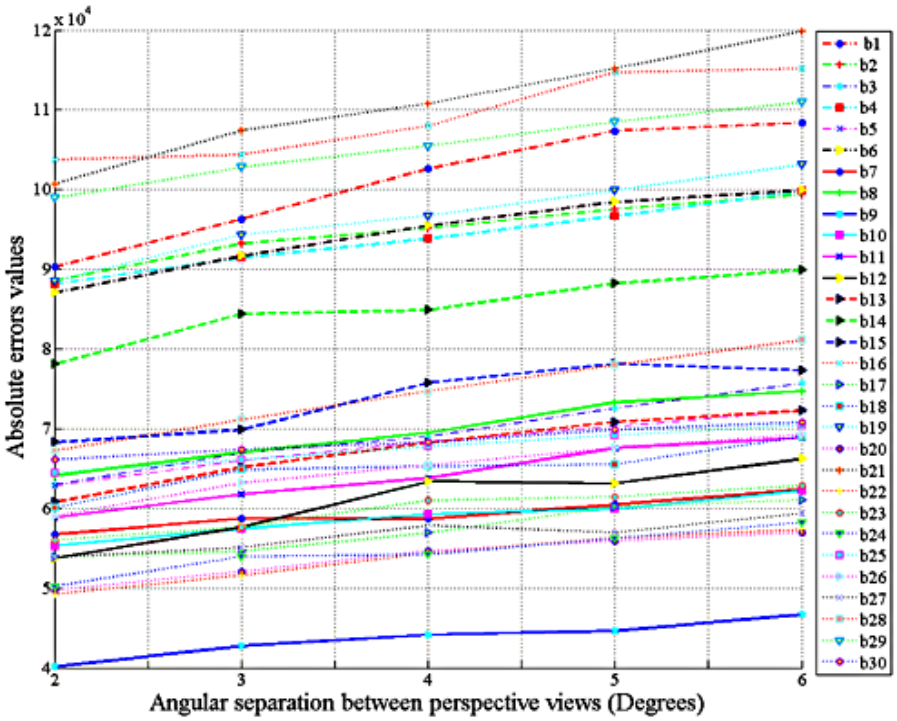

Figure 5.40: Total number of material class pixel errors for thirty colour coded bags at 2º, 3º, 4º, 5º and 6º of separation.

The upper and lower bounds of the maximum and minimum number of pixel errors recorded for any of the 30 bags is also graphically illustrated in figure 5.41 for completeness.

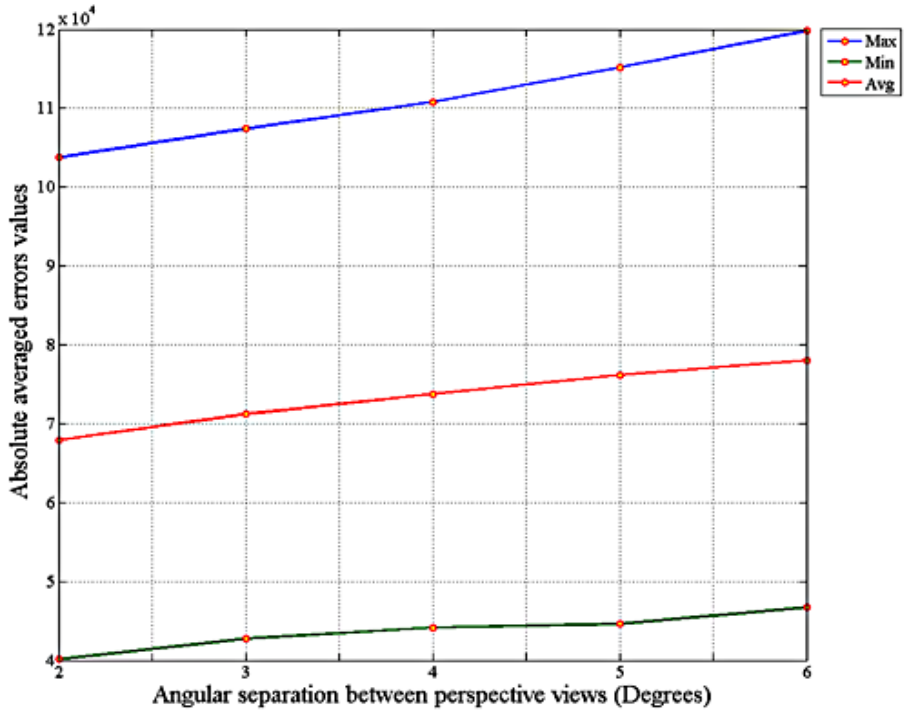

Figure 5.41: Maximum, minimum and average total number of pixel errors for thirty different bags as a function of X-ray beam angle.

Due to the large fluctuation in the amount of data recorded for each different test bag the total number of pixel errors was normalized with respect to the minimum amount recorded at a 2^0, see figure 5.42. For the comprehensiveness, the average number of normalized pixel errors as well as the maximum and minimum number obtained from any of the thirty bags is illustrated in figure 5.43.

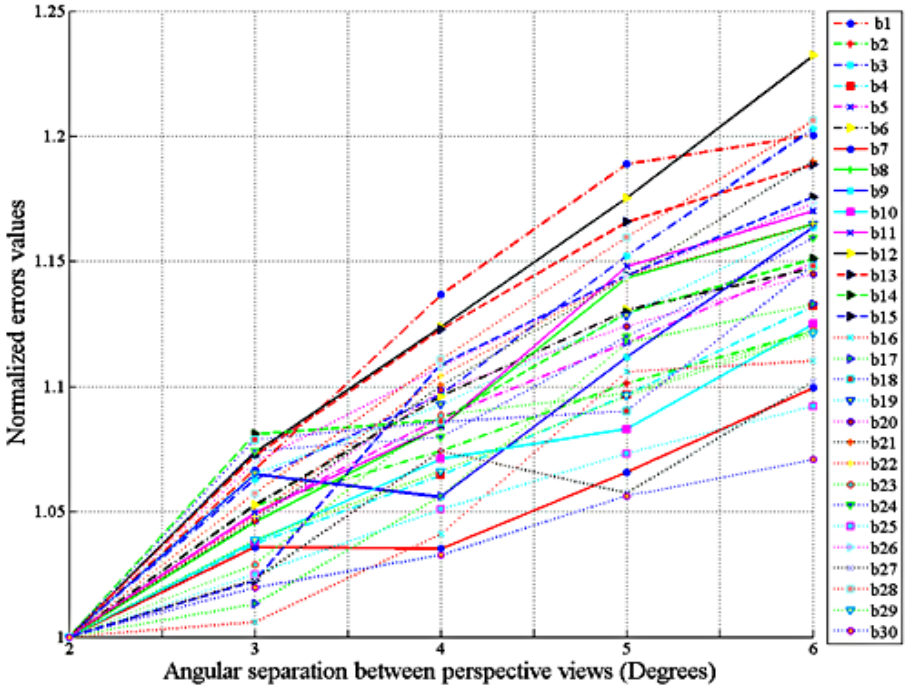

Figure 5.42: Normalized total number of material class pixel errors recorded for thirty different bags at 2^0, 3^0, 4^0, 5^0 and 6^0 of separation.

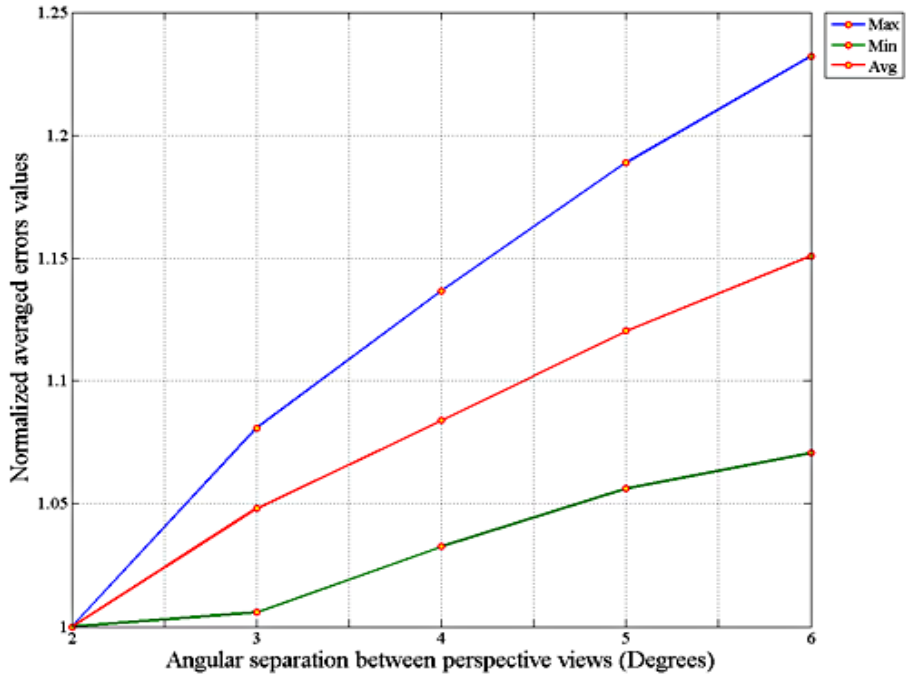

Figure 5.43: Maximum, minimum and average normalized number of pixel errors for thirty different bags as a function of X-ray beam angle.

As per the ERR-I analysis it will be useful to consider the imagery that produced the minimal (bag b9) and maximal (bag b21) total number of pixel errors at a 4^0 angular separation, see figure 5.44.

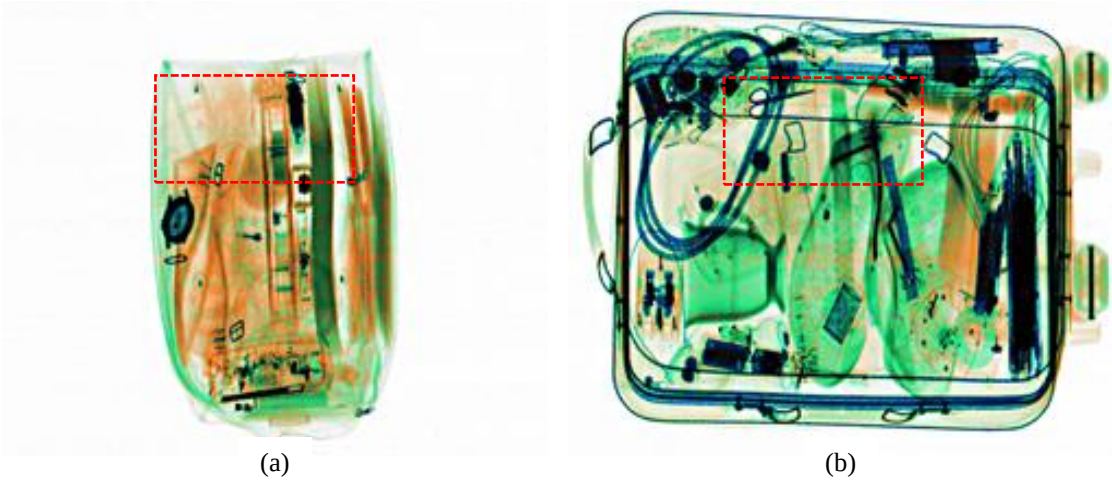

(a) (b)

Figure 5.44: Colour coded images where (a) bag b9 produced the minimum total number of material class pixel errors and (b) bag b21 produced the maximum total number of material class pixel errors; each at a 4^0 separation.

Colour coded bag images b9 and b21 illustrated in figure 5.44 produced the minimum and maximum total number of pixel errors, respectively. The contributory factors to this outcome will be understood from closer inspection of the ROIs (red rectangles) in the figure. The relatively simple structure and small size (area/footprint and volume) of b9 in figure 5.44 (a) produced the least number of resultant pixel errors. This bag also produced a relatively similar perspective views in comparison to the larger volume and more complex b21.

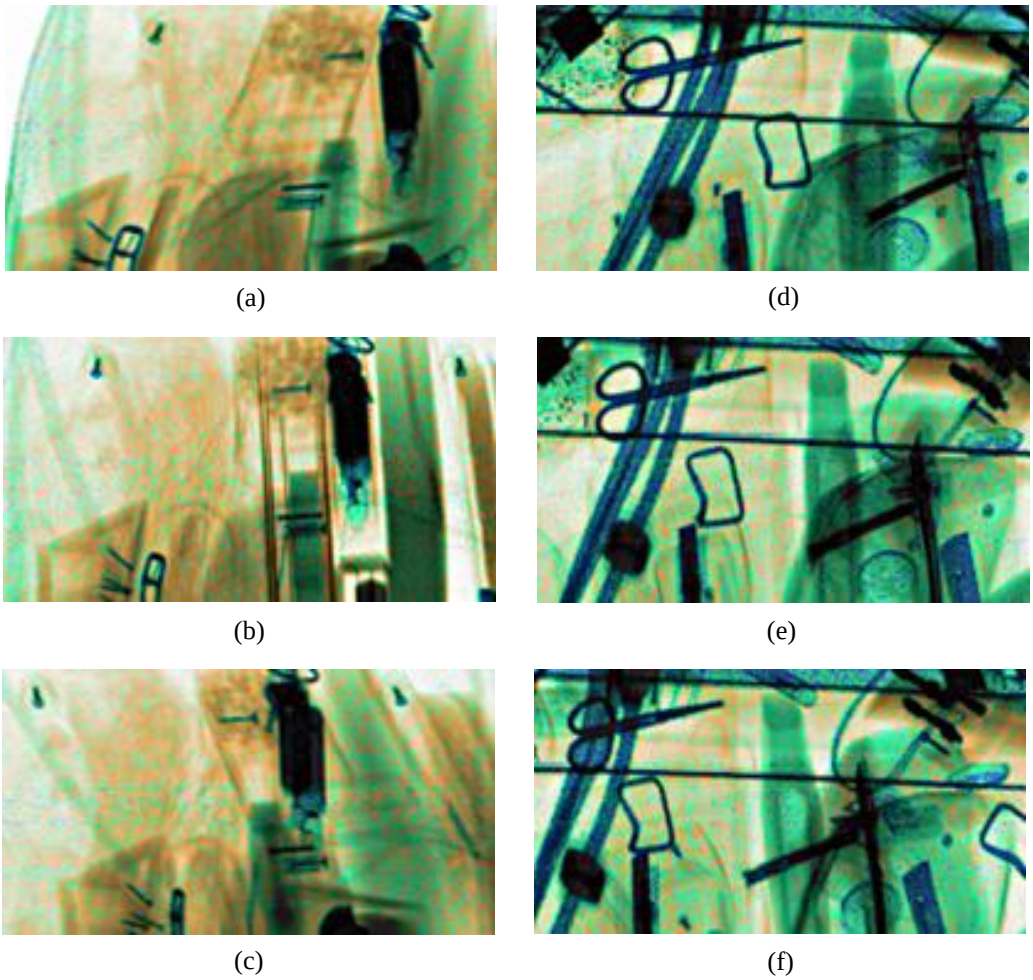

Figure 5.45: ROIs at separations of (a) -15^0, (b) 0^0 and (c) 15^0 (see figure 5.44 (a)) and similarly ROIs at separations of (d) -15^0, (e) 0^0 and (f) 15^0 (see figure 5.44 (b)).

Figure 5.45 (b) is the ROI extracted from the 0^0 view of b9 while (a) and (c) are taken at -15^0 and 15^0, respectively. Visually, the structure of the three ROIs is relatively simple and similar although they originated from three extreme views. In addition, the uncomplicated structure of b9 has produced a marginal in material class transitions when the bag is viewed at different perspectives. As a result, the increase in the pixel errors is relatively small. In contrast, the pixel errors recorded for b21 are significantly increased and are attributed to the presence of many multi-layered structures as indicated by the ROIs illustrated in figure 5.45 (d), (e) and (f). The ROIs confirm that there is a recognizable variation in terms of structure, overlap and material composition when the bag is viewed at different perspectives. Therefore, any change in the view

point might increase the potential for change in the material class, which results in relatively increased pixel errors.

5.7.3 Interim discussion and conclusion

The experimental work presented in this chapter explores the possibility of synthesising dual-energy imagery. Two different schemes have been used to match such imagery; namely direct matching and matching according to material segmentation information. It has been demonstrated that the former approach has increased the likelihood of matching and therefore its output has been exploited by the material based morphing to produce synthetic views. Two types of errors, termed ERR-I and ERR-II, have been used to measure the performance of material based morphing. Empirical results have shown that the total number of matches produced by the optimized SIFT reduces as the angular separation between the generating views increases. This effect is accompanied by an increase in the total amount of ERR-I and ERR-II. Material based morphing is designed to overcome the problem of linear cross-fade associated with typical morphing techniques. Material based morphing ensures that no material class other than the three valid material classes (O, M and X) is generated. However, it does tend to produce blurring artefacts around the edges of an object. This affect is inherent due to the colour encoding scheme employed to produce the synthetic view. Therefore, another experiment was planned to tackle problems associated with the linear cross-fade and edge blurring. The experiment employs a translation or warp based approach. Once again, this technique adopts the ‘industry standard’ colour palette for dual-energy X-ray imaging. The results and findings are reported in following chapter.

Chapter Six Translation based image synthesis algorithm

6.1 Introduction

The material based morphing approach to image synthesis, analysed in the previous chapter, has an inherent tendency to produce "ghosting" artefacts in the resultant synthetic imagery. The motivation for the research presented in this chapter was to establish whether warping or translating, i.e. shifting pixels from the left view towards the right view or vice versa, would be beneficial in diminishing such ghosting effects. The evaluation of the translation approach requires careful analysis of the amount of pixel errors generated as well as consideration of the smoothness of the visual transition from one frame to another within the resultant KDEX sequences.

The translation based image synthesis algorithm comprises two main parts; matching and warping. The warping involves the translation of original 'generating' pixels (without combining or cross fading, which constitutes a morph) in accord to the direct matching data. Thus, the synthetic views are generated by shifting the pixels in the perspective views towards each other, with no need of colour encoding schemes. This approach is designed to reduce the amount of ghosting present in the resultant synthetic imagery. The fidelity of the synthetic images is established by comparing them with GT and errors ERR-I and ERR-II are recoded as a function of X-ray beam angle. To establish the best approach, within the context of this research programme, a comparative analysis of the translation based image synthesis algorithm with the material based morphing algorithm was also conducted.

6.2 Experimental imagery and experimental setup

An identical experiment setup was employed for the comparison of the material based morphing algorithm with the translation based image synthesis algorithm. In particular, thirty luggage items (or bags) termed; b1, b2,….., b30 have been utilized. For ease of interpretation an identical bags sequence was adopted for all analysis. An example of a luggage items employed by both algorithms is shown in figure 5.7. A standardized approach to investigating the material based morphing algorithm employs seven sequential perspective images acquired and stored for each luggage item (producing a total number of 210 perspective images). The views are taken over an angular range of $\pm 3^0$ about the 0^0 view where the angular separation between each successive view is 1^0.

6.3 Dual-energy X-ray image synthesis via pixel shifting/warp

The translation based image synthesis algorithm conserves the material class of the pixels that compose the warped synthetic view. Therefore, it is not necessary to identify the material class of each pixel in the left view and its corresponding right view as there is no manipulation or processing of material class information required. In this chapter, linear interpolation of pixels along the motion axis has been applied to generate in-between views. The idea here is to avoid the linear cross-fading of non-aligned corresponding features, which can lead to ghosting and invalid pixel class data. Note that this approach does not preclude to the potential for numerous pixel errors (in comparison with GT) due to the 'post warp' invariant assignment of pixel class. Therefore, ERR-I and ERR-II are employed to measure the performance of the synthesis algorithm as a function of the X-ray beam angle.

6.4 Translation based image synthesis algorithm evaluation

The methodology adopted to evaluate the performance of 'translation' algorithm employs the ERR-I and ERR-II analysis, which is comprehensively described in Chapter Five. To recap, ERR-I is recorded using the formula presented in Equation 5.1, whereas ERR-II is recorded by comparing the material class of each synthetic pixel with its corresponding GT. This approach enables a direct analytical comparison of the two competing algorithms i.e. translation based synthesis versus morphing based synthesis.

6.5 Results and discussion

The images in figure 6.1 have been organized to enable the visual comparison of two synthetic images produced by different approaches with their GT. The image in figure 6.1 (a) is GT obtained at the normal view position or 0^0, while its corresponding synthetic views, produced by material based morphing and translation based algorithms, are shown in figure 6.1 (b) and (c), respectively. The angular separation between the perspective views is 2^0.

(a) (b) (c)

Figure 6.1: (a) GT at the normal or 0^0 view position, while (b) synthetic image produced by the material based morphing and (c) is the synthetic image produced by the translation based warp; each approach employs perspective views separated by 2^0.

It can be appreciated from a visual inspection of the 'competing' synthetic views in figure 6.1 that each is very similar to the GT. To explore the potential different characteristics of each approach the ROI highlighted by the red dashed rectangular in the GT 0^0 image in figure 6.2 is presented for further discussion.

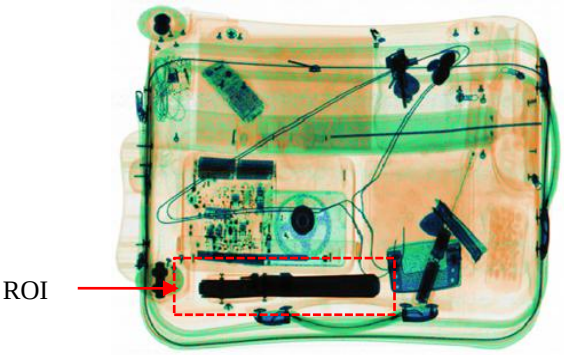

Figure 6.2: Normal 0^0 GT for b6, where the ROI highlights a handgun.

The ROI highlighted in figure 6.2 is used to probe a series of synthetic images produced using increased angular separations (2^0, 4^0 and 6^0) between the generating views. The resultant nine different ROIs for GT, morphing based and translation based synthesis are presented in figure 6.3, where the top row of images are identical GT (for ease of comparison), the second row are produced by material based morphing and the bottom row are produced employing a linear warp (or translation).

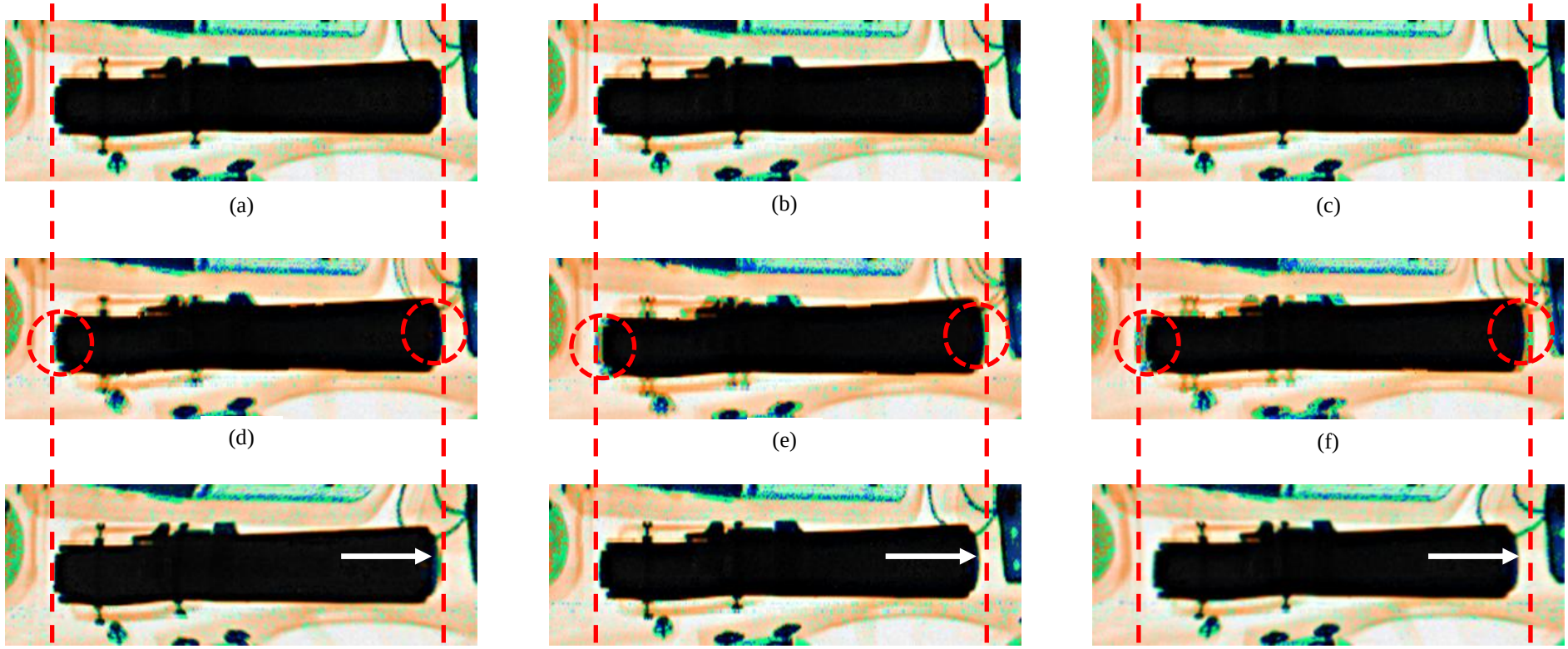

Figure 6.3: The top row (a), (b) and (c) are identical GT; the middle row (d), (e) and (f) were produced by material based morphing and; the bottom row (g), (h) and (i) were produced by warping; the synthetic views, from left to right, were obtained at 2^0, 4^0 & 6^0 of angular separation, respectively.

The dashed red lines in figure 6.3 act as common reference indicators to help gauge visually the relative position of the salient object boundaries. The synthetic views produced by material based morphing (middle row) demonstrate blurred object edges 'highlighted by the dashed red circles in figure 6.3 (d)-(f)'. It can be observed that for fine structures the 'blurring' can separate into the individual contributions from the two generating images to produce double image structures or ghosts. This blurring mechanism becomes increasingly apparent as the angular separation between the views is increased. These effects are broadly described in Chapter Five. It is interesting to consider that the dynamic nature of KDEX imagery might benefit from some instances of local edge blurring (i.e. not double images). For example, the natural lengthening of the horizontal or X-axis component encountered through the change in the X-ray beam angle can be (pseudo) corrected by blurring artefacts, see the white arrows in figure 6.3. While this effect may help smooth some visual transitions it is a by-product of an aberration and it is not easy to predict or control. However, much of this type of ghosting does become inconspicuous when introduced into KDEX imagery. Moving one's attention to the bottom row of warped images in figure 6.3 (g) - (i) it can be appreciated that ghosting is not present. In short the 'ghosting issue' is replaced by a geometric distortion. This distortion arises from the inability of a warp to adequately respond or process the changing size of a corresponding object's 'footprint' within the generating views. In other words, corresponding features change their shape and relative position dependent upon their three dimensionality and relative orientation. Consequently, there is inherently insufficient spatial information available in a single warped perspective image to alleviate the said affect. In practice this inadequacy can lead to spatial dislocations or jumps from one view to another view when GT and synthetic images are combined into a resultant KDEX sequence. Therefore, the gaps indicated by the white arrows in figure 6.3 produce disrupted transitions between GT and synthetic view. This affect has the potential to cause the human observer visual discomfort. Ultimately, human factors analysis is required to understand fully the impact upon user comfort, detection and identification. This aspect, being beyond the scope of the current research, is presented as further work on page 147.

The qualitative discussion presented above does not lead to a convincing argument for the primacy of either approach. To establish a quantitative basis for such a decision ERR-I and ERR-II are employed as good measures of relative algorithm performance.

The general trends of ERR-I and ERR-II were recorded for the material based morphing and translation based algorithms.

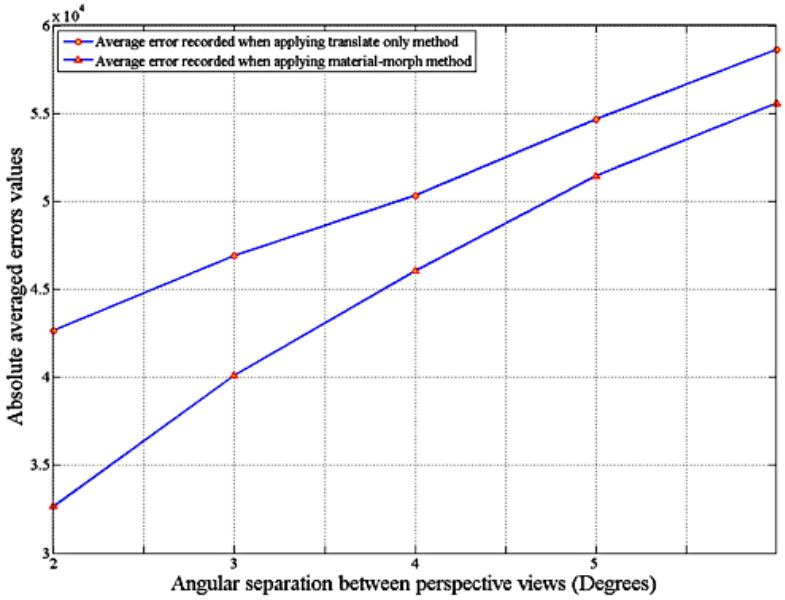

Figure 6.4: The average number of total pixel errors (ERR-I) recorded when utilizing material based morphing and translation based algorithms.

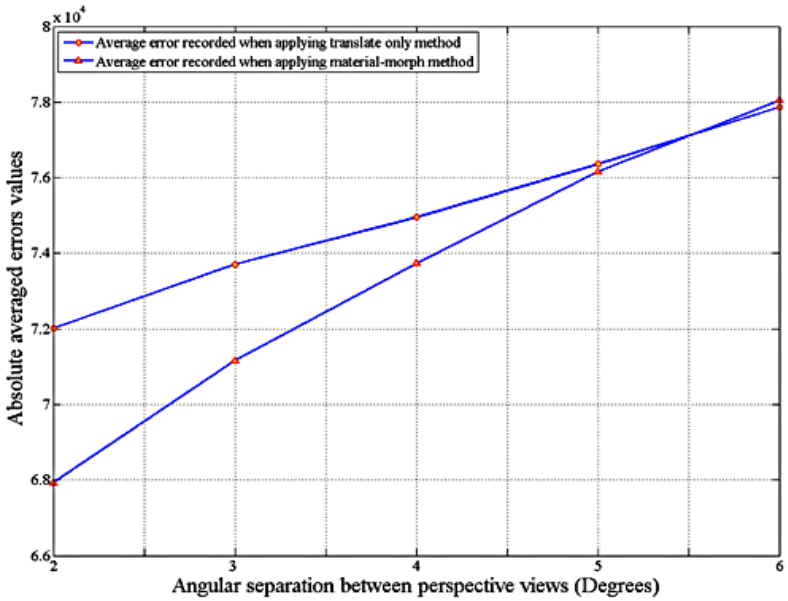

Figure 6.5: The average number of total pixel errors (ERR-II) recorded when utilizing material based morphing and translation based algorithms.

The general trends of ERR-I recorded for both algorithms are graphically illustrated in figure 6.4, while the ERR-II general trends are plotted in figure 6.5, for completeness. It is interestingly to note that in both algorithms, the average number of pixel errors "ERR-I and ERR-II" increased as the angular separation between the perspective views increased. It is somewhat surprising to observe that the material based morphing algorithm outperforms the translation based algorithm in terms of ERR-I and ERR-II. The ERR-II curves shown in figure 6.5 indicate that the translation based synthesis algorithm performs marginally better for separations between views that exceed 5^0.

6.5.1 Effectiveness of the matching algorithm on the performance of the translation based synthesis algorithm

The problem of ghosting along the edges of the objects is addressed by introducing the translation based synthesis algorithm; albeit with the potential for disrupted image transitions. In response to this finding the optimized SIFT algorithm "matching approach" is revisited and explored in the specific context of the translation based synthesis algorithm. Part of the motivation here concerns the observation that the position of keypoints can change abruptly around salient features as the perspective views are changed. In other words, keypoint positioning is not object centric as the algorithm does not employ intelligent interpretation of the three dimensional coordinate information associated with each object.

To open up the discussion, consider the images in figure 6.6 in which (a) and (b) are ROIs that have been extracted from pair of images separated by 6^0. Owing to the change of the view point, objects in figure 6.6 (a) has been located in different position compared to its corresponding object in the image of figure 6.6 (b). The image in figure 6.6 (c) is a combination of the images in figure 6.6 (a) and (b), which demonstrates the difference in relative positioning of the objects.

(a) (b) (c)

Figure 6.6: (a) and (b) are left and right perspective views separated by 6^0 of angular separation, while (c) is the combination of (a) and (b).

The matching algorithm can identify features that appear shape invariant in each perspective view. However, this is a very limited scenario in practice as very few objects are composed of an aggregate of features that can satisfy this condition. A more common place scenario is that as the viewing angle is changed the aggregate features change their shape as well as their relative position with respect one another. Consequently, keypoint positions can change near salient image structures from one view to the next view. For example, a keypoint in one view might be located at the centre of an object, but its corresponding keypoint in the other view is placed in a different relative position with regard to the same object. The images shown in figure 6.7 are ROIs extracted from two matched views of the luggage item named as b1 separated by 6^0 of separation. The ROIs are organized to demonstrate that some of keypoints which have been identified by SIFT, have not been centrally located with regard to the object under inspection. Two features in one view and their corresponding in the other view have been highlighted by white circles in the images of figure 6.7 (a) and (b) respectively.

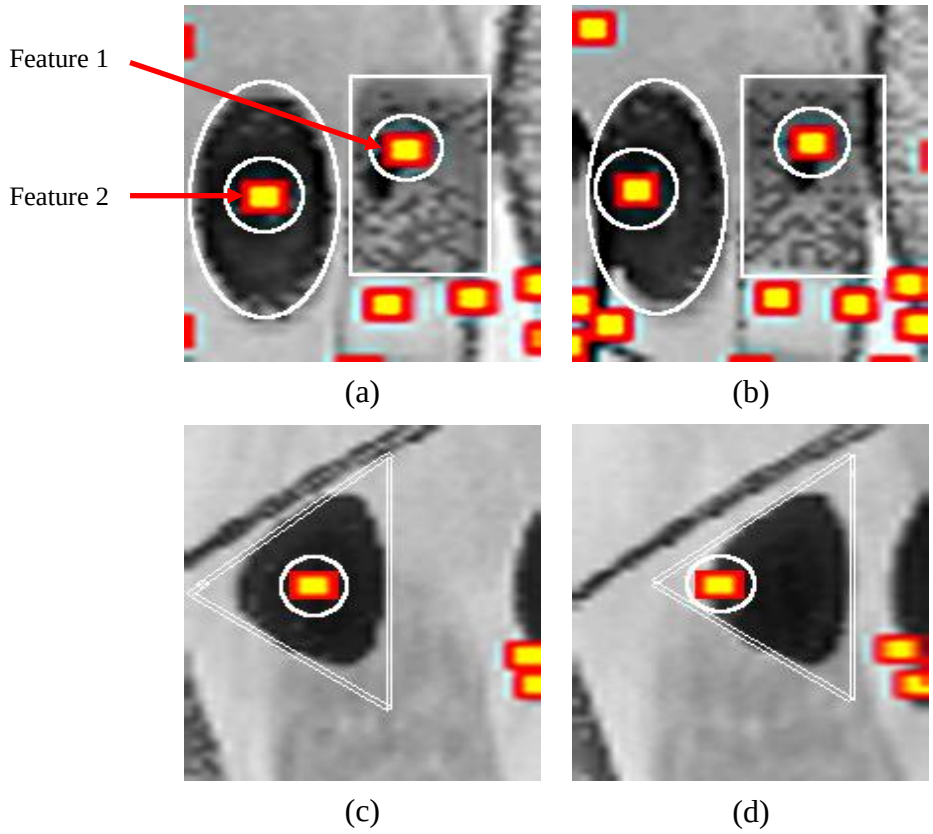

Figure 6.7: (a) and (b) are left and right perspective views separated by 6^0 extracted from bag b1, where the relative position of two features are highlighted with respect to the 'object'; (c) and (d) are a different example of perspective views separated by 6^0 exhibiting the same effect.

It is interesting to note that feature 1 in figure 6.7 (a) is shifted towards the right in the corresponding view in figure 6.7 (b); while feature 2 is shifted towards the left in the corresponding view in figure 6.7 (b). A similar observation is apparent for the feature highlighted by the white circle in figure 6.7 (c), which is relatively shifted towards the left in figure 6.7 (d). The ROIs presented in figure 6.8 also demonstrate the impact of overlapping conditions on the location of keypoints. The ROIs shown in figure 6.8 are extracted from two matched views, separated by 6^0, of bag b18. The image in figure 6.8 (a) shows two objects fully overlapping each other, where the central positioning of the keypoint is emphasized by the white circle.

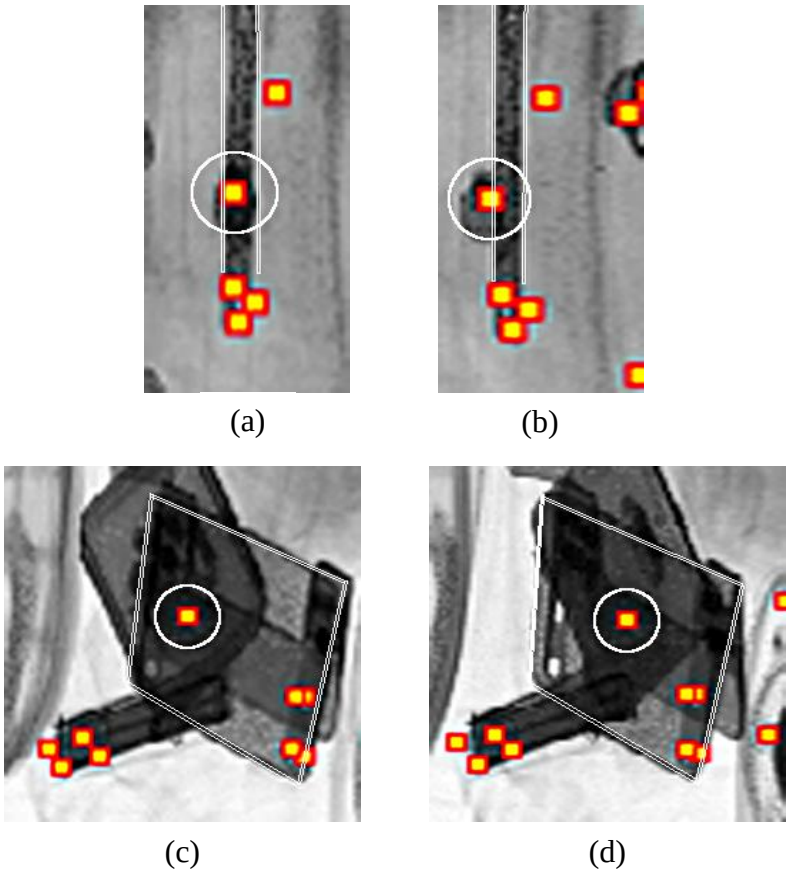

Figure 6.8: ROIs where keypoints are highlighted with regard to salient objects to demonstrate the effect of overlapping structure on the relative position of the keypoints; (a) and (b) are extracted from two perspective views, separated by 6^0, of bag b18, while (c) and (d) are extracted from bag b3.

As the view point is changed, the overlap condition is changed from fully to partially overlapping, as illustrated in figure 6.8 (b). In addition, the keypoint is shifted towards the left as highlighted by the white circle. The images in figure 6.8 (c) and (d) demonstrate the influence of overlapping conditions on locating the keypoint under more complicated overlapping situations. The centre of the feature highlighted by white circle in the image of figure 6.8 (c) is located near the border of the object emphasized by the white four-sided lines. This feature is located approximately at the centre of the same object in the presence of significant overlapping structures.

6.5.2 Interim conclusion

The investigation of synthesizing dual-energy X-ray imaging is presented in this chapter. The problem of ghosting around the object edges produced by the material based morphing synthesis algorithm was tackled by introducing the translation based image synthesis algorithm. However, the material based morphing algorithm recorded fewer pixel errors in comparison to the translation based algorithm as demonstrated by ERR-I and ERR-II analysis. Also the investigation has shown that due to the animated nature of KDEX, edge blurring might become beneficial and aid smooth visual transitions between frames. Evaluation of this approach in terms of human factors is beyond the scope of the current research and has been left for future investigation as presented in Chapter Seven. Exploring the relationship between the matching algorithm and translation based synthesis algorithm has revealed that in various cases, the relative location of keypoints can shift from view to view as a function of cluttering features. This effect can lead to spatial discontinuities between frames when encountered in KDEX imagery.

Chapter Seven Summary, conclusion and future work

7.1 Summary

The research findings presented in this thesis describe the design development and analysis of X-ray image synthesis algorithms. The synthetic imagery is generated by processing images obtained from a novel multiple view dual-energy X-ray scanning technique. The resultant synthetic views are then combined with the scanner views to form KDEX movie sequences in a visual display. The algorithmic approach copes with greyscale or colour coded materials discrimination imagery produced by the dual-energy X-ray technique. The motivation for this work is the reduction in the total number of X-ray detector arrays and associated X-ray collimators required for a given angular sweep or rotation in the resultant KDEX display. Another important benefit is that the amount of X-ray flux required by each inspection is also significantly reduced i.e. the total number of X-ray beams is reduced.

An essential requirement of the image morphing and warping algorithms developed in this work is the feature based solution to the correspondence problem. Yet, solving the correspondence problem is ill posed and compounded by the transparency property of the X-ray images. The nature of transmission imagery requires additional care and consideration to address the complexities of image matching and image synthesis. In this work an optimised version of the scale invariant feature transform referred to as "optimised SIFT" has been used as the matching algorithm and proposed to solve the correspondence problem in the KDEX imagery. The SIFT is bounded by additional criteria, which are of fundamental importance in the design of the imaging system. In particular, the matching algorithm has also been integrated with various morphing techniques to operate upon greyscale and colour coded X-ray images. For the purpose of smooth motion in the kinetic display angular separations of the order of 1^0 between successive views in the image sequences are employed. The intermediary synthetic views can be combined discreetly with the sensor views to provide a sequence of KDEX images. This consideration is the key requirement to improve the practical implementation and commercial viability of the KDEX technique through the reduction in the total number of physical sensors and associated hardware required for a given visual performance.

7.1.1 The matching algorithm

To improve the performance of the standard SIFT algorithm, two new criteria namely the epipolar line criterion and the disparity window have been proposed. These criteria exclude geometrically impossible matches to reduce the total number of incorrect matches. The line-scan imaging technique employed in this work produces minimal vertical disparity, a tolerance of ±1 pixel difference in the y-position is employed to define an epipolar line criterion and accommodate various practical fluctuations such as system noise. Therefore, any pair of corresponding matches is discarded if its difference along the vertical axis is greater than ±1 pixel. To further increase the accuracy of matching, a disparity window criterion has also been designed. The disparity window is a function of the spatiotemporal design parameters of the imaging system. Therefore, a suitable disparity window serves as an effective criterion to reject unfaithful matches. In the context of this work, the term "optimised SIFT" is used to describe the modified algorithm. To appreciate the support provided by the additional criteria, the optimized SIFT algorithm has been tested on 30 different luggage items or bags. A sequence of 7 views distributed symmetrically about the normal view position is captured for each different bag. Each successive image pair is separated by 1^0, with both L-R and R-L search directions employed to find corresponding matches. Therefore a total of 360 successive views have been obtained. The matching algorithm has also been tested under conditions typically encountered within X-ray images such as complex overlapping conditions, change in local contrast and repeated features within the same image frame.

The proposed matching algorithm has also been assessed as a function of X-ray beam angle, where the angle of separation between views was incrementally increased to a maximum of 6^0. The general trend of the total number of matches decreased as the angular separation is increased. In the colour coded imagery, the optimized SIFT algorithm is operated in different manner in comparison to the greyscale images. In general, the matching study of colour coded X-ray images was split into two approaches, namely direct matching and matching according to segmented materials information. The aim here was to determine, which of the two approaches would produce a higher number of matches. The results of each matching scheme have been normalized to prevent them from being dependent on the bag structure or its degree of complexity. The output of the feature matching stage is used as an input for the image

morphing stage (translation and colour encoding) to produce the resultant synthetic view.

7.1.2 The morphing algorithms

A range of morphing algorithms has been designed to cope with the transmission X-ray imagery. An epipolar based morphing technique has been instigated to generate greyscale intermediary views. An optimized SIFT algorithm is used rather than creating feature points manually as per common visible light morphing techniques. Also, epipolar based morphing has been devised to allow pixel interpolation only along the motion axis or horizontal display axis, as nominally no vertical disparity is present in the KDEX imagery. The performance of the epipolar based morphing has been compared with a typical morphing technique, which permits pixel interpolation along both vertical and horizontal axis. The analysis of the epipolar based morphing has shown that the synthetic images reduce in fidelity as the angular separation between views is enlarged.

Material based morphing has been developed to generate the colour coded synthetic views. The algorithm employs the optimized SIFT to inform pixel interpolation along the motion axis. The colour coding accommodates corresponding features that exhibit conflicting material classes. In other words, the class of the corresponding pixels in the left and right views are carefully processed to avoid generating invalid 'new materials or unsupported colours' i.e. the synthetic pixel is forced to belong to one three material classes (O, M and X). This approach has a tendency to blur edges or produce ghosting as the angular separation between views is increased. Two types of errors known as ERR-I and ERR-II have been recorded to evaluate the performance of the material based morphing. The general trends of error behaviour have been presented in both total and normalized values.

To address the ghosting generated by the material based morphing, a translation based image synthesis algorithm has been proposed. This approach employs the optimized SIFT to inform an image warping algorithm. The resultant synthetic is created by shifting the pixels in both perspective views towards each other with no alteration of the original pixel intensity values or material classification. Results obtained from operating the translation based image synthesis algorithm have revealed that the transition

between synthetic and GT KDEX frames was prone to localised spatial discontinuities or jumping. Similar to the material based morphing the translation based image synthesis algorithm has been assessed by recording the ERR-I and ERR-II in both total and normalized values. Both morphing algorithms have pros and cons, therefore; they have been compared through ERR-I and ERR-II to identify, which of the algorithms are superior. It is supposed that the better performing algorithm records fewer errors. The significance of KDEX image frame discontinuity has not been assessed.

7.2 Conclusion

7.2.1 The matching algorithms

In conclusion, the optimized SIFT has produced encouraging results in searching for X-ray image correspondences, although its performance is significantly reduced as the angular separation between views is incrementally increased. The transparency property of X-ray images posed a different set of challenges to SIFT in comparison to reflected visible light images. This can be appreciated from the matching results reported in Chapters 3, 4 and 5. Also, the complex masking inherent in KDEX imagery tends to increase the likelihood that the features of interest be partly or fully occluded in at least one view, hence the matching uncertainty can vary significantly between successive pairs of images. For example, overlapping structures comprised of many individual objects can present large fluctuations in corresponding pixel intensities. The effect is exacerbated for objects that have diverse properties in terms of material composition, thickness and shape. In terms of dual-energy X-ray imaging, the direct matching approach produced a relatively higher number of matches in comparison with the materials segmentation matching approach. Therefore, the direct matching approach was employed to supply keypoints to the colour image synthesis algorithms.

7.2.2 The morphing algorithms

The epipolar based morphing minimised common morphing artifacts such as ghosting, blurriness, fold-overs and holes due to warping failure. The highest fidelity intermediary views were synthesised by employing adjacent perspective images separated by the smallest angular increments used in this work, which is 2^0. The pixel errors increase in magnitude as the angular separation between views increase; this effect was largely independent of the actual angular separation from the normal or 0^0 position.

The material based morphing algorithm circumvented the possibility of generating new material class pixels and was, ultimately, found to be superior to a translation based synthesis algorithm. While the latter approach conserved pixel class information through image warping (i.e. no cross fading or blending of pixel properties) it produced shape discontinuities, which could disrupt the smooth transition between views. On the other hand the morphing approach demonstrated a different error mechanism that produced blurring and ghosting but recorded relatively fewer errors as defined by ERR-I and ERR-II. Also, the blurring tended to be visually acceptable in terms of the overall smoothness of the resultant KDEX sequence.

The only case where the translation based synthesis algorithm performed better than material based morphing was in ERR-II when the angular separation between views exceeded 5^0. Therefore, the material based morphing was demonstrated to be the superior approach for synthesising colour coded synthetic views.

7.2.3 Final conclusion

To sum up, the material presented in this thesis has demonstrated that greyscale or colour coded intermediary views may be successfully synthesised. The performance of the optimized SIFT 'matching algorithm' weakened as the angular separation expanded. In terms of the best conditions, the matching algorithms as well as the morphing algorithms produced the enhanced results when the angular separation between perspective views was 2^0. This finding is very significant as it eliminates the middle X-ray detector array in a group of three arrays. Therefore, a KDEX scanner requiring 21 views (±10 around the normal position or 0^0 view) requires only 11 X-ray sensor arrays in combination with the ability to synthesise the remaining 10 views. This work is of practical significance and enables a time multiplexed sequence alternating between synthetic and X-ray sensor views to produce high quality KDEX imagery.

7.3 Future work

Feasible developments on the work presented in this research are summarized in the following points:

7.3.1 Improvement in matching algorithm

Solving the correspondences is only part of the synthesis method explored in this work. The correspondence problem is an ill posed problem in computer vision applications, and it is exacerbated by the inherent transparency property of X-ray images. It has been established that performance of optimized SIFT significantly reduces when presented with spatially simple images. Therefore, a rigorous analysis of the SIFT parameters to increase the robustness and density of keypoints would enhance the fidelity of the synthetic views. Also, it might be worthwhile to combine the optimized SIFT algorithm with other feature matching techniques so more keypoints are generated.

7.3.2 Improvement in morphing algorithm

A topic of future work will be to investigate ways of extending the proposed morphing algorithms to handle problems such as ghosting, blurring and discontinuity while preserving objects shapes as well as the material classes of dual-energy X-ray images.

7.3.3 X-ray scatter imaging

Another interesting direction of investigation would be to apply the existing algorithms to coherently scattered or diffracted X-ray imagery currently under development by the University team. The techniques are highly sensitive and highly specific and enable materials to be identified as opposed to the crude ‘three class’ discrimination provided by dual-energy X-ray transmission techniques.

7.3.4 Human factors evaluation to support algorithm development

It is a major importance in the design of the KDEX imaging system to preserve the flow of 3D visual information to the observer. In another words, the validity of such synthesis algorithms is dependent upon human factors considerations, which might include the following:

- Investigate threat detection and identification performance as a function of the fidelity of the synthetic images.
- In the greyscale and colour coded experiments, the synthetic algorithms were evaluated as an angular separation between views was incrementally increased up to 6^0 therefore, the possible number of detectors that can be removed without destroying the flow of 3D visual information requires further investigation.

- In the case of colour coded images, two different methods were utilized to generate synthetic views; each has cons and pros. The material based morphing has produced ghosting around the edges of the object, but it has recorded a lower number of pixel errors compared to the translation based algorithm. Further work is required to establish whether the discontinuities and changes in object shapes produced by the translation based algorithm reduce threat detection and identification performance, response time or induce fatigue.

To conclude, the research findings set out in this Thesis are part of a larger body of ongoing research conducted by the University team. Nonetheless, the endeavour reported here has important implications for the successful implementation of the KDEX image capture and display technique and also provides the basis for several new research projects.

References

[1] D. Sheen, D. McMakin and T. Hall, "Three-dimensional millimeter-wave imaging for concealed weapondetection," *IEEE Trans. Microwave Theory Tech.,* vol. 49, pp. 1581-1592, 2001.

[2] D. M. Sheen, D. L. McMakin, H. Collins, T. E. Hall and R. H. Severtsen, "Concealed explosive detection on personnel using a wideband holographic millimeter-wave imaging system," *AEROSENSE Aerospace/Defense Sensing and Controls,* 1996.

[3] S. Singh and M. Singh, "Explosives detection systems (EDS) for aviation security," *Signal Process,* vol. 83, pp. 31-55, 1, 2003.

[4] V. Butler, R. W. Poole, "Reason Foundation and Reason Public Policy Institute," *Rethinking Checked-Baggage Screening,* 2002.

[5] W. Xie, "Simulation of X-ray imaging systems for luggage inspection," 1995.

[6] P. J. Bjorkholm and T. R. Wang, "Explosives detection using three-dimensional computer-assisted image analysis," in *Society of Photo-Optical Instrumentation Engineers (SPIE) Conference Series,* 1993, pp. 122-126.

[7] J. Yinon, "Peer Reviewed: Detection of Explosives by Electronic Noses," *Anal. Chem.,* vol. 75, pp. 98-105, 2003.

[8] P. Shea, T. Gozani and H. Bozorgmanesh, "A TNA explosives-detection system in airline baggage," *Nuclear Instruments and Methods in Physics Research Section A: Accelerators, Spectrometers, Detectors and Associated Equipment,* vol. 299, pp. 444-448, 1990.

[9] D. R. Singh and V. Morellas, "Imaging Methods and Systems for Concealed Weapon Detection," 2004.

[10] J. Eberhardt, S. Rainey, R. Stevens, B. Sowerby and J. Tickner, "Fast neutron radiography scanner for the detection of contraband in air cargo containers," *Applied Radiation and Isotopes,* vol. 63, pp. 179-188, 2005.

[11] C. Scarfone, W. C. Lavely, A. J. Cmelak, D. Delbeke, W. H. Martin, D. Billheimer and D. E. Hallahan, "Prospective feasibility trial of radiotherapy target definition for head and neck cancer using 3-dimensional PET and CT imaging," *Journal of Nuclear Medicine,* vol. 45, pp. 543-552, 2004.

[12] M. Ellenbogen and R. R. Biijani, "System and Method for CT Scanning of Baggage," 2008.

[13] G. van Kaick and S. Delorme, "Computed tomography in various fields outside medicine," *European Radiology Supplements,* vol. 15, pp. 74-81, 2005.

[14] Z. Ying, R. Naidu and C. R. Crawford, "Dual energy computed tomography for explosive detection," *Journal of X-Ray Science and Technology,* vol. 14, pp. 235-256, 2006.

[15] J. Evans, M. Robinson and S. Godber, "A new stereoscopic X-ray imaging technique using a single X-ray source: theoretical analysis," *NDT E Int.,* vol. 29, pp. 27-35, 1996.

[16] J. Evans and M. Robinson, "Design of a stereoscopic X-ray imaging system using a single X-ray source," *NDT E Int.,* vol. 33, pp. 325-332, 2000.

[17] H. Hon and J. Evans, "Multiple-view line-scan imaging," *IEE Proceedings-Optoelectronics,* vol. 149, pp. 45-50, 2002.

[18] J. Evans and H. Hon, "Dynamic stereoscopic X-ray imaging," *NDT E Int.,* vol. 35, pp. 337-345, 2002.

[19] Hon H.W, "The modelling of multiple beam X-ray systems using visible light," 2000.

[20] D. R. Proffitt, I. Rock, H. Hecht and J. Schubert, "Stereokinetic effect and its relation to the kinetic depth effect," *Journal of Experimental Psychology: Human Perception and Performance,* vol. 18, pp. 3-21, 1992.

[21] J. Evans, "Stereoscopic imaging using folded linear dual-energy x-ray detectors," *Measurement Science and Technology,* vol. 13, pp. 1388, 2002.

[22] J. Evans and M. Robinson, "Detecting improving and characterising material in 3D space," *Patent GB,* vol. 2360685, 2001.

[23] Wang T.W, "Target materials discrimination using stereoscopic dual-energy X-ray images," 2002.

[24] T. Wang, "Automated Materials Discrimination using 3D Dual Energy X Ray Images," 2002.

[25] S. E. Chen and L. Williams, "View interpolation for image synthesis," in *Proceedings of the 20th Annual Conference on Computer Graphics and Interactive Techniques*, 1993, pp. 279-288.

[26] S. M. Seitz and C. R. Dyer, "Physically-valid view synthesis by image interpolation," in *Representation of Visual Scenes, 1995.(in Conjuction with ICCV'95), Proceedings IEEE Workshop on*, 1995, pp. 18-25.

[27] S. Avidan and A. Shashua, "Novel view synthesis by cascading trilinear tensors," *IEEE Trans. Visual. Comput. Graphics*, vol. 4, pp. 293-306, 1998.

[28] S. Pollard, M. Pilu, S. Hayes and A. Lorusso, "View synthesis by trinocular edge matching and transfer," *Image Vision Comput.*, vol. 18, pp. 749-757, 6, 2000.

[29] A. Fusiello, S. Caldrer, S. Ceglie, N. Mattern and V. Murino, "View synthesis from uncalibrated images using parallax," in *Proc. of ICIAP*, 2003, pp. 146–151.

[30] O. Woodford, I. Reid, P. Torr and A. Fitzgibbon, "On new view synthesis using multiview stereo," in *Proc. BMVC*, 2007, pp. 1120–1129.

[31] J. Keinert, H. Dutta, F. Hannig, C. Haubelt and J. Teich, "Model-based synthesis and optimization of static multi-rate image processing algorithms," in *Proceedings of the Conference on Design, Automation and Test in Europe*, 2009, pp. 135-140.

[32] J. Evans, Y. Liu, J. Chan and D. Downes, "View synthesis for depth from motion 3D X-ray imaging," *Pattern Recog. Lett.*, vol. 27, pp. 1863-1873, 2006.

[33] L. N. Faria, N. D. A. Mascarenhas, C. E. Morón, J. H. Saito, R. R. Rosa and H. S. Sawant, "A parallel application for 3D reconstruction of coronal loops using image morphing," *Image Vision Comput.*, vol. 25, pp. 95-102, 1, 2007.

[34] T. Pereira, E. V. Brazil, I. Macêdo, M. C. Sousa, L. H. de Figueiredo and L. Velho, "Sketch-based warping of RGBN images," *Graphical Models*, vol. 73, pp. 97-110, 7, 2011.

[35] D. J. Halazonetis, "Morphing and Warping. Part I," *American Journal of Orthodontics and Dentofacial Orthopedics,* vol. 115, pp. 466-470, 4, 1999.

[36] D. J. Halazonetis, "Morphing and Warping: Part II," *American Journal of Orthodontics and Dentofacial Orthopedics,* vol. 115, pp. 706-708, 6, 1999.

[37] G. Farmelo, "X-rays: The First Hundred Years," *Physics Education,* vol. 32, 1997.

[38] D. G. Brown and R. F. Wagner, "Physics and statistics of medical imaging," *J. Digital Imaging,* vol. 2, pp. 194-211, 1989.

[39] K. Mori, J. Hasegawa, J. Toriwaki, H. Anno and K. Katada, "Recognition of bronchus in three-dimensional X-ray CT images with applications to virtualized bronchoscopy system," in *Pattern Recognition, 1996., Proceedings of the 13th International Conference on,* 1996, pp. 528-532 vol. 3.

[40] D. G. Brown and R. J. Jennings, "Detection and discrimination using x-radiation," in *Neural Networks, 1997., International Conference on,* 1997, pp. 2503-2506 vol. 4.

[41] C. Neubauer, "Intelligent X-ray inspection for quality control of solder joints," *Components, Packaging, and Manufacturing Technology, Part C, IEEE Transactions on,* vol. 20, pp. 111-120, 1997.

[42] W. Chao, "Demonstration of 12 nm resolution Fresnel zone plate lens based soft x-ray microscopy," 2010.

[43] D. Schafer and M. Annis, "Automatic detection of explosives using x ray imaging," in *Engineering Inst. of Canada, Canadian Conference on Electrical and Computer Engineering, Volumes 1 and 2 4 p(SEE N 93-30215 11-31),* 1990, .

[44] J. Evans, M. Robinson, S. Godber and R. Petty, "The development of 3-D (stereoscopic) imaging systems for security applications," in *Security Technology, 1995. Proceedings. Institute of Electrical and Electronics Engineers 29th Annual 1995 International Carnahan Conference on,* 1995, pp. 505-511.

[45] N. Murray, R. Lacey and P. Mason, "Exploitation of X-ray technology for the detection of contraband-aviation security applications," in *Security and Detection, 1997. ECOS 97., European Conference on,* 1997, pp. 13-18.

[46] R. Benjamin and S. Prakoonwit, "Automatic X-ray screening of aircraft hold luggage," in *Security and Detection, 1997. ECOS 97., European Conference on,* 1997, pp. 5-9.

[47] J. P. O. Evans, M. Robinson, D. Lacey and N. Murray, "Development of 3D x-ray systems for airport security applications," in *Proceedings of SPIE,* 1824,.

[48] J. P. O. Evans, S. X. Godber and M. Robinson, "Three-dimensional x-ray display techniques," in *Proceedings of SPIE,* 1994, pp. 161.

[49] JPO. Evans and M. Robinson, "Stereoscopic imaging using folded linear dual-energy x-ray detectors," *Measurement Science and Technology,* vol. 13, pp. 1388-1397, 2002.

[50] P. Sukovic and N. H. Clinthorne, "Penalized weighted least-squares image reconstruction for dual energy X-ray transmission tomography," *Medical Imaging, IEEE Transactions on,* vol. 19, pp. 1075-1081, 2000.

[51] R. Speller, G. Ensell and C. Wallis, "A system for dual-energy radiography," *Br. J. Radiol.,* vol. 56, pp. 461, 1983.

[52] T. Wang and J. Evans, "Stereoscopic dual-energy X-ray imaging for target materials identification," in *Vision, Image and Signal Processing, IEE Proceedings-* , 2003, pp. 122-130.

[53] J. Evans, "Kinetic depth effect X-ray (KDEX) imaging for security screening," in *Visual Information Engineering, 2003. VIE 2003. International Conference on,* 2003, pp. 69-72.

[54] J. Chan, P. Evans and X. Wang, "Enhanced color coding scheme for kinetic depth effect X-ray (KDEX) imaging," in *Security Technology (ICCST), 2010 IEEE International Carnahan Conference on,* 2010, pp. 155-160.

[55] Liu Yong, "View Synthesis for Depth from Motion 3D X-ray Imaging," 2008.

[56] J. Evans, Y. Liu and J. Chan, "Depth from motion 3D X-ray imaging for security screening," in *IEE International Symposium on Imaging for Crime Detection and Prevention (ICDP 2005),* 2005, pp. 5-8.

[57] I. Rock and B. Campbell, *An Introduction to Perception.* Macmillan New York, 1975.

[58] I. Howard and B. Rogers, "Seeing in depth: Depth perception (vol. 2)," *Toronto: I.Porteus,* 2002.

[59] H. Wallach and D. O'connell, "The kinetic depth effect." *J. Exp. Psychol.,* vol. 45, pp. 205, 1953.

[60] J. W. Chan, J. P. O. Evans, Y. S. Yong and A. Monteith, "Wire transfer function analysis for castellated dual-energy x-ray detectors," *Appl. Opt.,* vol. 43, pp. 6413-6420, 2004.

[61] M. Robinson and P. Evans, "3D Imaging with Line-Scanning," *Initial Publication with ISR (A1 14/1999),* 2000.

[62] K. H. Jo and A. Vavilin, "HDR Image Generation based on Intensity Clustering and Local Feature Analysis," *Comput. Hum. Behav.,* vol. 27, pp. 1507-1511, 2011.

[63] S. Mattoccia, F. Tombari and L. Di Stefano, "Stereo vision enabling precise border localization within a scanline optimization framework," *Computer Vision–ACCV 2007,* pp. 517-527, 2007.

[64] O. Woodford, P. Torr, I. Reid and A. Fitzgibbon, "Global stereo reconstruction under second-order smoothness priors," *Pattern Analysis and Machine Intelligence, IEEE Transactions on,* vol. 31, pp. 2115-2128, 2009.

[65] D. Min and K. Sohn, "Cost aggregation and occlusion handling with WLS in stereo matching," *Image Processing, IEEE Transactions on,* vol. 17, pp. 1431-1442, 2008.

[66] F. Tombari, S. Mattoccia and L. Di Stefano, "Segmentation-based adaptive support for accurate stereo correspondence," *Advances in Image and Video Technology,* pp. 427-438, 2007.

[67] Y. Shan and Z. Zhang, "Corner guided curve matching and its application to scene reconstruction," in *IEEE Computer Society Conference on Computer Vision and Pattern Recognition,* 2000, .

[68] A. C. Berg, T. L. Berg and J. Malik, "Shape matching and object recognition using low distortion correspondences," in *Computer Vision and Pattern Recognition, 2005. CVPR 2005. IEEE Computer Society Conference on,* 2005, pp. 26-33 vol. 1.

[69] H. Chui and A. Rangarajan, "A new point matching algorithm for non-rigid registration," *Comput. Vision Image Understanding,* vol. 89, pp. 114-141, 2003.

[70] T. Kanade and M. Okutomi, "A stereo matching algorithm with an adaptive window: Theory and experiment," *Pattern Analysis and Machine Intelligence, IEEE Transactions on,* vol. 16, pp. 920-932, 1994.

[71] Y. Boykov, O. Veksler and R. Zabih, "A variable window approach to early vision," *Pattern Analysis and Machine Intelligence, IEEE Transactions on,* vol. 20, pp. 1283-1294, 1998.

[72] O. Veksler, "Stereo correspondence with compact windows via minimum ratio cycle," *IEEE Trans. Pattern Anal. Mach. Intell.,* pp. 1654-1660, 2002.

[73] O. Veksler, "Fast variable window for stereo correspondence using integral images," in *IEEE Computer Society Conference on Computer Vision and Pattern Recognition,* 2003, .

[74] J. L. Lotti and G. Giraudon, "Adaptive window algorithm for aerial image stereo," in *Pattern Recognition, 1994. Vol. 1-Conference A: Computer Vision & Image Processing., Proceedings of the 12th IAPR International Conference on,* 1994, pp. 701-703 vol. 1.

[75] M. O'Neill and M. Denos, "Automated system for coarse-to-fine pyramidal area correlation stereo matching," *Image Vision Comput.,* vol. 14, pp. 225-236, 1996.

[76] O. Veksler, "Fast variable window for stereo correspondence using integral images," in *Computer Vision and Pattern Recognition, 2003. Proceedings. 2003 IEEE Computer Society Conference on,* 2003, pp. I-556-I-561 vol. 1.

[77] C. Li and L. Ma, "A new framework for feature descriptor based on SIFT," *Pattern Recog. Lett.,* vol. 30, pp. 544-557, 2009.

[78] Y. Chen and J. Z. Wang, "A region-based fuzzy feature matching approach to content-based image retrieval," *Pattern Analysis and Machine Intelligence, IEEE Transactions on,* vol. 24, pp. 1252-1267, 2002.

[79] M. Brown, R. Szeliski and S. Winder, "Multi-image matching using multi-scale oriented patches," in *Computer Vision and Pattern Recognition, 2005. CVPR 2005. IEEE Computer Society Conference on,* 2005, pp. 510-517 vol. 1.

[80] D. Bespalov, W. C. Regli and A. Shokoufandeh, "Local feature extraction and matching partial objects," *Comput. -Aided Des.,* vol. 38, pp. 1020-1037, 9, 2006.

[81] A. Baumberg, "Reliable feature matching across widely separated views," in *IEEE Computer Society Conference on Computer Vision and Pattern Recognition,* 2000, .

[82] K. Mikolajczyk and C. Schmid, "An affine invariant interest point detector," in *European Conference on Computer Vision,* 2002, pp. 128–142.

[83] A. Klaus, M. Sormann and K. Karner, "Segment-based stereo matching using belief propagation and a self-adapting dissimilarity measure," in *Pattern Recognition, 2006. ICPR 2006. 18th International Conference on,* 2006, pp. 15-18.

[84] J. Matas, O. Chum, M. Urban and T. Pajdla, "Robust wide-baseline stereo from maximally stable extremal regions," *Image Vision Comput.,* vol. 22, pp. 761-767, 2004.

[85] K. Mikolajczyk and C. Schmid, "A performance evaluation of local descriptors," *IEEE Trans. Pattern Anal. Mach. Intell.,* pp. 1615-1630, 2005.

[86] C. B. Perez and G. Olague, "Learning invariant region descriptor operators with genetic programming and the f-measure," in *International Conference on Pattern Recognition,* 2008, .

[87] M. Carcassoni and E. R. Hancock, "Spectral correspondence for point pattern matching," *Pattern Recognition,* vol. 36, pp. 193-204, 2003.

[88] H. Moravec, "Rover visual obstacle avoidance," in *International Joint Conference on Artificial Intelligence, Vancouver, Canada,* 1981, pp. 785-790.

[89] C. Harris, "Geometry from visual motion," 1993.

[90] C. Harris and M. Stephens, "A combined corner and edge detector," in *Alvey Vision Conference,* 1988, pp. 50.

[91] Z. Zhang, R. Deriche, O. Faugeras and Q. T. Luong, "A robust technique for matching two uncalibrated images through the recovery of the unknown epipolar geometry," *Artif. Intell.,* vol. 78, pp. 87-119, 1995.

[92] C. Schmid and R. Mohr, "Local grayvalue invariants for image retrieval," *IEEE Trans. Pattern Anal. Mach. Intell.,* vol. 19, pp. 530-535, 1997.

[93] K. Mikolajczyk and C. Schmid, "Indexing based on scale invariant interest points," 2001.

[94] D. G. Lowe, "Object recognition from local scale-invariant features," in *Iccv,* 1999, pp. 1150.

[95] K. Mikolajczyk and C. Schmid, "An affine invariant interest point detector," in *European Conference on Computer Vision,* 2002, pp. 128–142.

[96] M. Brown and D. G. Lowe, "Invariant features from interest point groups," in *British Machine Vision Conference, Cardiff, Wales,* 2002, pp. 656-665.

[97] D. G. Lowe, "Distinctive image features from scale-invariant keypoints," *International Journal of Computer Vision,* vol. 60, pp. 91-110, 2004.

[98] E. N. Mortensen, H. Deng and L. Shapiro, "A SIFT descriptor with global context," in *Computer Vision and Pattern Recognition, 2005. CVPR 2005. IEEE Computer Society Conference on,* 2005, pp. 184-190 vol. 1.

[99] P. Scovanner, S. Ali and M. Shah, "A 3-dimensional sift descriptor and its application to action recognition," in *Proceedings of the 15th International Conference on Multimedia,* 2007, pp. 357-360.

[100] P. Moreno, A. Bernardino and J. Santos-Victor, "Improving the SIFT descriptor with smooth derivative filters," *Pattern Recog. Lett.,* vol. 30, pp. 18-26, 2009.

[101] Z. Qi, R. Ting, F. Husheng and Z. Jinlin, "Particle Filter Object Tracking Based on Harris-SIFT Feature Matching," *Procedia Engineering,* vol. 29, pp. 924-929, 2012.

[102] Y. Ke and R. Sukthankar, "PCA-SIFT: A more distinctive representation for local image descriptors," in *IEEE Computer Society Conference on Computer Vision and Pattern Recognition,* 2004, .

[103] S. Zickler and A. Efros, "Detection of multiple deformable objects using PCA-SIFT," in *Proceedings of the National Conference on Artificial Intelligence,* 2007, pp. 1127.

[104] J. H. Hsiao, C. S. Chen, L. F. Chien and M. S. Chen, "A new approach to image copy detection based on extended feature sets," *Image Processing, IEEE Transactions on,* vol. 16, pp. 2069-2079, 2007.

[105] L. Juan and O. Gwon, "A Comparison of SIFT, PCA-SIFT and SURF," *International Journal of Image Processing (IJIP),* vol. 3, pp. 143, 2009.

[106] H. Bay, A. Ess, T. Tuytelaars and L. Van Gool, "Speeded-up robust features (SURF)," *Comput. Vision Image Understanding,* vol. 110, pp. 346-359, 2008.

[107] H. Bay, T. Tuytelaars and L. Van Gool, "Surf: Speeded up robust features," *Computer Vision–ECCV 2006,* pp. 404-417, 2006.

[108] J. Knopp, M. Prasad, G. Willems, R. Timofte and L. Van Gool, "Hough transform and 3d surf for robust three dimensional classification," *Computer Vision–ECCV 2010,* pp. 589-602, 2010.

[109] E. Delponte, F. Isgrò, F. Odone and A. Verri, "SVD-matching using SIFT features," *Graphical Models,* vol. 68, pp. 415-431, 0, 2006.

[110] E. Justino, L. S. Oliveira and C. Freitas, "Reconstructing shredded documents through feature matching," *Forensic Sci. Int.,* vol. 160, pp. 140-147, 7/13, 2006.

[111] Y. Cao and J. McDonald, "Improved feature extraction and matching in urban environments based on 3D viewpoint normalization," *Comput. Vision Image Understanding,* vol. 116, pp. 86-101, 1, 2012.

[112] V. Atalay and M. U. Yilmaz, "A matching algorithm based on linear features," *Pattern Recog. Lett.,* vol. 19, pp. 857-867, 7, 1998.

[113] J. Zhou and J. Shi, "A robust algorithm for feature point matching," *Comput. Graph.,* vol. 26, pp. 429-436, 6, 2002.

[114] Z. He, Y. Wang and H. Yu, "Feature-to-Feature based Laser Scan Matching in Polar Coordinates with Application to Pallet Recognition," *Procedia Engineering*, vol. 15, pp. 4800-4804, 2011.

[115] K. Cao, X. Yang, X. Tao, P. Li, Y. Zang and J. Tian, "Combining features for distorted fingerprint matching," *Journal of Network and Computer Applications*, vol. 33, pp. 258-267, 5, 2010.

[116] J. Chai and S. Hu, "Research on feature point extraction and matching in aerial photogrammetry," *Energy Procedia*, vol. 13, pp. 6962-6969, 2011.

[117] H. JI, W. YH and H. Sun, "SIFT feature matching algorithm with global information," *Opt.Precision Eng*, vol. 17, pp. 439-444, 2009.

[118] Z. Feng, B. Yang, Y. Chen, Y. Zheng and T. Xu, "Features extraction from hand images based on new detection operators," *Pattern Recognit*, 2010.

[119] C. Chua, Y. K. Ho and Y. Liang, "Rejection of mismatched correspondences along the affine epipolar line," *Image Vision Comput.*, vol. 18, pp. 445-462, 5/1, 2000.

[120] S. S. Brandt, "On the probabilistic epipolar geometry," *Image Vision Comput.*, vol. 26, pp. 405-414, 3/3, 2008.

[121] A. Fusiello and L. Irsara, "Quasi-euclidean uncalibrated epipolar rectification," in *International Conference on Pattern Recognition (ICPR)*, 2008, .

[122] H. H. P. Wu, M. T. Lee, P. K. Weng and S. L. Chen, "Epipolar geometry of catadioptric stereo systems with planar mirrors," *Image Vision Comput.*, vol. 27, pp. 1047-1061, 2009.

[123] E. Izquierdo, "Disparity/segmentation analysis: Matching with an adaptive window and depth-driven segmentation," *Circuits and Systems for Video Technology, IEEE Transactions on*, vol. 9, pp. 589-607, 1999.

[124] A. Jones, "Some theoretical aspects of the design of stereoscopic television systems," 1980.

[125] D. Friend and A. Jones, "A stereoscopic television system for reactor inspection," 1980.

[126] P. Benzie, J. Watson, P. Surman, I. Rakkolainen, K. Hopf, H. Urey, V. Sainov and C. von Kopylow, "A survey of 3DTV displays: techniques and technologies," *Circuits and Systems for Video Technology, IEEE Transactions on,* vol. 17, pp. 1647-1658, 2007.

[127] J. Sun, Y. Li, S. B. Kang and H. Y. Shum, "Symmetric stereo matching for occlusion handling," in *Computer Vision and Pattern Recognition, 2005. CVPR 2005. IEEE Computer Society Conference on,* 2005, pp. 399-406 vol. 2.

[128] D. Marr and T. Poggio, "Cooperative computation of stereo disparity," *Science,* vol. 194, pp. 283, 1976.

[129] Y. Mori, N. Fukushima, T. Yendo, T. Fujii and M. Tanimoto, "View generation with 3D warping using depth information for FTV," *Signal Process Image Commun,* vol. 24, pp. 65-72, 1, 2009.

[130] L. Yang, T. Yendo, M. P. Tehrani, T. Fujii and M. Tanimoto, "Artifact reduction using reliability reasoning for image generation of FTV," *Journal of Visual Communication and Image Representation,* vol. 21, pp. 542-560, 0, 2010.

[131] K. V. Mardia, J. M. Angulo and A. Goitía, "Synthesis of image deformation strategies," *Image Vision Comput.,* vol. 24, pp. 1-12, 1/1, 2006.

[132] S. M. Seitz and C. R. Dyer, "View morphing," in *Proceedings of the 23rd Annual Conference on Computer Graphics and Interactive Techniques,* 1996, pp. 21-30.

[133] S. Lee, G. Wolberg, K. Y. Chwa and S. Y. Shin, "Image metamorphosis with scattered feature constraints," *Visualization and Computer Graphics, IEEE Transactions on,* vol. 2, pp. 337-354, 1996.

[134] E. Shechtman, A. Rav-Acha, M. Irani and S. Seitz, "Regenerative morphing," 2010.

[135] B. Zitova and J. Flusser, "Image registration methods: a survey," *Image Vision Comput.,* vol. 21, pp. 977-1000, 2003.

[136] C. A. Glasbey and K. V. Mardia, "A review of image-warping methods," *Journal of Applied Statistics,* vol. 25, pp. 155-172, 1998.

[137] G. Wolberg, "Image morphing: a survey," *The Visual Computer,* vol. 14, pp. 360-372, 1998.

[138] J. Gomes, *Warping and Morphing of Graphical Objects.* Morgan Kaufmann, 1999.

[139] Z. Zhang, L. Wang, B. Guo and H. Y. Shum, "Feature-based light field morphing," *ACM Transactions on Graphics,* vol. 21, pp. 457-464, 2002.

[140] R. A. Manning and C. R. Dyer, "Interpolating view and scene motion by dynamic view morphing," in *Cvpr,* 1999, pp. 1388.

[141] T. Igarashi, T. Moscovich and J. F. Hughes, "As-rigid-as-possible shape manipulation," in *ACM Transactions on Graphics (TOG),* 2005, pp. 1134-1141.

[142] K. Fujimura and M. Makarov, "Foldover-free image warping," *Graphical Models Image Process,* vol. 60, pp. 100-111, 1998.

[143] T. Y. Lee, S. W. Yen and I. C. Yeh, "Texture mapping with hard constraints using warping scheme," *Visualization and Computer Graphics, IEEE Transactions on,* vol. 14, pp. 382-395, 2008.

[144] H. Seo and F. Cordier, "Constrained texture mapping using image warping," in *Computer Graphics Forum,* 2010, pp. 160-174.

[145] I. A. Sigal, H. Yang, M. D. Roberts and J. C. Downs, "Morphing methods to parameterize specimen-specific finite element model geometries," *J. Biomech.,* vol. 43, pp. 254-262, 2010.

[146] H. Kekre, T. Sarode and S. Patil, "A novel pixel based color transition method for 2D image morphing," in *Proceedings of the International Conference & Workshop on Emerging Trends in Technology,* 2011, pp. 357-362.

[147] K. Liu and J. Ostermann, "Realistic head motion synthesis for an image-based talking head," in *Automatic Face & Gesture Recognition and Workshops (FG 2011), 2011 IEEE International Conference on,* 2011, pp. 125-130.

[148] H. Lin, P. Du, W. Zhao, L. Zhang and H. Sun, "Image registration based on corner detection and affine transformation," in *Image and Signal Processing (CISP), 2010 3rd International Congress on,* 2010, pp. 2184-2188.

[149] P. Bhat, K. C. Zheng, N. Snavely, A. Agarwala, M. Agrawala, M. F. Cohen and B. Curless, "Piecewise image registration in the presence of multiple large motions," in *Computer Vision and Pattern Recognition, 2006 IEEE Computer Society Conference on,* 2006, pp. 2491-2497.

[150] G. Xiao-jun, H. Li-li and N. Yi, "Feature points based image registration between endoscope image and the CT image," in *Electric Information and Control Engineering (ICEICE), 2011 International Conference on,* 2011, pp. 2190-2193.

[151] L. Zagorchev and A. Goshtasby, "A comparative study of transformation functions for nonrigid image registration," *Image Processing, IEEE Transactions on,* vol. 15, pp. 529-538, 2006.

[152] S. Singh and M. Singh, "A dynamic classifier selection and combination approach to image region labelling," *Signal Process Image Commun,* vol. 20, pp. 219-231, 3, 2005.

[153] M. Vega, J. Mateos, R. Molina and A. K. Katsaggelos, "Astronomical image restoration using variational methods and model combination," *Statistical Methodology,* vol. 9, pp. 19-31, 0, 2012.

[154] S. Li, J. T. Kwok and Y. Wang, "Combination of images with diverse focuses using the spatial frequency," *Information Fusion,* vol. 2, pp. 169-176, 9, 2001.

[155] B. R. Condon, "Multi-modality image combination: Five techniques for simultaneous MR-SPECT display," *Comput. Med. Imaging Graphics,* vol. 15, pp. 311-318, 0, 1991.

[156] D. G. Lowe, "Object recognition from local scale-invariant features," in *International Conference on Computer Vision,* 1999, pp. 1150-1157.

[157] K. Mikolajczyk and C. Schmid, "Indexing based on scale invariant interest points," in *Proc. ICCV,* 2001, pp. 525-531.

[158] R. Gesick, C. Saritac and C. C. Hung, "Automatic image analysis process for the detection of concealed weapons," in *Proceedings of the 5th Annual Workshop on Cyber Security and Information Intelligence Research: Cyber Security and Information Intelligence Challenges and Strategies,* 2009, pp. 20.

[159] T. Lindeberg, "Detecting salient blob-like image structures and their scales with a scale-space primal sketch: a method for focus-of-attention," *International Journal of Computer Vision,* vol. 11, pp. 283-318, 1993.

[160] K. Mikolajczyk and C. Schmid, "Scale & affine invariant interest point detectors," *International Journal of Computer Vision,* vol. 60, pp. 63-86, 2004.

[161] G. F. Knoll, *Radiation Detection and Measurement.* Wiley, 2010.

[162] V. Vassiliades, P. Evans, L. Kaufman, J. W. Chan and D. Downes, "A human-centered approach for improving airport security screening," *CONTEMPORARY ERGONOMICS,* vol. 2008, pp. 127, 2008.

[163] J. W. Chan, J. P. O. Evans, Y. S. Yong and A. Monteith, "Wire transfer function analysis for castellated dual-energy x-ray detectors," *Appl. Opt.*, vol. 43, pp. 6413-6420, 2004.

[164] D. Lowe. (2005, July). SIFT demo program. [Online]. Available: http://people.cs.ubc.ca/~lowe/keypoints/.

Appendix A Images samples

Grayscale image samples at 0^0

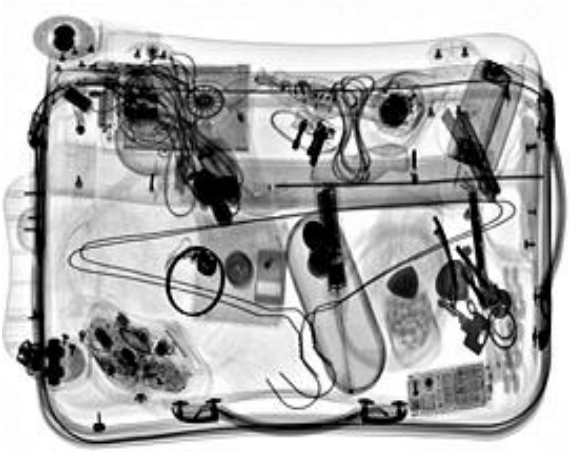

Bag 1

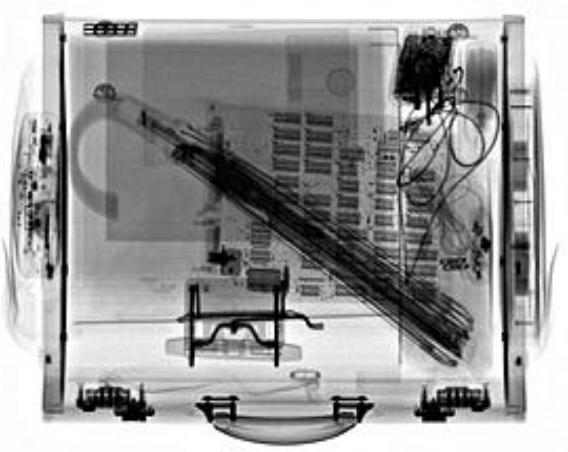

Bag 2

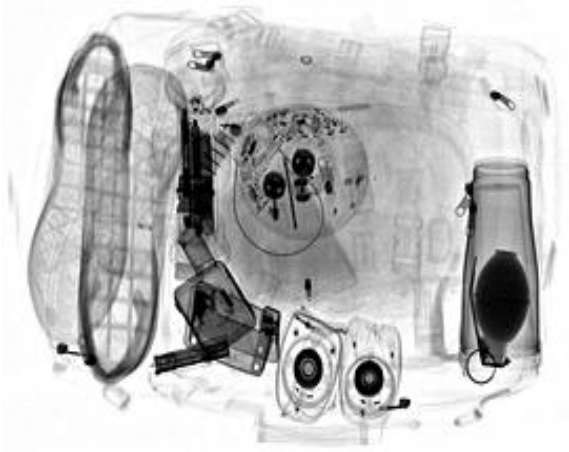

Bag 3

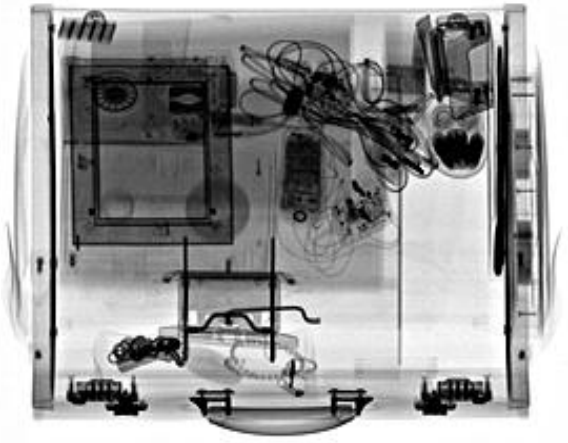

Bag 4

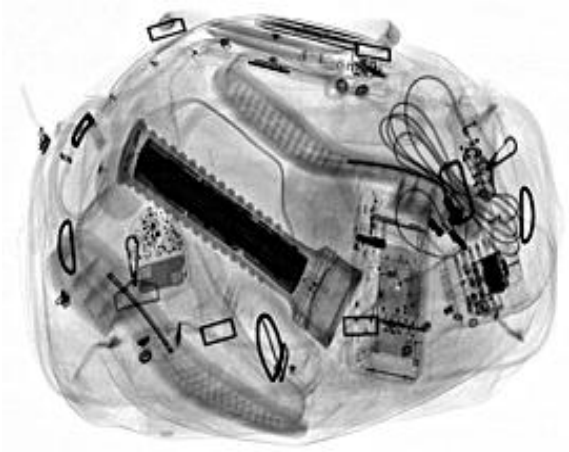

Bag 5

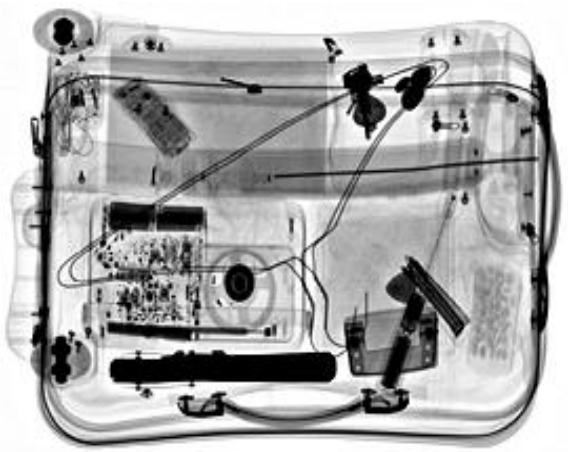

Bag 6

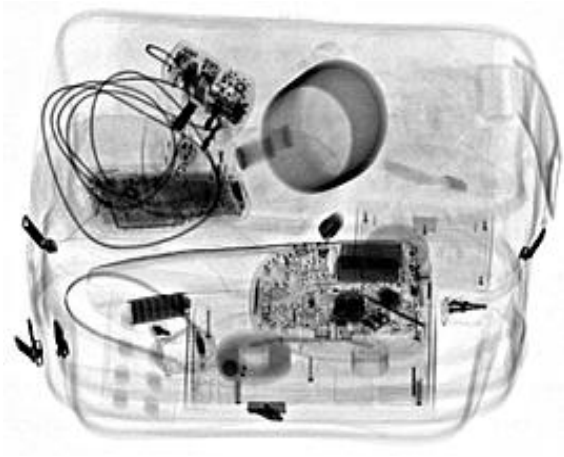

Bag 7

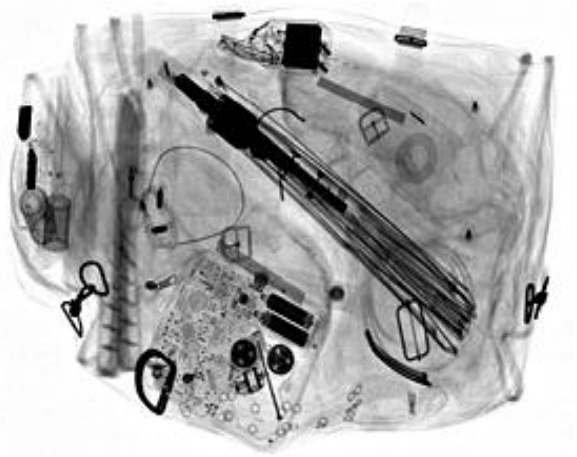

Bag 8

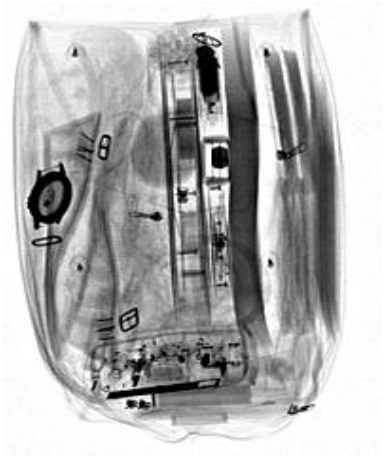

Bag 9

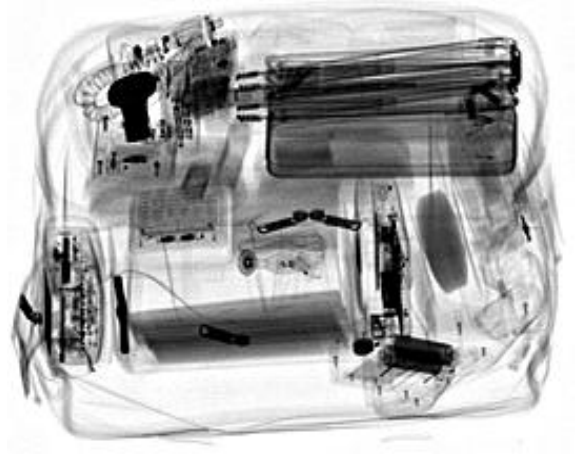

Bag 10

Bag 11

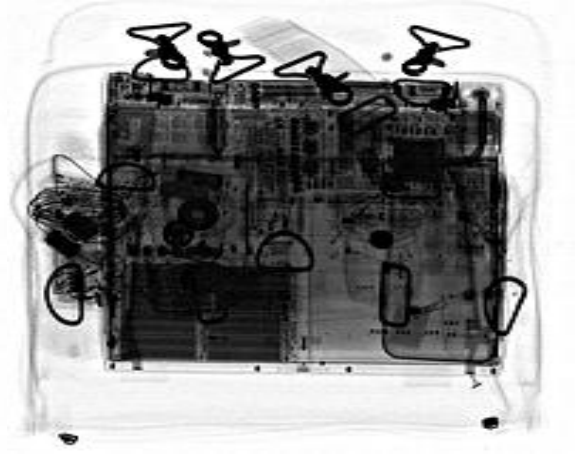

Bag 12

Bag 13

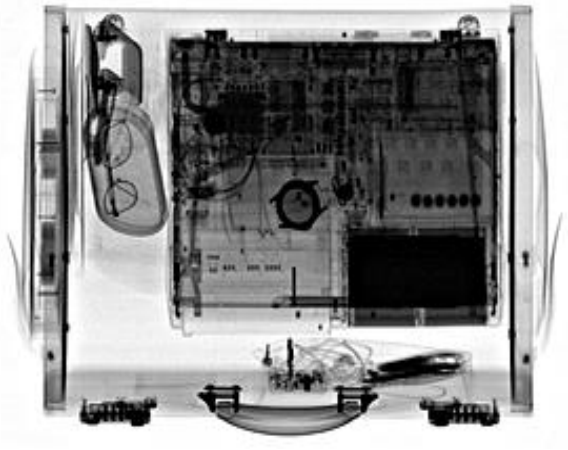

Bag 14

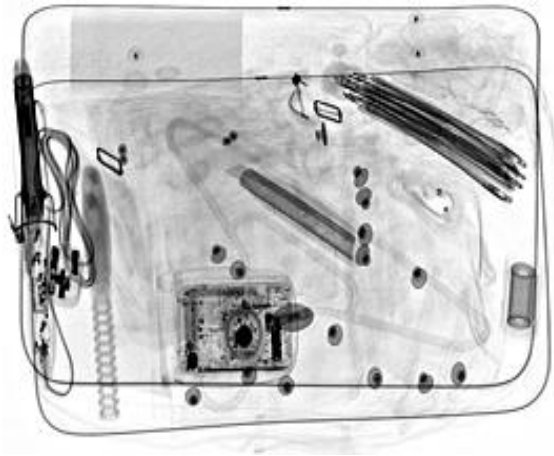

Bag 15

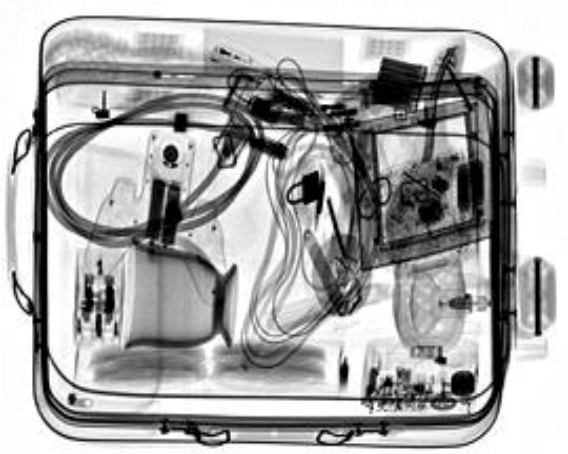

Bag 16

Bag 17

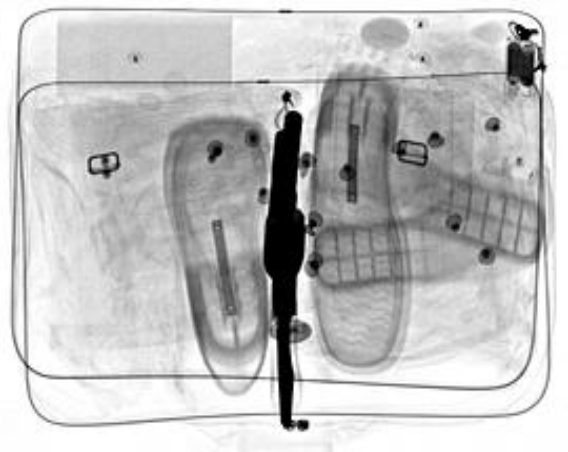

Bag 18

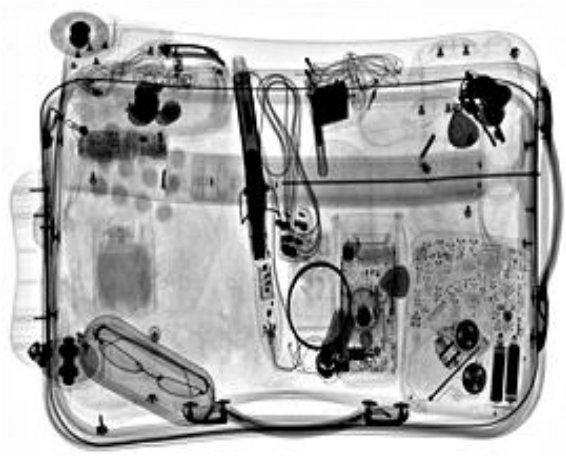

Bag 19

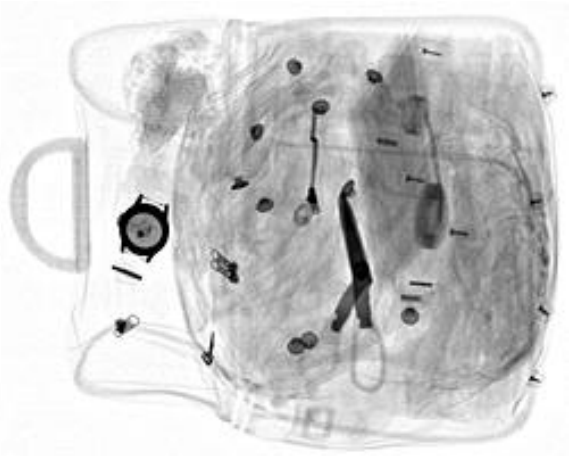

Bag 20

Bag 21

Bag 22

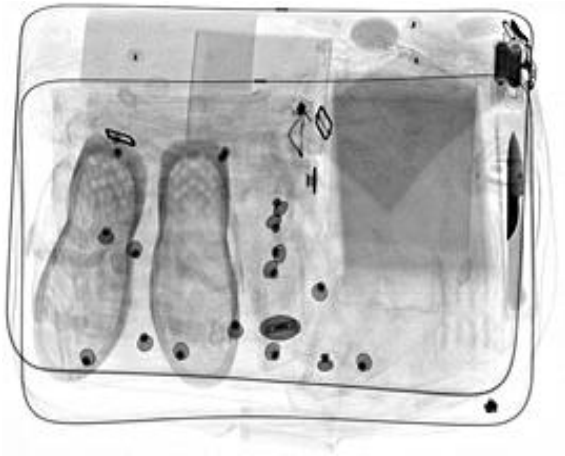

Bag 23

Bag 24

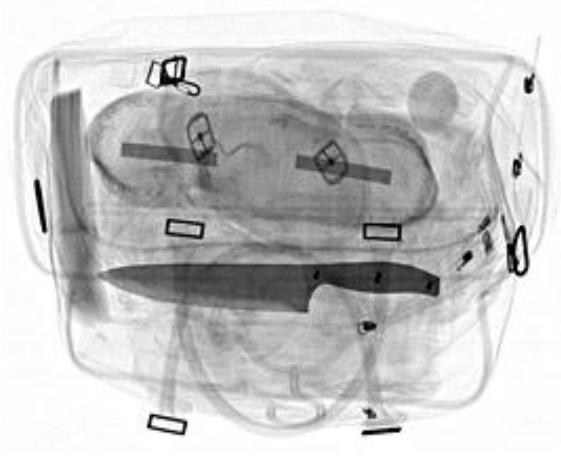

Bag 25

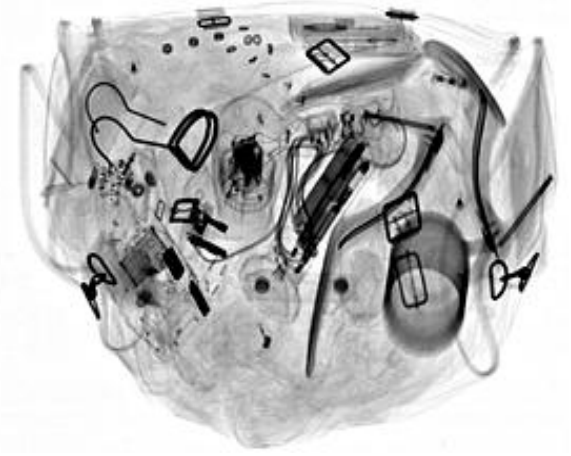

Bag 26

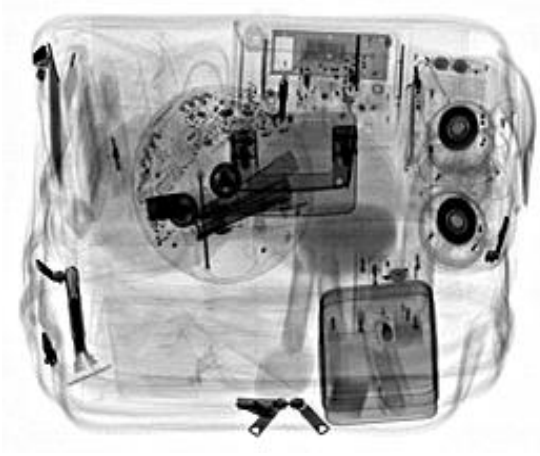

Bag 27

Bag 28

Bag 29

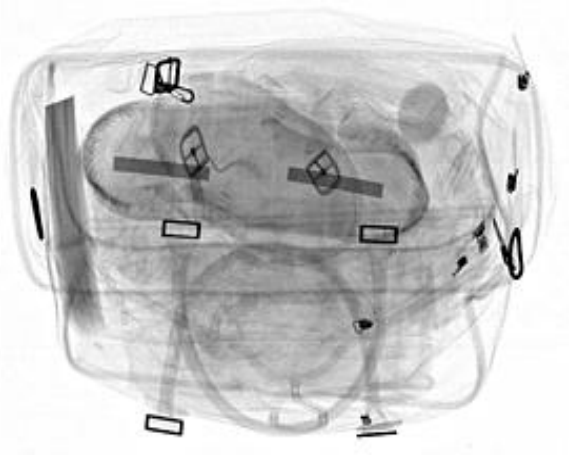

Bag30

Example of KDEX sequence of range (-3^0 to 3^0), "bag1" (greyscale)

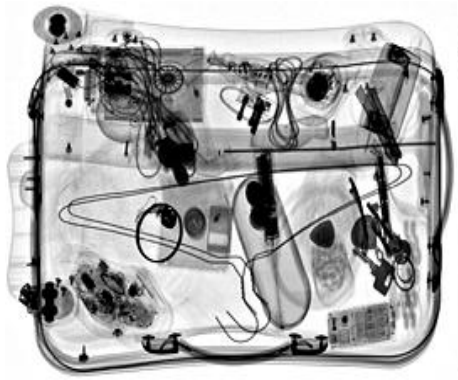

View at 0^0

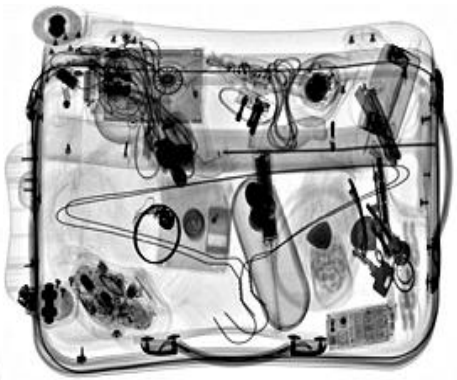

View at 1^0

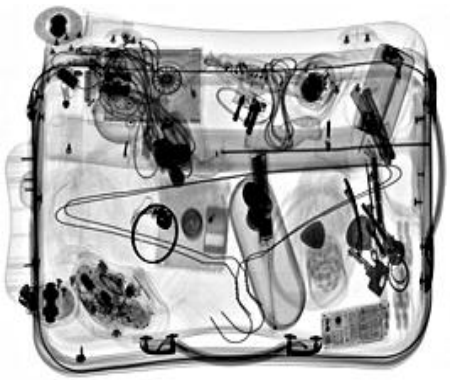

View at 2^0

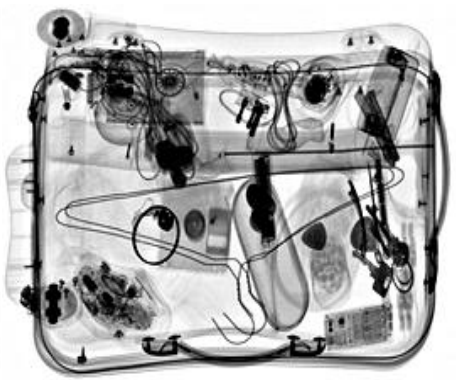

View at 3^0

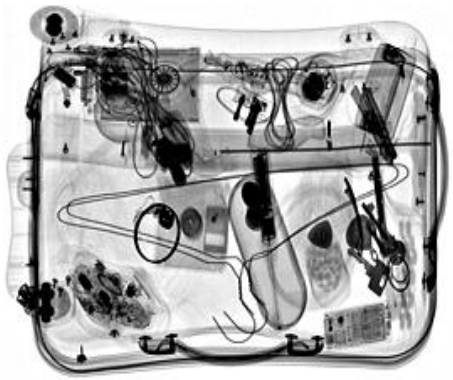

View at -1^0

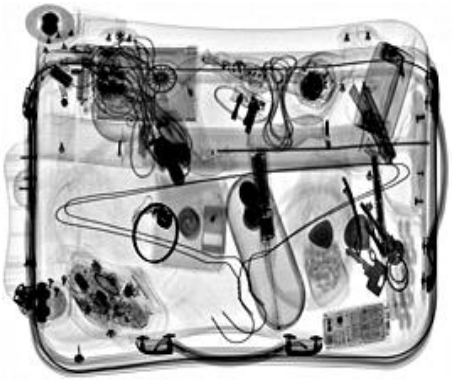

View at -2^0

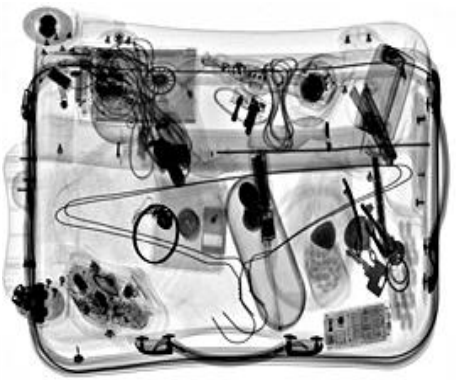

View at -3^0

Dual-energy image samples at 0^0

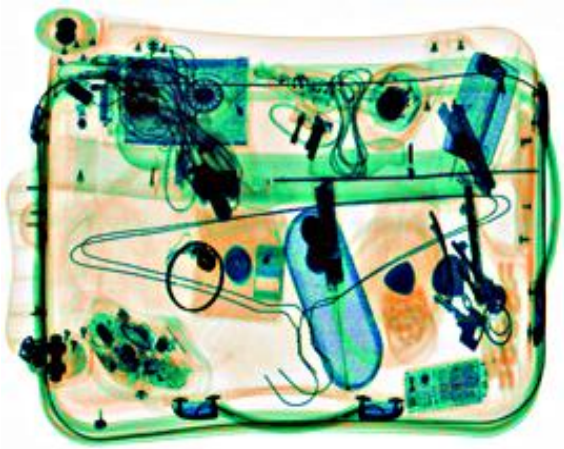

Bag 1

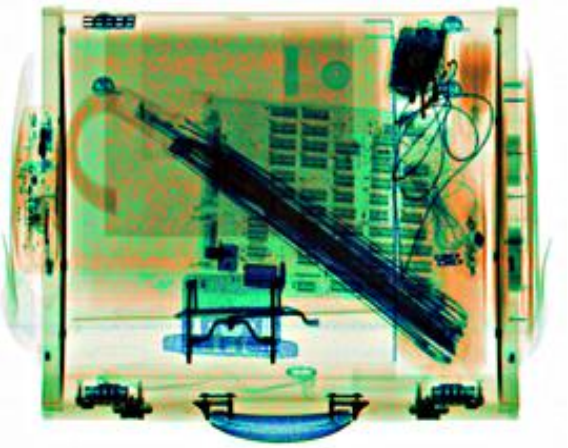

Bag 2

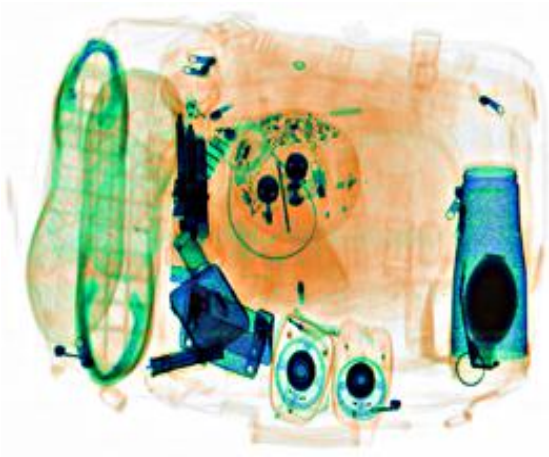

Bag 3

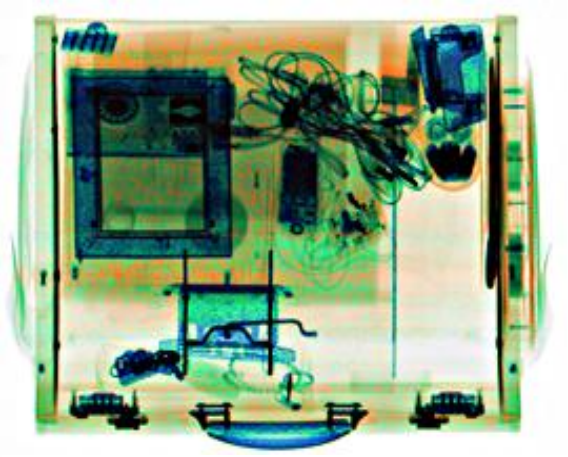

Bag 4

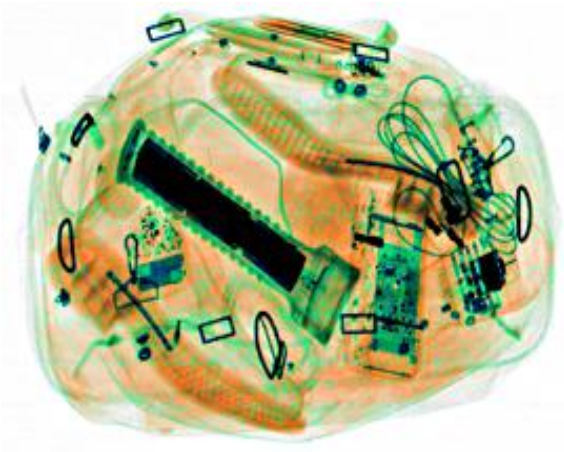

Bag 5

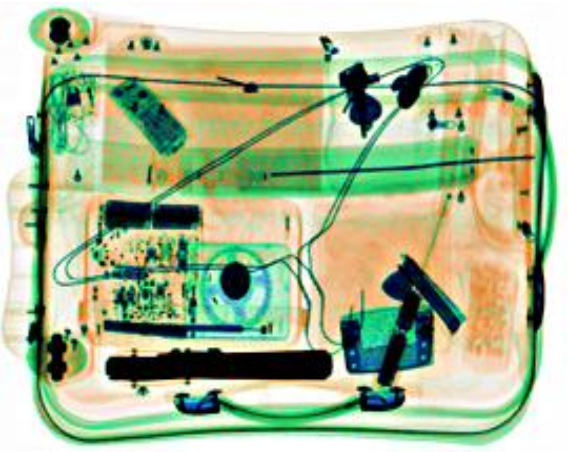

Bag 6

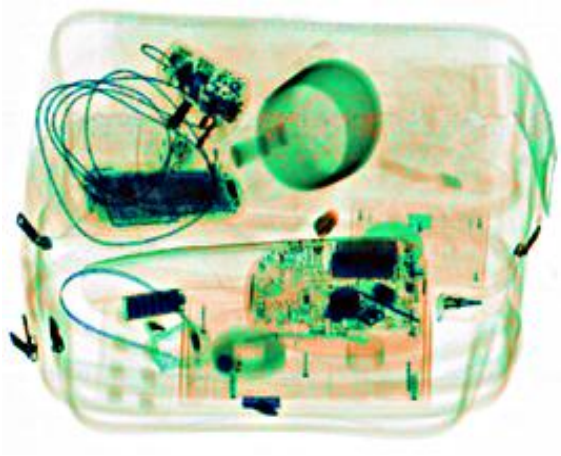

Bag 7

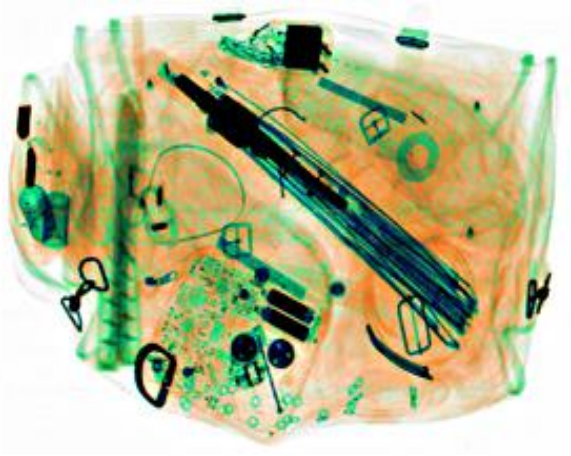

Bag 8

Bag 9

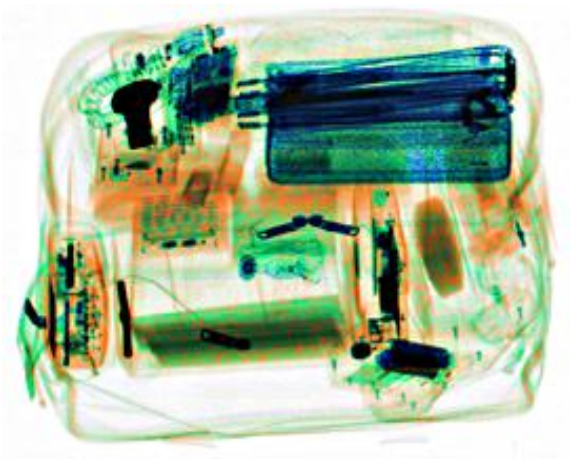

Bag 10

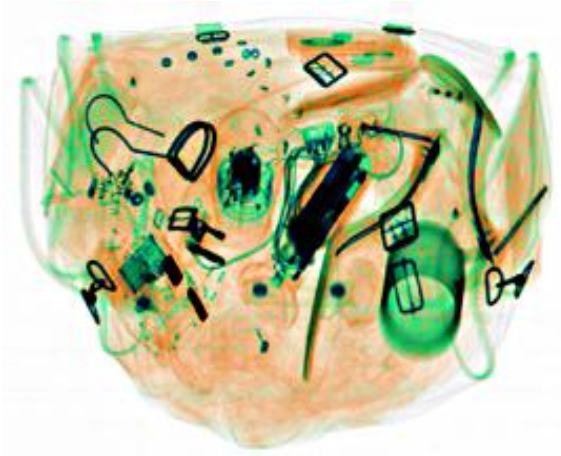

Bag 11

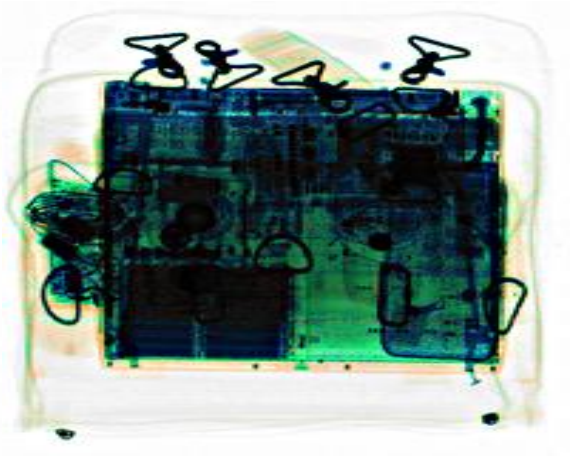

Bag 12

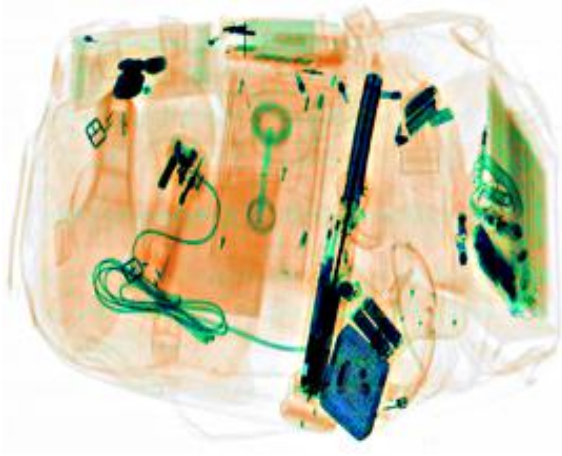

Bag 13

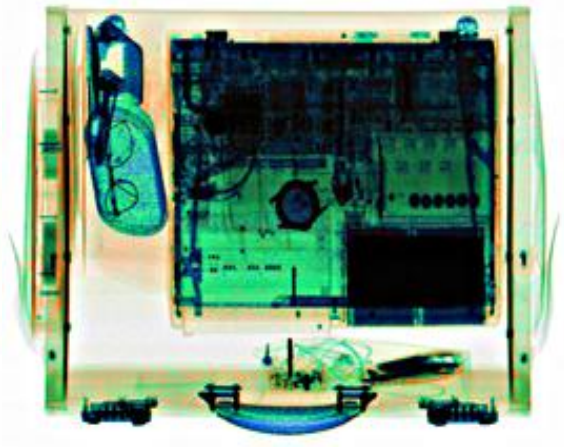

Bag 14

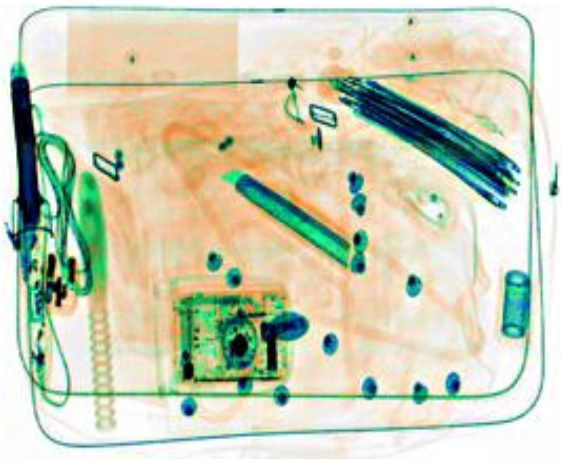

Bag 15

Bag 16

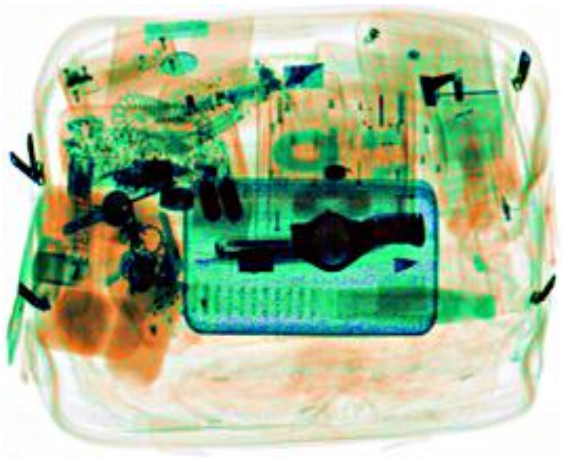

Bag 17

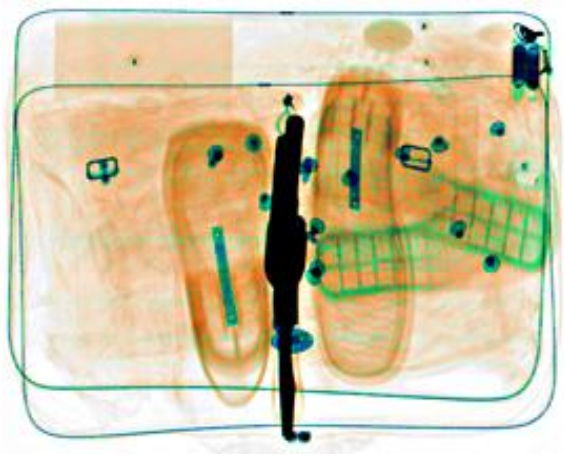

Bag 18

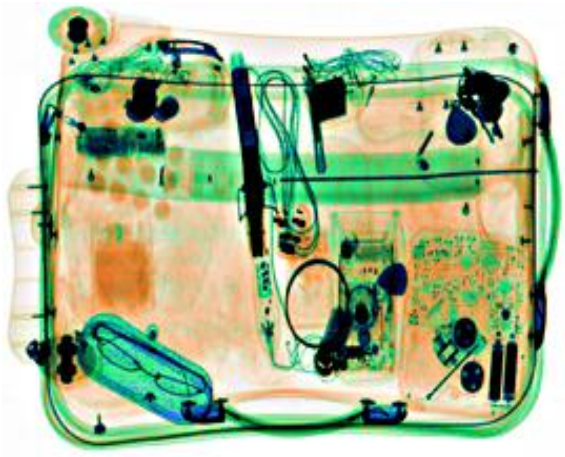

Bag 19

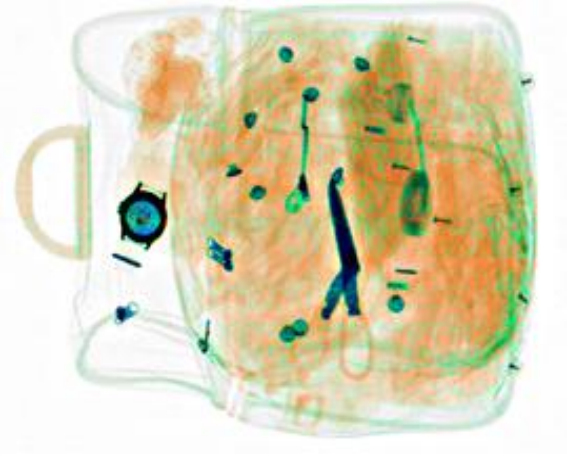

Bag 20

Bag 21

Bag 22

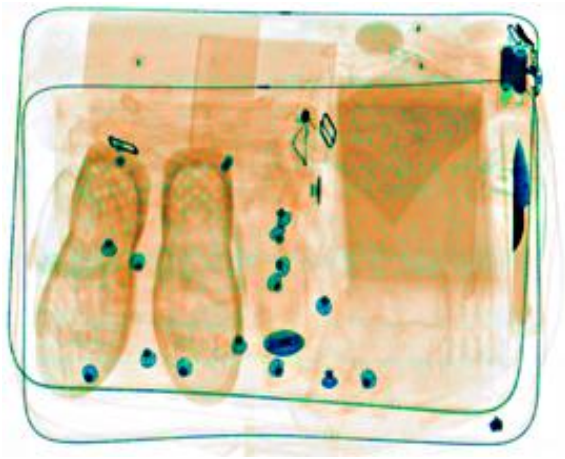

Bag 23

Bag 24

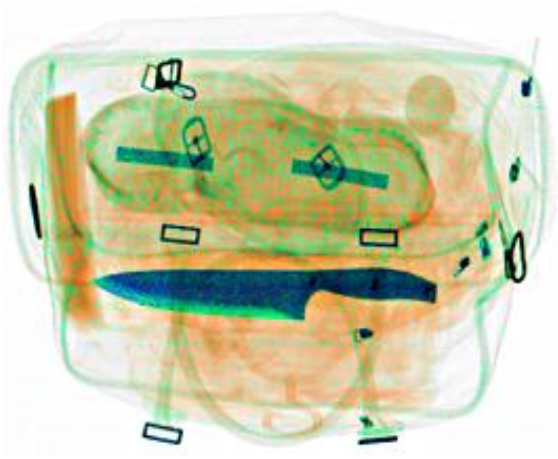

Bag 25

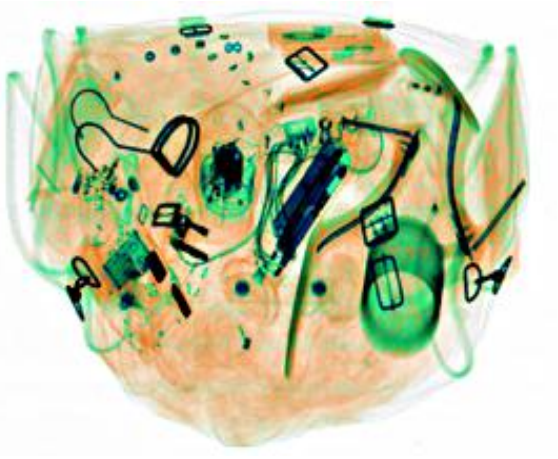

Bag 26

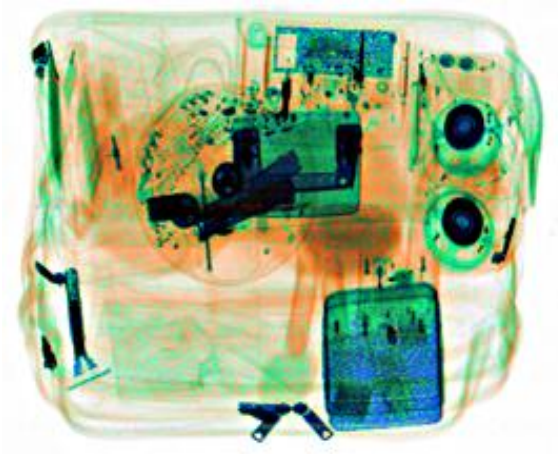

Bag 27

Bag 28

Bag 29

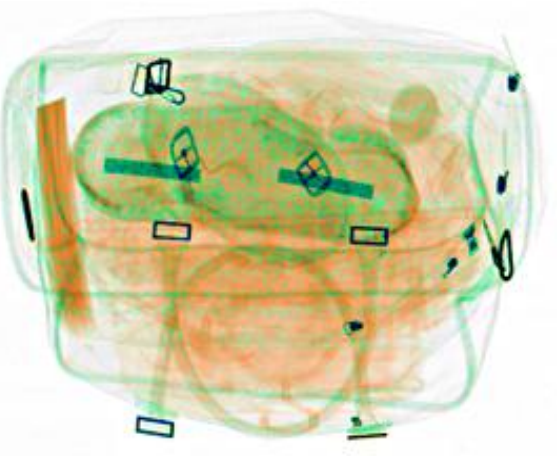

Bag 30

Example of KDEX sequence of range (-3^0 to 3^0), "bag1" (Dual-energy)

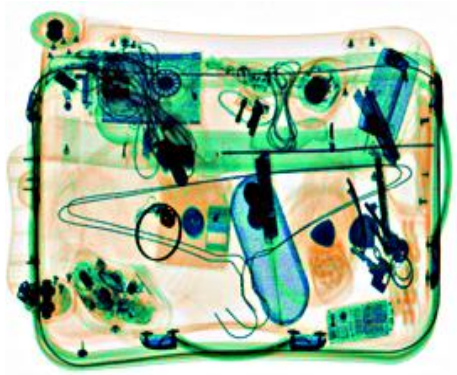

View at 0^0

View at 1^0

View at 2^0

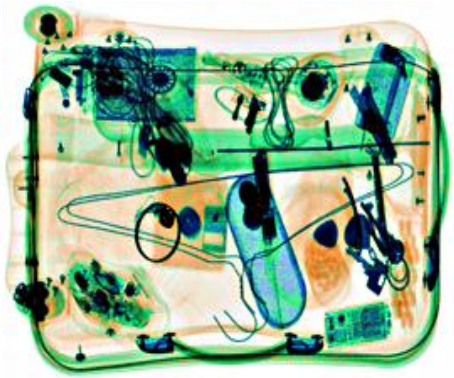

View at 3^0

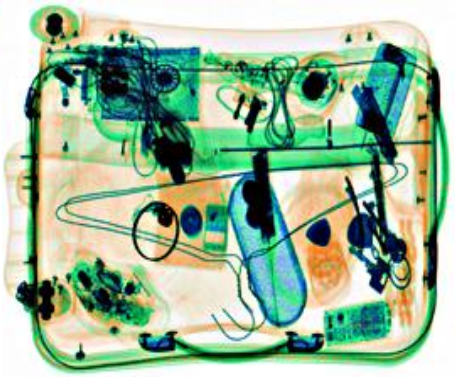

View at -1^0

View at -2^0

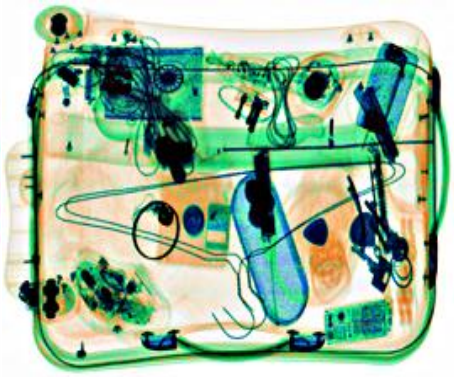

View at -3^0

Appendix B Tables for number of matches and number of pixel errors

The total number of matches and pixel errors in greyscale image sets.

Errors/Matches	No. of Pixel Errors					Average No. of Pixel Errors	No. of Matches
No. of Synthetic Views	1	2	3	4	5	###	###
Bags1							
2 Degree	93479	###	###	###	###	93479	1304
3 Degree	88514	100945	###	###	###	94730	1173
4 Degree	90201	111570	95802	###	###	102191	1022
5 Degree	94097	120911	116454	95964	###	106857	896
6 Degree	93325	120709	120274	111979	92003	107658	790
Bag 2							
2 Degree	72359	###	###	###	###	72359	832
3 Degree	62475	78108	###	###	###	70292	785
4 Degree	66763	87065	72464	###	###	75431	752
5 Degree	68515	91300	84377	71539	###	78933	579
6 Degree	69032	93463	88660	82724	78309	82438	503
Bag 3							
2 Degree	52002	###	###	###	###	52002	792
3 Degree	39403	55325	###	###	###	47364	631
4 Degree	43770	68284	48108	###	###	53387	526
5 Degree	45600	71390	58099	49943	###	56258	453
6 Degree	47559	74456	64474	63132	48284	59581	400
Bag 4							
2 Degree	71016	###	###	###	###	71016	951
3 Degree	62505	77448	###	###	###	69977	896
4 Degree	66715	85212	67994	###	###	73307	887
5 Degree	67204	86389	77285	65112	###	73998	741
6 Degree	68817	88717	83400	76459	70659	77610	694
Bag 5							
2 Degree	47257	###	###	###	###	47257	875
3 Degree	40362	55677	###	###	###	48020	778
4 Degree	39146	60907	43684	###	###	47912	684
5 Degree	40288	64644	55381	45459	###	51443	493
6 Degree	40902	67306	61187	56115	51001	55302	440
Bag 6							
2 Degree	90460	###	###	###	###	90460	1168
3 Degree	82725	96756	###	###	###	89741	1064
4 Degree	83092	103801	89014	###	###	91969	979
5 Degree	83842	107631	103469	84944	###	94972	863
6 Degree	83847	109055	109487	100636	83320	97269	788
Bag 7							
2 Degree	36839	###	###	###	###	36839	458
3 Degree	45091	44330	###	###	###	44711	391
4 Degree	47576	48345	44787	###	###	46903	342
5 Degree	49096	51590	52496	47252	###	50109	301
6 Degree	49886	53125	55113	54828	48319	52254	257
Bag 8							
2 Degree	62220	###	###	###	###	62220	586
3 Degree	67024	70011	###	###	###	68518	504
4 Degree	70454	80083	78476	###	###	76338	411
5 Degree	72018	84338	86007	76980	###	79836	363
6 Degree	72714	85671	90883	87750	77625	82929	322
Bag 9							
2 Degree	39136	###	###	###	###	39136	301
3 Degree	33647	43684	###	###	###	38666	227
4 Degree	35014	50400	38242	###	###	41219	208
5 Degree	36372	53892	51345	42908	###	46129	156

6 Degree	36436	54992	55307	52823	45051	48922	128
Bag 10							
2 Degree	42150	###	###	###	###	42150	599
3 Degree	44035	51272	###	###	###	47654	498
4 Degree	45690	58484	50170	###	###	51448	400
5 Degree	46907	61058	57748	45473	###	52797	334
6 Degree	47367	63125	62509	59334	53555	57178	290
Bag 11							
2 Degree	60573	###	###	###	###	60573	607
3 Degree	65909	65040	###	###	###	65475	524
4 Degree	70968	78587	74407	###	###	74654	434
5 Degree	73429	84262	88597	84361	###	82662	364
6 Degree	74602	87607	94108	93040	75597	84991	291
Bag 12							
2 Degree	76414	###	###	###	###	76414	504
3 Degree	75131	82284	###	###	###	78708	393
4 Degree	79788	91189	79616	###	###	83531	344
5 Degree	79847	95751	89764	92702	###	89516	286
6 Degree	81561	98144	95579	101992	86185	92692	238
Bag 13							
2 Degree	60856	###	###	###	###	60856	675
3 Degree	55801	65380	###	###	###	60591	465
4 Degree	62060	78665	59481	###	###	66735	371
5 Degree	61050	86198	77489	86703	###	77860	329
6 Degree	62752	89884	85515	98662	68178	80998	271
Bag 14							
2 Degree	83879	###	###	###	###	83879	911
3 Degree	74328	89233	###	###	###	81781	845
4 Degree	77483	97379	77634	###	###	84165	778
5 Degree	90009	109573	104156	102626	###	101591	662
6 Degree	89897	110940	106188	105505	88901	100286	621
Bag 15							
2 Degree	47991	###	###	###	###	47991	613
3 Degree	44691	54889	###	###	###	49790	559
4 Degree	47617	61776	51656	###	###	53683	555
5 Degree	64604	70356	66766	60266	###	65498	492
6 Degree	64932	73955	68857	67321	55849	66183	446
Bag 16							
2 Degree	90201	###	###	###	###	90201	1253
3 Degree	85247	100522	###	###	###	92885	1105
4 Degree	89888	116309	91074	###	###	99090	1009
5 Degree	92092	123422	112874	95283	###	105918	876
6 Degree	93997	128398	121848	115677	93952	110774	819
Bag 17							
2 Degree	49284	###	###	###	###	49284	551
3 Degree	41353	49956	###	###	###	45655	493
4 Degree	42588	57484	43807	###	###	47960	424
5 Degree	43154	60099	54798	44404	###	50614	352
6 Degree	43476	62041	62041	55719	43706	53397	275
Bag 18							
2 Degree	51260	###	###	###	###	41260	306
3 Degree	38353	47923	###	###	###	43138	266
4 Degree	41000	49772	39998	###	###	43590	237
5 Degree	42333	53472	48057	39869	###	45933	210
6 Degree	43076	54976	50601	43735	36338	45745	197
Bag 19							
2 Degree	88600	###	###	###	###	88600	1216
3 Degree	82917	91768	###	###	###	87343	1114
4 Degree	91319	109335	95330	###	###	98661	1051
5 Degree	94292	116112	113504	94595	###	100602	932
6 Degree	92677	114877	113610	105648	100887	105540	849
Bag 20							
2 Degree	34697	###	###	###	###	34697	197
3 Degree	39164	38258	###	###	###	38711	176

4 Degree	42523	44563	42248	###	###	43111	151
5 Degree	44861	51654	52480	47690	###	49171	124
6 Degree	45948	52136	54430	53371	45286	50234	115
Bag 21							
2 Degree	92204	###	###	###	###	92204	1166
3 Degree	92355	94723	###	###	###	93539	1080
4 Degree	106591	116934	66026	###	###	96517	906
5 Degree	106766	119683	93164	88442	###	102014	795
6 Degree	106894	121760	106518	90601	87246	102604	673
Bag 22							
2 Degree	49717	###	###	###	###	49717	499
3 Degree	44813	52558	###	###	###	48686	345
4 Degree	50011	63254	51839	###	###	55035	234
5 Degree	52390	67344	61057	57902	###	59673	200
6 Degree	54094	71699	69027	72734	58927	65296	145
Bag 23							
2 Degree	43447	###	###	###	###	43447	284
3 Degree	34746	47167	###	###	###	40957	247
4 Degree	35650	47096	36651	###	###	39799	244
5 Degree	37755	51022	43635	36377	###	42197	210
6 Degree	38913	53561	47183	41574	33336	42913	186
Bag 24							
2 Degree	48104	###	###	###	###	48104	394
3 Degree	47100	44899	###	###	###	46000	323
4 Degree	47751	49734	47129	###	###	48205	274
5 Degree	48717	51769	52344	48050	###	50220	235
6 Degree	49806	53242	55455	53949	49078	52306	207
Bag 25							
2 Degree	31331	###	###	###	###	31331	278
3 Degree	26034	38527	###	###	###	32281	263
4 Degree	26559	42460	29563	###	###	32861	234
5 Degree	26902	44188	37695	30329	###	34779	183
6 Degree	27703	45895	41569	37431	39791	38478	165
Bag 26							
2 Degree	64499	###	###	###	###	64499	665
3 Degree	67382	72212	###	###	###	69797	542
4 Degree	70093	80134	72342	###	###	74190	462
5 Degree	71429	83838	83437	73009	###	77928	430
6 Degree	73224	88008	90889	88681	77988	83758	355
Bag 27							
2 Degree	46835	###	###	###	###	46835	438
3 Degree	50776	49925	###	###	###	50351	373
4 Degree	54865	59103	55140	###	###	56369	342
5 Degree	56205	60867	61086	53845	###	58001	269
6 Degree	57585	63554	65752	64459	57264	61723	237
Bag 28							
2 Degree	64629	###	###	###	###	64629	840
3 Degree	56973	71622	###	###	###	64298	773
4 Degree	59042	82806	63076	###	###	68308	680
5 Degree	60562	85454	76727	60776	###	70880	531
6 Degree	61260	89008	85089	78261	72098	77143	493
Bag 29							
2 Degree	73064	###	###	###	###	73064	790
3 Degree	76290	79837	###	###	###	78064	734
4 Degree	72886	90747	70653	###	###	78095	550
5 Degree	72148	89595	79392	65333	###	76617	550
6 Degree	74049	93083	87704	83687	67334	81171	483
Bag 30							
2 Degree	40490	###	###	###	###	40490	247
3 Degree	42371	45245	###	###	###	43808	206
4 Degree	45041	50228	47310	###	###	47526	190
5 Degree	45927	51628	52376	48173	###	49526	175
6 Degree	47237	54621	57334	55412	49639	52849	154

The total number of matches using direct matching on dual-energy data.

	No. of Correct Matches							No. of Incorrect Matches					
Degree of separation	1 Degree	2 Degree	3 Degree	4 Degree	5 Degree	6 Degree		1 Degree	2 Degree	3 Degree	4 Degree	5 Degree	6 Degree
Bag 1	1354	1144	960	872	778	679		283	327	383	404	406	406
Bag 2	936	772	626	557	495	450		214	233	290	318	299	342
Bag 3	616	512	445	383	340	312		124	169	169	190	187	190
Bag 4	858	783	720	654	655	571		212	225	234	261	264	272
Bag 5	840	709	609	520	445	380		149	190	208	236	246	245
Bag 6	1095	966	874	781	730	667		246	260	300	275	304	322
Bag 7	512	423	366	287	271	259		93	207	140	139	138	165
Bag 8	686	514	433	330	302	263		167	235	289	326	331	334
Bag 9	356	256	204	149	126	112		83	118	128	142	131	146
Bag 10	529	421	329	301	263	224		105	132	144	142	149	155
Bag 11	707	610	509	448	375	358		168	158	200	227	249	243
Bag 12	518	456	382	347	334	282		108	106	135	134	155	185
Bag 13	525	470	408	344	339	323		138	155	150	181	167	185
Bag 14	669	577	508	469	447	402		187	220	230	202	231	225
Bag 15	614	579	565	482	404	433		143	170	168	198	183	189
Bag 16	1190	967	873	767	705	649		334	378	429	401	443	449
Bag 17	570	487	383	318	269	229		116	132	146	148	179	171
Bag 18	277	249	209	176	172	149		104	82	113	108	121	124
Bag 19	1176	1051	957	849	766	694		235	280	259	286	322	312
Bag 20	182	154	128	108	88	87		58	74	97	91	109	104
Bag 21	1239	998	878	755	675	617		326	421	451	443	446	445
Bag 22	575	351	279	210	173	151		192	267	281	265	299	291
Bag 23	218	217	180	184	164	152		90	87	103	85	91	112
Bag 24	492	393	323	285	261	232		74	123	131	132	136	132
Bag 25	222	163	141	141	121	118		88	157	145	145	157	152
Bag 26	715	592	514	425	398	351		125	174	184	220	232	243
Bag 27	500	358	333	252	241	215		87	133	150	155	158	151
Bag 28	812	677	549	441	401	374		164	201	222	279	269	281
Bag 29	765	620	528	476	413	356		303	316	358	392	390	373
Bag 30	233	156	141	139	121	118		47	102	105	112	116	108

The total number of matches using materials segmentation information on dual-energy data.

Matches	No. of Matches									
	Correct				Incorrect				Total Correct	Total Incorrect
Material Class	O	X	M	G	O	X	M	G		
Bag 1										
1 Degree	194	282	337	113	190	299	203	70	926	762
2 Degree	181	260	279	104	177	303	197	79	824	756
3 Degree	139	242	231	75	216	273	218	102	687	809
4 Degree	126	206	217	65	207	299	214	96	614	816
5 Degree	112	185	169	57	223	284	223	100	523	830
6 Degree	109	180	174	49	228	294	244	93	512	859
Bag 2										
1 Degree	123	161	176	96	168	239	169	66	556	642
2 Degree	91	120	136	64	163	249	148	84	411	644
3 Degree	88	98	125	62	164	234	172	69	373	639
4 Degree	73	77	108	57	171	255	166	75	315	667
5 Degree	63	98	99	50	164	226	152	83	310	625
6 Degree	67	88	72	60	203	248	170	86	287	707
Bag 3										
1 Degree	121	124	148	58	101	158	110	36	451	405
2 Degree	124	113	141	62	102	151	106	42	440	401
3 Degree	121	111	113	44	105	138	122	48	389	413
4 Degree	84	89	111	52	93	164	125	50	336	432
5 Degree	81	86	95	48	125	146	120	42	310	433
6 Degree	68	59	88	31	109	157	121	39	246	426
Bag 4										
1 Degree	137	171	252	172	169	248	160	78	732	655
2 Degree	105	126	219	155	189	238	183	77	605	687
3 Degree	97	122	206	138	187	238	181	71	563	677
4 Degree	96	130	206	126	163	237	158	82	558	640
5 Degree	88	115	204	119	183	229	145	73	526	630
6 Degree	84	101	174	119	189	251	196	72	478	708
Bag 5										
1 Degree	185	187	89	52	135	209	107	30	513	481
2 Degree	174	153	78	44	148	190	111	26	449	475
3 Degree	138	126	65	29	163	210	113	41	358	527
4 Degree	127	113	54	36	169	196	123	40	330	528
5 Degree	121	97	43	33	175	212	123	35	294	545
6 Degree	118	94	53	26	144	213	103	38	291	498
Bag 6										
1 Degree	203	223	203	99	183	311	136	46	728	676
2 Degree	190	219	211	88	213	271	179	53	708	716
3 Degree	175	182	185	71	196	304	143	62	613	705
4 Degree	153	181	182	62	184	275	186	67	578	712
5 Degree	149	189	152	61	197	247	188	60	551	692
6 Degree	145	148	146	64	206	258	179	63	503	706
Bag 7										
1 Degree	65	133	82	33	77	151	93	30	313	351
2 Degree	69	144	78	28	86	115	71	23	319	295
3 Degree	52	117	74	28	82	114	56	26	271	278
4 Degree	47	115	64	27	88	141	67	26	253	322
5 Degree	47	103	51	25	90	137	66	21	226	314
6 Degree	40	85	59	24	87	144	67	23	208	321
Bag 8										
1 Degree	181	197	122	66	182	242	79	36	566	539
2 Degree	148	148	66	63	197	239	109	37	425	582
3 Degree	137	134	59	54	178	246	133	41	384	598
4 Degree	104	105	44	42	175	261	139	53	295	628

5 Degree	98	94	42	49	211	230	136	52	283	629
6 Degree	76	94	38	42	187	252	129	54	250	622
Bag 9										
1 Degree	111	88	26	31	132	122	23	24	256	301
2 Degree	96	62	15	26	140	123	39	22	199	324
3 Degree	67	56	8	17	162	136	37	26	148	361
4 Degree	44	44	10	18	161	126	30	26	116	343
5 Degree	42	34	21	16	173	152	19	21	113	365
6 Degree	36	25	12	15	167	127	25	29	88	348
Bag 10										
1 Degree	89	92	133	62	111	105	88	27	376	331
2 Degree	72	78	142	43	98	140	74	39	335	351
3 Degree	58	74	103	31	106	109	85	23	266	323
4 Degree	43	62	98	29	103	120	85	45	232	353
5 Degree	40	51	111	32	111	112	85	44	234	352
6 Degree	37	47	103	24	104	120	75	35	211	334
Bag 11										
1 Degree	218	175	94	56	168	198	83	31	543	480
2 Degree	178	152	62	51	175	198	99	38	443	510
3 Degree	142	131	50	40	176	181	96	54	363	507
4 Degree	137	111	53	39	193	206	103	42	340	544
5 Degree	131	100	41	43	159	199	107	31	315	496
6 Degree	117	100	46	31	186	195	94	43	294	518
Bag 12										
1 Degree	36	157	326	385	47	124	170	165	904	506
2 Degree	33	141	292	284	44	141	168	183	750	536
3 Degree	36	107	274	265	34	140	167	185	682	526
4 Degree	32	84	260	205	37	140	164	186	581	527
5 Degree	30	64	249	207	49	160	178	171	550	558
6 Degree	28	53	215	168	41	164	199	181	464	585
Bag 13										
1 Degree	178	132	105	33	124	130	87	38	448	379
2 Degree	140	128	97	28	116	128	91	41	393	376
3 Degree	127	101	79	21	132	109	83	43	328	367
4 Degree	120	103	50	16	119	124	96	29	289	368
5 Degree	105	92	52	9	154	126	97	49	258	426
6 Degree	99	75	48	16	125	134	89	45	238	393
bag 14										
1 Degree	62	169	299	343	107	221	199	142	873	669
2 Degree	56	160	282	325	111	243	177	128	823	659
3 Degree	44	140	246	255	114	251	194	149	685	708
4 Degree	47	139	235	258	115	227	199	173	679	714
5 Degree	38	138	202	241	117	243	211	154	619	725
6 Degree	33	116	188	243	128	242	207	155	580	732
Bag 15										
1 Degree	119	137	120	21	73	128	97	5	397	303
2 Degree	105	119	112	21	73	150	99	10	357	332
3 Degree	100	119	91	21	86	150	119	13	331	368
4 Degree	97	104	82	13	91	119	107	10	296	327
5 Degree	87	85	73	10	71	147	111	18	255	347
6 Degree	86	87	78	10	77	147	108	9	261	341
Bag 16										
1 Degree	136	256	355	117	133	253	251	70	864	707
2 Degree	106	234	283	82	169	300	254	68	705	791
3 Degree	112	207	240	72	155	301	255	48	631	759
4 Degree	106	211	222	68	158	254	258	66	607	736
5 Degree	93	205	213	60	139	295	256	88	571	778
6 Degree	80	182	176	55	167	271	288	85	493	811
Bag 17										
1 Degree	97	125	49	90	94	128	64	21	361	307
2 Degree	83	139	59	81	75	143	59	29	362	306

3 Degree	82	134	35	67	99	131	72	33	318	335
4 Degree	56	102	30	55	108	141	76	31	243	356
5 Degree	60	86	22	46	81	155	78	47	214	361
6 Degree	62	80	25	45	104	128	64	41	212	337
Bag 18										
1 Degree	105	54	46	20	127	177	46	8	225	358
2 Degree	94	54	29	14	110	162	57	15	191	344
3 Degree	85	33	33	12	120	127	56	9	163	312
4 Degree	68	33	21	14	116	167	49	11	136	343
5 Degree	71	28	27	13	106	131	49	9	139	295
6 Degree	60	39	25	9	122	131	60	11	133	324
Bag 19										
1 Degree	219	259	230	135	199	293	160	47	843	699
2 Degree	196	230	215	118	216	247	150	60	759	673
3 Degree	160	223	207	102	192	273	173	64	692	702
4 Degree	131	190	176	96	190	301	178	78	593	747
5 Degree	129	180	152	84	181	304	187	85	545	757
6 Degree	131	189	147	68	180	281	198	73	535	732
bag20										
1 Degree	52	35	27	4	81	88	26	6	118	201
2 Degree	44	33	21	5	91	90	24	9	103	214
3 Degree	41	26	17	4	75	78	41	7	88	201
4 Degree	32	22	14	3	83	83	29	10	71	205
5 Degree	33	28	19	4	79	93	39	6	84	217
6 Degree	27	22	19	3	85	90	46	5	71	226
bag21										
1 Degree	110	251	338	119	182	322	261	82	818	847
2 Degree	84	206	280	114	183	313	237	80	684	813
3 Degree	92	216	243	87	185	328	271	115	638	899
4 Degree	78	187	219	76	183	305	282	106	560	876
5 Degree	62	165	208	74	184	309	277	100	509	870
6 Degree	64	143	187	62	193	301	241	101	456	836
bag22										
1 Degree	146	96	47	60	173	132	86	72	349	463
2 Degree	99	80	32	34	188	170	88	93	245	539
3 Degree	76	58	34	17	167	159	91	96	185	513
4 Degree	56	63	26	21	192	146	108	90	166	536
5 Degree	43	54	19	18	178	148	109	79	134	514
6 Degree	52	36	24	17	193	139	83	89	129	504
bag23										
1 Degree	78	34	55	3	103	96	55	3	170	257
2 Degree	83	27	50	5	100	107	52	3	165	262
3 Degree	96	26	43	4	80	118	52	4	169	254
4 Degree	75	27	37	3	98	94	55	1	142	248
5 Degree	69	27	44	2	103	100	51	5	142	259
6 Degree	69	19	45	3	105	102	55	6	136	268
bag24										
1 Degree	90	184	108	93	87	142	68	38	475	335
2 Degree	70	113	90	69	94	130	82	56	342	362
3 Degree	84	101	68	60	90	150	71	50	313	361
4 Degree	66	71	68	46	89	140	92	68	251	389
5 Degree	68	81	68	53	84	155	91	68	270	398
6 Degree	64	78	51	39	90	130	85	62	232	367
bag25										
1 Degree	44	36	34	4	116	121	58	2	118	297
2 Degree	44	30	32	0	110	110	68	0	106	288
3 Degree	50	26	20	0	110	115	83	0	96	308
4 Degree	41	24	18	0	99	124	77	0	83	300
5 Degree	44	22	17	0	113	125	72	0	83	310
6 Degree	34	24	16	0	108	117	74	0	74	299
bag26										

1 Degree	181	182	119	68	183	184	101	33	550	501
2 Degree	168	135	96	53	161	200	87	38	452	486
3 Degree	149	123	78	39	179	206	96	44	389	525
4 Degree	128	108	83	48	184	209	109	27	367	529
5 Degree	114	114	72	42	182	191	111	41	342	525
6 Degree	126	83	79	39	185	184	97	51	327	517
Bag 27										
1 Degree	98	116	80	63	96	174	81	21	357	372
2 Degree	79	116	59	37	88	157	100	39	291	384
3 Degree	70	103	50	29	101	154	94	40	252	389
4 Degree	75	88	43	22	108	155	98	34	228	395
5 Degree	52	92	39	23	88	137	92	47	206	364
6 Degree	62	94	23	14	92	143	102	38	193	375
Bag 28										
1 Degree	190	188	145	74	161	200	119	35	597	515
2 Degree	190	167	122	47	141	189	130	65	526	525
3 Degree	137	128	70	34	181	219	168	66	369	634
4 Degree	122	94	75	35	186	197	173	77	326	633
5 Degree	119	101	59	19	186	198	154	72	298	610
6 Degree	114	93	48	22	194	230	138	54	277	616
Bag 29										
1 Degree	138	182	117	23	167	296	168	46	460	677
2 Degree	119	175	103	22	153	280	171	56	419	660
3 Degree	94	142	115	16	166	288	163	55	367	672
4 Degree	77	142	103	18	173	296	176	53	340	698
5 Degree	86	117	98	13	163	290	180	60	314	693
6 Degree	88	105	90	14	173	277	185	62	297	697
Bag 30										
1 Degree	57	37	28	0	78	111	36	0	122	225
2 Degree	41	31	19	0	91	104	51	0	91	246
3 Degree	34	41	21	0	98	104	55	0	96	257
4 Degree	31	45	17	0	105	107	52	0	93	264
5 Degree	39	41	21	0	90	116	39	0	101	245
6 Degree	24	25	12	0	112	110	49	0	61	271

The total number of pixel errors according to material based morphing image synthesis algorithm.

Error I and II	No. of Pixel Errors (ERR-I)							No. of Pixel Errors (ERR-II)					
No. of Synthetic Views	1	2	3	4	5	Average of ERR-I		1	2	3	4	5	Average of ERR-II
Bag 1													
2 Degree	52606	###	###	###	###	52606		90279	###	###	###	###	90279
3 Degree	76240	80718	###	###	###	78479		96333	96283	###	###	###	96308
4 Degree	77068	93132	82450	###	###	84217		102620	104190	101035	###	###	102615
5 Degree	80536	103746	104013	83866	###	93040		107375	109185	108220	104533	###	107328
6 Degree	78898	104008	110769	104356	72835	94173		108459	110699	110629	108456	103614	108371
Bag 2													
2 Degree	48028	###	###	###	###	48028		88576	###	###	###	###	88576
3 Degree	58051	59871	###	###	###	58961		93849	92576	###	###	###	93213
4 Degree	59412	68512	59856	###	###	62593		95436	95461	94577	###	###	95158
5 Degree	60344	75784	75401	61567	###	68274		96595	99224	98059	96300	###	97545
6 Degree	61739	80329	83861	79380	62239	73510		98423	100712	100459	100479	96856	99386
Bag 3													
2 Degree	30323	###	###	###	###	30323		62966	###	###	###	###	62966
3 Degree	37452	38425	###	###	###	37939		67194	66637	###	###	###	66916
4 Degree	40970	51648	39048	###	###	43889		68496	69495	69201	###	###	69064
5 Degree	47562	61056	59952	41582	###	52538		72011	72904	73232	72045	###	72548
6 Degree	49856	67700	71426	65911	47918	60562		74517	75946	76467	75884	75867	75736
Bag 4													
2 Degree	43653	###	###	###	###	43653		88154	###	###	###	###	88154
3 Degree	54209	55392	###	###	###	54801		91272	91598	###	###	###	91435
4 Degree	57531	66665	53872	###	###	59356		93638	94570	93344	###	###	93851
5 Degree	64698	76567	74322	55895	###	67871		95787	97269	97860	95813	###	96682
6 Degree	66113	81717	84341	79276	66728	75635		97769	100287	100776	100499	99640	99794
Bag 5													
2 Degree	28148	###	###	###	###	28148		62928	###	###	###	###	62928
3 Degree	35554	36315	###	###	###	35935		66093	65963	###	###	###	66028
4 Degree	39720	50831	40028	###	###	43526		67966	68483	68865	###	###	68438
5 Degree	41851	56937	56234	41093	###	49029		69427	71006	70535	70361	###	70332
6 Degree	43472	61882	66819	61967	46395	56107		71270	73164	73066	73458	70649	72321
Bag 6													
2 Degree	41533	###	###	###	###	41533		87077	###	###	###	###	87077
3 Degree	54800	53387	###	###	###	54094		91447	91867	###	###	###	91657

4 Degree	60636	70511	61522	###	###	64223		94778	96155	95386	###	###	95440
5 Degree	59932	77924	77307	62739	###	69476		96593	99385	99470	98315	###	98441
6 Degree	59825	80956	83367	77626	56223	71599		97754	100726	100996	100859	99135	99894
Bag 7													
2 Degree	25608	###	###	###	###	25608		56713	###	###	###	###	56713
3 Degree	28613	32464	###	###	###	30539		58286	59200	###	###	###	58743
4 Degree	28049	33972	25736	###	###	29252		58614	59760	57760	###	###	58711
5 Degree	29967	38208	37763	25545	###	32871		61033	60784	61067	58903	###	60447
6 Degree	30643	41354	43782	40081	31760	37524		62807	62611	62838	61591	61929	62355
Bag 8													
2 Degree	31309	###	###	###	###	31309		64113	###	###	###	###	64113
3 Degree	40155	40434	###	###	###	40295		67340	66765	###	###	###	67053
4 Degree	42976	52485	45599	###	###	47020		70093	69682	68716	###	###	69497
5 Degree	56892	67369	63324	49182	###	59191		72928	74628	73625	72035	###	73304
6 Degree	58630	71703	72873	64874	45592	62734		73897	75731	75341	73990	74459	74684
Bag 9													
2 Degree	25575	###	###	###	###	25575		40135	###	###	###	###	40135
3 Degree	36144	40016	###	###	###	38080		42753	42728	###	###	###	42741
4 Degree	33529	40351	30407	###	###	34762		42514	42642	41979	###	###	42378
5 Degree	44238	52319	51222	35972	###	45938		44260	45342	44645	44235	###	44621
6 Degree	46002	58087	62014	57093	43204	53280		46086	47351	46831	47058	46172	46700
Bag 10													
2 Degree	29603	###	###	###	###	29603		55328	###	###	###	###	55328
3 Degree	32899	38029	###	###	###	35464		57187	57673	###	###	###	57430
4 Degree	31463	45550	36941	###	###	37985		58794	60054	58953	###	###	59267
5 Degree	34673	43140	42899	31723	###	38109		59866	60044	60521	59255	###	59922
6 Degree	36225	47866	52297	46866	31967	43044		61807	62143	62998	62607	61634	62238
Bag 11													
2 Degree	30598	###	###	###	###	30598		58852	###	###	###	###	58852
3 Degree	35039	37114	###	###	###	36077		62224	61296	###	###	###	61760
4 Degree	35752	45671	37419	###	###	39614		64191	63099	64293	###	###	63794
5 Degree	45500	57202	55732	42076	###	50128		67298	68466	66900	67542	###	67552
6 Degree	46025	58597	62882	58481	40414	53280		68207	69542	68670	69640	68253	68862
Bag 12													
2 Degree	26951	###	###	###	###	26951		53714	###	###	###	###	53714
3 Degree	37857	35560	###	###	###	36709		57500	57836	###	###	###	57668
4 Degree	43123	51355	47951	###	###	47476		62571	63834	63689	###	###	63365

5 Degree	38818	50167	50891	44057	###	45983		62194	63404	63863	63042	###	63126
6 Degree	39741	53622	57547	56931	45036	50575		64704	66062	66877	67064	66198	66181
Bag 13													
2 Degree	24001	###	###	###	###	24001		60793	###	###	###	###	60793
3 Degree	34711	32833	###	###	###	33772		65434	64936	###	###	###	65185
4 Degree	38856	48334	36995	###	###	41395		68178	68766	67829	###	###	68258
5 Degree	35593	54313	54862	39196	###	45991		69352	71977	71827	70293	###	70862
6 Degree	35064	56164	60789	54772	34250	48208		70043	73220	73862	72991	71204	72264
Bag 14													
2 Degree	48580	###	###	###	###	48580		78106	###	###	###	###	78106
3 Degree	62882	65817	###	###	###	64350		84317	84541	###	###	###	84429
4 Degree	60921	72178	62738	###	###	65279		84149	85750	84725	###	###	84875
5 Degree	61832	76452	78120	66040	###	70611		87771	88293	89190	87598	###	88213
6 Degree	61316	78172	82993	80085	63305	73174		89041	90163	90782	90415	89104	89901
Bag 15													
2 Degree	17998	###	###	###	###	17998		68304	###	###	###	###	68304
3 Degree	18772	19410	###	###	###	19091		69502	70168	###	###	###	69835
4 Degree	26800	38342	40450	###	###	35197		74502	76411	76303	###	###	75739
5 Degree	34203	41680	44007	41804	###	40424		77391	77853	79019	78375	###	78160
6 Degree	32269	39316	41182	37181	37511	37492		76688	77089	77531	76347	78815	77294
Bag 16													
2 Degree	68258	###	###	###	###	68258		103746	###	###	###	###	103746
3 Degree	58920	60403	###	###	###	59662		103794	104931	###	###	###	104363
4 Degree	63112	76922	63790	###	###	67941		107516	108925	107570	###	###	108004
5 Degree	69100	93910	96267	76595	###	83968		112848	115298	116309	114441	###	114724
6 Degree	62672	88125	96444	93165	67662	81614		113269	115499	116720	115731	114676	115179
Bag 17													
2 Degree	28004	###	###	###	###	28004		53898	###	###	###	###	53898
3 Degree	25580	25423	###	###	###	25502		54871	54345	###	###	###	54608
4 Degree	27822	36248	29177	###	###	31082		56812	56992	57002	###	###	56935
5 Degree	29745	45613	46563	35347	###	39317		59301	60796	60484	60316	###	60224
6 Degree	29088	45376	51118	49386	33673	41728		59722	61248	61461	61721	61133	61057
Bag 18													
2 Degree	20971	###	###	###	###	20971		60105	###	###	###	###	60105
3 Degree	28568	30433	###	###	###	29501		64679	65007	###	###	###	64843
4 Degree	25499	33604	26226	###	###	28443		64796	65591	65403	###	###	65263
5 Degree	20754	30781	33343	23079	###	26989		63754	65773	66686	65898	###	65528

6 Degree	23475	38225	43914	38244	24569	33685		66910	69087	70381	70090	68590	69012
Bag 19													
2 Degree	52332	###	###	###	###	52332		88535	###	###	###	###	88535
3 Degree	67237	70135	###	###	###	68686		93513	94308	###	###	###	94310
4 Degree	69155	82270	67878	###	###	82101		95698	97527	96981	###	###	96735
5 Degree	68598	90342	92014	71711	###	80666		97379	101164	101202	99835	###	99895
6 Degree	70675	95907	103415	96550	73100	87929		99690	104135	104358	104493	102949	103125
Bag 20													
2 Degree	12581	###	###	###	###	12581		49768	###	###	###	###	49768
3 Degree	15849	16782	###	###	###	16316		51954	52214	###	###	###	52084
4 Degree	17761	24919	19737	###	###	20806		54070	54956	54980	###	###	54669
5 Degree	16473	27162	28501	20113	###	23062		55824	55642	56113	56207	###	55947
6 Degree	16433	28407	32159	29357	19490	25169		56946	56829	57305	57665	56149	56979
Bag 21													
2 Degree	56888	###	###	###	###	56888		100703	###	###	###	###	100703
3 Degree	65847	72792	###	###	###	69320		106971	108815	###	###	###	107393
4 Degree	73212	91591	75836	###	###	80213		109980	111824	110636	###	###	110813
5 Degree	80798	103582	104056	76281	###	91179		113837	116201	116513	114103	###	115164
6 Degree	84258	112272	119817	112767	86641	103151		117546	120533	121640	120185	119210	119823
Bag 22													
2 Degree	30084	###	###	###	###	30084		49232	###	###	###	###	49232
3 Degree	36074	37790	###	###	###	36932		51640	51552	###	###	###	51596
4 Degree	39608	47983	40955	###	###	42849		54132	54499	54453	###	###	54361
5 Degree	43118	52993	53814	41559	###	47871		55853	56596	56638	56190	###	56319
6 Degree	43409	55631	58121	54437	38634	50046		56560	57764	57893	58047	56496	57352
Bag 23													
2 Degree	11926	###	###	###	###	11926		56028	###	###	###	###	56028
3 Degree	15903	16439	###	###	###	16171		56762	58538	###	###	###	57650
4 Degree	18938	24011	29807	###	###	24252		59452	61552	61971	###	###	60992
5 Degree	18082	26617	27805	21994	###	23625		60850	61305	63498	60252	###	61476
6 Degree	17209	27233	31842	29950	19030	25053		61444	62268	64961	61990	63773	62887
Bag 24													
2 Degree	26647	###	###	###	###	26647		50221	###	###	###	###	50221
3 Degree	34183	34758	###	###	###	34471		53958	53944	###	###	###	53951
4 Degree	32298	39096	29193	###	###	33529		53993	54655	54025	###	###	54224
5 Degree	32848	43980	44283	32537	###	38412		55379	56607	56766	56223	###	56244
6 Degree	33291	46064	49096	45679	35741	41974		56804	58245	58793	58768	58505	58223

Bag 25													
2 Degree	10787	###	###	###	###	10787		64483	###	###	###	###	64483
3 Degree	13817	14935	###	###	###	14376		66522	65677	###	###	###	66100
4 Degree	15539	20531	14373	###	###	16814		67897	67059	68348	###	###	67768
5 Degree	16628	24588	24087	14167	###	19868		68730	69662	68696	69728	###	69204
6 Degree	17044	27226	29688	25459	15707	23025		69752	71041	69795	71318	70202	70422
Bag 26													
2 Degree	27084	###	###	###	###	27084		59047	###	###	###	###	59047
3 Degree	39875	38436	###	###	###	39156		63042	63281	###	###	###	63162
4 Degree	42442	48954	39806	###	###	43734		65194	65719	65348	###	###	65420
5 Degree	43210	57905	55428	41767	###	49578		66085	68085	68630	67379	###	67545
6 Degree	44227	62412	64466	58722	39977	53961		67494	69911	70430	69866	68657	69272
Bag 27													
2 Degree	26813	###	###	###	###	26813		53884	###	###	###	###	53884
3 Degree	27935	29084	###	###	###	28510		55057	55180	###	###	###	55119
4 Degree	33087	41970	31271	###	###	35443		57741	58332	57585	###	###	57886
5 Degree	30344	39206	37742	27441	###	33683		56621	57323	57463	56522	###	56982
6 Degree	31541	44304	46103	42880	32341	39434		58878	60175	60300	59531	57992	59375
Bag 28													
2 Degree	47070	###	###	###	###	47070		67239	###	###	###	###	67239
3 Degree	50132	49818	###	###	###	49975		71406	70774	###	###	###	71090
4 Degree	53444	67132	57935	###	###	59504		74406	74944	74693	###	###	74681
5 Degree	61946	73846	72945	56660	###	66349		77602	79224	78103	76976	###	77976
6 Degree	63211	76812	80926	76585	59449	71397		80207	81816	81603	81127	80743	81099
Bag 29													
2 Degree	45767	###	###	###	###	45767		98960	###	###	###	###	98960
3 Degree	54421	58178	###	###	###	56300		102533	103049	###	###	###	102791
4 Degree	58637	71015	56575	###	###	62076		105063	105834	105603	###	###	105500
5 Degree	63099	78932	77933	57128	###	69273		106484	109000	109561	108862	###	108477
6 Degree	64275	84086	86884	81194	57296	74747		108878	110851	111867	112129	110913	110928
Bag 30													
2 Degree	9919	###	###	###	###	9919		66121	###	###	###	###	66121
3 Degree	13591	13527	###	###	###	13559		67140	67702	###	###	###	67421
4 Degree	15397	20297	14071	###	###	16588		68103	68596	68153	###	###	68284
5 Degree	14564	24942	26367	15126	###	20250		69163	69898	70347	69947	###	69839
6 Degree	14518	26611	31312	27709	16643	23359		69855	70819	71417	71457	70444	70798

The total number of pixel errors according to translation based image synthesis algorithm.

Error I and II	No. of Pixel Errors (ERR-I)							No. of Pixel Errors (ERR-II)					
No. of Synthetic Views	1	2	3	4	5	Average of ERR-I		1	2	3	4	5	Average of ERR-II
Bag 1													
2 Degree	69291	###	###	###	###	69291		92802	###	###	###	###	92802
3 Degree	81207	84059	###	###	###	82633		97507	102020	###	###	###	99764
4 Degree	82168	90100	95718	###	###	89329		98907	99709	102540	###	###	100385
5 Degree	75940	90106	100075	111994	###	94529		95213	101392	105501	110612	###	103180
6 Degree	74052	88931	100074	111544	118440	98608		94771	101636	106242	111037	114030	105543
Bag 2													
2 Degree	55702	###	###	###	###	55702		89318	###	###	###	###	89318
3 Degree	52537	61191	###	###	###	56865		89522	91991	###	###	###	90757
4 Degree	53069	61271	67751	###	###	60697		89280	91657	95136	###	###	92024
5 Degree	48041	62221	71210	77131	###	64651		88485	92695	94849	97749	###	93445
6 Degree	48585	62265	71582	78246	83476	68831		88378	92024	95076	98234	99472	94637
Bag 3													
2 Degree	38407	###	###	###	###	38407		66897	###	###	###	###	66897
3 Degree	37674	47757	###	###	###	42716		66873	69178	###	###	###	68026
4 Degree	32923	45942	57723	###	###	45529		65420	68244	71811	###	###	68492
5 Degree	32209	44273	57663	67327	###	50368		65429	68313	71858	76716	###	70579
6 Degree	31479	41977	55489	65571	72219	53347		65248	67555	71042	74783	75934	70912
Bag 4													
2 Degree	55031	###	###	###	###	55031		90462	###	###	###	###	90462
3 Degree	57139	61518	###	###	###	59329		90485	91087	###	###	###	90786
4 Degree	54757	60641	64002	###	###	59800		89683	91288	93068	###	###	91346
5 Degree	52545	60819	67159	70866	###	62847		88469	91569	94034	95953	###	92506
6 Degree	41788	56590	66317	73625	77395	63143		84932	90363	94072	97326	98401	93019
Bag 5													
2 Degree	26137	###	###	###	###	26137		65764	###	###	###	###	65764
3 Degree	31762	39094	###	###	###	35428		67838	69390	###	###	###	68614
4 Degree	27654	38737	50593	###	###	38995		66899	69428	72426	###	###	69584
5 Degree	28574	38957	49625	59585	###	44185		67676	70133	71598	74816	###	71056
6 Degree	25855	37342	50492	60839	68534	48612		67181	69607	71157	74837	75830	71722
Bag 6													
2 Degree	52168	###	###	###	###	52168		90907	###	###	###	###	90907
3 Degree	46029	60223	###	###	###	53126		91971	92296	###	###	###	92133

4 Degree	55525	63703	74717	###	###	64648		90584	96049	99467	###	###	95367
5 Degree	54843	63748	77698	85829	###	70530		90813	95106	99712	101961	###	96898
6 Degree	52935	62726	74861	84125	87965	72522		89599	94544	98344	101597	102087	97234
Bag 7													
2 Degree	29098	###	###	###	###	29098		58329	###	###	###	###	58329
3 Degree	29805	32094	###	###	###	30950		58341	60437	###	###	###	59389
4 Degree	27425	31265	35491	###	###	31394		58980	59255	60973	###	###	59736
5 Degree	26896	30925	36477	41063	###	33840		58126	59740	60513	61671	###	61671
6 Degree	26539	30196	36171	45206	48026	37228		58167	60889	61733	62899	64975	61733
Bag 8													
2 Degree	52044	###	###	###	###	52044		72610	###	###	###	###	72610
3 Degree	49869	60503	###	###	###	55186		72881	74987	###	###	###	73934
4 Degree	50555	58280	63935	###	###	57590		73159	75108	76785	###	###	75017
5 Degree	43140	54282	63747	72711	###	58470		72712	74983	75671	77722	###	75272
6 Degree	42491	54910	63443	72977	78277	62420		72368	73432	76816	77242	79254	75822
Bag 9													
2 Degree	43101	###	###	###	###	43101		44244	###	###	###	###	44244
3 Degree	40795	45740	###	###	###	43268		44301	45522	###	###	###	44911
4 Degree	41208	43253	48249	###	###	44237		43648	48864	46455	###	###	46322
5 Degree	36911	48238	56852	64312	###	51578		43982	46775	46882	48733	###	46593
6 Degree	38503	45970	52101	59362	63239	51835		429079	447183	46861	48536	51739	46980
Bag 10													
2 Degree	39687	###	###	###	###	39687		56344	###	###	###	###	56344
3 Degree	45848	49321	###	###	###	47585		57699	59459	###	###	###	58579
4 Degree	44847	48882	56463	###	###	50064		57555	59423	61792	###	###	59590
5 Degree	39482	49692	55533	61682	###	51597		56059	58914	61610	63345	###	59982
6 Degree	35505	45975	51066	57234	61682	50292		55402	58094	60218	61883	63461	59812
Bag 11													
2 Degree	38138	###	###	###	###	38138		64926	###	###	###	###	64926
3 Degree	36572	48723	###	###	###	42648		65652	67177	###	###	###	66415
4 Degree	36101	48614	61345	###	###	48687		65525	66965	70746	###	###	67745
5 Degree	36857	53450	63815	73959	###	57020		65739	70536	72169	75424	###	70967
6 Degree	41088	55524	66649	76183	82813	64451		66570	70408	72747	75952	78277	72791
Bag 12													
2 Degree	57636	###	###	###	###	57636		62598	###	###	###	###	62598
3 Degree	53779	62910	###	###	###	58345		60215	65999	###	###	###	63107
4 Degree	52044	61674	69405	###	###	61041		59475	65205	68654	###	###	64445

5 Degree	54319	59743	66696	71503	###	63065		57882	64498	66628	70054	###	64766
6 Degree	56207	53062	68326	67981	71928	63501		55728	62065	64517	68753	70448	64302
Bag 13													
2 Degree	22388	###	###	###	###	22388		61496	###	###	###	###	61496
3 Degree	22310	40426	###	###	###	31368		66203	71203	###	###	###	63107
4 Degree	27499	41412	52610	###	###	40507		66657	71172	74754	###	###	70861
5 Degree	29887	40417	52452	61867	###	46156		66495	71135	74819	77675	###	72531
6 Degree	21062	38308	52530	62032	69663	48719		64873	70626	74829	77899	80388	73723
Bag 14													
2 Degree	71863	###	###	###	###	71863		84227	###	###	###	###	84227
3 Degree	72787	78296	###	###	###	75542		84540	87451	###	###	###	85996
4 Degree	70691	76741	80305	###	###	75912		83613	86634	88333	###	###	86193
5 Degree	72134	79054	83972	87349	###	80627		84012	87420	89671	91357	###	88115
6 Degree	70045	76665	82187	86086	88104	80617		82957	86090	88832	90168	91150	87839
Bag 15													
2 Degree	28456	###	###	###	###	28456		78950	###	###	###	###	78950
3 Degree	27141	34307	###	###	###	30724		78500	82362	###	###	###	80431
4 Degree	30830	39503	47056	###	###	39130		79505	83503	85969	###	###	82992
5 Degree	30307	39724	46254	52499	###	42196		78998	82663	85925	87733	###	83830
6 Degree	21560	32196	41288	47377	58331	40150		76504	79956	83541	85334	89229	82913
Bag 16													
2 Degree	70647	###	###	###	###	70647		100996	###	###	###	###	100996
3 Degree	69762	89504	###	###	###	79633		101991	109926	###	###	###	105959
4 Degree	65582	82690	92803	###	###	80358		102777	104651	109829	###	###	105752
5 Degree	69668	83393	95306	106816	###	88796		101924	107457	111805	116385	###	109393
6 Degree	87662	100746	111399	121485	127408	109740		108424	115111	120281	124153	128088	119211
Bag 17													
2 Degree	39276	###	###	###	###	39276		56649	###	###	###	###	56649
3 Degree	39977	46224	###	###	###	43101		56840	58939	###	###	###	57890
4 Degree	40157	46417	54009	###	###	46861		56995	58985	62300	###	###	59427
5 Degree	38596	45825	53149	55773	###	48336		54716	57987	61362	64823	###	59722
6 Degree	37143	44657	50193	57168	61755	50183		56137	59139	60577	63469	65276	60920
Bag 18													
2 Degree	22536	###	###	###	###	22536		68981	###	###	###	###	68981
3 Degree	21003	27014	###	###	###	24009		68020	70483	###	###	###	69252
4 Degree	19691	26098	31424	###	###	25738		67260	69992	72504	###	###	69919
5 Degree	23264	26941	33871	39782	###	30965		69099	71012	73012	75139	###	72066

6 Degree	23404	26615	31986	37358	43138	32500		68922	71062	72977	75279	77136	73075
Bag 19													
2 Degree	72185	###	###		###	72185		92779	###	###	###	###	92779
3 Degree	69541	80457	###	###	###	74999		92083	95275	###	###	###	93679
4 Degree	66360	77295	87300	###	###	76985		90798	93617	97576	###	###	93997
5 Degree	61007	74272	87341	96891	###	79878		89659	94564	98982	103113	###	96580
6 Degree	50132	67936	84620	96786	103986	80692		86804	92793	98505	103408	106256	97553
Bag 20													
2 Degree	14170	###	###	###	###	14170		55252	###	###	###	###	55252
3 Degree	16038	21705	###	###	###	18872		55712	57601	###	###	###	56657
4 Degree	12498	21065	28032	###	###	20532		54889	57659	59990	###	###	57513
5 Degree	13494	21970	29335	35181	###	24995		54952	56574	59223	61286	###	58009
6 Degree	12800	21278	28524	34644	39038	27257		54733	56485	58925	60833	61979	58591
Bag 21													
2 Degree	80359	###	###	###	###	80359		99538	###	###	###	###	99538
3 Degree	72668	93610	###	###	###	83139		96903	104166	###	###	###	100535
4 Degree	64191	85660	100444	###	###	83432		95081	102056	107121	###	###	101419
5 Degree	74276	93646	108876	119377	###	99044		97156	104177	110062	114105	###	106375
6 Degree	78868	99560	116076	127756	136773	111807		100555	108520	115376	119982	124033	113693
Bag 22													
2 Degree	31872	###	###	###	###	31872		53238	###	###	###	###	53238
3 Degree	30624	44719	###	###	###	37672		52874	56884	###	###	###	54879
4 Degree	30197	44562	55233	###	###	43331		52844	56867	60090	###	###	56600
5 Degree	31098	43893	53069	60767	###	47207		52792	56557	59101	61892	###	57586
6 Degree	31269	44485	53496	61118	66020	51278		52850	56820	59136	62050	63251	58821
Bag 23													
2 Degree	16792	###	###	###	###	16792		65069	###	###	###	###	65069
3 Degree	15446	22662	###	###	###	19054		66820	70347	###	###	###	68584
4 Degree	15508	28175	37007	###	###	26897		67095	71311	72104	###	###	70170
5 Degree	20315	24590	29114	35602	###	27405		68041	70465	72511	72862	###	70970
6 Degree	16685	23614	28514	34442	37328	28117		67303	70035	72834	73322	75917	71882
Bag 24													
2 Degree	37497	###	###	###	###	37497		50954	###	###	###	###	50954
3 Degree	39425	44487	###	###	###	41956		51635	53700	###	###	###	52668
4 Degree	37528	42741	48344	###	###	42871		50925	52943	54976	###	###	52948
5 Degree	35513	39739	50491	51599	###	44336		49174	50212	53232	56293	###	52228
6 Degree	32035	37667	49815	48534	51117	43834		49845	50713	51537	54725	55736	52511

Bag 25													
2 Degree	14631	###	###	###	###	14631		68793	###	###	###	###	68793
3 Degree	11354	19138	###	###	###	15246		69703	71055	###	###	###	70379
4 Degree	9088	17933	26416	###	###	17812		68985	71017	73598	###	###	71200
5 Degree	10176	18914	27499	34628	###	22804		69858	72464	74035	76253	###	73153
6 Degree	18550	31866	40566	47911	52941	38367		72404	75729	77516	80053	81288	77398
Bag 26													
2 Degree	38536	###	###	###	###	38536		65808	###	###	###	###	65808
3 Degree	34726	49391	###	###	###	42059		64974	68288	###	###	###	66631
4 Degree	33842	48938	60959	###	###	47913		64699	67740	70749	###	###	67729
5 Degree	37767	50289	62030	72457	###	55636		65893	69190	72571	75089	###	70686
6 Degree	27625	48080	61376	70527	79260	57374		61890	67551	70747	72883	75577	69730
Bag 27													
2 Degree	27607	###	###	###	###	27607		53946	###	###	###	###	53946
3 Degree	26602	37544	###	###	###	32073		53181	55865	###	###	###	54523
4 Degree	25575	37043	43475	###	###	35364		52957	55744	58008	###	###	55570
5 Degree	29743	37615	45246	50973	###	40894		53919	56299	58813	60687	###	57430
6 Degree	20868	32472	40798	47390	51966	38699		52082	54938	57757	59871	61258	57181
Bag 28													
2 Degree	52277	###	###	###	###	52277		72990	###	###	###	###	72990
3 Degree	59106	71482	###	###	###	65294		75349	80024	###	###	###	77687
4 Degree	50468	64949	76406	###	###	63941		73248	77690	82879	###	###	77939
5 Degree	49948	60147	72148	77262	###	64876		67551	74067	78830	82585	###	75758
6 Degree	49534	62617	72422	81110	87637	70664		72243	77981	81590	85271	88717	81160
Bag 29													
2 Degree	63496	###	###	###	###	63496		102793	###	###	###	###	102029
3 Degree	59107	72725	###	###	###	65916		100079	103979	###	###	###	102777
4 Degree	58777	64494	74770	###	###	66014		99052	103123	106156	###	###	102793
5 Degree	45571	61671	76710	87378	###	67833		98342	103396	105317	108823	###	103970
6 Degree	56363	74956	88035	100186	107206	85349		99838	106000	109912	114173	116058	109196
Bag 30													
2 Degree	18881	###	###	###	###	18881		73570	###	###	###	###	73570
3 Degree	14290	22478	###	###	###	18384		71846	74636	###	###	###	73241
4 Degree	15993	28057	29917	###	###	24656		76160	74282	76082	###	###	75508
5 Degree	14508	20322	30112	37485	###	25606		72552	74083	76768	78530	###	75483
6 Degree	13946	20151	29775	37231	42373	28695		72333	73960	76504	78421	79086	76060